Large Eddy Simulation of the Flow and Mixing Field in an Internal Combustion Engine

Vom Fachbereich Maschinenbau
an der Technischen Universität Darmstadt
zur
Erlangung des Grades eines Doktor-Ingenieurs (Dr.-Ing.)
genehmigte

D i s s e r t a t i o n
vorgelegt von

M.Sc. Dmitry Goryntsev
aus Sankt Petersburg (Russische Föderation)

Berichterstatter:	Prof. Dr.-Ing. Johannes Janicka
Mitberichterstatter:	Prof. Dr. rer. nat. Michael Schäfer
Tag der Einreichung:	06.11.2007
Tag der mündlichen Prüfung:	18.12.2007

Darmstadt 2007
D 17

Acknowledgements

The present work has been carried out for the last five years during my scientific fellowship at the Institute of Energy and Powerplant Technology (EKT), Darmstadt University of Technology. First of all I would like to express my sincere gratitude to the head of the Institute and my supervisor Prof. Dr.-Ing. Johannes Janicka for his excellent guidance, interminable enthusiasm, constant helpful advice, precious discussions and encouragement during the whole period of my scientific research at Darmstadt University. I also would like to thank him for the chance to work in his team, to take part in numerous conferences where I had the possibility to present my scientific results, to obtain a doctoral degree at his institute and to get acquainted with the world of IC-engines.

I wish to thank Prof. Dr. rer. nat. Amsini Sadiki and Dr. rer. nat Andreas Dreizler for the inspirational discussions and many useful suggestions while working on this thesis. I would like to acknowledge Prof. Dr. rer. nat. Michael Schäfer for his willingness to report on my work.

This work would not have been possible without a close collaboration with Dr.-Ing. Markus Klein. I would like to express my appreciation for his constant readiness to provide help and to discuss the present work notwithstanding him being busy. His important advice and suggestions have gratefully influenced this work. I express also my acknowledgment for his willingness to review this manuscript.

I want to thank especially Dr. Alexander Maltsev for spending his time reading my thesis and giving me important advice. Furthermore, my special thanks go to my colleagues at University Darmstadt Dr. Elena Schneider, Dr. Martin Freitag, Michael Hage, Benjamin Böhm, Andreas Ludwig, Dr. Bernhard Wegner, Dr. Ying Huai and Dr. Rajani Akula and many others, due to their substantial assistance and at the same time critical comments I was able to work in a pleasant atmosphere on the one hand and spurring on further efforts on the other hand. I also would like to express my hearty thanks to my room colleagues Desislava Dimitrova, Lukas Schneider and Christof Kittler, whose cheerful mood and humor made me enjoy my everyday life and work at EKT.

My appreciations are extended to all my friends, who supported me mentally and with their precious advice during the whole period of my scientific research, especially, Dr. Mikhail Sizov, Dr. Alexander Yun, Dmitro Dzivenko, Igor Abakumov, Kirill Nazarov and Rodion Riabzev.

I am truthfully thankful to my family and especially to my girlfriend Margaret Voznesenskaya for their enormous trust in me, their help and support and also their comprehension, when I was unattainable during the crucial phase of working on my thesis. They always managed to cheer me up in difficult moments and I really appreciate their faith and patience and dedicate this work to them.

Hiermit erkläre ich, dass ich die vorliegende Dissertation selbstständig verfasst und keine anderen als die angegebenen Hilfsmittel verwendet habe. Ich habe bisher noch keinen Promotionsversuch unternommen.

Dmitry Goryntsev
Darmstadt, October 2007

Quam quisque norit artem, in hac se exerceat!

Cicero

Contents

Nomenclature **VII**

1. Introduction **1**
1.1. Motivation . . . 1
1.2. Description of in-cylinder flow . . . 4
1.3. Cycle-to-cycle fluctuations . . . 5
1.4. Literature review . . . 7
1.4.1. Single-phase flow . . . 7
1.4.2. Multiphase flow . . . 9
1.4.3. Experimental investigations of cycle-to-cycle variations . . . 11
1.4.4. Supplementary literature . . . 12
1.5. Objectives and strategy . . . 13
1.6. Structure of the manuscript . . . 14

2. The governing equations for turbulent multiphase flow **15**
2.1. The fluid phase equations . . . 16
2.2. Turbulence . . . 17
2.2.1. Turbulent scales . . . 18
2.2.2. Reynolds averaged Navier-Stokes equations . . . 20
2.2.3. Direct numerical simulation . . . 21
2.2.4. Large eddy simulation . . . 21
2.3. Spray dynamics . . . 25
2.3.1. The spray equations . . . 25
2.3.2. Collision model . . . 26
2.3.3. Breakup model . . . 27
2.3.4. Evaporation model . . . 28
2.3.5. Droplet acceleration . . . 28
2.3.6. Gas-spray interaction terms . . . 29
2.3.7. Spray wall interaction . . . 29
2.4. Summary . . . 29

3. Model implementation and validation of the KIVA-3V-LES code **30**
3.1. An overview of the KIVA-3V code . . . 30
3.1.1. The numerical scheme . . . 30
3.1.2. Initial and boundary conditions . . . 34
3.2. Implementation of LES in KIVA-3V . . . 35
3.3. Validation of the KIVA-3V-LES code . . . 36
3.4. Parallelization based on the variation of initial conditions . . . 38
3.5. Summary . . . 42

4. Grid generation for internal combustion engines **43**
4.1. Overview of the existing grid generation tools for KIVA-3V . . . 43
4.1.1. KIVA preprocessor program K3PREP . . . 43
4.1.2. Ansys ICEM CFD mesh generator . . . 44

4.2. Generation of block-structured grids for realistic IC-engines 44
4.2.1. Limitations of the KIVA-3V program 46
4.2.2. Planning and building the block topology in ICEM CFD Hexa 47
4.2.3. Examples of grids for IC-engine geometries 50
4.3. Conclusions 52

5. Results and discussion: single-phase flow **53**
5.1. Configuration and numerical setup 53
5.2. Large eddy simulation of the single-phase flow in an IC-engine 55
5.2.1. Cycle-to-cycle fluctuations 56
5.2.2. Variability of global charge motion 70
5.2.3. Comparison of LES and PIV measurement data 71
5.2.4. Comparison of LES and RANS results 75
5.3. Conclusions 75

6. Verification of the results **77**
6.1. Theoretical background 77
6.2. The effect of mesh resolution on the flow field in a simplified engine geometry . . 78
6.3. Estimation of statistical errors 84
6.4. Estimation of modeling and numerical errors 85
6.5. Conclusions 87

7. Results and discussion: two-phase flow **90**
7.1. Calibration of the spray model 90
7.2. Large eddy simulation of an IC-engine considering two-phase flow 93
7.2.1. Evolution of the mixture formation process in an air-guided DISI IC-engine 94
7.2.2. Influence of cycle-to-cycle fluctuations on the mixing field 95
7.2.3. Comparison of LES and RANS results 101
7.3. Conclusions 104

8. Conclusions **105**

References **109**

Nomenclature

Latin symbols

Symbol	Definition	Unit
A_0	dimensionless constant	-
C_D	drag coefficient	-
C_S	Smagorinsky model parameter	-
c	arbitrary constant	-
c_p	heat capacity at constant pressure	$\mathrm{m}^2/\mathrm{s}^2 \cdot \mathrm{K}$
D	diffusion coefficient	m^2/s
d	domain dimension	m
E_{LESIQ}	LES index of quality	various
E_{SGMV}	systematic grid and model variation	various
E_w	turbulent kinetic energy density	$\mathrm{m}^3/\mathrm{s}^2$
$\mathbf{F}$	droplet acceleration term	m/s^2
$\mathbf{F}^s$	rate of gain per unit volume due to the spray	$\mathrm{kg}/\mathrm{s}^2 \cdot \mathrm{m}^2$
f	probability distribution function	-
g	gravity	m/s^2
h	enthalpy	$\mathrm{kg} \cdot \mathrm{m}^2/\mathrm{s}^2$
$\mathbf{I}$	unit tensor	-
I	specific internal energy	$\mathrm{kg} \cdot \mathrm{m}^2/\mathrm{s}^2$
I	moment of inertia	$\mathrm{kg} \cdot \mathrm{m}^2$
$\mathbf{J}$	heat flux vector	kg/s^3
J_w	wall heat flux	kg/s^3
K	thermal conductivity	$\mathrm{kg} \cdot \mathrm{m}/\mathrm{K} \cdot \mathrm{s}^3$
Kn	Knudsen number	-
k	turbulent kinetic energy	$\mathrm{m}^2/\mathrm{s}^2$
k_w	wave number	$1/\mathrm{m}$
L	characteristic length	m
L	angular momentum	$\mathrm{kg} \cdot \mathrm{m}^2/\mathrm{s}$
l	length scale	m
Nu	Nusselt number	-
$\mathbf{n}$	unit outward normal to the surface	m
Pr	Prandtl number	-
p	pressure	$\mathrm{kg}/\mathrm{s}^2 \cdot \mathrm{m}$
Q	source term	$\mathrm{kg}/\mathrm{m} \cdot \mathrm{s}^3$
R_0	universal gas constant	$\mathrm{J}/\mathrm{kmol} \cdot \mathrm{K}$
Re	Reynolds number	-

Symbol	Definition	Unit
r	droplet radius	m
S_{ij}	rate-of-strain tensor	1/s
SR_z	swirl number	-
T	temperature	K
TR_x	sideways-tumble number	-
TR_y	normal-tumble number	-
t	time	s
U	characteristic velocity	m/s
$\mathbf{u}$	velocity vector: $\mathbf{u} = u(x,y,z,t)\mathbf{i} + v(x,y,z,t)\mathbf{j} + w(x,y,z,t)\mathbf{k}$	m/s
u_p	mean piston speed	m/s
u_r	fluid velocity relative to the grid velocity	m/s
u,v,w	velocity components	m/s
$\mathbf{x}$	position vector: $\mathbf{x} = x\mathbf{i} + y\mathbf{j} + z\mathbf{k}$	m
x,y,z	spatial coordinates	m
W	molecular weight	kg/mol
We	Weber number	-
w_b	mean streamwise velocity	m/s
w_τ	mean friction velocity	m/s

Greek symbols

Symbol	Definition	Unit
α	model variation factor	-
α	parallel fraction	-
β	grid refinement factor	-
ε	turbulent kinetic energy dissipation rate	m^2/s^3
λ	relative air/fuel ratio	-
λ_{free}	mean free part of molecules	m
μ	dynamic fluid viscosity	$kg/m \cdot s$
ν	kinematic fluid viscosity	m^2/s
ν_{eff}	effective viscosity	m^2/s
ν_τ	turbulent viscosity	m^2/s
ρ	density	kg/m^3
ρ_m	mass density of species m	kg/m^3
$\boldsymbol{\sigma}$	viscous stress tensor	$kg/s^2 \cdot m$
τ	time scale	s
τ_{ij}	subgrid stress tensor	m^2/s^2
ω	engine speed	rad/s

Symbol	Definition	Unit
Δ	filter width	m
Δ	grid size	m
Δt	time step	s

Operators

Operator	Definition
$\mathbf{R}$	rotation matrix
δ	Dicar delta function
∇	vector operator: $\nabla = \mathbf{i}\frac{\partial}{\partial x} + \mathbf{j}\frac{\partial}{\partial y} + \mathbf{k}\frac{\partial}{\partial z}$

Subscripts

Subscripts	Definition
bu	breakup
coll	collision
d	droplet quantity
i	integral scale
i, j, k	coordinate directions
inj	injection
k	Kolmogorov scale
m	species *m*
mean	averaged quantity
n	cycle number
rms	root mean square
τ	Taylor scale

Superscripts

Superscripts	Definition
c	source terms due to chemistry
s	source terms due to spray

Abbreviations

Abbreviations	Definition
ALE	Arbitrary Lagrangian-Eulerian
BDC	Bottom Dead Center
CA	Crank Angle
CAD	Computer-Aided Design
CFD	Computational Fluid Dynamics
CFL	Courant-Friedrichs-Lewy
CPU	Central Processing unit / Processor
DDM	Discrete Droplet Model
DISI	Direct Injection Spark Ignition
DNS	Direct Numerical Simulation
DSMC	Direct Simulation Monte Carlo
FID	Flame Ionization Detection
FSI	Fuel Stratified Injection
FVM	Finite Volume Method
GDI	Gasoline Direct Injection
HC	Hydrocarbon
IC	Internal Combustion
ICE	Internal Combustion Engine
LCV	Laser Correlation Velocimetry
LDA	Laser Doppler Anemometry
LDV	Laser Droplet Velocimetry
LEM	Linear Eddy Model
LES	Large Eddy Simulation
NO_x	Nitrogen Oxides
PDA	Phase Doppler Anemometry
PDC	Partial Donor Cell
PFI	Port Fuel Injection
PIV	Particle Image Velocimetry
QSOU	Quasi Second Order Upwind
RANS	Reynolds Averaged Navier-Stokes
rms	Root Mean Square
RNG	ReNormalization Group
rpm	Revolutions per Minute
SIMPLE	Semi-Implicit Method for Pressure-Linked Equations
SGS	Subgrid-Scale
TAB	Taylor Analogy Break-up
TDC	Top Dead Center
VCM	Variable Charge Motion

Chapter 1

Introduction

1.1. Motivation

The call for environmentally compatible and economical vehicles, still satisfying demands for high performance, necessitates immense efforts to develop innovative engine concepts. Whereas direct injection gasoline engines promise considerable fuel savings, they are prone to large variations in the flow and mixing field which may lead to incomplete combustion. Modern internal combustion (IC) engine concepts like the Gasoline Direct Injection (GDI) offer a great chance to meet current and future emission standards. Especially air-guided direct injection systems used to instantiate stratified charge at part load allow for an optimised fuel consumption and a low level of emissions. During this crucial process, the engine is very sensitive to cycle-to-cycle variations of the flow and mixing field. These fluctuations may result in combustion failures leading to a total loss of the energy stored in a full cylinder load and to the ejection of unburnt hydrocarbons into the environment.

Due to the extreme conditions inside a typical IC-engine (high combustion temperatures and pressures, precipitation of soot and other combustion products, etc.) experimental techniques are sometimes limited in approaching the above mentioned problem. Alternatively, computer simulations (Computational Fluid Dynamics, CFD) offer the opportunity to carry out repetitive parameter studies with clearly defined boundary conditions in order to investigate various configurations.

This work is dedicated to the detailed investigation of the phenomenon of cycle-to-cycle variations in a realistic IC-engine in order to achieve a better understanding of their nature, origin and their influence on the flow and mixing field within a combustion chamber, and also in order to create a base for future improvements. The Large Eddy Simulation (LES) method has been used to carry out the investigations of a realistic internal combustion engine geometry. The choice of the method was, on the one hand, determined by the following factors: complexity of geometry, highly unsteady processes in the combustion chamber, etc. On the other hand, it has been shown in a number of research works [57, 169] that the LES technique has the potential to simulate such highly unsteady and complex phenomena accurately.

As it is known, turbulent flows are very complex and represent a highly unsteady, always three-dimensional motion which consists of eddies with a wide spectrum of sizes. CFD offers various methods for the investigation of turbulent flows including mass and heat transfer. The most widespread approaches from the practical point of view are the Reynolds averaged Navier-Stokes equations (RANS) methodology and LES. Previous studies [58, 59] of the author as well as a literature review [144] have shown that the commonly used RANS turbulence approach is not able to capture the highly unsteady flow field in an IC-engine set-up. The RANS approach provides a good prediction of the mean flow structure inside the combustion chamber, but all information relative the unsteady effects, especially the cycle-to-cycle variations, is lost in this process. The necessity of modeling the whole turbulent energy spectrum is the second severe restriction of this approach. Nevertheless, the RANS modeling approach based on different variations of the $k-\varepsilon$ model has been most frequently used to predict various engineering turbulent flows in industrial applications. The popularity of this method is caused by advantages like fast turn around times due to moderate mesh resolution and the possibility to calculate a 3D sector mesh or a 2D geometry instead of considerating the whole 3D computational domain.

However, due to recent progresses in computer power LES may become suitable to engineering applications in the near future.

Direct Numerical Simulation (DNS) solves the full instantaneous three dimensional Navier–Stokes equations without introducing any model for turbulent motion and provides detailed information over all flow parameters. Since all the scales of motion have to be resolved, DNS has a stringent restriction in terms of Reynolds number. Such calculations are very expensive with reference to memory requirements and they are very time consuming. DNS can be realized for a few practical applications at moderate Reynolds numbers only but at present time it is obviously not the method for engineering calculations. As it has been mentioned in the work of Piomelli [131], DNS can be mainly used as a tool for investigating the physics of turbulence. The main advantage of DNS consists in the lack of the requirement of models for turbulence and combustion. This makes DNS useful for studying and developing new models.

Large eddy simulation is based on resolving the large-scale turbulent motion while the small subgrid scales of motion are modelled, in other words the complexity and accuracy of LES is between RANS and DNS. The principal advantages of LES over RANS are the capability of resolving the unsteady features of turbulent motion over a wide spectrum of scales and reduction of the modeling impact on the predicted results. Compared to RANS, the LES approach provides higher prediction accuracy and allows for a simplified modeling of turbulent effects in single- and multiphase reacting flows. In comparison with DNS, LES allows simulating flows at higher Reynolds numbers. LES is considerably more expensive than RANS techniques especially for one- or two-dimensional steady flows. The LES approach demands high resolution computational grids in order to resolve the scales in the inertial range together with small time steps. LES always requires the consideration of the full three-dimensional configuration. During a long time the major limitation for applying LES to industrial configurations was the high computational costs.

The utilization of LES to industrial applications became possible in connection with large progresses in computer performance, parallel calculations and advanced numerical methods which are able to exploit efficiently the computational resources [161]. Presently LES is a powerful engineering tool for analyzing of complex turbulent flows including heat and mass transfer, aerodynamic noise generation, combustion and so forth. A number of research works, e.g. [30, 66, 170] confirms the possibility of using LES to investigate flow, mixing and combustion in reciprocating engines. Successful application of LES to engine flows has enhanced the understanding of in-cylinder turbulence generation, integral time and length scales, heat and mass transfer rates, reaction rates and cycle-to-cycle variations.

The current study is focused on the consideration of a realistic four-stroke Direct Injection Spark Ignition (DISI) engine with an air-guided tumble system [132], where the liquid fuel is directly injected into a combustion chamber and in-cylinder charge motion is used for mixture preparation. Schematically an air-guided DISI engine is shown in figure 1.1. A detailed description and classification of DISI engines as well as a review of automotive history is given in [189]. Overall information about the fundamentals of IC-engines can be found in [68]. A review of the most prominent recent technological developments with reference to improvement of parameters of IC-engines is given in [13, 90].

Internal combustion engines arose from a simple concept with a few moving parts more than 100 years ago. Technological progress allowed IC-engines to become one of prime sources of motive power while significantly increasing the complexity of combustion systems. Modern DISI engines have an essential potential for performance optimization, e.g. to increase fuel economy, reduce emission and so on. In general, there are three basic concepts of combustion chambers of DISI engines that provide an ignitable fuel stratification to the spark plug at the time of ignition [16]. Figure 1.2 shows wall-guided (a), air-guided (b) and spray-guided (c) direct injection combustion systems. All of these concepts are characterized by the geometry of the piston-bowl, location of the spark plug and by the type and arrangement of the injector.

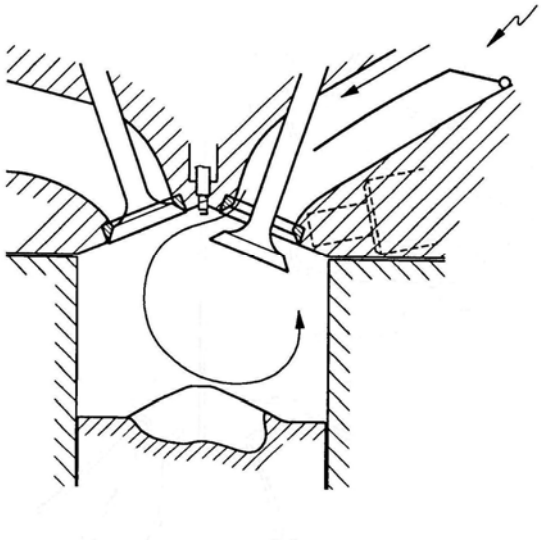

Figure 1.1: Tumble air motion and particularly shaped piston crown for a petrol DISI IC-engine.

The wall-guided concept is the so-called first generation of DISI engines (figure 1.2.a), where the stratified charge is formed by directing the fuel spray towards a piston crone. As a rule, the fuel spray is reflected from the piston bowl towards the spark plug. Wall-guided direct injection provides a good ignition stability and fuel economy gain of the order of 10% compared to Port Fuel Injection (PFI) engines [64, 188]. The main drawback of the system consists in the effects of liquid fuel film on the piston surface. Wall-guided systems produce also high amounts of unburned hydrocarbon (HC) and soot emissions mainly due to poor mixture stratification at low loads and ineffective mixture homogenization at high loads [33]. Wall-guided systems were the most widespread in the year 2000 in engine development and currently they are used in Mitsubishi, Peugeot, Toyota, Volkswagen, etc. production engines.

In the air-guided system (figure 1.2.b) the intake flow, generated by specific intake port geometries and supported by the geometry of a piston, contributes to formation of a tumble flow in the combustion chamber delivering the fuel to the spark plug. The in-cylinder charge motion (swirl and tumble) is used for spray deflection and mixture preparation. The air-guided charge motion concept can be referred to the current generation with high fuel economy gains relative to PFI engines.

a) b) c)

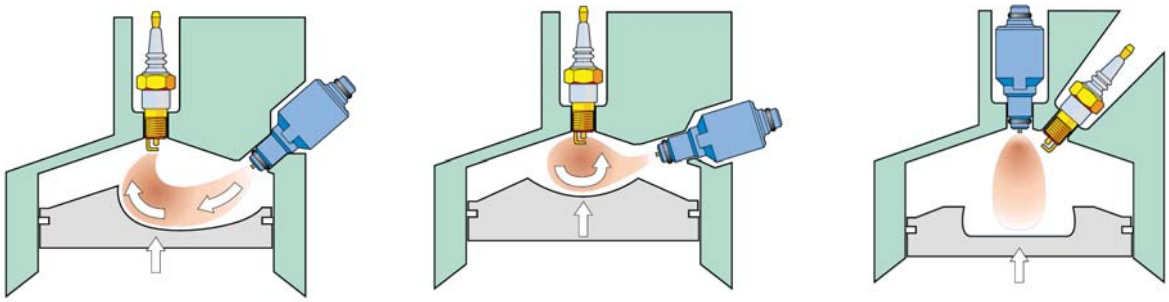

Figure 1.2: Classification of direct injection combustion systems. a) Wall-guided system; b) Charge motion or air-guided system; c) Spray / jet guided fuel injection system. Figures taken from [102].

The spray-guided concept (figure 1.2.c) is based on high-pressure electronic injectors, which provide a well define fuel spray, i.e. the spray is directly targeted towards the spark plug. Spray-guided engines provide sufficiently low soot and hydrocarbon emissions, wide stratified charge operating range with up to 15% better fuel economy compared to PFI engines. The spray-guided concept was introduced by Daimler-Chrysler AG with piezoelectric injection in 2005. Daimler-Chrysler AG and BMW Group use currently spray-guided injection systems coupled with piezoelectric injectors in production while further research with multi-hole injectors is being carried out.

1.2. Description of in-cylinder flow

The in-cylinder charge motion often plays a dominant role in processes of preparation and conveyance of fuel mixture towards the spark plug in DISI engines. Air motion in the combustion chamber is three-dimensional, highly turbulent and includes a wide spectrum of length and time scales. In a macroscopic way it can be characterized as a combination of swirl, sideways-tumble and normal-tumble (also known as squish) [68], which are schematically shown in figure 1.3.

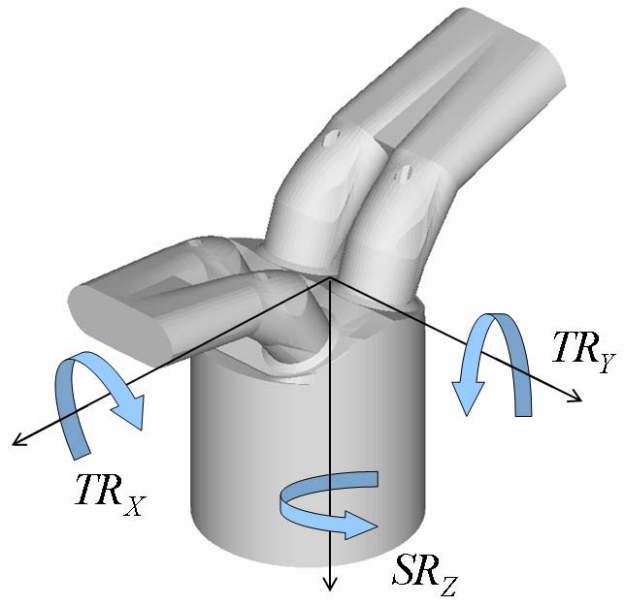

Figure 1.3: Definition of in-cylinder flow: sideways tumble TR_X, normal tumble TR_Y and swirl SR_Z.

Swirl is defined as the rotation of the charge motion around the cylinder axis. It is mostly formed during intake stroke by the incoming flow into the combustion chamber possessing an initial angular momentum. The swirl, quantified with the swirl number SR_z, is one of the important parameters which enhances mixing during the intake and compression strokes. The components of motion around the specific axes that are perpendicular to the cylinder axis are denoted as sideways- (TR_x) and normal-tumble (TR_y) as depicted in figure 1.3. Tumble motion appears during intake stroke and is generated by the inlet flow and piston geometry. Also it is used to provide the fuel vapor cloud to the spark plug. As well as swirl, tumble is defined by the radial air motion that occurs towards the end of the compression stroke, when the piston and the

cylinder head approach each other. At the end of the compression stroke (near top dead center, TDC) tumble motion disappears and transforms into turbulence.

In most DISI combustion systems the swirl and tumble motions are used together to gain the desired air-fuel mixing. It is used to precipitate the air-fuel mixing by growing turbulence levels and enhanced combustion processes. Further it was found, that it assists the mixture stratification, which is rather significant in stratified operation mode. In most recent developments tumble seems to be the predominant mechanism because it gives the benefit of high velocities close to the cylinder walls and improves evaporation of wall fuel films. Additionally, it directs the fuel vapor cloud to a centrally situated spark plug guided by piston geometry and motion.

A number of numerical works, e.g. [53, 82, 126, 165] as well as experimental researches, e.g. [1, 75, 93, 95, 137] are dedicated to investigation of the effects of swirl and tumble in-cylinder motion on characteristics of DISI engines. The overall conclusion is that in-cylinder tumble motion can be efficiently utilized in order to increase the turbulence intensity inside the combustion chamber near the end of compression stroke and, as a consequence, results in considerable improvements in the combustion process and engine performance.

1.3. Cycle-to-cycle fluctuations

One of the most important problems in the design of DISI engines is the cycle-to-cycle variations of the flow, mixing and combustion processes. As a result they lead to poor driveability, high fuel consumption with high hydrocarbons emissions as well as periodic oscillation in engine speed of DISI combustion systems at idle conditions [53, 120].

The following definition can be applied to characterize the cycle-to-cycle phenomenon: *Cyclic fluctuations are non-repeatable statistically independent variations of gas-dynamics parameters which are induced by the turbulence nature of the flow.* It means that during operation of a reciprocating IC-engine the flow fields or gas-dynamical parameters as well as the combustion within a given cylinder are different from cycle to cycle at the same crank angle.

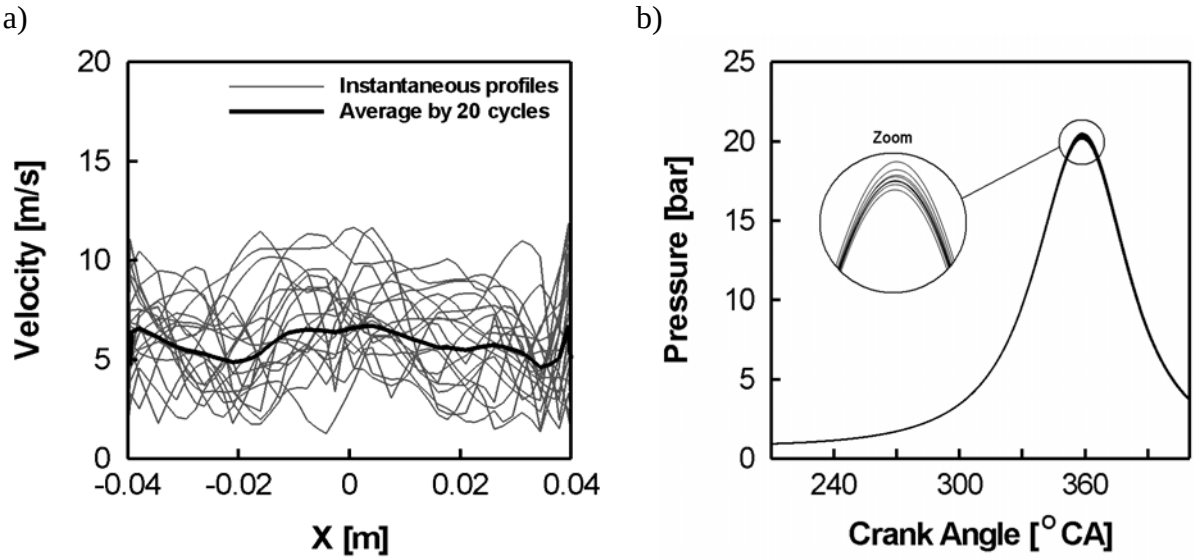

Figure 1.4: Cycle-to-cycle fluctuations in a combustion chamber; a) Cyclic velocity variations during compression stroke; b) Averaged in-cylinder pressure.

The phenomenon of cycle-to-cycle variations causes several important effects on an IC-engine. As an example, figure 1.4.a shows the instantaneous and mean velocity profiles obtained at the centerline in the cross section of a combustion chamber for 20 consecutive engine cycles. Figure 1.4.b presents the averaged cylinder pressure for 10 consecutive cycles. A misfire is one of the most extreme cases of cyclic variations. In that case cycle-to-cycle fluctuations are directly linked with variations in work output and, therefore, with the vehicle driveability [68]. The elimination of cycle-to-cycle fluctuations can lead to an increase in power output up to 10 percent [158] and an increase in fuel economy of up to 6 percent [99], but it should be also noted [163] that a total disappearance of this phenomenon is not desirable for the reason of engine management systems and knock control.

There are many factors that cause or influence the cycle-to-cycle fluctuations. Taking into account that the cyclic velocity variations are only a part of the more general case of combustion variations, these factors are in detail: 1) mixture composition, 2) geometrical factors, 3) cylinder charging, 4) ignition factors and 5) in-cylinder flow. A description of these phenomena is collected in table 1.1. More details can be found in [14, 120].

Table 1.1: Influencing factors for cycle-to-cycle fluctuations.

	Factor	**Description**
1.	Mixture composition	Air-fuel ratio, fuel type, mixture inhomogeneity, residual gas fraction.
2.	Geometrical factors	Shape of a combustion chamber, compression ratio, adjustable tumble-system.
3.	Cylinder charging	Fluctuations in the efficiency with which a cylinder sucks fresh gas are a cause of cycle-to-cycle fluctuations.
4.	Ignition	Type of ignition system, ignition timing, discharge characteristic, spark plug factor.
5.	In-cylinder flow	Turbulence intensity and scales, swirl and tumble flows.

The nature of cycle-to-cycle variations is of particular interest. Cyclic fluctuations arise even under constant conditions and consecutive engine cycles do not precisely repeat each other. The turbulence appears naturally from the intake processes, representing the random or in other words irregular nature, exciting various turbulent phenomena within the combustion chamber from cycle to cycle. Thereby, the random nature of turbulence is one fundamental reason of cycle-to-cycle variations in the combustion chamber.

Combustion variability as a more complicated process depends on many other factors such as in-cylinder flow field, fuel spray preparation, spark plug interaction, flame propagation and many others. Theoretically, each of them can be considered as a potential source of combustion variability but the dominant source of misfires at optimum spark timing is an unfavorable in-cylinder motion and cyclic variability of parameters near the spark plug.

In spite of a considerable amount of works dedicated to the characterization of cycle-to-cycle variations, only a few of them are dedicated to the study of this phenomenon using the LES method. In contrast to experimental works where in general a big number of engine cycles is taken into consideration [15, 27, 40] the investigations in numerical works are generally restricted to 10 consecutive cycles (see, for instance [132, 180]). This is evidently insufficient for generating qualitatively good statistical data. In the present work up to 50 consecutive engine cycles have been simulated for a realistic IC-engine configuration which is a considerable extension of previous work [57 - 62].

1.4. Literature review

The utilization of the RANS technique, mostly based on variants of the well-known $k-\varepsilon$ turbulence model, for investigations of IC-engines can be found in an extensive amount of publications, e.g. [117, 154]. RANS based approaches made a big contribution to the advances in IC-engine modeling [30, 184]. At present the number of RANS applications to IC-engines seems to decrease. In one of the more recent works [126] the flow characteristics inside the cylinder of a heavy-duty direct injection Diesel engine with different combustion chambers were analyzed by using RANS and compared with Laser Droplet Velocimetry (LDV) measurements. The flow characteristics inside the cylinder equipped with different piston configuration were also compared. The achieved results confirmed that the piston geometry had little influence on the in-cylinder flow during the intake stroke and the first part of compression stroke, while the bowl shape plays a significant role near TDC and in the early stage of the expansion stroke.

As it was mentioned above, in connection with the lack of information available in RANS together with recent advances in computer power, the LES technique is getting more and more adopted in industrial applications. At present the overwhelming majority of numerical researches related to engines is carried out using this method. Some of the most interesting works regarding the investigation of IC-engines will be presented in the following. The overview will be split in four subsections: single-phase flow, two-phase flow, experimental works and supplementary literature.

1.4.1. Single-phase flow

Relatively recently LES was applied widely to the study of in-cylinder flows. In the view of it, the overwhelming part of these studies deals with motored engines without combustion and without spray dynamics. The prerequisites of using LES for in-cylinder flows, advantages and disadvantages of LES and RANS approaches were examined by Haworth [65]. This work presents also a discussion about LES, various subgrid-scale (SGS) models and their application to complex flows such as occurring in IC-engines. A short discussion regarding the nature of cycle-to-cycle fluctuations of in-cylinder flow and combustion is also presented. It is concluded that cyclic flow variability is nothing more than a result of large-length-scale, long-time-scale turbulence. Celik et al. [29] reported about application of the KIVA program to the prediction of in-cylinder turbulence for IC-engines. The code has been extended to LES by integration of several subgrid scale models. Some preliminary results from an on-going study to predict turbulent fluctuations, and the statistics of turbulence quantities in the combustion chamber without consideration of the cycle-to-cycle variations are discussed. At the same time the work of Haworth and Jansen [66] presents the results of LES in a reciprocating IC-engines based on three various SGS turbulence models (constant-coefficient Smagorinsky, dynamic Smagorinsky and Lagrangian dynamic Smagorinsky model). Quantitative results are presented for three canonical flows and for a simplified piston-cylinder assembly with moving piston and fixed central valve. Computations are compared with experimental results, with direct-numerical simulation data, and with rapid-distortion theory where appropriate. The conclusion is drawn that LES is a powerful tool in understanding and predicting in-cylinder processes in reciprocating engines. In the past 10 years a number of research works have been published on the application of LES to in-cylinder engine flows [30, 37, 65, 66, 160, 170, 180], etc. They essentially considered cold flow simulations, and demonstrated the ability of LES to resolve flow structures in engineering applications. A review of computations based on LES in IC-engines was provided by Celik et al. (2001) [30]. It was shown and concluded that LES has great potential for engine applications.

The method has achieved further development in reference [183], where the LES analysis of turbulent flow and heat transfer in IC-engines during compression and expansion strokes using different SGS models is performed. The capability of LES for engine configurations has been explored in [169], where two simple IC-engine geometries have been treated with a LES code, called AVBP (developed at CERFACS). The LES results for both swirl and non swirl cases have been considered and compared with experimental data. Also, the influence of the numerical scheme (2^{nd} and 3^{rd} order) and of the mesh type (structured versus unstructured) was investigated for both configurations. A new SGS model was proposed and the effectiveness of LES compared to RANS is confirmed in [79]. Cycle-to-cycle variability in a variable air-guiding system has been considered in [45]. The investigation showed that it is possible to improve flow stability in the combustion chamber during the important compression phase and to increase the kinetic energy by changing the design of the intake manifold. The influence of the intake air flow on the cyclic variability of in-cylinder air motion, on inflammation and combustion has been analyzed using the STAR-CD [28] CFD code and various experimental techniques.

Reference [170] is dedicated to LES predictions of aerodynamics through diesel engine intake ports under steady flow conditions. For the first test case, swirling flows are investigated through an axisymmetric sudden expansion. The LES predicted swirl profile is compared with experimental data. For the second test case, a sudden expansion with a valve is tested and the discharge coefficient is compared with experimental data. For the third test case, the same approach is applied to a real engine geometry which has two intake ports. Both the swirl profile and the discharge coefficient are calculated and compared with experiments, and the prediction error of LES is of the order of 10%.

As it is mentioned in [30], the first attempt to explore the ability of LES to reproduce cyclic in-cylinder turbulence in a four-stroke engine is reported in [110]. The implementation of LES in the KIVA-3V code, validation and the confirmation of the possibility to successfully carry out calculations for the whole IC-engine geometry are reported in [57]. Based on [57] LES analysis for in-cylinder flow inside a test engine geometry was carried out in [59]. This work investigates the impact of the inlet duct geometry on the in-cylinder flow by means of comparing three different configurations. One of the first attempts of applying LES to the examination of cycle-to-cycle fluctuations in an engine by simulating a number of consecutive engine cycles is given in [58, 59]. In order to characterize the cycle-to-cycle variations in an IC-engine, LES calculations have been performed for up to 20 engine cycles using a generic four stroke IC-engine geometry. A suitable parallelization strategy has been applied in order to create a reasonable number of statistical samples. Phase-averaged statistics have been presented for characteristic crank angles. They show strong cyclic variations during the inlet stroke mainly influenced by the annular jet formed during intake. The compression phase is characterized by a rather homogenous turbulent flow field with root mean square (rms) values up to 50% of the mean flow. Variations of the engine geometry and artificial disturbances of the velocity field indicate that the valve-port region might be the possible origin of the cyclic variations of the flow field.

Fischer et al. [44] investigate the effect of a variable tumble system on in-cylinder charge motion in DISI engines. It is shown that the air-guiding system can lead to a significant reduction of the cyclic variability of the in-cylinder air flow.

Among the most recent works, references [41, 60, 180] investigate the cycle-to-cycle variability of in-cylinder flow by modeling of consecutive engine cycles. Vermorel et al. [180] demonstrate the application of LES to the simulation of 9 consecutive engine cycles of a single cylinder PFI four valve engine. The obtained results are compared with experimental finding of cycle-to-cycle cylinder pressure evolution. It is confirmed that LES captures qualitatively the observed cycle-to-cycle fluctuations and can be used to identify the reasons of cyclic variability in a piston engine. It is also reported that instead of 9 minimum 50 engine cycles have to be considered in order to get statistically relevant results.

1.4.2. Multiphase flow

There are a lot of researches and publications devoted to investigation of the fuel spray injection processes and to refining existing spray models. In CFD the spray modeling is realized by a set of different sub-models, like collision, breakup, evaporation, etc. The success of the modeling of spray and combustion depends mainly on the accuracy of the sub-models integrated in a reliable CFD code as reported by Golovitchev et al. [55]. Thus, improvement in the spray injection modeling can be achieved by refining the single sub-models. This explains partially the big variety of works dedicated to the modification or improvement of existing and the development of new sub-models. For that reason some attention will be given to the works dedicated to the improvement of models for the KIVA-3V code. A recent review of LES-based methods for the prediction of turbulent two-phase flows can be found in [147].

The application of the KIVA-3V code based on a renormalization group (RNG) variant of the $k-\varepsilon$ model for a parametric study of gaseous mixing in direct-injection engines is considered in [123]. The parameters explored include the effects of piston-bowl geometry, various parameters of injection as well as number of injectors and initial swirl ratio on mixing. It is shown that a combination of the optimum values of the parameters yields a dramatic improvement in mixture homogeneity for a given engine design and operating condition. However, the pronounced changes in mixture quality associated with speed and load changes illustrate the fact that in the complicated engine environment, changes in operating conditions can have drastic effects on combustion and emissions.

Intake, compression, and combustion modeling of a Caterpillar diesel engine using a modified variant of the KIVA-II and KIVA-3 codes based on RNG RANS approach is reported in [50]. Modifications of the original code include improvements to the turbulence, heat transfer, spray, ignition, combustion and emission sub-models. Consideration of various intake generated properties and determination which of these properties are most influential in each stage of combustion and in the formation of pollutants are pointed out. It is shown that swirl has the most influential role in diffusion burn mixing by increasing the area of the fuel and air interface.

The effect of transient in-cylinder air motion on fuel spray characteristics in a side-injection GDI IC-engine is discussed in [82]. KIVA-3V was used to perform RANS simulations during intake and compression stroke. In that case the fuel spray jet was much stronger than ambient swirl and tumble motion and thereby it was concluded that the influence of the in-cylinder charge motion on fuel spray processes is insignificant for the given configuration of IC-engine. Multidimensional modeling of a GDI engine by KIVA-3V, which includes the LISA spray model [151, 153] with focus on fuel-air mixture preparation under a wide range of engine operating conditions has been done in reference [165]. In contract to [82] the results report a significant role of in-cylinder flow structures with a dominant role of swirl motion on spray development, fuel mixing and mixture distribution.

It is important to mention the works of Menon at al. [159, 160] as well where LES coupled with the linear eddy model (LEM) for SGS mixing has been implemented in the KIVA-3V code in order to investigate the unsteady fuel-air mixing process in a DISI engine.

Reference [36] analyses the influence of liquid fuel compressibility on the simulation of sprays produced by high-pressure injection systems. Two different equations have been introduced into the KIVA-3V code to calculate the liquid-phase density. The first one determines the fuel density by using a second-order function of drop temperature and pressure, while the second one also takes into account the quantity of air dissolved in the fuel. Breakup, vaporization, and collision models as well as the energy, momentum, and air-spray mass exchange equations were modified so that each droplet would have a different density, according to its position and evolution. A comparison between experimental and numerical data for sprays injected in a constant-volume vessel at ambient temperature and pressure has been carried out to test the capability of the modified KIVA-3V subroutines.

Numerical simulation using the STAR-CD package has been done in [2] to characterize the interaction of in-cylinder charge motion, geometry of combustion chamber (focused on piston-bowl crone configuration) and fuel spray propagation. It was concluded that CFD simulation provides detailed information about important characteristics of the mixture formation and can be applied for detailed optimization of piston-bowl geometry and injection pressure and timing.

Castagne et al. [27] discuss the analysis of mixture preparation and combustion in wall- and spray-guided DISI engines by consideration of the amplitude of the air-fuel ratio fluctuations at the spark plug. The concentration obtained by high-speed flame ionization detection (FID) measurement for 250 cycles was used for adjusting the spray model parameters. Very large cycle-to-cycle variations of air-fuel ratio at spark plug were observed in stratified mode for both wall- and spray-guided combustion systems.

In order to simulate accurately GDI engine operation under homogeneous charge conditions, a series of works [177 - 179] are focused on development of a set of computational models, including fuel injection, wall impingement and stratified combustion which were implemented into the KIVA-3V code. To validate the newly developed models, the comparison of the fuel injection and air-fuel mixing with experiments was performed in a single-cylinder optical GDI engine.

The problems regarding the mixture formation in a GDI engine using the KIVA-based code with modified $k-\varepsilon$ model are discussed in [145, 146]. The atomization of a hollow cone fuel spray generated by a high pressure swirl injector is studied by means of a numerical technique. The validation of the model was made comparing the numerical penetration and spray morphology with experimental results. Both stratified charge (at part load) and nearly homogeneous conditions (at higher loads) were modelled for different engine speeds. The results show that the interaction between the air motion and the fuel spray, the leading factor in spray atomization, is fundamental to realize an efficient mixture formation and combustion locally very lean, typical of stratified charge combustion. The numerical results globally show that the stratification at part load is the most crucial and critical step, and if the air flow is not well coupled with the fuel spray, the combustion could be incomplete with higher exhaust emissions.

Since the source code of KIVA-3V is available and includes a collection of various sub-models, it provides a good opportunity for evolution and improvement of the code. A lot of works are reported about the improvement of the several sub-models, especially regarding to spray dynamics. e.g. [12, 56, 121, 173, 177]. New models for injection, evaporation and wall impingement of a liquid phase spray were developed and described in [92]. Implementation of equations for multicomponent fuel evaporation of airborne fuel droplets and wall film into KIVA-3V is given in [173]. A new drop drag sub-model [98], a model for liquid-phase density calculation [36] and many others have been implemented in the KIVA family codes.

Reitz and Rutland [138] report about significant progress in development and validation of CFD models for diesel engine combustion and emissions. A modified version of the KIVA code with improved sub-models for liquid breakup, drop distortion and drag, spray-wall impingement with rebounding, sliding and breaking-up drops, wall heat transfer with unsteadiness and compressibility, multi step kinetics ignition and laminar-turbulent characteristic time combustion models, Zeldovich NO_x formation, and soot formation with Nagle-Strickland-Constable oxidation, based on RNG $k-\varepsilon$ model has been used. The intake flow CFD modeling results show that the details of the intake flow process influence the engine performance.

A set of computational models, including fuel injection, wall impingement and stratified combustion, has been developed by Vanzieleghem et al. [178] and implemented in to KIVA-3V. The KIVA-3V code has been used for RANS simulations of GDI engine. To validate the results of the fuel injection and air-fuel mixing modeling, comparisons of all the engine processes were performed with experiments on a single-cylinder optical GDI engine. The model results have been found in a good agreement with the experimental data.

A 3D reacting flow modeling approach is presented in [76] for predictions of compression ignition, combustion, NO_x and soot emissions over a wide range of operating conditions in a diesel engine. The ignition and combustion models are based on a modified eddy dissipation concept which has been implemented into the KIVA-3V code with RNG version of the $k-\varepsilon$ model. In addition, a realistic transition model based on the local normalized fuel mass fraction is implemented to shift from ignition to combustion. The NO_x formation and destruction processes are based on the extended Zeldovich reaction mechanism. The modeling approach demonstrates promising predictive capabilities at reasonable computational costs.

Analyses of cyclic fluctuations of the in-cylinder charge motion and the mixture formation in a DISI engine using laser optical diagnostics and LES has been done in [132]. Particle image velocity (PIV) technique has been used to characterize the cyclic variability of in-cylinder charge motion. Further the measurement data was applied as initial intake pressure boundary conditions for LES simulation of 10 engine cycles. The fluctuations of mixture formation and the causes of cyclic fluctuations have been discussed.

Goryntsev et al. [61, 62] focus on the influence of cycle-to-cycle variations of the flow and mixing field in a DISI engine using LES. Especially the effect of the cycle-to-cycle variations on the fuel-air mixing close to the ignition point has been investigated. Comparison of LES results for two-phase flow with experimental data is also provided. The analysis has shown strong cyclic variations during intake, mainly at the tip of the intake jet, and during compression, mainly at the center of the tumble motion. The impact of cyclic velocity fluctuations on fuel spray injection and mixing processes is also discussed.

1.4.3. Experimental investigations of cycle-to-cycle variations

A big amount of work is dedicated to experimental investigations of various parameters of in-cylinder processes in engines. Modern experimental measurement techniques have the capability to investigate highly unsteady phenomena in more details and doubtless make a contribution to improve their understanding and ultimately help to increase combustion and overall engine performance. A review of measurement techniques can be found in [14].

An experimental investigation of the cyclic variations and instability of the jet flows in the cylinders of a dual-intake port gasoline engine under both steady state and motored engine conditions using laser Doppler anemometry (LDA) and spectral analysis techniques is discussed in [69]. Analysis of the obtained results allows to draw the conclusion, that cyclic velocity variations may be substantial in reciprocating engines and can result in an overestimation of true turbulence levels by as much as 100%. The intake jet flapping is considered as one possible source of origins for cycle-to-cycle fluctuations.

The cycle-to-cycle fluctuations in the large-scale velocity structures of high and low swirl in-cylinder flows were characterized in [140] using PIV measurements. The results demonstrate the fundamental differences in the undirected, i.e. low swirl and directed (high swirl) flows. Funk et al. [52] extend this work to the analysis of the Reynolds-decomposed turbulence properties such as kinetic energy, length scales and dissipation which were directly measured for the above mentioned two cases. It was shown that at TDC of compression stroke, the low swirl flow is dominated by turbulence at the largest scales, whereas the high swirl flow has a considerably lower turbulence Reynolds number.

Application of time-resolved PIV data based on instantaneous flow pictures to the analysis of cycle-to-cycle variations of in-cylinder flows for 32 engine cycles is reported in [40]. It is shown that cyclic variations increase during the compression process and near TDC the level of the cyclic variability decreases to reach the one of those obtained at the beginning of the intake stroke. Investigation of correlations between cycle-to-cycle variations and combustion parameters of a spark ignition engine has been done in [187].

The cycle-to-cycle variations in the early stages of combustion in a stratified-charge engine can be associated with variations in both the local value of air-fuel ratio near the spark plug around ignition time and the volume averaged value of the air-fuel ratio. Aleiferis et al. [4] analysed the possible sources of such air-fuel variability by considering the in-cylinder field of fuel-droplet distribution during the early intake stroke.

Application of high speed PIV to investigation of cyclic variability in IC-engines is also considered in [174]. Cyclic variability data has been obtained by temporal filtering of the data on single engine cycles and for each measurement point. The obtained data shows that changing the axial swirl level via the inlet port geometry has a significant effect on the cyclic variability of the flow in the latter half of the compression stroke.

In work [127] the PIV technique has been adapted to the two-phase flow in a pressure vessel to investigate the interaction between the injected fuel droplets and the surrounding air. The results show a detailed overview of the spray propagation and its effects on the gas phase. Additionally, the PIV has been used to investigate the interaction between the two phases in the cylinder during compression stroke. A strong effect of the injected droplets on the gas phase and the tumble structure has been shown.

The analysis of combustion fluctuation in a direct injection IC-engine has been done in [51] by the laser-induced fluorescence technique. It has been concluded that the combustion fluctuation is dominated by the mixture concentration at the spark position and timing. The combustion fluctuation near the best injection timing is due to the cycle-to-cycle variations of the unburned fuel existing at the cavity edge during the latter combustion period.

1.4.4. Supplementary literature

It is significant to note in the conclusion of the literature review that the KIVA-3V program is widely adopted in industrial applications as well as in scientific circles which is confirmed by the big number of published results, both theoretical and applied, and by a reasonable amount of dissertations, see for instance [34, 35, 53, 111, 122, 185, 149].

Finally, it is necessary to comment on a number of doctoral theses dedicated to the investigation of IC-engines. Simulation of a turbulent spray diffusion flame with pollutant formation in a realistic Diesel engine using KIVA-3V code with standard spray model has been carried out in [35]. Additionally, models for the description of ignition, chemistry, chemistry-turbulence interactions and radiation have been implemented, tested and compared with experimental data.

Numerical simulations of spray combustion phenomena with an emphasis on the turbulence and chemistry interaction effects using a detailed chemistry approach coupled with the standard $k-\varepsilon$ or RNG models have been done in [111]. The turbulence and chemistry interaction model accounts for the effects of turbulent micro-mixing on the chemical reaction rates. Improved sub-models for turbulence and chemistry interaction using a detailed chemistry approach as well as the Kelvin-Helmholtz Rayleigh-Taylor breakup model by Reitz [139] have been implemented in the KIVA-3V code. Mesh dependence analysis as well as the influence of the turbulence parameters on the liquid penetration were discussed. Results of numerical simulations were compared with experimental data and it was pointed out, that the standard collision model in KIVA-3V is extremely grid dependent.

The physics of hollow-cone sprays emerging from high-pressure swirl-injectors used in DISI engines and different models that can be used in a numerical code for steady state modeling have been reviewed in [34]. Several sub-models were implemented in the KIVA-3V code and validated using experimental data. A discussion about experimental techniques which can be applied to cycle-to-cycle measurements was given. Causes and influences of combustion cyclic variations and some comparisons between experimental and modeling results is given in

reference [14]. The primary causes for high level hydrocarbon emissions in fuel stratified injection (FSI) engine were investigated experimentally in [164]. Through a comparison of a standard multi point injection and the FSI engine, it was found that the primary cause of HC emissions was related to the piston form and modification of the piston surface leads to a reduction of up to 30% HC-emissions. It was concluded that realization of all investigated HC reduction methods can result in a total decrease of up to 80% of the HC-emissions relative to the reference FSI engine at 5000 rpm.

A limited number of works has been published regarding LES of turbulent combustion in IC-engines, e.g. [77, 152, 156]. The study of combustion in DISI engines using LES with a dedicated model for premixed, spark ignited combustion has been carried out in [143].

Specification of boundary conditions is a very important part of a successful LES application to turbulent processes. A discussion of procedures to define boundary conditions for Navier-Stokes equations for reacting flows and a review of different types of boundary conditions are given in [134]. Specifying boundary conditions is a critical part in compressible DNS and LES codes [108, 171]. In [108] the importance of boundary conditions was stressed and a new simple formulation to implement characteristic boundary conditions in compressible DNS/LES codes was described. In order to represent the effects of the wall layer on the turbulent core of the flow for LES, various approximate boundary conditions which model the interaction between the inner and outer layer, are proposed in [129]. This allows significant reduction of the time required to obtain converged statistics, and may make the extension of LES to flows of engineering interest feasible.

1.5. Objectives and strategy

At present time there are a lot of experimental and computational works, dissertations, conferences and symposia dedicated to the study of different processes in IC-engines. Such a great interest is partially caused by the role which IC-engines take in everyday life and partially by the variety and complexity of processes taking place in IC-engines. Nevertheless, a number of important fundamental questions are still not reflected sufficiently in the literature. The following aspects represent the main goals of the present research:

- The confirmation and examination of LES possibilities for modeling and accurate prediction of highly unsteady complex phenomena based on utilization of the KIVA-3V code to realistic engine configurations.

- Characterization of the cycle-to-cycle variations of flow and mixing field in an air-guided direct spray injection IC-engine to achieve a better understanding of their nature and origin using the large eddy simulation method by performing up to 50 consecutive full engine cycles.

- Characterization of the impact of cycle-to-cycle fluctuations on the fuel spray penetration, mixture preparation and cyclic variability of the fuel vapor cloud near the spark plug.

The investigation is done using the large eddy simulation method. LES is at present a universally recognized method to solve the tasks of modeling of transitional processes in IC-engines. The standard Smagorinsky model was used as a subgrid-scale model. It also should be mentioned here that the combustion process is kept beyond the scope of the present work. Hence, this work can represent a basis for further systematical analysis of flows in a combustion chamber.

1.6. Structure of the manuscript

This work contains seven main chapters and it is organized as follows: Chapter 2 presents the basics of the turbulence modeling including the consideration of single- and two-phase flow. Basic concepts about the characteristics of turbulent flows and the technique of their modeling are discussed at the beginning of chapter 2. Emphasis is placed on the consideration of LES. The spray governing equations are shortly summarized and a review of basic subgrid-scale models is given. Chapter 3 introduces the numerical procedures used in this work. An overview of the widely-used KIVA-3V CFD code and the utilized numerical scheme are presented. The second part focuses on the implementation and verification of a subgrid-scale model in KIVA-3V. Parallelization aspects are also considered in chapter 3. Some challenges of grid generation for complex geometries are considered in chapter 4.

The main results of IC-engine simulations for a single-phase flow are collected in chapter 5. Firstly the configuration and numerical setup are described. Then analysis of velocity cycle-to-cycle variations in the combustion chamber is given. The next paragraphs describe the mean flow properties during intake, compression, expansion and exhaust strokes and comparison of LES, RANS and experimental data. Estimation of numerical, modeling and statistical errors on the prediction of cycle-to-cycle variations are considered in chapter 6. The main results of IC-engine simulations for two-phase flow are collected in chapter 7. Conclusions from the present study are given in the last chapter 8.

Chapter 2

The governing equations for turbulent multiphase flow

The description of different numerical approaches which can be applied for simulation of the turbulence phenomenon, the governing equations and various turbulence models are given in the current chapter. The discussion starts with the consideration of the governing equations for the fluid phase. Then a description of different numerical techniques used for simulation of turbulence as well as various subgrid-scale models is given. Finally, some information concerning spray dynamics and specification of various sub-models is provided.

Generally there are three regimes of flow namely laminar, transient and turbulent. The realization of one or another behavior for the given configuration can be determined through the dimensionless Reynolds numbers [141] which is defined by the relation of inertial forces to viscous forces:

$$Re = \frac{UL\rho}{\mu} = \frac{UL}{\nu}, \tag{2.1}$$

where U is the characteristic velocity, L is the characteristic length, ρ is the fluid density, μ and ν are the dynamic and kinematic fluid viscosity, respectively. The transient regime occurs at the transition from laminar flow to turbulence and vice versa.

In practical applications the various flow regimes can be classified based on the Knudsen number given by the following relation:

$$Kn = \frac{\lambda_{free}}{L}, \tag{2.2}$$

where λ_{free} is the mean free part of molecules and L is a representative physical length scale. The flow is continuous when the Knudsen number tends to zero. At the examination of such kinds of flows the gas microstructure can be neglected and the Euler or Navier-Stokes equations can be considered**.** At the Knudsen number tending to infinity the flow regime can be considered as the free-molecular regime where molecular collisions with solid surfaces play a dominating role. The investigation of the free-molecular regime requires utilization of molecular-kinetic theory [19] based on the Boltzmann equation or statistical approaches like Direct Simulation Monte Carlo (DSMC) method [20]. A transient regime is realized at the finite Knudsen numbers and it also requires taking into account the intermolecular interactions.

It is assumed that the continuum regimes occur at the Knudsen number $Kn \le 10^{-2}$ although substantively the range of applicability of one or another theory depends on many other factors as well. As it has been shown in chapter 1, the in-cylinder flow in IC-engines is characterized as highly transient, three-dimensional, compressible and turbulent. Such flows can be described using continuum mechanics.

2.1. The fluid phase equations

Simulations of IC-engines have to include the consideration of the transient three-dimensional dynamics of evaporating fuel sprays interacting with flowing multicomponent gases undergoing mixing, ignition, chemical reactions and heat transfer. Such kind of flows is mathematically described by the Navier-Stokes equations coupled with the state relations. It is assumed that the theory of continuum mechanics is valid in these equations e.g. the smallest turbulent eddy is larger than the mean free length of the molecules [21]. The unsteady equations of motion of turbulent, chemically reactive mixture of ideal gases, coupled to the equations for a single-component vaporizing fuel spray are given in this section. The governing equations can be used to solve both laminar and turbulent flows. The mass, momentum and energy equations for three-dimensional chemically reacting fluid flow [7] can be written in the following way:

Conservation of mass for each species m of a multi-component mixture:

$$\frac{\partial \rho_m}{\partial t} + \nabla \cdot (\rho_m \mathbf{u}) = \nabla \cdot \left[\rho D \nabla \left(\frac{\rho_m}{\rho} \right) \right] + \dot{\rho}_m^c + \dot{\rho}^s \delta_{m1}, \tag{2.3}$$

where t is the time, ρ_m is the mass density of species m, ρ - the total mass density, $\mathbf{u}$ - the fluid velocity vector and D is the diffusion coefficient. The terms $\dot{\rho}_m^c$ and $\dot{\rho}^s \delta_{m1}$ represent the source terms due to chemistry and spray, respectively, δ is the Dirac delta function. A definition of $\dot{\rho}_m^s$ will be given in paragraph 2.3.6.

Conservation of momentum is given in the following form:

$$\frac{\partial (\rho \mathbf{u})}{\partial t} + \nabla \cdot (\rho \mathbf{u}\mathbf{u}) = -\nabla p - A_0 \nabla (2/3 \rho k) + \nabla \cdot \boldsymbol{\sigma} + \mathbf{F}^s + \rho g, \tag{2.4}$$

where p is the fluid pressure, k is the turbulent kinetic energy, $\boldsymbol{\sigma}$ - the viscous stress tensor, $\mathbf{F}^s$ - the rate of gain per unit volume due to the spray and g - the specific body force. The dimensionless quantity A_0 is equal to zero in laminar and to unity in the turbulent case.

The viscous stress is defined by:

$$\boldsymbol{\sigma} = \mu \left[\nabla \mathbf{u} + (\nabla \mathbf{u})^T \right] - \frac{2}{3} \mu \nabla \cdot \mathbf{u} \, \mathbf{I}, \tag{2.5}$$

where μ is the dynamic viscosity and $\mathbf{I}$ is the unit dyadic.

The conservation equation for the specific internal energy is:

$$\frac{\partial (\rho I)}{\partial t} + \nabla \cdot (\rho \mathbf{u} I) = -p \nabla \cdot \mathbf{u} + (1 - A_0) \boldsymbol{\sigma} : \nabla \mathbf{u} - \nabla \cdot \mathbf{J} + A_0 \rho \varepsilon + \dot{Q}^c + \dot{Q}^s, \tag{2.6}$$

where I is the specific internal energy, exclusive of chemical energy, ε is the dissipation rate of turbulent kinetic energy. $\dot{Q}^c$ and $\dot{Q}^s$ are the source terms due to the chemical heat release and spray interactions respectively. $\mathbf{J}$ is the heat flux vector which is the sum of contributions due to heat conduction and enthalpy diffusion given by:

$$\mathbf{J} = -K \nabla T - \rho D \sum_{\mathrm{m}} h_m \nabla (\rho_m / \rho), \tag{2.7}$$

where T is the fluid temperature, h_m is the specific enthalpy of species m and K is the thermal conductivity.

The equations of state are assumed to be of an ideal gas, giving equations for pressure, internal energy, specific heat of mixture and specific enthalpy respectively as

$$\begin{aligned} p &= R_0\, T \sum_m (\rho_m / W_m)\,, \\ I(T) &= \sum_m (\rho_m / \rho)\, I_m(T)\,, \\ c_p(T) &= \sum_m (\rho_m / \rho)\, c_{pm}(T) \end{aligned} \tag{2.8}$$

and

$$h_m(T) = I_m(T) + R_0 T / W_m\,,$$

where R_0 is the universal gas constant, W_m and $I_m(T)$ are the molecular weight and the specific internal energy of species m, respectively. The coefficient $c_{pm}(T)$ refers to the specific heat at constant pressure.

Finally, it should be mentioned that no chemical reactions will be considered in this work and therefore, the terms $\dot{\rho}_m^c$ and $\dot{Q}^c$ are neglected.

2.2. Turbulence

Turbulent motions can be found in most technical and industrial applications and are characterized by chaotic, stochastic property changes. There are a lot of definitions for turbulence and turbulent flows. For instance, Bradshaw [25] gave the following formulation of turbulence: "Turbulence is a three-dimensional time-dependent motion in which vortex stretching causes velocity fluctuations to spread to all wavelengths between a minimum determined by viscous forces and a maximum determined by the boundary conditions of the flow."

The transition between laminar and turbulent flow is characterized by the Reynolds number [167], see equation (2.1). Turbulent flows enclose a wide spectrum of features where the most important are the following ones:

- irregular nature (and consequently, can be described using statistical methods);
- three-dimensional and rotational;
- diffusivity (one of the most important features of turbulence according to an engineering point of view which causes an enhanced mixing property);
- high Reynolds number;
- dissipative in nature;
- wide range of scales of motion.

A list of different complexity levels of turbulent flows and their level of computational difficulty is pointed in reference [135]. The flow in the cylinder of an engine is listed as the most complex to compute due to the fact that the flow is thee-dimensional and is neither statistically

stationary nor homogeneous [53], i.e. the statistics of the flow vary with time and position. A more completed overview can be found in references [25, 72, 96, 135].

2.2.1. Turbulent scales

A turbulent flow encloses eddies of a wide range of scales. Most part of the kinetic energy of the turbulent motion is contained in the large scale structures. The energy is transferred from these larger eddies to smaller scale structures due to an inertia mechanism. The process lasts till the viscous forces start to dominate and the small eddies dissipate and viscous dissipation of energy finally takes place. It is known that the smallest scales of turbulence are the Kolmogorov microscales of length, time and velocity [87, 88]:

$$l_k \equiv (\nu^3/\varepsilon)^{1/4}, \quad \tau_k \equiv (\nu/\varepsilon)^{1/2}, \quad u_k \equiv (\nu\,\varepsilon)^{1/4} \tag{2.9}$$

where ε is the dissipation rate. It should be noted that the Kolmogorov Reynolds number $Re_k = u_k l_k/\nu$ is equal to one hence the balance between inertia and viscous effects is required in the smallest scale structures.

Another widely used length scale from statistical turbulence theory is the Taylor microscale. The definition is given by

$$l_\tau^{\,2} = \frac{\overline{u'^2}}{\overline{(\partial u'/\partial x)^2}}. \tag{2.10}$$

In most experiments the length scales are also defined using a characteristic scale l_i which is the proper length of the domain and is called integral length scales. l_i can be defined as the distance after which the self correlation of the velocity components vanishes. An estimation of integral length scales can be given by the following equation:

$$l_i \sim \frac{k^{3/2}}{\varepsilon}, \tag{2.11}$$

where the proportionality constant is of the order of unity. Taylor scales l_τ characterize the range of scales that are very small compared to integral scales l_i and at the same time very large compared to Kolmogorov microscales l_k. Therefore, there is the following relation between their quantities: $l_k << l_\tau << l_i$. The turbulent kinetic energy spectrum $E_w(k_w)$ in dependence of the wave number k_w is schematically plotted in figure 2.1, where $k_w = 2\pi/l$. More detailed information can be found in [100, 135].

Turbulent in-cylinder flows are characterized by a wide spectrum of time and length scales which change from the largest eddies down to the Kolmogorov microscales. The largest eddies are characterized by the integral length scale l_i which is comparable to the largest flow structures determined by the geometry of the flow, e.g. the intake jet. The largest eddies transfer their energy sequentially to smaller eddies (it is a so-called energy cascade) until the inertia forces are sufficiently small compared to the effects of dissipation, therefore all length scales, including integral l_i as well as the smaller Taylor and Kolmogorov length scales are important and have to be considered.

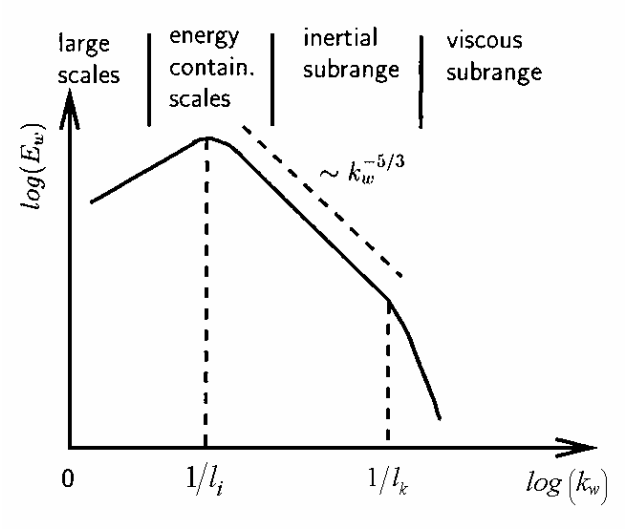

Figure 2.1: Schematic turbulent kinetic energy spectrum.

An assessment of turbulence scales which are relevant to the engine geometry and speed, the resulting turbulent flow field and the effect of compression ratio on turbulence scales is very important. An extensive review concerning turbulence modeling in IC-engines focused on evaluation of turbulence intensity and length scales for in-cylinder flows has been given by Yavuz [185]. The summary concerning the turbulence length and time scales is shown in table 2.1. The relevant length and time scales pertaining to both geometry and turbulence are reviewed in the works of Heywood [67], Reynolds [142] and computed in [154]. Results and conclusions obtained in [185] can be summarized in the following way:

- The turbulence intensity is found to scale with the mean engine speed. The maximum turbulent intensity at TDC is approximately equal to 50% of the mean piston speed.
- The turbulence intensity is naturally correlated with intake flow parameters near TDC.
- The temporal length scales increase with crank angle during the intake and compression strokes.
- The in-cylinder turbulence near TDC of compression is nearly isotropic in the absence of intake generated swirling flow. During intake the turbulent flow is neither homogeneous nor isotropic.
- The flow regimes inside the boundary layer as well as the main vortex motion inside the cylinder can be characterized by a Reynolds number defined as

$$Re = u_p L / \nu , \tag{2.12}$$

where u_p is the mean piston speed, L is the stroke, ν is the kinematic viscosity.

Table 2.1: Estimated length and time scales for an automotive-size engine at a speed of 1000 rpm (deduced from [67, 185]).

Scale	Estimated value	Engine stroke
l_i	10.0 mm	intake stroke
l_i	2.0 – 5.0 mm	compression, near TDC
l_τ	1.0 mm	
l_k	0.01 mm	
τ_i	1.0 ms	
τ_τ	0.1 ms	

2.2.2. Reynolds averaged Navier-Stokes equations

The RANS method is based on time- or ensemble-averaging the Navier-Stokes equation coupled with appropriate turbulence models [181]. The averaging procedure obviously results in a loss of information contained in the instantaneous equations. Different procedures which are used to handle the closure problem lead to different RANS turbulent models. The first limitation of RANS is that the approach provides information about the mean flow while all information relative to the instantaneous processes, e.g. cyclic variability is lost. The second one is that the effects of all scales of motion have to be modeled which makes modeling a challenging task. Grid or time step refinement improves the numerical accuracy but does not inherently increase the dynamic range of scales that are resolved.

The most widely used model of turbulence in IC-engine applications is the $k-\varepsilon$ model. The standard $k-\varepsilon$ model [91] which is included in the KIVA-3V code [7] solves the equations for the turbulent kinetic energy k and its dissipation rate ε:

$$\frac{\partial \rho k}{\partial t}+\nabla\cdot(\rho\,\mathbf{u}\,k)=-\frac{2}{3}\rho\,k\nabla\cdot\mathbf{u}+\boldsymbol{\sigma}:\nabla\,\mathbf{u}+\nabla\cdot\left[\left(\frac{\mu}{Pr_k}\right)\nabla\,k\right]-\rho\,\varepsilon+\dot{W}^s, \tag{2.13}$$

$$\frac{\partial \rho \varepsilon}{\partial \rho}+\nabla\cdot(\rho\,\mathbf{u}\,\varepsilon)=-\left(\frac{2}{3}c_{\varepsilon_1}-c_{\varepsilon_3}\right)\rho\varepsilon\nabla\cdot\mathbf{u}+\nabla\cdot\left[\left(\frac{\mu}{Pr_\varepsilon}\right)\nabla_\varepsilon\right]+\frac{\varepsilon}{k}\left[c_{\varepsilon_1}\,\boldsymbol{\sigma}:\nabla\,\mathbf{u}-c_{\varepsilon_2}\rho\varepsilon+c_s\dot{W}^s\right]. \tag{2.14}$$

The quantities c_{ε_1}, c_{ε_2}, c_{ε_3}, Pr_k and Pr_ε are constants whose values are determined from experiments and some theoretical considerations. Standard values of these constants are given in table 2.2. Source terms involving the quantity $\dot{W}^s$ arise due to interaction with the spray.

Table 2.2: Standard values of $k-\varepsilon$ turbulence model constants.

Model Constant	c_{ε_1}	c_{ε_2}	c_{ε_3}	Pr_k	Pr_ε
Value	1.44	1.92	–1.0	1.0	1.3

2.2.3. Direct numerical simulation

Direct numerical simulation means the solution of the unsteady three dimensional Navier-Stokes equations and the state relations for all scales of turbulence without introduction of any models. The whole spectrum of motion from large energy carrying eddies down to the Kolmogorov microscales must be resolved on the computational mesh. Since both spatial and temporal scales must be resolved, the method imposes strict limitations on the grid resolution as well as the time step. Taking the Kolmogorov scales given by equation (2.9) into account an estimation of the required grid size can be given. Consideration of the Courant-Friedrichs-Lewy (CFL) criterion yields in addition a restriction for the time step. The scaling for the number of grid points required for DNS is given by the following expression:

$$N_{DNS} = \left(\frac{L}{l_k} \right)^3 \cdot Re_t^{-9/4}, \tag{2.15}$$

where Re_t is a turbulent Reynolds number.

Direct numerical simulation [107] is one of the most accurate numerical methods but since the computational costs are very high, DNS can only be realized at low Reynolds number and serves mainly as a tool for fundamental research in turbulence [46, 84] as well as a development tool for new turbulence models. A DNS application to the in-cylinder flow in an internal combustion engine has so far not been reported in the literature.

2.2.4. Large eddy simulation

Large eddy simulation is a multiscale technique with a complexity intermediate between DNS and the RANS approaches. The fundamental idea of LES is based on the separation of turbulent scales [135], where large, energy-containing eddies are directly computed while small-scale turbulent structures are considered to be uniform and are therefore modeled. LES can be more accurate than the RANS approach because the small scales tend to be more isotropic and homogeneous than the larger ones, and thus are more amenable to universal modeling. Furthermore, the modeled subgrid scale stresses contribute only a small fraction to the total turbulent stresses.

The separation between the large and small scales is based on a filtering operation with a filtering function G. The filter removes all finer fluctuations and the governing equations only describe the space-filtered fields. The instantaneous flow field is split into the resolved large scales ($\overline{\phi}$) and the modeled small scales (ϕ'), see equation (2.16). The extraction of the resolved large scale part from the original variables is mathematically defined by the convolution of the original variables with a filter function G.

$$\varphi = \overline{\varphi} + \varphi' \tag{2.16}$$

The LES filtering operation is given by

$$\overline{\varphi}(x_i, t) = \int_{-\infty}^{+\infty} \int \int \left(G(x_i') \varphi(x_i - x_i') \right) dx_i' . \tag{2.17}$$

The most commonly used filter functions are the sharp Fourier cut-off, the Gaussian and the top-hat filter [74, 128]. Usually, the non-resolved small scales are determined by the computational grid, causing the resolved scales to be partly affected by the numerical scheme used to describe the governing equations. For instance, one typical filter kernel is a heaviside (top-hat) function defined by

$$G = \begin{cases} \frac{1}{\Delta^3} & if \ \left|\mathrm{x_i} - x'\right| < \frac{1}{2}\Delta \\ 0 & otherwise \end{cases}. \tag{2.18}$$

Recent reviews of LES can be found in the following references [18, 94, 104, 130].

Subgrid-Scale Models

The filtering operation of the governing equations results in additional subgrid-scale stress terms, equations (2.19), which represent the interaction between the resolved large scale and the unresolved small scale part of the flow [74]. The problem of turbulent closure is the expression of these unknown SGS contributions in terms of the resolved large scale quantities. Thereby, subgrid-scale models are used to simulate energy transfer between the resolved and unresolved part of the flow.

$$\tau_{ij} = \overline{u_i u_j} - \overline{u_i}\,\overline{u_j} \tag{2.19}$$

Most of the current subgrid-scale models are based on the eddy viscosity approach, which assumes that small scale turbulence affects the flow in the same way as the molecular viscosity. Therefore, the fine structure term τ_{ij} may be modeled by adding a turbulent viscosity ν_t to the molecular viscosity ν_{mol}, resulting in an effective viscosity $\nu_{eff} = \nu_t + \nu_{mol}$. Thereby, the concept of eddy viscosity relates the subgrid-scale stresses τ_{ij} to the large scale strain-rate tensor $\overline{S}_{ij}$:

$$\tau_{ij} - \frac{1}{3}\tau_{kk}\delta_{ij} = -2\nu_t \overline{S}_{ij}, \tag{2.20}$$

where

$$\overline{S}_{ij} = \frac{1}{2}\left(\frac{\partial \overline{u}_i}{\partial x_j} + \frac{\partial \overline{u}_j}{\partial x_i}\right). \tag{2.21}$$

In addition to the concept of eddy viscosity, a second major assumption is equilibrium between production and dissipation of small scale kinetic energy. Although the large scales are generally not in equilibrium, the equilibrium hypothesis is likely to be realistic at the level of the small scales which tend to equilibrium much faster. Considering a transport equation similar for the SGS kinetic energy, the equilibrium assumption leads to the following simplified formulation:

$$-\tau_{ij}\overline{S}_{ij} = \varepsilon_v, \tag{2.22}$$

where ε_v is the viscous dissipation of the SGS energy. Formula (2.22) illustrates the assumption that the small scales of motion adjust instantaneously to the perturbations of the large scales and implies the existence of an inertial subrange, where viscous effects are negligible and inertial effects dominate [74]. In the inertial subrange, the energy follows the universal Kolmogorov spectrum, where the kinetic energy is transferred from the large scales to increasingly smaller scales until it is finally dissipated.

Smagorinsky model

The Smagorinsky model [155] is based on the equilibrium hypothesis (2.22) and proposes that the eddy viscosity is proportional to the local strain-rate tensor:

$$v_t = l^2 \left|\overline{S}\right|, \tag{2.23}$$

where

$$\left|\overline{S}\right| = \sqrt{2\overline{S}_{ij}\overline{S}_{ij}} \,. \tag{2.24}$$

The length scale l characterizes the small eddies and is chosen proportional to the local length scale associated with the filtering procedure through the coefficient C:

$$l = C^{\frac{1}{2}}\Delta \,. \tag{2.25}$$

The coefficient $C_S = C^{\frac{1}{2}}$ is called the Smagorinsky constant and used in the frame of the Smagorinsky model to yield

$$v_\tau = (C_S\Delta)^2 \left|\overline{S_{ij}}\right|, \tag{2.26}$$

where for non-uniform grid the filter width is defined by the grid size Δ in the following way:

$$\Delta = (\Delta_x\Delta_y\Delta_z)^{1/3} \,. \tag{2.27}$$

Here Δ_x, Δ_y and Δ_z are the grid size in x, y and z directions, respectively. The theoretical values for the Smagorinsky constant, assuming a Kolmogorov spectrum [74], are $C_S = 0.18 - 0.23$, but often a value of $C_S = 0.1$ is used. Nevertheless, the coefficient has to be tuned for the specific applications.

Germano dynamic model

The drawbacks of Smagorinsky model are the non-universal value of the constant as well as the overprediction of turbulence in laminar regions. A solution of these problems can be found by applying the dynamic procedure. A method for dynamic evaluation of the subgrid-scale model coefficient has been proposed by Germano et al. [54]. In the dynamic procedure the coefficient $C_D = f(x,y,z,t)$ is calculated locally in each time step based on two different filter

widths, namely a test filter whose width $\widetilde{\Delta}$ is larger than the grid filter-width Δ with filter ratio $\widetilde{\Delta}/\Delta = 2$.

An exact relationship can be derived between the subgrid-scale stress tensors at the two different filter widths (the "Germano identity") [65]. Substitution of a Smagorinsky form for the subgrid-scale stress into the Germano identity, along with some additional assumptions [97], leads to a closed form local expression for the quantity $C_S\Delta^2$:

$$C_S\Delta^2 = \frac{L_{ij}M_{ij}}{2M_{ij}M_{ij}}, \tag{2.28}$$

where L_{ij} and M_{ij} are the second-order tensors that are computable from the LES-resolved velocity field:

$$L_{ij} = \overline{u_{ij}u_{ij}} - \widetilde{\overline{u}}_{ij}\widetilde{\overline{u}}_{ij}, \tag{2.29}$$

$$M_{ij} = \overline{|\overline{S}|\overline{S}_{ij}} - \left(\widetilde{\Delta}/\Delta\right)^2 |\widetilde{\overline{S}}|\widetilde{\overline{S}}_{ij}. \tag{2.30}$$

Here L_{ij} is the contribution of the turbulent stress between test-filter and grid-filter scale, M_{ij} is a function of the resolved rate-of-strain. It is important that the dynamic model returns not simply the value of the model coefficient C_S, but the product of C_S and the square of the filter width Δ^2; only the filter width ratio $\widetilde{\Delta}/\Delta$ needs to be specified in M_{ij}. It can be argued that the ratio should be more uniform than the filter width itself on non-uniform deforming meshes [66].

All Smagorinsky based models assume the equilibrium between production and dissipation of kinetic energy in small scales which is difficult to be met in complex configurations. Nevertheless, they appear to produce satisfactory results in a number of engineering flows.

Lagrangian dynamic model

Meneveau et al. [103] proposed to accumulate the averages required in the dynamic model over flow pathlines rather than over directions of statistical homogeneity. This again leads to a closed-form expression for $C_S\Delta^2$ that involves the two second-order tensors of equations (2.29) and (2.30). The Lagrangian form of the dynamic model requires the solution of two additional transport equations for quantities that represent weighted averages of $L_{ij}M_{ij}$ and $M_{ij}M_{ij}$ over fluid-particle trajectories. In addition, it requires the specification of a relaxation time scale that corresponds to a Lagrangian memory time for fluid elements. The resulting model is applicable to arbitrary statistically non-homogeneous turbulent flows.

Additional information and discussion of various subgrid-scale models can be found in the following references [3, 66, 74, 105, 131].

2.3. Spray dynamics

There are three concepts for spray modeling namely the Eulerian-Lagrangian, the Eulerian- Eulerian and the droplet distribution function methods. At present time the spray description is mostly based on the discrete droplet model (DDM) coupled with a Lagrangian approach [166]. While the gas phase is given by an Eulerian approach, the transport of the liquid phase is defined by a certain number of representative particles, which represent a number of droplets with the same typical properties. The coupling between the gas and liquid phases is achieved by the source terms. The governing equations have to incorporate the effects of spray which include an additional mass density source term $\dot{\rho}_m^s$ for each injected species, a momentum source term $\mathbf{F}^s$ and a heat source due to the spray interaction $\dot{Q}^s$. Also a negative rate term which represents the dispersion of the spray droplets due to turbulent eddies $\dot{W}^s$ has to be included into the turbulence modeling equations.

The spray and fluid interactions have to account for the effects of the droplet aerodynamic drag, turbulence effects, evaporation, droplet oscillation and distortion, droplet breakup, collision and coalescence. The properties of each computational particle at the time of injection are assigned by a Monte Carlo based discrete sampling technique with appropriate probability distribution function f. The particles and fluid interact by exchanging mass, momentum and energy. Turbulence effects on the droplets are accounted for in one of two ways [7]: When the time step is smaller than the droplet turbulence correlation time, a fluctuating component is added to the local mean gas velocity when calculating each particle's mass, momentum, and energy exchange with the gas [42]. When the time step exceeds the turbulence correlation time, turbulent changes in droplet position and velocity are chosen randomly from analytically derived probability distributions [115]. Droplet collisions and coalescence are accounted for [114], and a model for droplet aerodynamic breakup has been described by O'Rourke and Amsden [116]. Volume displacement and dense spray effects on the exchange rates are neglected.

2.3.1. The spray equations

In order to calculate the mass, momentum and energy exchange between the spray and the gas, one must account for a distribution of droplet sizes, velocities and temperatures. In many sprays drop Weber numbers [71] are larger than unity and drop oscillations, distortions and breakup must be considered. Drop collisions and coalescences are also important in many engine sprays [49, 106]. A mathematical formulation that is capable to represent these complex physical processes is the spray equation formulation [182].

The spray is represented by a finite number of discrete parcels and every parcel contains a number of droplets with the same properties. The particles are tracked through the flow field in the Lagrangian fashion. In the spray equation formulation, the spray droplets are represented by a droplet probability distribution function f. The Monte Carlo based discrete particle technique [6, 24] is applied in the sense that one samples randomly from assumed probability distribution functions governing droplet properties at injection, collision and turbulent modulation.

The droplet distribution function f has ten independent variables in addition to time and it is defined in such a way that

$$f(\mathbf{x}, \mathbf{v}, r, T_d, y, \dot{y}, t)\, d\mathbf{v}\, dr\, dT_d\, dy\, d\dot{y} \tag{2.31}$$

is the probable number of droplets per unit volume at position $\mathbf{x}$ and time t with velocities in the interval $(\mathbf{v}, \mathbf{v}+d\mathbf{v})$, radii in the interval $(r, r+dr)$, temperatures in the interval (T_d, T_d+dT_d),

and displacement parameters in the interval ($y, y+dy$) and ($\dot{y}, \dot{y}+d\dot{y}$). The time evolution of f is obtained by solving a form of the spray equation [7],

$$\frac{\partial f}{\partial t}+\nabla_{\mathbf{x}}\cdot(f\,\mathbf{v})+\nabla_{\mathbf{v}}\cdot(f\,\mathbf{F})+\frac{\partial}{\partial r}(f\,R)+\frac{\partial}{\partial T_d}(f\dot{T}_d)+\frac{\partial}{\partial y}(f\,\dot{y})+\frac{\partial}{\partial \dot{y}}(f\,\ddot{y})=\dot{f}_{coll}+\dot{f}_{bu}. \qquad (2.32)$$

The quantities $\mathbf{F}$, R, $\dot{T}_d$ and $\ddot{y}$ are the time rates of change, following an individual drop, of its velocity, radius, temperature, and oscillation velocity $\dot{y}$, respectively. $\dot{f}_{coll}$ and $\dot{f}_{bu}$ represent the probability source terms due to droplet collisions and breakups.

2.3.2. Collision model

In the standard droplet collision model [114] two parcels can collide when they occupy the same computational cell and collision is based on a probability function. The collision model is one of the weakest from the spray sub-models [111], since the model is inherently grid dependent [150] as the collision frequency depends on the grid size. There are two possibilities for two colliding parcels (marked 1 and 2): a) Coalescence, i.e. two parcels produce a new single droplet with new temperature and velocity, calculated by a mass averaging procedure; b) Separation, i.e. during collision the parcels maintain their mass, temperature and energy except velocity. The impact parameter b is compared to the critical impact parameter b_{cr} to define the type of collision. If the collision impact parameter b is less than a critical value b_{cr}, the droplets coalesce. The critical impact parameter b_{cr} is given by

$$b_{cr}^2=(r_1+r_2)^2\,min\left(1.0,\,2.4\,f(\gamma)/We_L\right), \qquad (2.33)$$

where the Weber number We_L, $f(\gamma)$, γ and $\overline{T}_d$ are given by

$$f(\gamma)=\gamma^3-2.4\,\gamma^2+2.7\,\gamma, \qquad (2.34)$$

$$\gamma=r_2/r_1 \quad \text{where} \quad r_1\le r_2, \qquad (2.35)$$

$$We_L=\rho_d\left|\mathbf{v}_1-\mathbf{v}_2\right|r_1/a\,(\overline{T}_d) \ \text{ and} \qquad (2.36)$$

$$\overline{T}_d=\frac{r_1^3T_{d_1}+r_2^3T_{d_2}}{r_1^3+r_2^3}, \qquad (2.37)$$

where ρ_d is the liquid density and the quantity a is the liquid surface tension coefficient. Thereby, the probable number of droplets resulting from a collision between two parcels is determined by a collision probability density function σ:

$$\sigma=\frac{b_{cr}^2}{(r_1+r_2)^2}\,\delta\left[r-\left(r_1^3+r_2^3\right)^{\frac{1}{3}}\right]\delta\left[\mathbf{v}-\frac{r_1^3\,\mathbf{v}_1+r_2^3\,\mathbf{v}_2}{r_1^3+r_2^3}\right]\delta\left[T_d-\frac{r_1^3T_{d_1}+r_2^3T_{d_2}}{r_1^3+r_2^3}\right]\delta(y-y_2)\,\delta(\dot{y}-\dot{y}_2) \qquad (2.38)$$

$$+\frac{2}{(r_1+r_2)^2}\int_{b_{cr}}^{r_1+r_2}\left[\delta(r-r_1)\delta(\mathbf{v}-\mathbf{v}_1')\delta(T_d-T_{d_1})\delta(y-y_1)\delta(\dot{y}-\dot{y}_1)\right.$$

$$\left.+\delta(r-r_2)\delta(\mathbf{v}-\mathbf{v}_2')\delta(T_d-T_{d_2})\delta(y-y_2)\delta(\dot{y}-\dot{y}_2)\right]\,bdb\,,$$

where

$$\mathbf{v}_1'=\frac{r_1^3\mathbf{v}_1+r_2^3\mathbf{v}_2+r_2^3(\mathbf{v}_1-\mathbf{v}_2)\dfrac{b-b_{cr}}{r_1+r_2-b_{cr}}}{r_1^3+r_2^3}$$

and

$$\mathbf{v}_2'=\frac{r_1^3\mathbf{v}_1+r_2^3\mathbf{v}_2+r_1^3(\mathbf{v}_2-\mathbf{v}_1)\dfrac{b-b_{cr}}{r_1+r_2-b_{cr}}}{r_1^3+r_2^3}\,.$$

The collision source term $\dot{f}_{coll}$ due to collision in equation (2.32) is given by

$$\begin{aligned}\dot{f}_{coll}=\frac{1}{2}\iint f(\mathbf{x},\mathrm{v}_1,r_1,T_{d_1},y_1,\dot{y}_1,t)\,f(\mathbf{x},\mathbf{v}_2,r_2,T_{d_2},y_2,\dot{y}_2,t)\,\pi(r_1+r_2)^2|\mathbf{v}_1-\mathbf{v}_2|\\ \left[\sigma(\mathbf{v},r,T_d,y,\dot{y},\mathbf{v}_1,r_1,T_{d_1},y_1,\dot{y}_1,\mathbf{v}_2,r_2,T_{d_2},y_2,\dot{y}_2)\right.\\ \left.-\delta(\mathbf{v}-\mathbf{v}_1)\delta(r-r_1)\delta(T_d-T_{d_1})\delta(y-y_1)\delta(\dot{y}-\dot{y}_1)\right]\\ -\delta(\mathbf{v}-\mathbf{v}_2)\delta(r-r_2)\delta(T_d-T_{d_2})\delta(y-y_2)\delta(\dot{y}-\dot{y}_2)\\ d\mathbf{v}_1\,dr_1\,dT_{d_1}dy_1\,d\dot{y}_1\,d\mathbf{v}_2\,dr_2\,dT_{d_2}dy_2\,d\dot{y}_2\,.\end{aligned}\qquad(2.39)$$

2.3.3. Breakup model

The Taylor analogy break-up (TAB) model has been proposed by O'Rourke and Amsden [116]. The model is based on Taylors analogy between an oscillating and distorted drop and a forced spring-mass system, and considers the effects of the liquid viscosity on the oscillations of small droplets, and predicts that there is no unique critical Weber number [70] of droplet breakup. The breakup source term $\dot{f}_{bu}$ is given by

$$\dot{f}_{bu}=\int f(\mathbf{x},\mathbf{v}_1,r_1,T_{d_1},1,\dot{y}_1,t)\,\dot{y}_1 B(\mathbf{v},r,T_d,y,\dot{y},\mathbf{v}_1,r_1,T_{d_1},\dot{y}_1,\mathbf{x},t)\,d\mathbf{v}_1 dr_1\,dT_{d_1}d\dot{y}_1\,.\qquad(2.40)$$

The probability function B of the broken droplets is

$$B = g(r)\delta(T_d - T_{d_1})\delta(y)\delta(\dot{y})\frac{1}{2\pi}\int \delta[\mathbf{v} - (\mathbf{v}_1 + w\mathbf{n})]d\mathbf{n}\,, \tag{2.41}$$

where $g(r)$ is the size distribution and w is the magnitude of the velocity of the resulting droplets.

2.3.4. Evaporation model

Evaporating liquid sprays are represented by a discrete-particle technique [42], in which each computational particle represents a number of droplets of identical size, velocity and temperature. Probability distributions govern the assignment of droplet properties at injection or the changes in drop properties at downstream locations. The liquid parcels receive their thermal energy from the gas phase. This energy is utilized to increase the liquid temperature and to overcome the latent heat of evaporation in order to evaporate the fuel. Unless the gas is saturated with vapor fuel, evaporation always takes place and reduces the droplet radius. If the transferred heat delivered by the gas is insufficient, the droplet temperature will decrease. Detailed description of evaporation sub-model can be found in [7].

2.3.5. Droplet acceleration

The droplet acceleration term $\mathbf{F}$ has contributions due to aerodynamic drag and gravitational force and is given by

$$\mathbf{F} = \frac{3}{8}\frac{\rho}{\rho_d}\frac{|\mathbf{u} + \mathbf{u}' - \mathbf{v}|}{r}(\mathbf{u} + \mathbf{u}' - \mathbf{v})C_D + g \tag{2.42}$$

The dynamic drag model in KIVA-3V takes into account the distortion of airborne droplets due to the surrounding gas flow by using Taylor's analogy between a drop and a spring-mass system [10]. However, the droplet has been treated as a rigid sphere in the calculation of the drag coefficient C_D for which

$$C_D = \begin{cases} 24/Re_d\left(1 + Re_d^{2/3}/6\right) & Re_d \le 1000 \\ 0.424 & Re_d > 1000 \end{cases}, \tag{2.43}$$

where

$$Re_d = \frac{2\rho\,|\mathbf{u} + \mathbf{u}' - \mathbf{v}|\,r}{\mu_{air}(\hat{T})},$$

$$\hat{T} = \frac{T + 2T_d}{3}.$$

The gas turbulence velocity $\mathbf{u}'$ is added to the local mean gas velocity while calculating the droplet's drag and vaporization rate.

2.3.6. Gas-spray interaction terms

The spray phase interacts with the gas by the following way:

$$\dot{\rho}^s = -\int f\,\rho_d\, 4\pi r^2 R\, d\mathbf{v}\, dr\, dT_d\, dy\, d\dot{y}\,, \tag{2.44}$$

$$\mathbf{F}^s = -\int f\,\rho_d \left(4/3\,\pi\, r^3\,\mathbf{F}' + 4\pi\, r^2 R\,\mathbf{v}\right) d\mathbf{v}\, dr\, dT_d\, dy\, d\dot{y}\,, \tag{2.45}$$

$$\dot{\mathbf{Q}}^s = -\int f\,\rho_d \left(4\pi r^2 R\left[I_l(T_d) + \tfrac{1}{2}(\mathbf{v}-\mathbf{u})^2\right] + 4/3\,\pi\, r^3\left[c_l \dot{T}_d + \mathbf{F}'\cdot(\mathbf{v}-\mathbf{u}-\mathbf{u}')\right]\right) d\mathbf{v}\, dr\, dT_d\, dy\, d\dot{y} \tag{2.46}$$

and

$$\dot{W}^s = -\int f\,\rho_d\, 4/3\,\pi\, r^3\,\mathbf{F}'\cdot\mathbf{u}'\, d\mathbf{v}\, dr\, dT_d\, dy\, d\dot{y}\,. \tag{2.47}$$

2.3.7. Spray wall interaction

Detailed description of boundary conditions for the spray equations is given in [7]. The description of the basic model has been presented in [118] while reference [112] contains a detailed description of all extensions to the spray wall interaction sub-model for KIVA-3V. For the sake of brevity those details will not be repeated here.

2.4. Summary

At present time the basic method which allows studying of transient processes in IC-engines is RANS. The RANS approach generally predicts the mean flow satisfactorily, nevertheless it loses the important information regarding unsteady phenomena, in particular about cycle-to-cycle fluctuations. DNS possesses a multitude of advantages compared to RANS and LES but is rather hard to realize from the point of view of computational costs. The large eddy simulation approach is based on the idea of resolving the large-scale turbulent motion and modeling the small sub-grid scales of motion taking into account the hypothesis of isotropy of small scale turbulence.

Simulation of spray processes is mostly based on the Lagrangian discrete droplet method and incorporates a number of sub-models. The coupling between the liquid and gas phases is achieved by source terms. Various sub-models account for the effects of turbulent dispersion, collision and coalescence, droplet oscillation and distortion, evaporation, droplet breakup and wall interaction.

Chapter 3

Model implementation and validation of the KIVA-3V-LES code

This chapter starts with a description of basic features of the KIVA-3V code, which is widely used for the simulation of IC-engine fluid dynamics. The numerical scheme, the specification of boundary conditions and the implementation of a subgrid-scale model into the KIVA-3V program are considered. Next, the validation of the new code named KIVA-3V-LES based on the simulation of the turbulent flow in a square duct configuration is provided. Finally, special attention is put on the realization of parallel calculations in KIVA-3V.

3.1. An overview of the KIVA-3V code

The KIVA-3V computer program was developed by Los Alamos National Laboratory and has found widespread application for the simulation of IC-engines in the automotive industry, especially for in-cylinder flows. The KIVA-3V [6 - 10] code is a transient, three-dimensional, multiphase, multi-component program developed for the numerical analysis of chemically reacting flows with sprays in engine geometries with arbitrary piston shape. The range of validity of the code extends from low speed to supersonic flows for both laminar and turbulent regimes. The conservation equations described in the chapter 2 are discretized using the finite volume method (FVM) on an arbitrary hexahedral mesh applying the arbitrary Lagrangian-Eulerian (ALE) method [73, 136]. A stochastic particle method is used in order to calculate evaporating liquid sprays including the effects of droplet collisions and aerodynamic breakup. The program offers two different RANS models (standard $k-\varepsilon$ and an optional RNG $k-\varepsilon$ model) to account for turbulence effects.

The KIVA-3V code is written in FORTRAN and consists of a set of different sub-programs (or subroutines) which are controlled by a main routine. Since the success of numerical simulation of various physical processes in IC-engines depends on the sub-models used, the access to the source code is an essential element of development, implementation and validation of sub-models. The program structure allows modifying and extending the existing code easily. The input data is provided in ITAPE* files which contain the computational grid and the definition of all parameters of the considered case.

The computational grid can be generated by the KIVA pre-processor program named K3PREP (for sufficiently simple configurations) or by third-party software, for example, ICEM CFD [11]. The details of using ICEM CFD and creating the grids for complex geometries will be discussed in chapter 4.

3.1.1. The numerical scheme

The discretization of the governing equations given in the previous chapter in KIVA-3V involves a combination of the arbitrary Lagrangian-Eulerian finite volume method for spatial discretization and the variably implicit time discretization scheme.

Temporal differencing

KIVA-3V uses the first-order difference for approximation of all time derivatives of a quantity (Q):

$$\frac{\partial Q}{\partial t} \approx \frac{Q^{n+1} - Q^n}{\Delta t^n}, \tag{3.1}$$

where $\Delta t^n = t^{n+1} - t^n$ is the time step and $n = 0, 1, 2 \ldots$ is the cycle number. Each computational cycle is performed in three separated stages. In phase A the influence of the spray droplet interaction, wall film particles and chemical reactions on gas quantities are computed. Phase B consists of fluid diffusion and droplet velocity calculations and solves the governing equations in Lagrangian form using a finite volume scheme. Phase C is the rezoning or the Eulerian stage, in which the grid is moved to new locations and fluxes of mass, momentum, energy and turbulence quantities are exchanged. The general structure of the KIVA-3V program and different phases are shown in figure 3.1. The most time consuming phase is the implicit fluid diffusion calculated in phase B.

Phase A involves the effects of combustion chemistry and spray droplet interactions and constitutes a Lagrangian calculation in which computational cells move with the fluid. Phase A calculates the spray droplet collision, oscillations and breakup terms ($\dot{f}_{coll}$, $\dot{f}_{bu}$), the mass and energy due to the chemistry and spray ($\dot{\rho}_m^c$, $\dot{\rho}^s$, $\mathbf{F}^s$, $\dot{Q}^c$ and $\dot{Q}^s$), see chapter 2.

Phase B consists mainly of fluid diffusion and droplet velocity calculations and as phase A constitutes a Lagrangian calculation. Phase B calculates in a coupled, implicit fashion the pressure gradient in the momentum equation, the velocity dilatation terms in mass and energy equations, the spray momentum source term, and the terms due to diffusion of mass, momentum, and energy. During phase B the remaining source terms in the turbulence equations are also calculated. The solution procedure is based on the SIMPLE method [125], which solves individual equations using the conjugate residual method [113]. The SIMPLE algorithm is an iterative procedure consisting of the two following steps: 1) The pressure field is frozen and other flow quantities are solved for; 2) Then the obtained terms are frozen and implicit finite difference equations are solved for the pressure correction term. Further the predicted and corrected pressure fields are compared and the process is repeated till convergence. The Lagrangian equations for phase B quantities, namely species density, velocity, temperature, pressure, turbulent kinetic energy and turbulent dissipation rate are solved using the conjugate residual method [113, 172]. Since the species and turbulence equations are weakly coupled to the flow field solution, they are not included in the SIMPLE iteration loop and are solved independently. The time step Δt in phase B is determined based on accuracy rather than stability conditions because diffusion terms are differenced implicitly and the convective terms are sub-cycled, hence there are no stability restrictions on Δt.

In phase C the flow field is frozen and remapping onto a new computational grid takes place, where the convective transport associated with the moving mesh relative to the fluid is calculated. The convection time step is based on the Courant stability condition $u_r \Delta t / \Delta x < 1$, where u_r is the fluid velocity relative to the grid velocity. Finally, the cell properties are updated using the state equations while the density is calculated by summing the individual species densities. There are two types of advection schemes provided in KIVA-3V: Quasi-Second-Order Upwind (QSOU) differencing [176] and Partial Donor Cell (PDC) differencing. The QSOU scheme is more accurate than PDC, even though it has first-order spatial truncation errors and would be expected to be less accurate than PDC, which is second-order accurate in space. However, PDC is an implicit method and therefore less accurate. QSOU represents a

monotonous scheme that does not introduce new minima or maxima in the calculated solution. PDC differencing is less accurate but significantly faster than the QSOU scheme. The PDC can be used when speed is more important than accuracy or when the cell Reynolds numbers is less than 2.

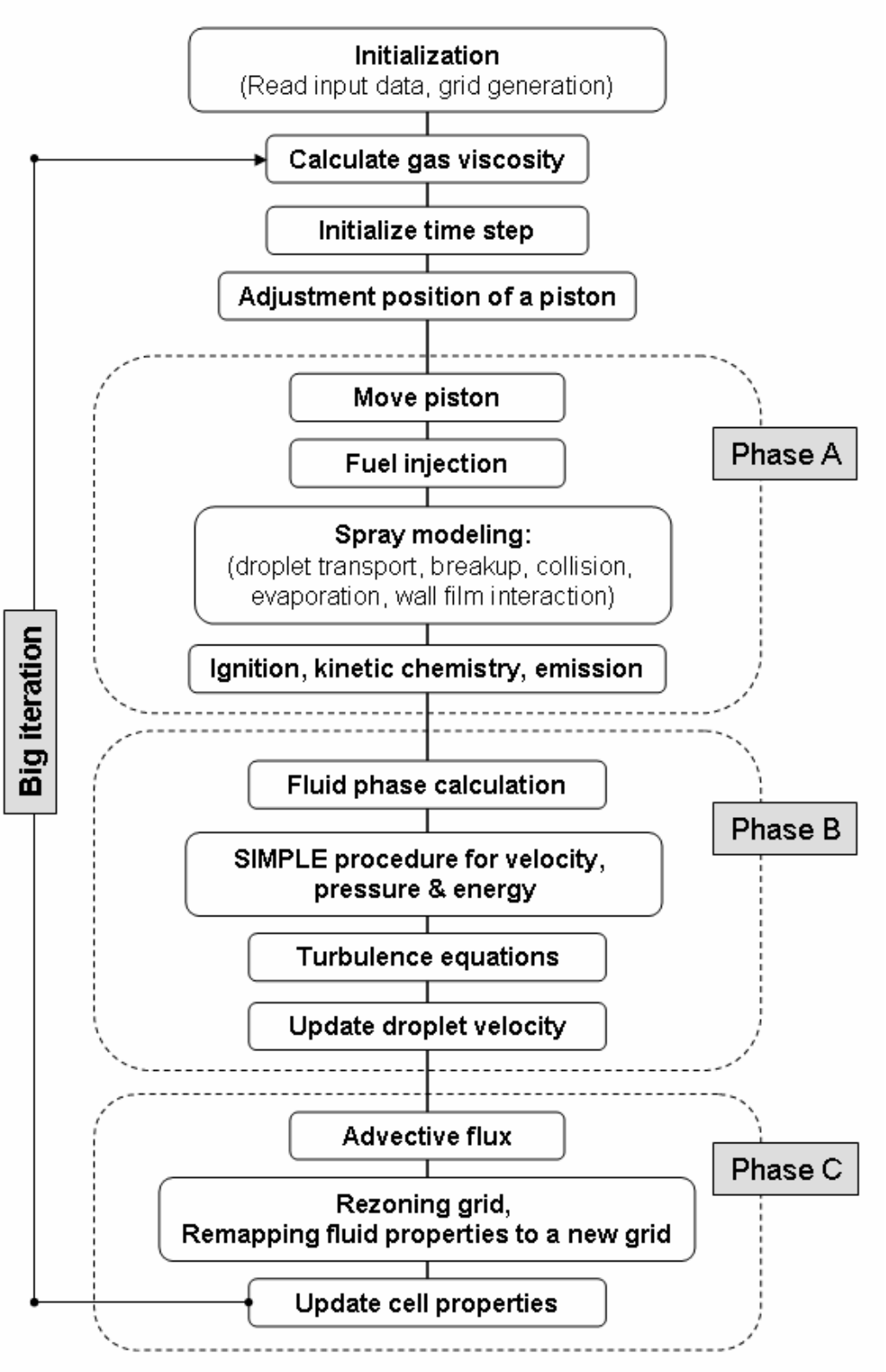

Figure 3.1: General structure of the KIVA-3V program.

Spatial differencing

The conservation equations are discretized using the finite volume method on an arbitrary hexahedral mesh applying the ALE approach [73, 136]. Spatial differences are formed on a mesh which subdivides the computational domain into a number of small hexahedrons. The corners of the cells, the vertices, can be move with the fluid (Lagrangian), be held fixed (Eulerian), or be moved in any other prescribed manner. The mesh can conform to curved boundaries and can move in order to follow changes in the combustion chamber geometry [7]. The conservation equations are spatially discretized using the control volume method. A typical cell is shown in figure 3.2.a. The vertices are conventionally numbered as depicted in the figure. The cells are indexed by integers (i, j, k), which are its coordinates in logical space. The indices (i, j, k) also label the vertices, with the understanding that vertex (i, j, k) is vertex 4 of cell (i, j, k).

Auxiliary cells are defined as surrounding a vertex (i, j, k), with cell edges meeting the midpoint of the surrounding regular cell edges, and vertices placed appropriately within the surrounding normal cells to cover one quarter of each of the surrounding normal cell areas. These cells are called momentum cells as their main use is in differencing the momentum equations. The portion of a momentum cell lying within a regular cell is shown in figure 3.2.b. The momentum cell (i, j, k) is centered about vertex (i, j, k) as illustrated in figure 3.2.c by the example of cross section of a typical finite-difference cell.

In the ALE method velocities are located at the cell vertices. Therefore no interpolation is required when determining the vertex motion in the Lagrangian phase of the calculation, while thermodynamic quantities such as pressure, temperature, etc. are located at cell centers. Spatial differencing is performed by integrating the differential term over the volume of a typical cell.

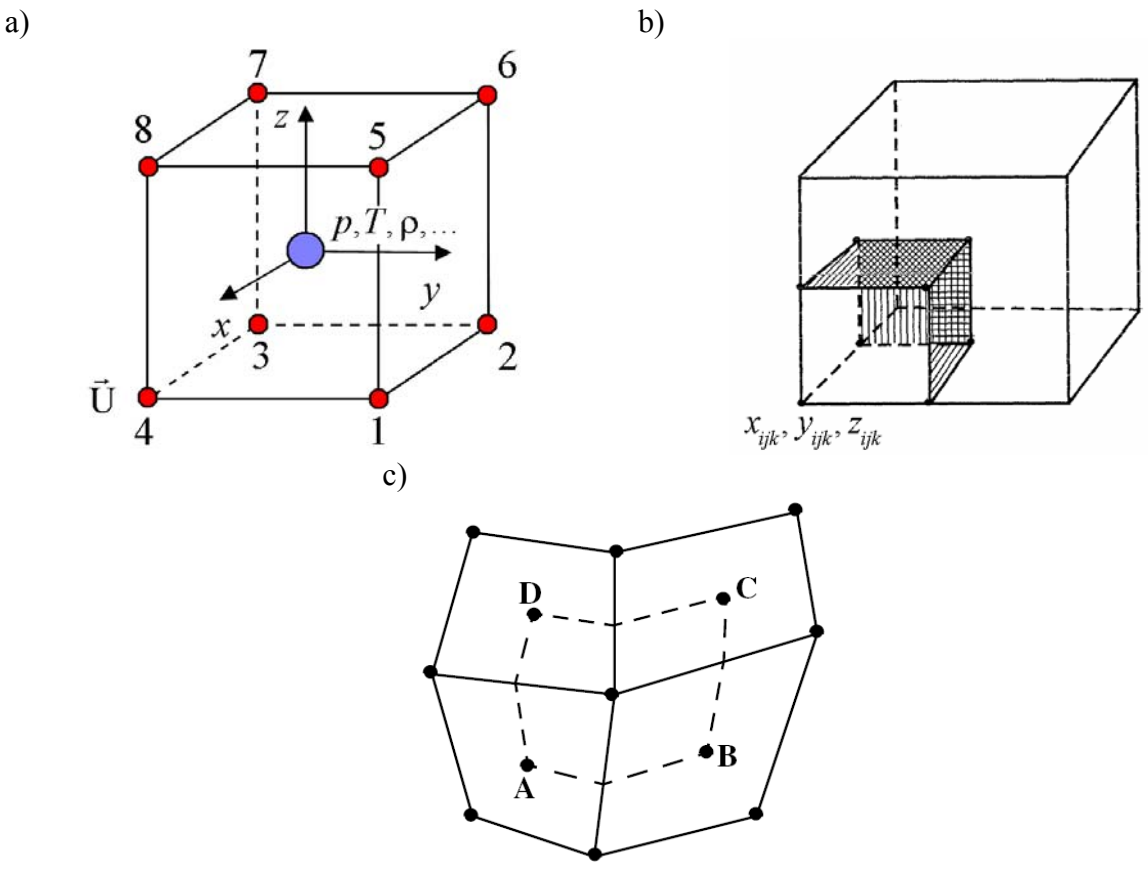

Figure 3.2: a) Typical finite-difference cell; b) The portion of a momentum cell lying within the regular cell; c) Momentum cell (i, j), shown in dashed lines, and its associated regular cell.

The differential form of the governing equations (2.3, 2.4 and 2.6) described in chapter 2 without chemistry and spray is given by

$$\frac{\partial \rho}{\partial t} + \nabla \cdot (\rho \mathbf{u}) = 0, \tag{3.2}$$

$$\frac{\partial (\rho \mathbf{u})}{\partial t} + \nabla \cdot (\rho \mathbf{u}\,\mathbf{u}) = -\nabla p + \nabla \boldsymbol{\sigma} + \rho g, \tag{3.3}$$

$$\frac{\partial (\rho I)}{\partial t} + \nabla \cdot (\rho \mathbf{u} I) = -p \nabla \cdot \mathbf{u} + (1 - A_0)\boldsymbol{\sigma} : \nabla \mathbf{u} - \nabla \cdot \mathbf{J}. \tag{3.4}$$

The equations of motion are formulated with a grid velocity $\mathbf{u}_g$, which varies from $\mathbf{u}_g = 0$ to $\mathbf{u}_g = \mathbf{u}$ for the pure Eulerian and the pure Lagrangian formulations, respectively. In the integral ALE formulation the conservation equations (3.2-3.4) are given in the following way [73, 133, 148]:

$$\frac{d}{dt}\int_V \rho \, d\mathbf{x} + \int_S \rho \, (\mathbf{u} - \mathbf{u}_g) \cdot \mathbf{n} \, dS = 0, \tag{3.5}$$

$$\frac{d}{dt}\int_V \rho \mathbf{u} \, d\mathbf{x} + \int_S \left[\rho \mathbf{u} \, (\mathbf{u} - \mathbf{u}_g) - \boldsymbol{\sigma}\right] \cdot \mathbf{n} \, dS + \int_V \nabla p \, d\mathbf{x} + \int_V \rho g \, d\mathbf{x} = 0, \tag{3.6}$$

$$\frac{d}{dt}\int_V \rho I \, d\mathbf{x} + \int_S \left[\rho I (\mathbf{u} - \mathbf{u}_g) + \mathbf{J}\right] \cdot \mathbf{n} \, dS + \int_V p \nabla \mathbf{u} \, d\mathbf{x} - (1 - A_0)\int_V \boldsymbol{\sigma} : \nabla \mathbf{u} \, d\mathbf{x} = 0. \tag{3.7}$$

The equations are descretized with the standard finite volume discretization after converting volume integrals with the divergence theorem into surface integrals.

3.1.2. Initial and boundary conditions

Boundary conditions used in KIVA-3V can be split into physical and numerical boundary conditions and also boundary conditions for the particle phase:

- Physical boundary conditions: rigid wall (free-slip, no-slip, law-of-the-wall, fixed or adiabatic temperature wall), periodic and spray injector;
- Boundary conditions for the liquid phase;
- Numerical boundary conditions: inflow and outflow boundary conditions for pressure and velocity.

For the rigid no-slip boundary condition the gas velocity is set equal to the wall velocity w_{wall} as given below:

$$\mathbf{u} = w_{wall} \mathbf{k}, \tag{3.8}$$

where $\mathbf{k}$ is the component of the unit vector and the wall is assumed to be moving with speed w_{wall} in the z direction. On rigid free-slip boundaries only the fluid velocity normal to surface has to be considered and is set equal to the normal wall velocity since the tangential components of $\boldsymbol{\sigma}_{wall}$ are zero:

$$\mathbf{u} \cdot \mathbf{n} = w_{wall}\, \mathbf{k} \cdot \mathbf{n} \,. \tag{3.9}$$

By definition, the wall stress $\boldsymbol{\sigma}_{wall}$ and the wall heat flux J_{wall} are determined as following:

$$\boldsymbol{\sigma}_{wall} = \boldsymbol{\sigma} \cdot \mathbf{n} \,, \quad J_{wall} = -k \nabla T \cdot \mathbf{n} \,, \tag{3.10}$$

where $\mathbf{n}$ is the unit outward normal to the wall and $\boldsymbol{\sigma}$ is the stress tensor defined by equation (2.5), see chapter 2.

For turbulent law-of-the-wall as well as free-slip conditions the normal gas velocity is determined by equation (3.9). Definition of the tangential components can be found in [7]. Temperature boundary conditions on rigid walls are introduced by specifying either the wall temperature or the wall heat flux J_{wall}, see equation (3.10). For a fixed temperature wall at either free- or no-slip boundaries the gas temperature is set equal to the wall temperature and the wall heat flux J_{wall} is determined implicitly from equation (2.7). For fixed temperature walls using the turbulent law-of-the-wall condition, $J_{wall} = f(Pr, T, \mathbf{u})$ is determined from the modified Reynolds analogy formula, see [7]. For adiabatic temperature wall J_{wall} is set equal to zero $J_{wall} = -k \nabla T \cdot \mathbf{n} = 0$.

Periodic boundary conditions are used in KIVA-3V only when the flow field is assumed to have an N-fold periodicity about the z-axis. When this assumption is used, the computational region is composed of points in the pie-shaped sector $0 \le \theta \le 2\pi/\mathrm{N}$, where θ satisfies $\cos(\theta) = \mathrm{x}/\sqrt{\mathrm{x}^2 + \mathrm{y}^2}$ and $\sin(\theta) = \mathrm{y}/\sqrt{\mathrm{x}^2 + \mathrm{y}^2}$. The periodic boundaries are those for which $\theta = 0$ and $\theta = 2\pi/\mathrm{N}$. The conditions imposed on these boundaries can be inferred from the assumed N-fold periodicity. For a scalar quantity q the requirement is that $q(r, \theta, \mathrm{z}) = q(r, \theta + 2\pi/\mathrm{N}, \mathrm{z})$, where $r = \sqrt{x^2 + y^2}$. For a vector $\mathbf{v}$ the requirement is that $\mathbf{v}(r, \theta + 2\pi/\mathrm{N}, \mathrm{z}) = \mathbf{R} \cdot \mathbf{v}(r, \theta, \mathrm{z})$, where $\mathbf{R}$ is the rotation matrix corresponding to the angle $2\pi/\mathrm{N}$.

Boundary conditions for the spray equations were briefly considered in section 2.3.7. Another type of physical boundary for the spray equations is the spray injector – a point in space at which a droplet mass flow rate and a distribution of droplet sizes, velocities, temperatures and oscillation parameters are specified. There is an arbitrary number of spray injectors which can be used in a single calculation. The mass flow rate for each injector is constant during injection time and is zero otherwise. Injected droplets may have monodisperse or χ - squared size distributions, velocities of all injected droplets are u_{inj} and can be set as function of time $u_{inj} = f(t)$.

3.2. Implementation of LES in KIVA-3V

The large eddy simulation method based on the classical Smagorinsky model [155] has been implemented into the KIVA-3V code. A detailed description of the model is given in section 2.2.4 in chapter 2. As it has been mentioned before, eddy-viscosity models account for

the global effects of subgrid-scale turbulent structures by an increased effective viscosity $\nu_{eff} = \nu_{mol} + \nu_t$, where in case of the Smagorinsky model ν_t is calculated according to equation (2.26) with the filter width $\Delta = (\Delta_1 \Delta_2 \Delta_3)^{1/3}$. In equation (2.26) the model constant C_S was taken to be 0.1 following typical literature values. This value has been used for the overwhelming number of calculations presented in this work, unless stated otherwise. The Smagorinsky model is known to be simple and robust and requires only limited additional computer resources.

3.3. Validation of the KIVA-3V-LES code

Before attempting to investigate engine-like configurations, the new KIVA-3V-LES code was assessed for a canonical flow configuration. For this propose, a numerical simulation for a fully developed turbulent flow in a square duct has been performed to validate the KIVA-3V-LES code. This configuration has on the one hand been chosen because of its geometric simplicity and on the other hand because of the fact that a transverse mean motion occurs which classical one or two equations RANS models fail to predict. The results obtained were compared with LES and DNS data from the literature [57].

Figure 3.3 shows the coordinate system and geometry for the square duct flow. The dimensions of the computational domain are $d \times d \times 6 \cdot d$. This deceptively simple geometry is described by only one parameter, the Reynolds number. In this case the Reynolds number, see equation (3.11), based on the mean friction velocity and duct width is $\mathrm{Re}_\tau = 600$ [23] which corresponds to $\mathrm{Re}_b = 10320$ based on the mean streamwise velocity.

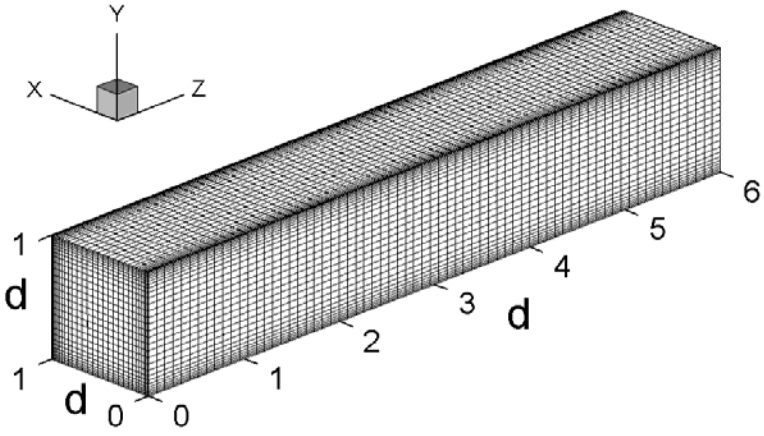

Figure 3.3: Geometry of square duct and computational grid.

Table 3.1 shows a summary of the flow properties for the square duct, assuming standard sea level properties for air. A non-uniform mesh in X and Y directions with $30 \times 30 \times 70$ grid points was used for this test case. Boundary and initial conditions were formulated in the following way: periodic boundary conditions were specified in the streamwise direction, no-slip boundary conditions were set on the wall. The calculations started from a turbulent initial velocity flow field obtained by the so-called inflow-generator [81] (see paragraph 3.4 for more details).

$$Re_\tau = \frac{w_\tau \cdot d}{\nu}, \qquad Re_b = \frac{w_b \cdot d}{\nu} \tag{3.11}$$

Table 3.1: Flow parameters for the square duct.

Flow properties	Re_τ	Re_b	w_τ, [m/s]	w_b, [m/s]	d, [m]	dp/dz, [Pa/m]	g_z, [m^2/s]
Values	600	10320	0.169	2.906	0.05	-2.954	2.284

KIVA-3V does not allow to use simultaneously periodic boundary conditions in streamwise direction and to set a pressure gradient in the same direction. To overcome this problem the gravitation coefficient given by equation (3.12) was used to impose a volume force corresponding to the pressure gradient.

$$g_z = -\frac{dp}{dz}\cdot\frac{1}{\rho},\quad \bar{\tau}_w = -\left(\frac{d}{4}\right)\cdot\frac{dp}{dz},\quad w_\tau = \sqrt{\frac{\tau_w}{\rho}} \tag{3.12}$$

The LES results of the square duct simulation are shown in figure 3.4. Direct numerical simulation [23] data and LES results obtained with the well known FASTEST-3D [80] code are available for this test case. Figure 3.4.a shows the mean streamwise velocity profiles for the 3 cases in the outlet section of the square duct, figure 3.4.b shows the fluctuations. All results shown in figure 3.4 are normalized by the mean friction velocity w_τ. The mean velocity profiles in the KIVA-3V-LES and FASTEST-LES were averaged in time and the agreement turned out to be reasonably good considering the relatively coarse mesh. Small distinctions between KIVA-3V-LES and FASTEST-LES results can be explained by the fact that on the one hand FASTEST-3D uses a better numerical scheme, on the other hand the velocity values in FASTEST-LES are stored in the center of the cell. It means that using the same grid, the first point is much closer to the wall in the FASTEST-LES case. Figure 3.4.c shows the mean secondary velocity vectors obtained by KIVA-3V-LES. It is well visible in this figure, that the corner vortices produced by the secondary flow are captured in this simulation. Although some asymmetry is still evident in the plot, the overall features of the secondary flow are well-predicted by the KIVA-LES simulation.

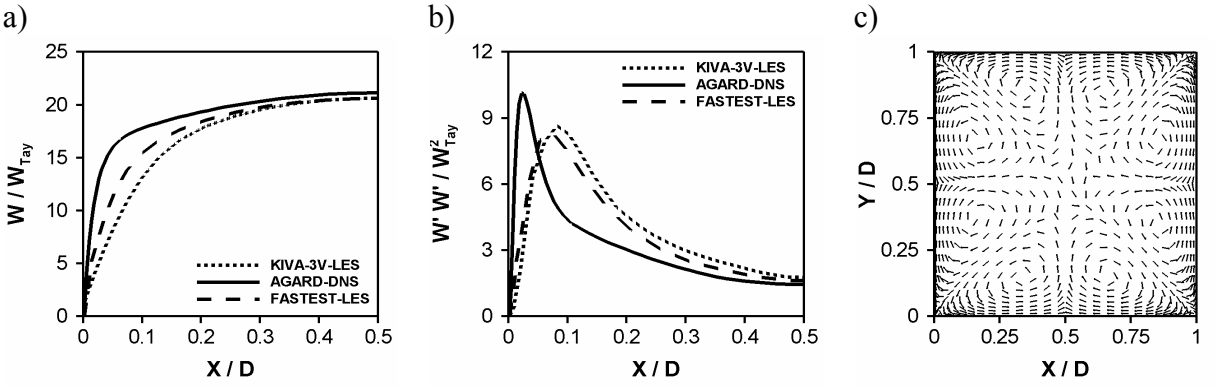

Figure 3.4: a) Mean velocity profile; b) Fluctuations; c) Velocity flow field.

Generally, good agreement is obtained between the KIVA-3V-LES, FASTEST-LES and DNS mean velocity and fluctuation profiles and mean secondary velocity field. Results of a parametric study of the square duct configuration using KIVA-3V-LES can be found in [162] while reference [57] reports about the successful application of KIVA-3V-LES for the prediction of turbulent effects in engine-like geometries. A discussion about the utilization of KIVA-3V-LES for the investigation of a complex swirling and tumbling flow in a complex configuration is given in [78].

3.4. Parallelization based on the variation of initial conditions

Due to the highly unsteady turbulent nature of engine flows statistical methods are necessary to investigate the cycle-to-cycle in-cylinder phenomena. Good statistics requires a high number of statistically independent samples for averaging and therefore extensive computer resources. A reasonable engine LES for example requires computational grids with up to 500.000 control volumes, resulting in computation time of several weeks for one engine cycle on a standard Pentium 4 CPU. Hence, there is a strong necessity to investigate possible parallelization techniques.

The feasibility of parallelization and the efficiency of parallel algorithms are determined by the structure of the process to be modeled as well as the architecture and characteristics of the computer system. The development of any parallel algorithm starts with the decomposition of a general problem [22, 119]. The whole task is divided into a series of independent or slightly dependent sub-tasks which are solved in parallel. The classification of principal types of parallel algorithms can be found for instance, in reference [119]. The application of one or another parallelization strategy mainly depends on the considered tasks.

Generally, there are four parallelization approaches in CFD: the first type is the parallelization by coarse-grained independent sub-tasks. The algorithm consists in the reiteration of statistically independent modeling procedures of a given flow on several processors. The realization of this method for parallel calculations of unsteady processes is discussed in references [89, 101]. The second type is the spatial decomposition of the computational domain. Calculations in each region represent sub-tasks which are solved in parallel, e.g. each processor performs calculations of the flow in its own region. The transfer of information about the flow in sub-regions is accompanied with data exchange between the processors. Therefore these sub-tasks are not independent. The third method is the algorithmic decomposition which consists in the execution of different parts of the same procedures on different processors. The fourth type is the combined decomposition which includes various combinations of the types considered above.

For example, considering chemically reactive flows using KIVA-3V more than 90 percent of the computing time is spend for the chemistry part as reported in [5, 17]. In this case the parallelization efforts mainly have to be focused on the chemical module of the code and can be realized by splitting among all available nodes (CPU). For static geometries as well as for multicylinder IC-engines the domain- and solver-based parallel algorithms can be also applied.

With respect to the simulation of non-reacting flows for a single cylinder geometry a true parallelization, in the sense of a domain decomposition, of the KIVA-3V code is not straightforward and an alternative approach based on coarse-grain parallelization has been used. This method of parallelization allows obtaining a very high speedup and efficiency with the part of parallel calculations up to $\alpha = 0.99 - 0.999$ [26], where α is the parallel fraction defined in one of the two ways:

$$\alpha = \frac{t_{parall}}{t_{total}}, \qquad \alpha = \frac{p\,(S_p - 1)}{S_p (p-1)}. \tag{3.7}$$

Here t_{parall} is the run time of the parallel procedures, t_{total} is the overall run time, p is the number of processors and S_p is the speedup, given by $S_p(p,\alpha) = t_1/t_p$, where t_1 is the execution time of the sequential algorithm and t_p is the execution time of a given parallel algorithm on the computer system using p processors.

The technique used in the present work is based on the idea that starting several simulations with different initial conditions will yield statistically independent results for each cycle. Therefore the number of samples can be increased by performing independent simulations with different initial conditions on several processors. Instead of starting the simulations from zero a developed flow field from a previous simulation has been used together with superimposed disturbances in order to create statistically independent realizations of the flow.

The problem of efficient generation of artificial turbulent initial and inflow conditions for LES is the subject of many research works, for instance [84]. Devesa et al. [38] present an experimental and numerical study of the interaction between an air jet and a tumbling flow in a model engine configuration. LES is performed using the so-called single-cycle strategy where the initial conditions at bottom dead center (BDC) are obtained from PIV measurements in order to perform several simulations only of those parts of one engine cycles that are of interest. Results show a significant influence of the initial conditions on LES results and it was concluded that this strategy will be probably of limited value for engine simulations using LES. In contrast to [38], Goryntsev et al. [57, 59] report about a successful application of artificial initial conditions for simulation of reciprocating engines and obtaining a statistically independent solution for in-cylinder flow using LES.

References [81, 83, 85] describe a method of artificial generation of initial conditions and transient inflow conditions for DNS and LES. The common approach is to generate a pseudo-turbulent velocity field in 3D and superimpose it to the mean velocity field. Different strategies for generating artificial turbulent velocity data are discussed in [85] and the possible application to complex configurations is illustrated by the example of an IC-engine geometry.

A different random flow generation technique which can be used to prescribe inlet conditions as well as initial conditions for inhomogeneous anisotropic divergence free vector fields representing turbulent velocity fluctuations was developed and validated in the work of Smirnov et al. [157]. This technique can be also used to generate the initial (or inlet) conditions for LES in order to reduce time and memory requirements of the LES simulation.

A strong impact of the flow field in the inlet section on the velocity profiles inside the combustion chamber has been shown in [57, 59]. As the intake flow has a typical structure with very low cycle-to-cycle variations (less than 5% of the mean inlet velocity) the addition of artificial disturbances to the inlet velocity profile during the intake stroke is an efficient way of forcing different instantaneous realizations of the flow possessing, however, the identical mean behavior. Schematically the process is shown in table 3.2. Performing the IC-engine simulations is split up in the following steps: 1) Using one serial CPU for performing the simulation of a few engine cycles (e.g. 3). 2) Starting with this flow field weak random fluctuations are added at the inlet plane to the existing intake flow during the whole intake stroke. This process is repeated on N-CPUs with different velocity disturbances. 3) From the next engine cycle on all CPUs are working in the serial computation regime calculating different flow realizations. The advantages of this parallelization strategy are: a) the task on each CPU can be managed independent from all other CPUs; b) computer systems of various architectures can be used for the parallel calculations; c) the approach results in high efficiency calculations with no communication overhead.

In order to illustrate this hypothesis the simulation of an IC-engine with standard valve-ports, as shown in figure 3.5.a, and engine parameters, as documented in table 3.3, has been carried out. The valve lift curves are given in figure 3.5.b. A serial simulation of three consecutive engine cycles has been stopped at the beginning of the 4^{th} cycle. At this point 2 different random velocity profiles were added to the existing intake flow (at the intake plane of the intake port) during the intake stroke: one with an amplitude of 1.5% and a higher intensity field with an amplitude of 5% of the mean inlet velocity. Figure 3.6 illustrates the resulting distributions of absolute velocity in the combustion chamber along the line $z = 0.06\,\text{m}$ during compression stroke at crank angle $CA = 300°$ for the standard (a) and 2 disturbed configurations (b) and (c) respectively.

Table 3.2: Illustration of the parallelization strategy based on variation of initial conditions.

CPU – 1	**CPU – 2**	...	**CPU – N**
Step 1: Performing a few engine cycles using CPU 1.			
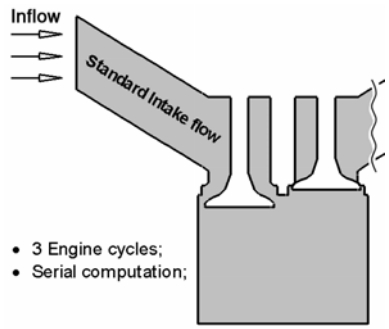	Is not used		Is not used
Step 2: Continuation of serial computation on CPU 1. Cloning this task on CPUs 2, .., N and addition of random velocity fluctuations at the inlet plane of the intake port.			
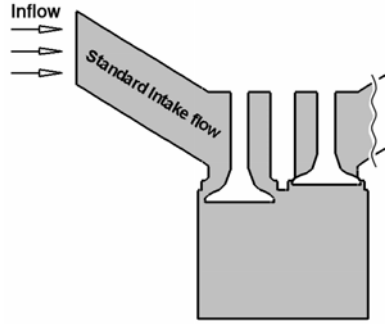	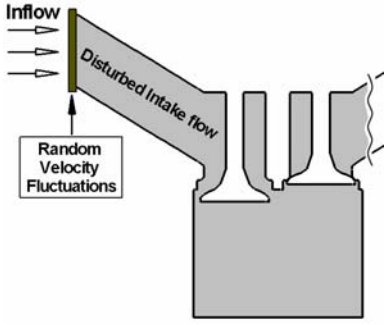	…	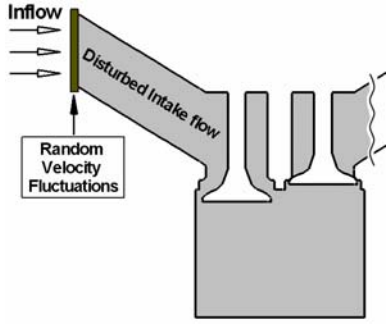
Step 3: Continuation of serial computation on CPUs 1, 2, .., N.			
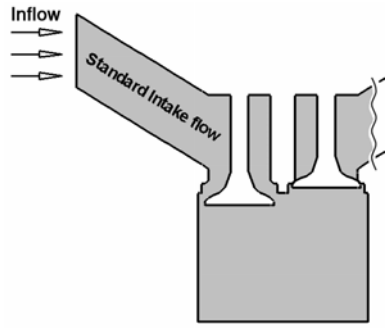	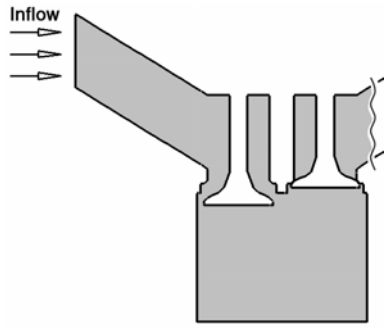	…	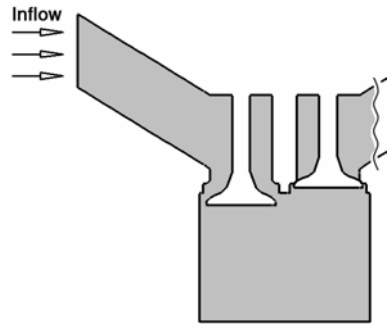

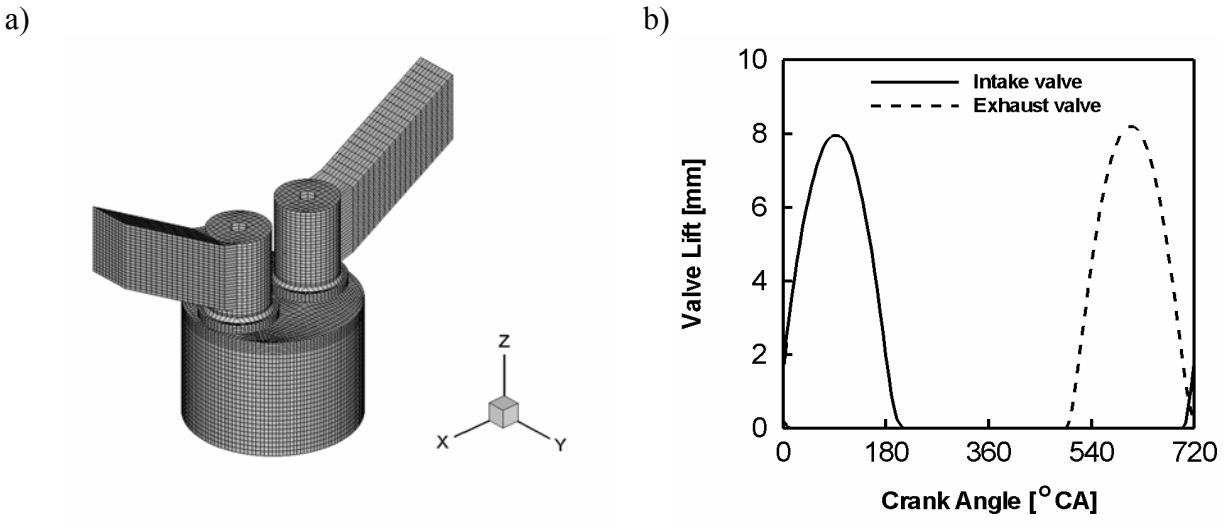

Figure 3.5: a) IC-engine with two vertical valves; b) Valve lift profiles.

Table 3.3: Parameters of the "VV" IC-engine.

Bore [mm]	Stroke [mm]	Clearance height [mm]	Engine speed [rpm]	Inlet valve opening [deg]	Inlet valve closure [deg]	Exhaust valve opening [deg]	Exhaust valve closure [deg]
82.55	92.075	5.70	1600	-20°	210°	500°	730°

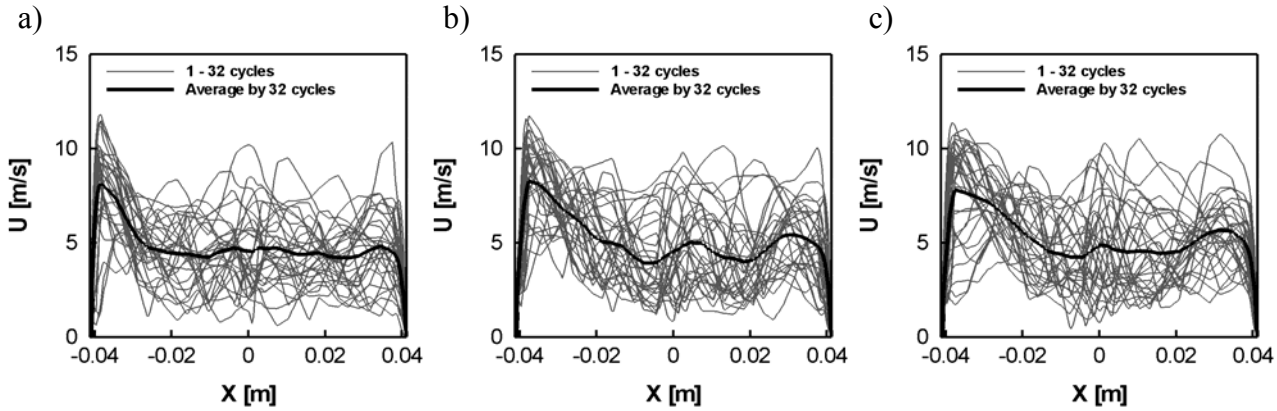

Figure 3.6: Velocity distribution in the combustion chamber, 32 engine cycles, $CA = 300°$, $z = 0.06\,m$; a) standard intake conditions, b) ± 1.5% velocity fluctuations, c) ± 5.0% velocity fluctuations.

Comparison of the instantaneous profiles (figure 3.6) shows similar fluctuation amplitudes for all cases. Figure 3.7 directly compares the mean velocity profiles averaged over 32 engine cycles for intake (a) and compression (b) stroke for the three set-ups under

consideration. The results demonstrate the good agreement of the different mean profiles with similar velocity magnitudes and the same shape of the curves. The maximal differences between average velocity profiles for the considered cases at $CA = 120°$ and $CA = 240°$ are of the order of 10%.

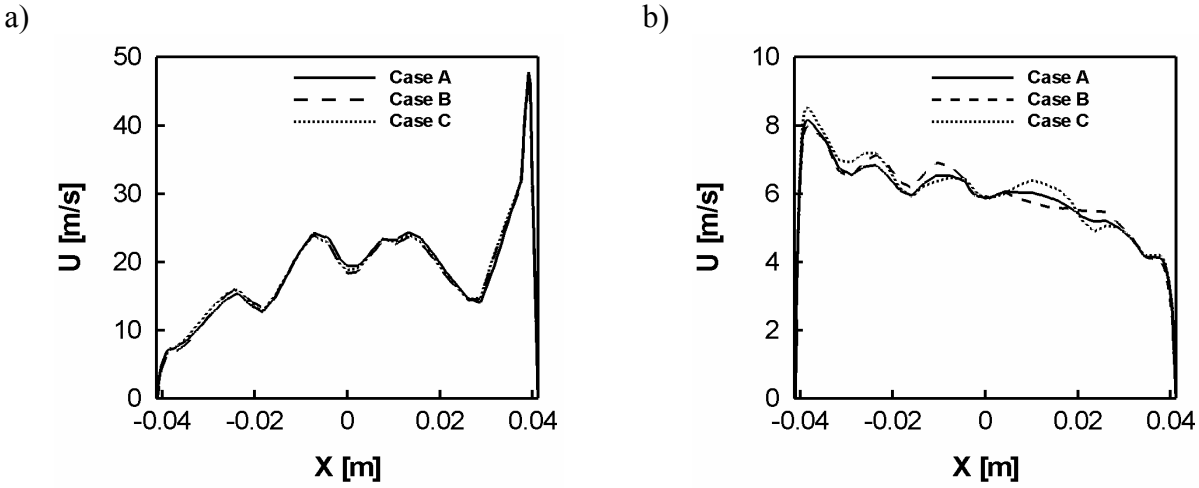

Figure 3.7: Comparison of mean velocity profiles, averaged over 32 engine cycles, for standard intake conditions (case A), ± 1.5% (case B) and ± 5.0% (case C) velocity fluctuations, $z = 0.06\,\text{m}$; a) $CA = 120°$, intake stroke; b) $CA = 240°$, compression stroke.

It can be concluded that creating different initial conditions by disturbing an existing intake flow field yields statistically independent realizations of the same engine flow. Consequently, this technique may be used to carry out parallel simulations in the sense explained above in order to obtain IC-engine flow field statistics in a more reasonable amount of time. It should be also mentioned that disturbing the flow in the combustion chamber as described above was not sufficient in order to obtain independent flow realizations. This possibly points towards the origin of the cycle-to-cycle variations in the valve-port area.

3.5. Summary

The design of new engine concepts requires more understanding of the unsteady processes inside the engines and demands for an increasing help from CFD modeling. The KIVA-3V code is widely used in the automotive community for the simulations of IC-engine fluid dynamics. Access to the source code provides possibilities for developing of new and refining of existent sub-models. As it has been shown in the work of Celik et al. [29], KIVA-3V is not the most suitable code for LES. Nevertheless, by carefully controlling the numerical errors and using relatively fine grid resolution the unsteady dynamics of turbulent flows can be captured reasonably well. In order to account for the highly unsteady and complex processes of in-cylinder flow a LES subgrid-scale model has been implemented into the code. A square duct configuration was used to validate the new KIVA-3V-LES code and results were found to be in a good agreement with available DNS and LES data.

As the analysis of transient phenomena requires a big number of samples in order to obtain qualitatively good statistics, the possibility of parallel calculations has been considered. Since a true parallelization of the KIVA-3V code is not straightforward an alternative approach based on the variation of initial conditions was developed and validated by the results of the simulated benchmark cases.

Chapter 4

Grid generation for internal combustion engines

Simulation of IC-engines encloses the physical modeling as well as the computational grid handling. Modern IC-engines have very complicated geometry with complex shapes of head, piston, valve-ports, etc., moreover, they contain a moving piston and valves. The computational grid should have a reasonable quality for the whole engine cycle. Some challenges of grid generation are considered in the present chapter. Due to the complexity of the concerned geometries (moving piston and canted valves, intricate shape of head, piston, bowl, etc.) grid generation for KIVA-3V is an extremely complicated task. Only a few program packages have tools or interfaces to generate a grid for the KIVA-3V program: Ansys ICEM CFD, KIVA preprocessor program. A short description of these grid generation programs and the philosophy of mesh generation are presented below. Furthermore, the principal KIVA-3V limitations for calculation of complex IC-engines as well as a technique of overcoming these difficulties are outlined. As the consideration of grid generation problems is not the main focus of the present work, modifications of the source code will not be considered. Thus only grids which can be adapted to the existing or a slightly modified code were taken into consideration. Finally, planning and building an initial block topology in ICEM CFD Hexa are discussed and examples of the various grids for IC-engine geometries are shown.

4.1. Overview of the existing grid generation tools for KIVA-3V

The KIVA-3V formulation is based on Cartesian coordinates and uses a block-structured mesh with connectivity defined through indirect addressing. Structured grid generation is very effective when relatively simple geometries are considered (2D channel, square duct, etc.). Unfortunately, creating a mesh for complex geometries (like IC-engines) for transient analysis in KIVA-3V is inherently difficult and causes a long user interaction time. Almost all grid generators use an inefficient “trial and error” strategy which can be very time consuming. At present time only a limited number of grid generators can be applied to create a mesh for KIVA-3V, namely: K3PREP (included in the KIVA package), G-Smooth [168] and Ansys ICEM CFD Hexa [11]. However, the G-Smooth software developed by Convergent Thinking [168] is not a commercial or academic software and hence not available.

4.1.1. KIVA preprocessor program K3PREP

The KIVA-3V package includes a basic grid generator named K3PREP which writes a file conforming to the needed specifications. K3PREP is not designed to generate very complex geometries that KIVA-3V is capable of running, but it can define a variety of useful block shapes and patch them together in a straightforward manner, allowing moderately complex geometries to be constructed in a reasonable amount of time. Further, the user can modify the source code in K3PREP to tailor it to specific needs. K3PREP reads an input file named IPREP which may be as short as 11 lines to define a simple single-block mesh, or may extend hundreds of lines for more complex meshes with curved boundaries [8 – 10].

The advantages of K3PREP can be summarized in the following way: a) It is easy to use in order to create a grid for simple geometries (2D channel, square duct, coarse grid for an IC-

engine with vertical valves, etc.); b) The program is included in the KIVA-3V package together with a documentation and samples; c) As an open source code it can be modified to adapt it to specific needs.

The disadvantages of the K3PREP program are: a) It is not applicable to complex geometries; b) The mesh quality is insufficient; c) A modification of the grid resolution and also the addition or deletion of elements creates severe difficulties; d) It is impossible to import an existing computer-aided design (CAD) geometry.

4.1.2. Ansys ICEM CFD mesh generator

ICEM CFD Hexa is a commercial software package with wide possibilities based on a global block-structured topology providing a top-down approach to mesh generation. ICEM CFD Hexa provides a semi-automatic approach to the building of a multi-block structured hexahedral mesh. The program supports import of CAD surfaces and then automatically generates a global block around the geometry. The desired shape can be obtained by subdividing the initial block into smaller blocks and assigning them to different materials. To reflect the characteristic features of the geometry to be meshed, the block structure can be interactively adjusted to the underlying CAD geometry [11]. The mesh generator has an interface for KIVA-3V which includes selection of the version (KIVA-3 or KIVA-3V), setup of the boundary conditions and preparation of the grid file.

ICEM CFD Hexa offers the following advantages: a) Import / export of CAD geometries is possible; b) The program provides the possibility to add, delete and modify existing geometry or its parts; c) There is an easy way to manage the number of cells and also the cell distribution. The program has also features to check the quality of the mesh with a variety of criteria, which assists to specify and fix possible problems.

The drawbacks are: a) Despite its high functionality and numerous checking features e.g. for non-convex cells and cells with negative volumes, the program has no tools for automatic fixing of bad cells (in the case of KIVA-3V); b) The mesh generation using ICEM CFD Hexa is still a time-consuming task and depends heavily on the experience of a user.

4.2. Generation of block-structured grids for realistic IC-engines

Although a detailed consideration of grid generation problems is beyond the scope of this manuscript, the general principles of grid generation will be reviewed in this section. The author has spent a huge amount of time to generate reasonable grids of realistic IC-engine conformable to LES. The large eddy simulation method poses stronger requirements to the quality of a computational grid and its resolution. As mentioned before, K3PREP can not be used for grid generation of a realistic IC-engine, such as considered in the framework of this manuscript, therefore ICEM CFD Hexa has been used. The general principles of the block-structured grid generation used in KIVA-3V are given below.

Generation of a block-structured mesh is based on decomposing the engine geometry into several different zones, schematically shown in figure 4.1.a. The idea of decomposition is to split the complicated parts of the engine, especially the combustion chamber, into several separate domains with either simpler geometry or less mesh movement. Also it is possible to distinguish zones like inlet and exhaust ports with a complex geometry but static mesh. The blocking, on the one hand, allows to obtain a qualitatively good grid and on the other hand, to simplify the processing of the mesh considerably. The zones with moving boundaries are split as far as possible into more simple domains. The grid in such areas is not only easier to create, but it is also easier to control during the simulation.

In case of the "BMBF" engine the combustion chamber is divided into free much simpler zones as depicted in figure 4.1.a: squish (I), head (II) and bowl (III). The initial mesh is generated when the piston is at BDC and all valves are closed. Detailed information about decomposition strategy and meshing is collected in table 4.1.

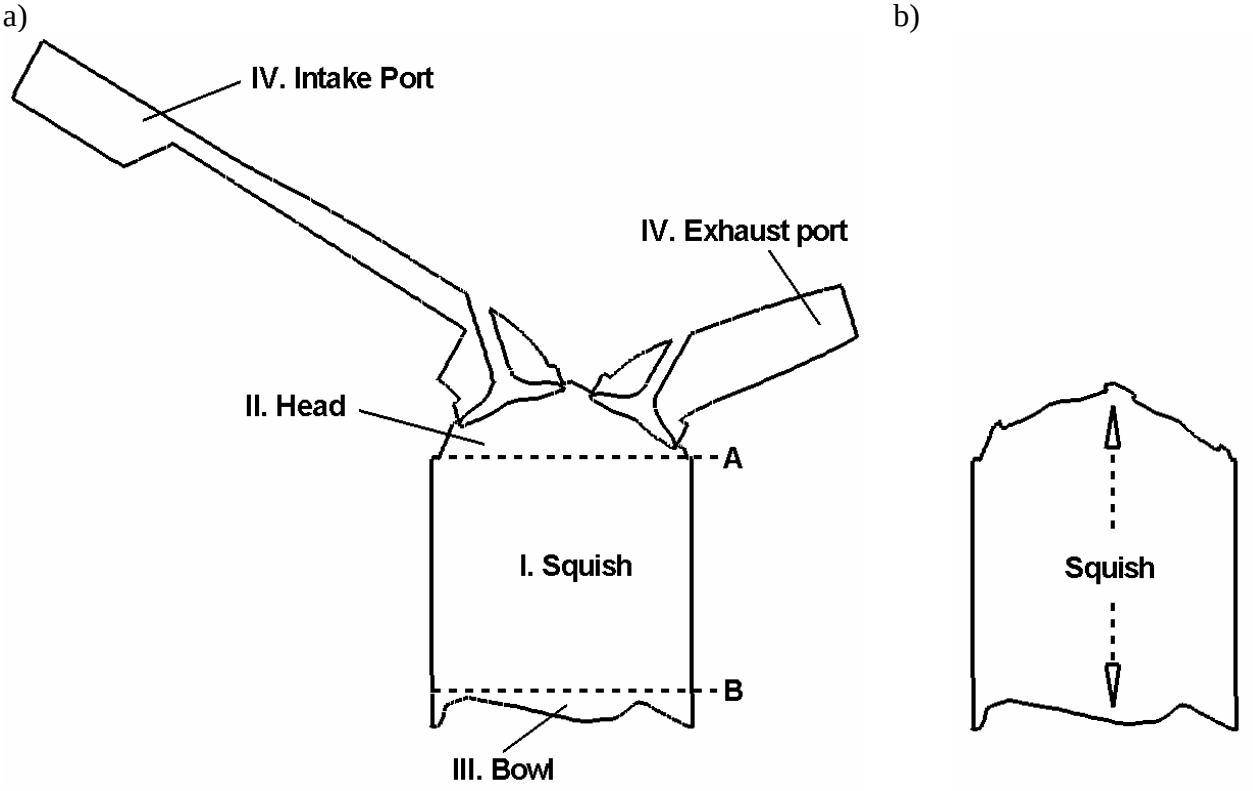

Figure 4.1: a) Geometry decomposition of "BMBF" IC-engine; b) Single-cylinder geometry which represents a combustion chamber of an IC-engine with closed valves.

Table 4.1: Description of decomposition strategy and mesh behavior.

No.	Region	Description
I.	Squish	Moving mesh between two parallel surfaces A-B, see figure 4.1.a. KIVA-3V requires that Z coordinates are the same all around the circumference of the cylinder at every level through the vertical range of piston travel.
II.	Head	Complex head geometry with non-moving initial mesh. Mesh movement appears mainly due to the valves and partially due to the piston motions. Grid management can be realized by application of special rezoners for certain types of head geometries.
III.	Bowl	Complex bowl geometry with non-moving initial mesh. Mesh does not change but translates with the piston during engine simulation.
IV.	Intake and exhaust ports	Complex geometry, non-moving mesh.

The quality of the final mesh and the specification of the geometry in the intake / exhaust ports and bowl regions is completely defined by the quality and accuracy of the initial grid. The squish region (figure 4.1.a) consists at the initial stage of a cylindrical mesh with parallel surfaces A-B. The mesh in that zone changes considerably during the simulation, but as a consequence of the blocking it becomes possible to manage the cell distribution efficiently. Most of the difficulties appear during creation and controlling of the grid in the head region (figure 4.1.a) due to the simultaneous influence of the moving valves and piston. In that region the initial grid, as well as the number and distribution of the cells depend on the type and the peculiarities of the rezoner. More detailed information can be found in [9, 186].

4.2.1. Limitations of the KIVA-3V program

The approach mentioned above has significant advantages during mesh generation and has been used in KIVA-3V rezoner strategy. However, it results in the impossibility to simulate a real engine stroke for certain configurations (for instance, see figure 4.2). The current version of KIVA-3V does not support the possibility to simulate a configuration where the piston crown goes inside the head zone. To simulate such a case the squish region has to be combined with the head which leads to a different grid generation strategy and requires a modification of the rezoner.

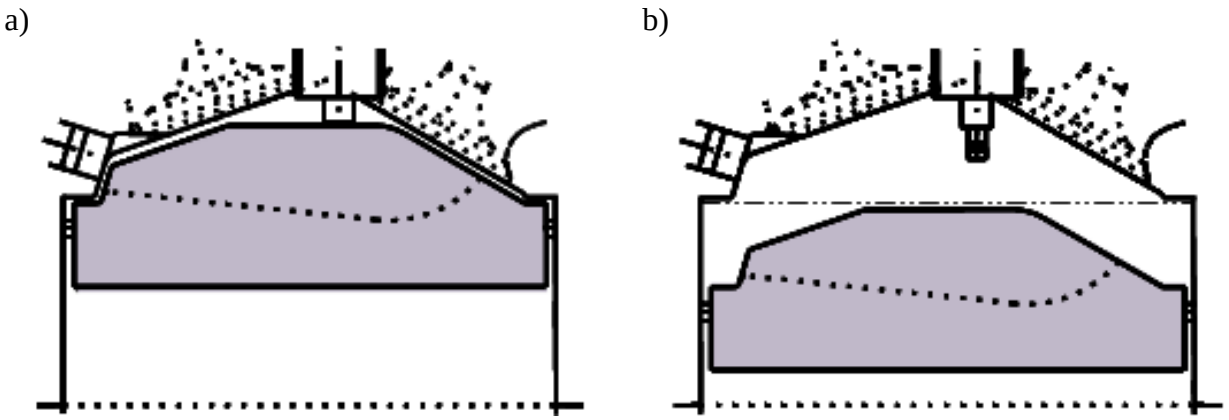

Figure 4.2: Illustration of KIVA-3V limitations: a) Real engine stroke, piston is at TDC; b) Engine stroke (TDC) which can be calculated by KIVA-3V.

The following approach (see figure 4.3) has been suggested to overcome the problem mentioned above: Step 1: The simulation starts using the original geometry and stops at the beginning of compression stroke at CA = 210.0°. Step 2: At this crank angle all valves are closed and the combustion chamber can be represented by much simpler blocking shown in figure 4.1.b and grid. This is a single cylinder geometry which represents the combustion chamber of the "BMBF" IC-engine during compression and expansion stroke. All CFD parameters are transferred to the new grid. This allows to calculate the real engine stroke for a given value of clearance while the calculation using the original geometry is continued (in order to calculate the flow field in the ports). Even the simulation of the single cylinder geometry requires some minor changes of the code. Furthermore, a manual control of cell distribution has been realized in order to provide a better cell allocation. Step 3: At the beginning of the expansion stroke all data is copied back from the simple to the original grid and the calculations are continued using the general mesh. This strategy allowed to perform successfully the "BMBF" IC-engine calculations

without serious modifications of the KIVA-3V code and to provide the required quality of the results.

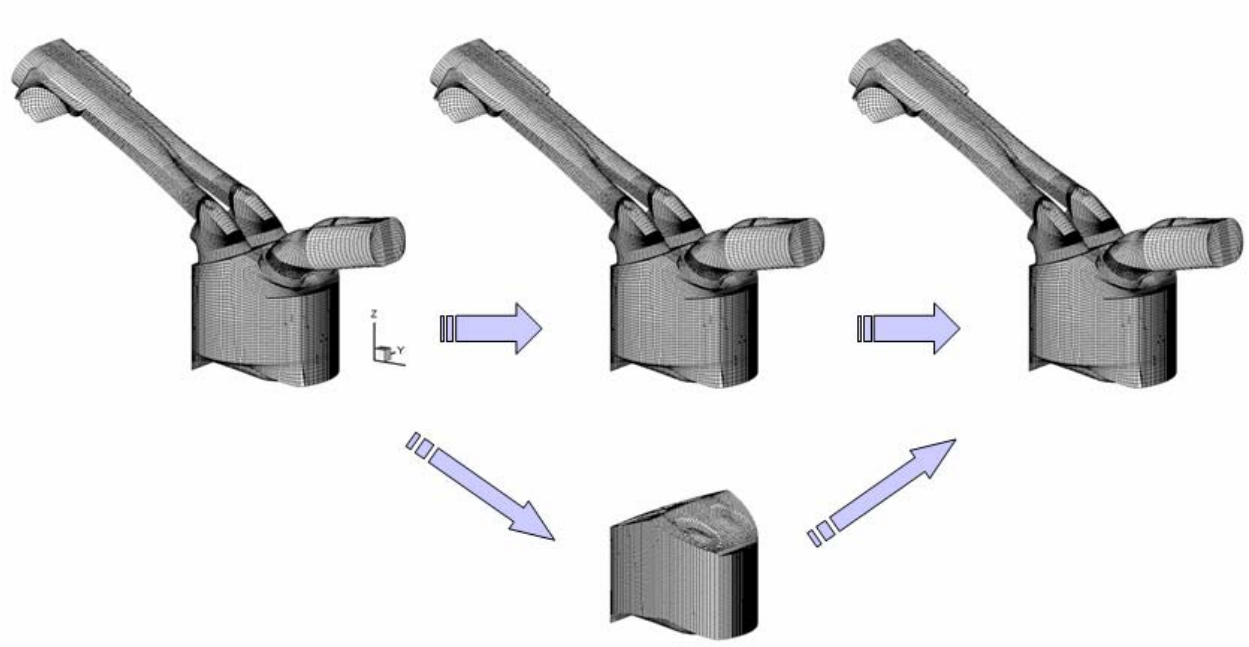

Figure 4.3: Performing of a full engine cycle for the "BMBF" IC-engine using KIVA-3V.

4.2.2. Planning and building the block topology in ICEM CFD Hexa

Multi-block structured grid represents a complex domain by a number of much simpler separated blocks. In case of a three-dimensional domain the block topology consists of information about vertices, edges, faces and blocks and the relationship between each of them. Vertices are associated with points, edges – with lines or surfaces, faces are connected with surfaces of the CAD geometry. Blocks which represent the individual parts of an IC-engine (e.g. intake valve, exhaust port, piston-bowl) usually are united into families, for which different boundary conditions have to be applied.

The so-called top-down method is used for planning and building the block topology. The essence of the top-down principle is to create one block over the whole geometry with subsequent fragmentation in order to capture all details of interest. The mesh generation process starts from CAD cleanup, i.e. surface repair and curves extraction. It is necessary to fix any holes or gaps in the CAD data, especially if their size has the same order of magnitude as the element size or larger, otherwise they will cause problems during mesh generation. Curves are required for sharp transitions between surfaces and for the definition of boundary conditions between two families and they are absolutely necessary for mesh generation for KIVA-3V. Curves have to be extracted from surfaces where the geometry features need to be captured (e.g. bevels at valve bottom, piston-bowl) and from surface intersections (e.g. squish and head, port and head, etc.).

Unfortunately, while mesh generation for KIVA-3V the O-Grid tool of ICEM CFD can not be used due to the cell definition as shown in figure 4.4. All vertices have to possess 4 (in an external) or 8 (in an internal block) adjacent cells (a) and no vertices may have 3 or 6 adjacent cells (b), i.e. i, j, k must line up throughout. Therefore, there remains only the possibility to use the basic blocking feature with the ability to split and to join created blocks.

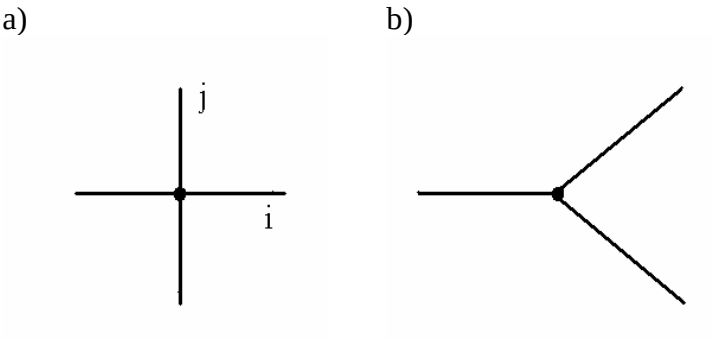

Figure 4.4: The vertices in “structured” (a) and “unstructured” (b) grids.

After checking the CAD data the next step in mesh generation is the design of the initial topology. A global block surrounding the geometry is automatically generated by ICEM CFD Hexa as shown in figure 4.5.a. By subdividing this block into smaller blocks (see figure 4.5.b) the main details of the engine, namely cylinder, head and ports can be assigned. In the sequel each of these parts is split in turn into smaller blocks in order to extract fine parts of interest such as valves, valve stems and so on.

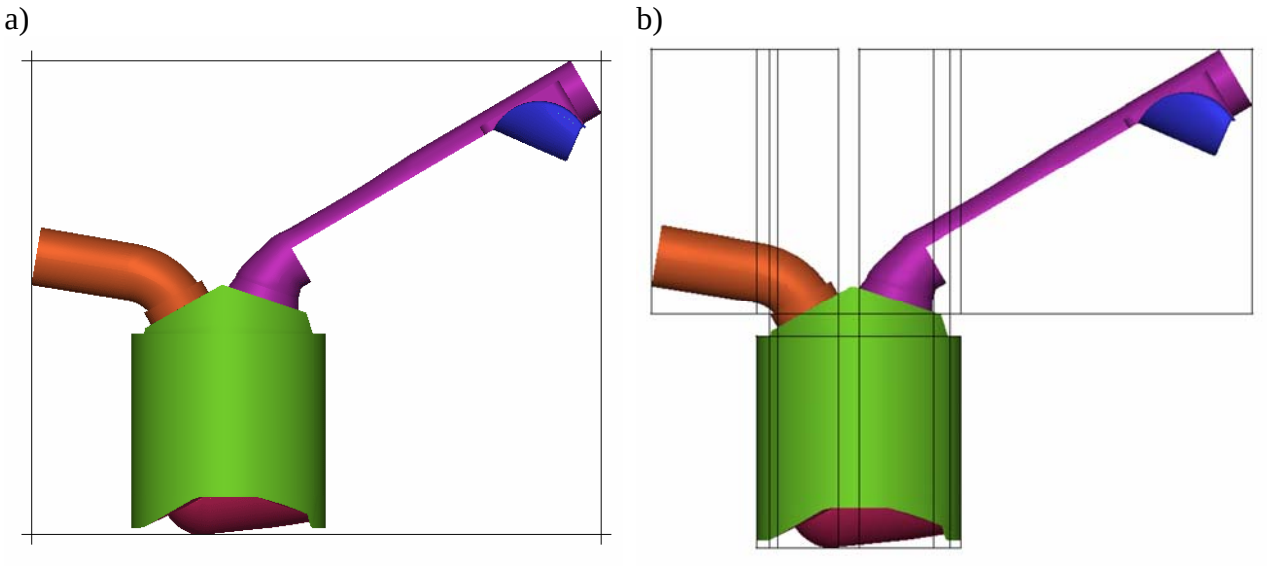

Figure 4.5: Illustration of the generation of the initial topology: a) Global block around the CAD geometry, X-Z plane of 3D initial block; b) Subdivision into smaller blocks which represent the basic details of an IC-engine like cylinder, head, intake and exhaust ports.

As it was mentioned above, the grid in the intake and exhaust ports is static and can be created separately. Severe difficulties arise during planning the block topology for the head and valves parts. In order to represent valves and valve stems the global block (figure 4.6.a) is divided into 11 sub-blocks in X and 9 sub-blocks in Y directions as shown in figure 4.6.b. To reflect the characteristic features of the geometry to be meshed, the block structure is adjusted to the underlying CAD geometry (figure 4.7.a) and certain blocks are merged. Splitting of the initial block in Z-direction is also necessary (see figure 4.7.b) in order to separate bowl and squish (marked A), squish and head (B), and to represent bottom (C) and top (D) valve surfaces and dome (E).

After creation of the initial topology all blocks are split, joined together or deleted and all features are captured, the edges have to be associated with curves as well as faces with surfaces. Next the required grid resolution is set and finally the computing of the mesh can be performed. Usually it is necessary to check the quality of the mesh at first by visual inspection and then mathematically using the ICEM CFD checking tools. The most time consuming part is very often the adjustment of the grid and the rescue from non-convex cells and cells with negative volumes. This part consists as a rule of playing with vertex positions, variation of edges associations, mesh resolutions and so forth. There is no universal way to improve the quality and to accelerate the process of mesh generation. In the overwhelming majority of cases the completion of the grid generation procedure is in the first place based on experience and on a successful choice of the initial topology.

a) b)

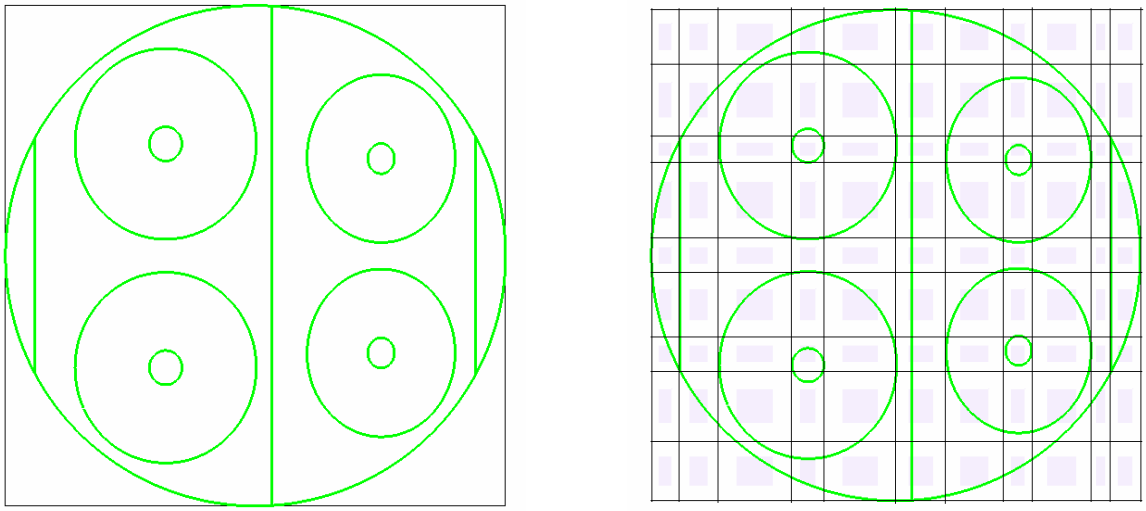

Figure 4.6: Initial (a) and split initial block (b), X-Y plane.

a) b)

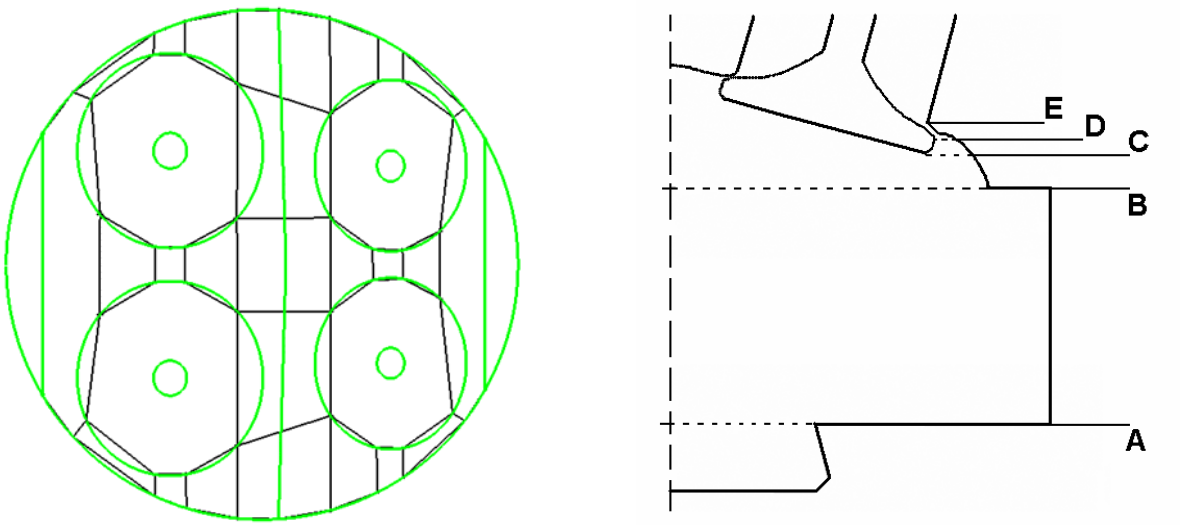

Figure 4.7: Split blocks: a) Adjustment of the vertices during creation of the topology for the head part of the engine, X-Y plane; b) Segregation of the global block in Z-direction, X-Z plane.

4.2.3. Examples of grids for IC-engine geometries

The grids of some parts of the "BMBF" IC-engine as well as the computational grid for the whole engine geometry are shown in this section. Mesh generation passes through three stages, namely geometry preparation, blocking and meshing. This evolution is schematically shown in figure 4.8 for the example of a valve and valve stem. The topology for this case consists of 4 blocks (b), which allow to represent all design features as it can be seen in figure 4.8.c. KIVA-3V tolerates valve skirts up to 5 cells high but practically for canted valves, the skirts height is limited to 1 or 2 cells.

a) b) c)

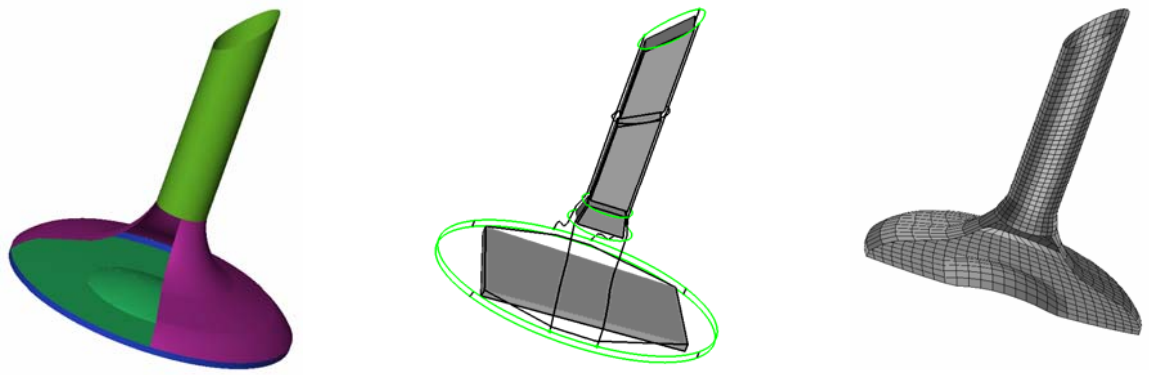

Figure 4.8: Blocking and mesh for valve and valve stem. a) CAD data; b) Blocking in ICEM CFD Hexa; c) Part of the computational grid.

Geometry, block topology and computational grid for the head part of the "BMBF" IC-engine are shown in figure 4.9. The engine has four canted valves, two intake valves with declination of 19 degrees to the axis X and two exhaust valves with 30 degrees declination. This is a strong complicative factor from the grid generation point of view. During the initial stage of block topology building the number of blocks was approximately equal to 100 and for the final topology the number has been reduced to 17 blocks, see table 4.2.

a) b) c)

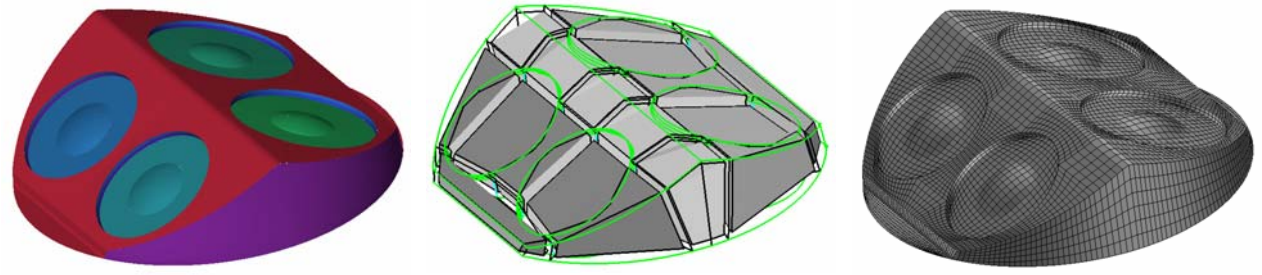

Figure 4.9: Blocking and mesh for head part with 4 canted valves. a) CAD data; b) Blocking in ICEM CFD Hexa; c) Computational grid.

The final block topology for the whole "BMBF" IC-engine geometry is shown in figure 4.10.b and consists of 5 relatively independent parts like bowl, squish, head, intake / exhaust ports and includes 150 blocks.

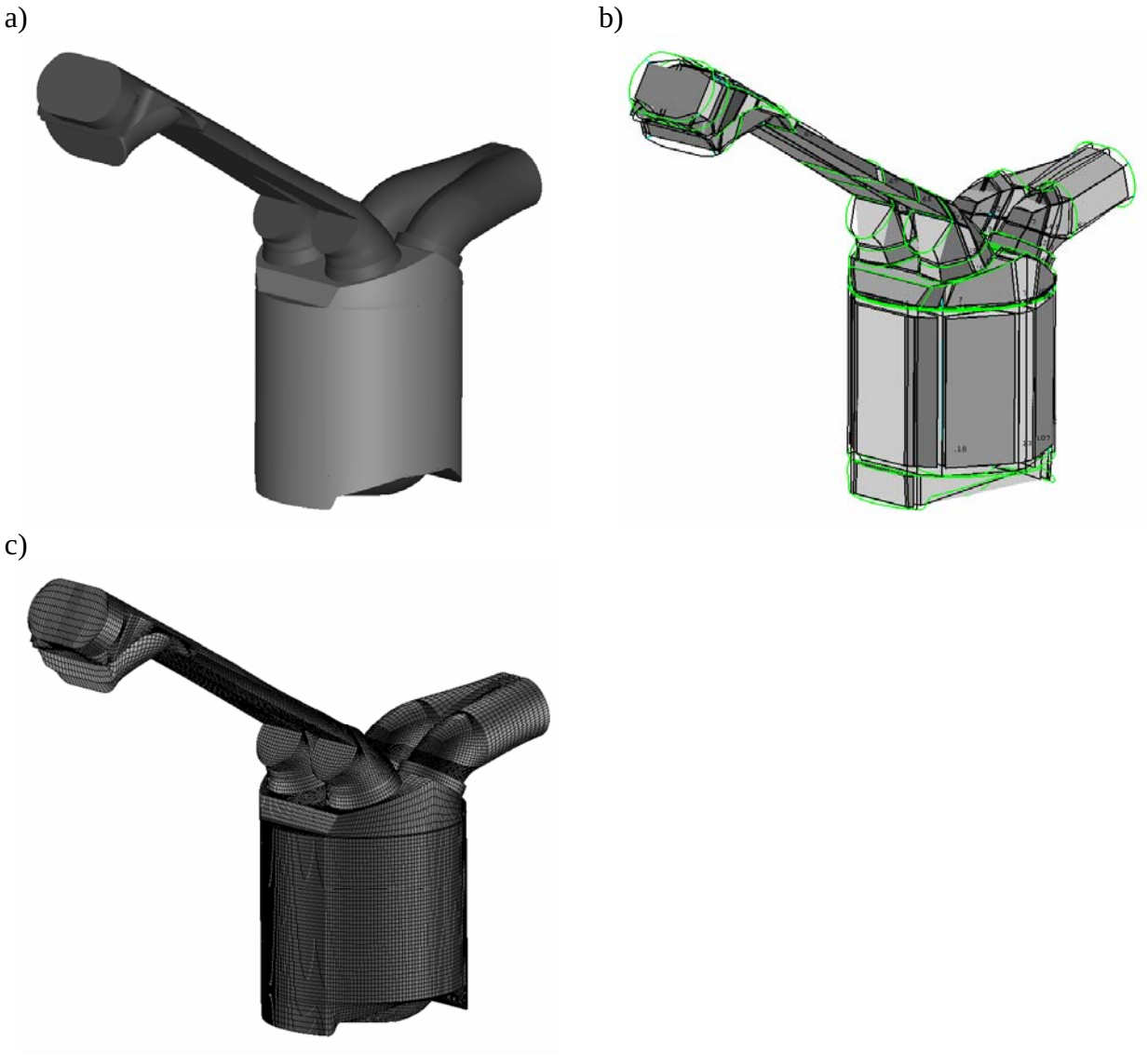

Figure 4.10: Block topology and computational grid for "BMBF" IC-engine. a) CAD data; b) Blocking in ICEM CFD Hexa; c) Computational grid.

Table 4.2: Amount of blocks in IC-engine geometry.

Region	Number of blocks
Squish	57
Piston-Bowl	3
Cylinder Head	17
Intake / Exhaust ports	57
Valves & Stems	16
Total:	**150**

4.3. Conclusions

K3PREP preprocessor program can be applied to create grids for relatively simple geometries with uniform cell distribution. Thus, the geometry and the computational grid for a square duct (see chapter 3) and an IC-engine with 2 vertical valves (see chapter 5) have been created with K3PREP. In order to create meshes for more complex cases ICEM CFD Hexa program has to be used. At present time ICEM CFD Hexa is the only program, which is able to generate grids for these complex geometries to be used in KIVA-3V. The CAD data can be imported in ICEM CFD. The program provides sufficiently high quality of the grids which represent the characteristic features of the geometry. The computational mesh for the “BMBF” IC-engine (see chapters 5 – 7) has been created by ICEM CFD Hexa. In order to be able to perform a real engine stroke calculation for a geometry with a pronounced piston crown an additional simplified mesh has been used to overcome the problems appearing through the piston motion near TDC.

Chapter 5

Results and discussion: single-phase flow

The main results of IC-engine simulations for single-phase flow are presented and discussed in this chapter. Firstly, the basic engine specification and the parameters of the calculations are summarized. Then the analysis of velocity cycle-to-cycle variations in the combustion chamber based on the consideration of 50 full engine cycles is provided for intake, compression, expansion and exhaust strokes. The next paragraphs describe the cyclic variability of the mean flow properties for the whole engine cycle. Finally, the comparison between LES and available experimental data is provided and the differences between averaged LES results and RANS predictions are examined.

5.1. Configuration and numerical setup

The investigated configuration represents the "BMBF" four-stroke direct spray injection engine [63] with variable charge motion (VCM) system shown in figure 5.1. This is a realistic IC-engine with 4 canted valves with an asymmetric cylinder head and an asymmetric piston bowl. The considered IC-engine relates to air-guided tumble combustion systems where the VCM serves to adjust and to optimize the parameters within the combustion chamber. The variable tumble system controls the in-cylinder charge motion which enables controlled guidance of the fuel penetration towards the spark plug. The main parameters of the engine are summarized in table 5.1. The valve lift curves are given in figure 5.2. Here and later the following notation is used: The engine cycle begins with $CA = 0°$, i.e. top dead center. Hence, the $CA = 0° - 180°$ range corresponds to the intake stroke, $CA = 180° - 360°$ is the compression stroke, $CA = 360° - 540°$ is the expansion stroke and $CA = 540° - 720°$ is the exhaust stroke.

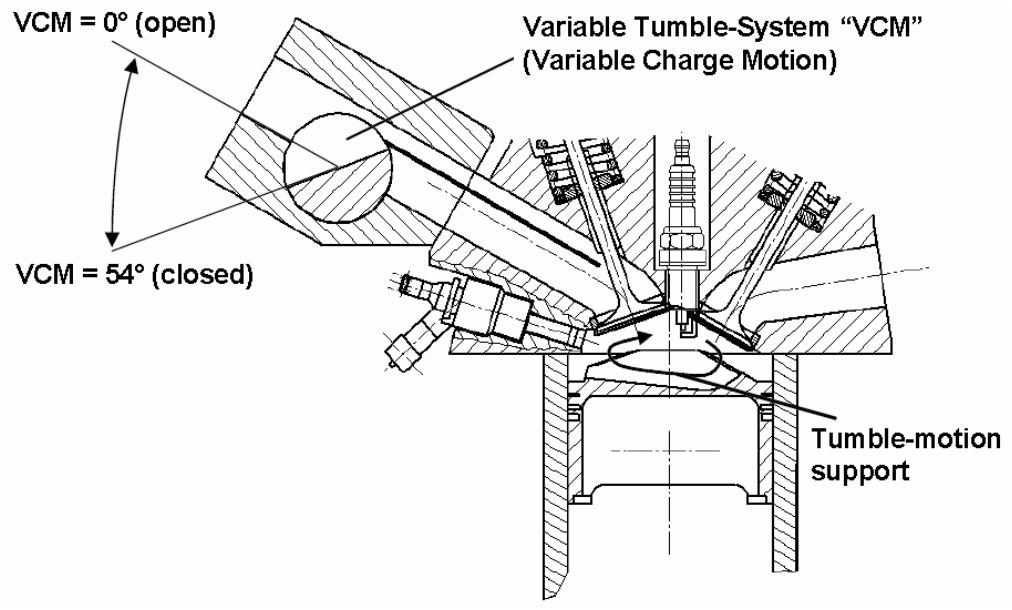

Figure 5.1: Configuration of the "BMBF" IC-engine with variable tumble system. Figure taken from [132].

The computational geometry (figure 5.3) and 2 different grids, namely fine and coarse, see table 5.2, were created using ICEM CFD Hexa. More details regarding mesh generation can be found in chapter 4. A relatively fine grid with 320.000 control volumes ($78 \times 68 \times 50$ in the cylinder at BDC) and a coarse grid with 150.000 control volumes provide a mesh resolution of the order of $\Delta_{fine} \approx 1.0\,mm$ and $\Delta_{coarse} \approx 1.6\,mm$, respectively. No-slip velocity boundary conditions at the walls and pressure inlet / outlet boundary conditions for the intake / exhaust ports were applied. The intake and exhaust duct pressure was set equal to the atmospheric pressure.

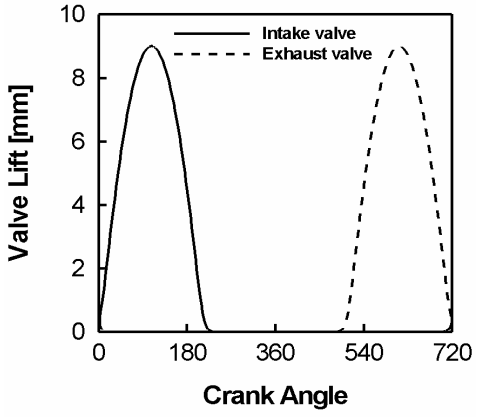

Figure 5.2: Valve-lift definition.

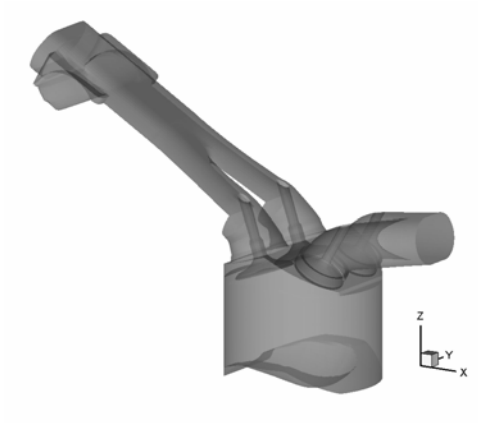

Figure 5.3: Geometry of the "BMBF" IC-engine for KIVA-3V.

Table 5.1: Parameters of the „BMBF" IC-engine.

Bore	85 mm
Stroke	85 mm
Clearance height	0.8 mm
Connecting road length	141 mm
Engine speed	2000 rpm
Compression ratio	10.5
Inlet valve opening	-24°
Inlet valve closure	240°
Exhaust valve opening	480°
Exhaust valve closure	-24°

Table 5.2: Computational grids specification.

Region	**Fine grid (c.v.)**	**Coarse grid (c.v.)**
Combustion chamber	200.000	100.000
Piston bowl	27.000	14.000
Head and intake / exhaust ports	93.000	36.000
Total:	**320.000**	**150.000**

5.2. Large eddy simulation of the single-phase flow in an IC-engine

The main results discussed in this chapter were obtained on the fine computational grid with the previously described geometry and parameters (refer to table 5.1). LES has been performed for 50 full engine cycles. The aim of these calculations was to study the flow field inside a DISI engine and to analyse and characterize the nature and origin of the cycle-to-cycle variations in great detail during the full engine stroke under motored conditions. In addition, a series of LES and RANS simulations using a coarse grid were carried out. All variants of the engine calculations for single-phase flow are summarized in table 5.3. The main purpose of the coarse grid simulations was the assessment of the simulation error as discussed in chapter 6.

Table 5.3: Specification of different engine simulations.

No.	**Method**	**Type of grid**	**Amount of engine cycles**
1.	LES	fine	50
2.	LES	coarse	40
3.	LES with modified SGS model	coarse	40
4.	RANS	coarse	10

The flow field for the whole geometry has been saved every 15° crank angle. The number of statistically independent samples needed for sufficient statistics has been reached using a parallelization technique described in chapter 3. Based on this strategy a sequential computation was split into 8 parallel calculations. The acquired simulation data was used for obtaining detailed statistics of an entire engine cycle from 0° to 720° crank angle. The parallel calculations yielded altogether 50 samples for each output crank angle, from which mean absolute velocity and standard deviation (or root mean square, rms) values were calculated. For a discussion about statistical errors the reader is referred to chapter 6.

The “BMBF” configuration has been used for experimental (PIV for single-phase, phase Doppler anemometry (PDA) and laser correlation velocimetry (LCV) for two-phase flow) as well as for numerical investigations in the framework of the “Verbundprojekt Zyklische Schwankungen bei der Verbrennung” in cooperation with RWTH Aachen, TU Darmstadt (EKT) and TU Munich [43, 63, 132, 175] and is characterized by strong cycle-to-cycle variations of velocity in the combustion chamber [57 - 60]. Hence, experimental data was to some extent available and will be used for comparison with the LES data.

The following paragraphs present a study and discussion of the results for single-phase flow. In section 5.2.1 velocity cycle-to-cycle fluctuations are analyzed for the whole engine cycle and an individual discussion is provided for each engine stroke. The variability of globally

averaged in-cylinder flow quantities is discussed in section 5.2.2. Comparison of LES results with experimental data and RANS is given in section 5.2.3 and 5.2.4, respectively.

Figure 5.4 provides the mean and the standard deviation of intake velocity (a) and intake pressure (b) obtained in the inlet duct in front of the variable motion system for 20 consecutive engine cycles. Regardless of the fact that the inlet duct pressure was set equal to atmospheric pressure for all simulations, there are marginal cycle-to-cycle differences of the order of 2 mbar in the intake pressure traces. The profiles of mean intake pressure and its variation are very similar to results obtained from test bench measurements [132] in the identical engine configuration at the same operation condition. This confirms that the numerical simulation of the considered IC-engine takes place under realistic intake boundary conditions.

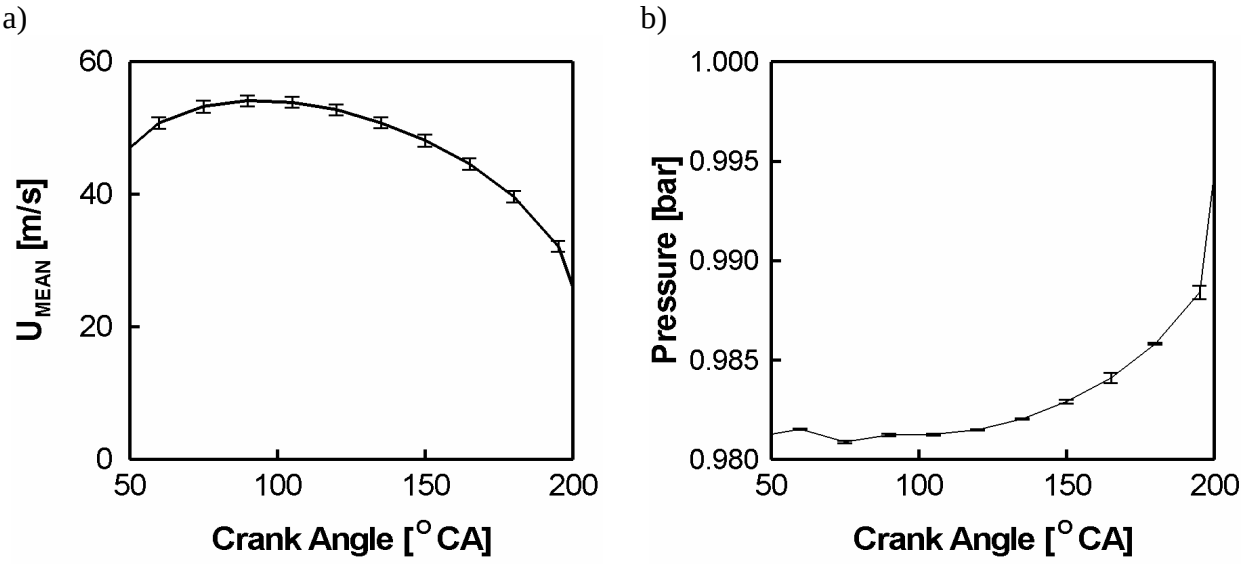

Figure 5.4: Variation of intake boundary conditions in the intake port for 20 consecutive engine cycles. Mean profile and standard deviation of intake velocity (a) and intake pressure (b).

5.2.1. Cycle-to-cycle fluctuations

Location and intensity of the velocity cyclic variations are discussed in terms of mean flow properties, rms and normalized standard velocity deviation and are presented for each engine stroke separately.

a. Intake stroke

The flow field during the intake stroke is governed by the negative pressure resulting from the descending piston. Once the intake valves are opened, a flow with a peak absolute velocity of about 220 m/s arises in the intake port. The flow passes through the narrow top part of the intake duct since the lower part of the intake port is closed by variable tumble system. The maximum velocity in the valve slit region is approximately 170 m/s leading to a highly turbulent flow field inside the combustion chamber. Figure 5.5 shows the typical velocity flow field in the cross section of the engine at $y = 0.018\,\mathrm{m}$ during the intake stroke. Due to the variable tumble system there is a pronounced intake jet towards the cylinder head, impinging on the cylinder wall at the exhaust side and forming a circular motion at the center of combustion chamber or in other words, normal-tumble motion.

As it was mentioned in chapter 1, the in-cylinder charge motion starts to arise during the intake stroke. Figure 5.6.a illustrates the initial stage of formation of the tumble motion in the cross section of the combustion chamber at $CA = 105°$ close to the maximum valve lift. The flow field in the cross section is formed as a result of the interaction between a sufficiently weak in-cylinder motion and two symmetrical intake jets. Instantaneous velocity profiles obtained along the center line ($z = 0.05\,m$) are shown in figure 5.6.c for 50 consecutive cycles providing information of velocity behavior through the combustion chamber. Figure 5.9.a illustrates the mean velocity profiles at various z positions. At the exhaust side of the cylinder, close to the tips of the intake jets velocity magnitude is 3 times higher compared to its value at the opposite side. Figures 5.6 (b, d) show the cycle-to-cycle fluctuations in terms of the velocity standard deviation. Clearly the strongest absolute velocity fluctuations occur at the exhaust side, near the cylinder wall at the tip of the intake jet as well as at the center of the incipient tumble flow.

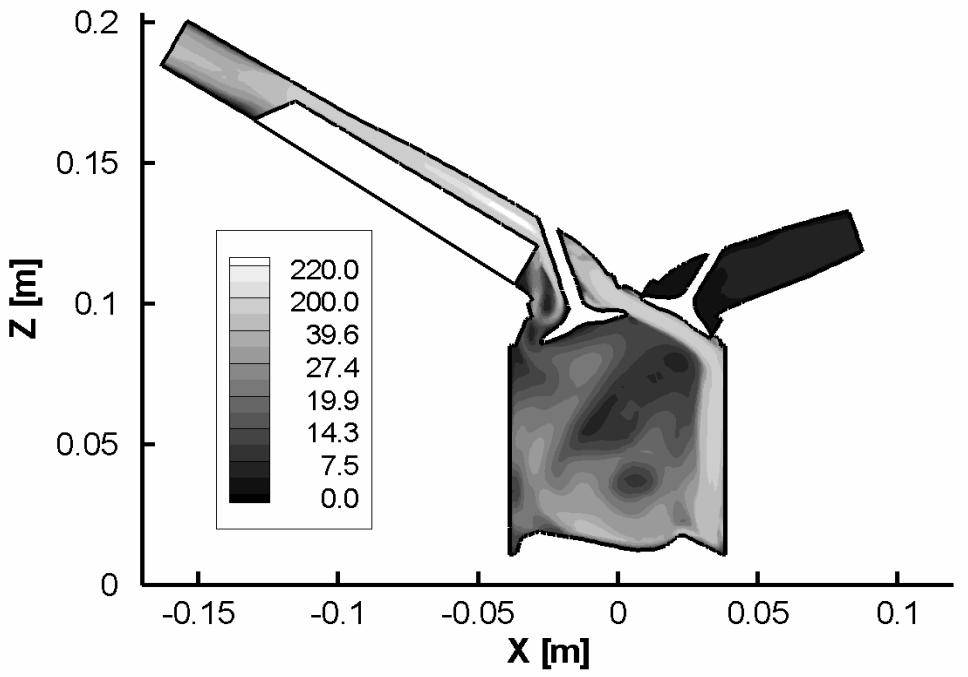

Figure 5.5: Mean velocity flow field averaged over 50 engine cycles in the cross section of the engine at $y = 0.018\,m$ during intake stroke, $CA = 105°$.

The evolution of the mean flow structure in different transverse sections of the combustion chamber at $CA = 105°$ is depicted in figure 5.7. At the exhaust side there is a high speed layer with a well-defined structure near the cylinder wall. The layer has symmetrical structure relative to the cross section which is especially visible at the top of cylinder (figure 5.7, $z = 0.08\,m$). Immediately below the intake jets there are 2 circular low velocity regions which are divided from each other by a high-speed area arising from the interaction of the intake jets. The intake jets pass along the wall through the cylinder towards the piston bowl, turn as the result of the reflection from the piston crone, forming a distinct structure of the flow. Thereby, a high-speed layer with maximal magnitudes of velocity is formed close to the cylinder wall at the exhaust side. The evolution of the flow structures in the X-Y plane, moving from the head to the piston, shows that the vortex flow is observed at first only in the wall area at the exhaust side ($z = 0.08\,m$), then it shifts to the center of the combustion chamber ($z = 0.07 - 0.06\,m$). Eddies, continuing to shift toward the opposite side of the cylinder ($z = 0.05 - 0.03\,m$) constitute the pronounced symmetrical flow in the X-Y plane.

The high speed area examined above is characterized by the highest intensity of cycle-to-cycle fluctuations, especially near the cross section in the interaction zone of the two jets. Figure 5.8 shows the standard velocity deviation in the same X-Y sections as considered above. This zone is rather local in nature at $z = 0.08\,\text{m}$ but it is broadening when approaching the piston. Further, the area with the highest amplitude of cyclic variations is also observed at the center of the normal-tumble motion (figure 5.8, $z = 0.05\,\text{m}$, $x = -0.25\,\text{m}$).

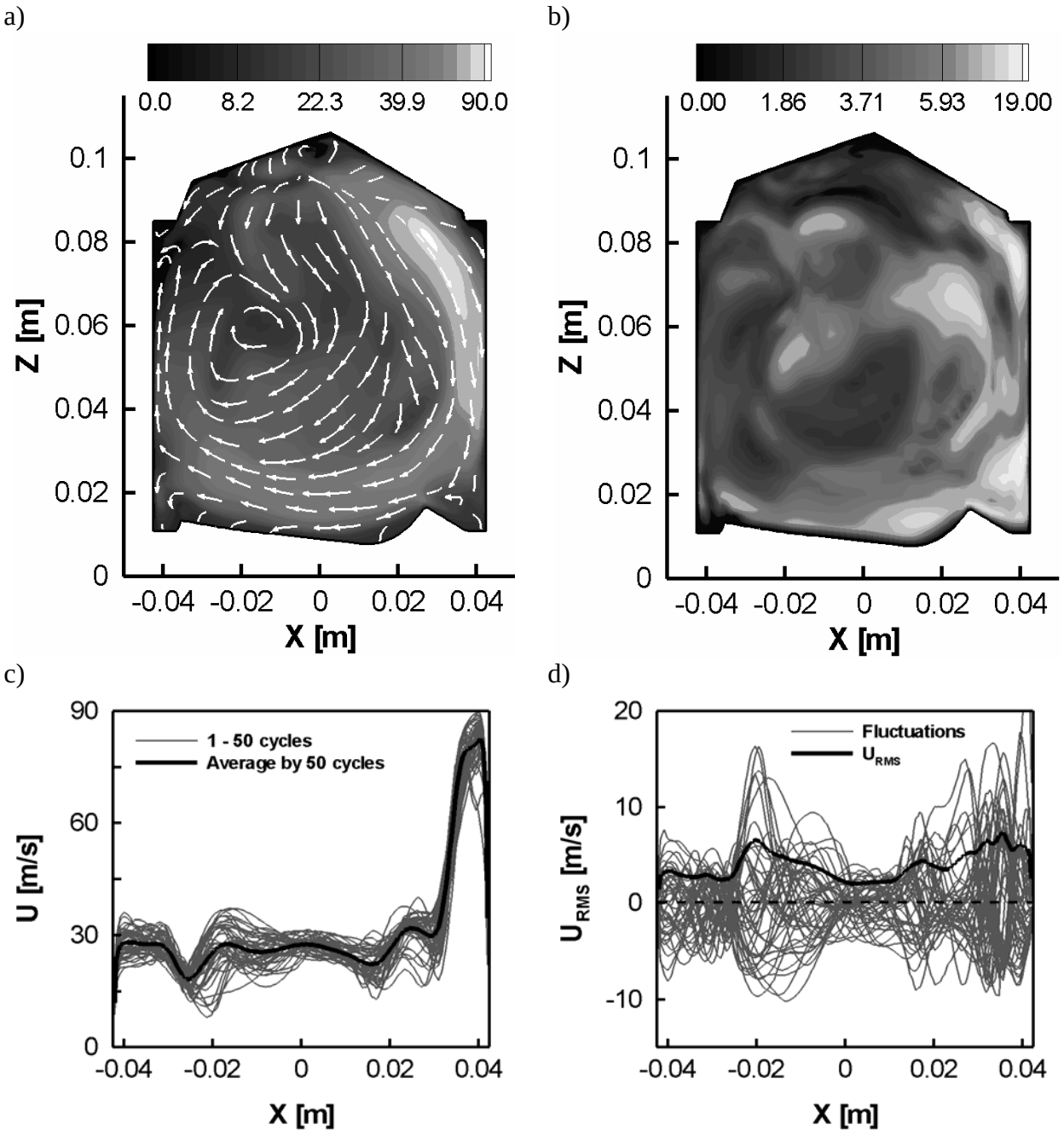

Figure 5.6: Velocity vector plot and mean velocity flow field in the cross section of the combustion chamber at $CA = 105°$, averaged over 50 engine cycles (a), standard deviation of velocity (b), instantaneous velocity profiles at $z = 0.05\,\text{m}$ for each individual cycle and mean velocity profile (c), u_{rms} profile at $z = 0.05\,\text{m}$ together with the instantaneous fluctuations for each individual cycle (d).

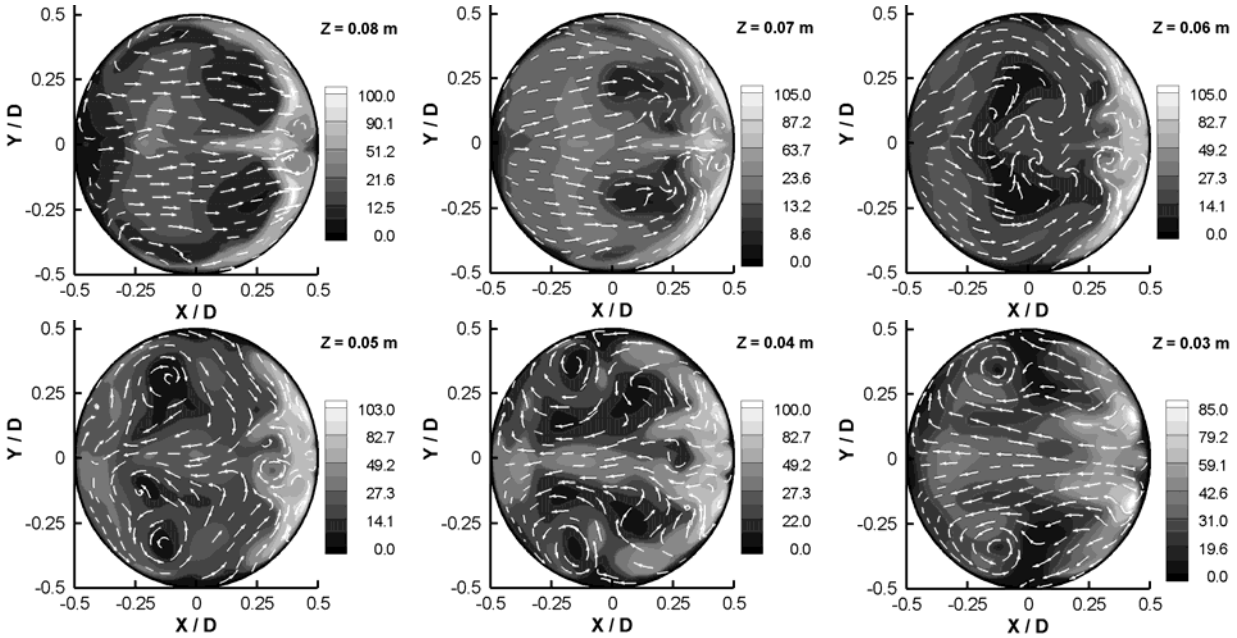

Figure 5.7: Streamlines and average velocity flow field for different sections (X-Y plane) of the combustion chamber during intake stroke at $CA = 105°$.

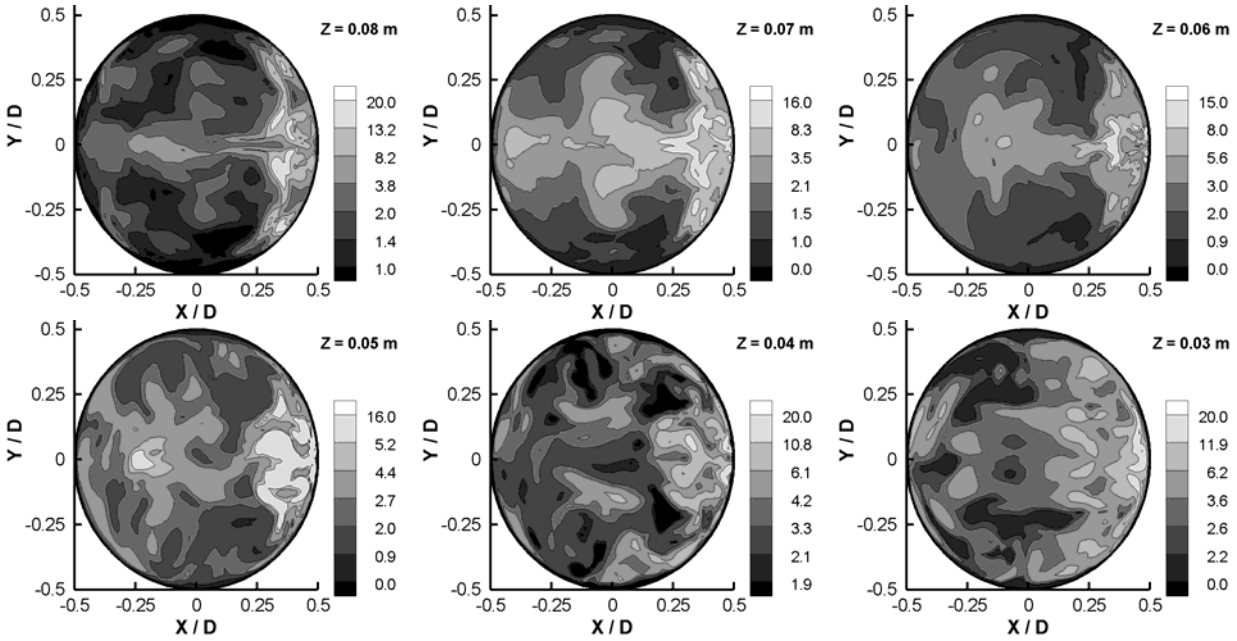

Figure 5.8: Isolines of the standard velocity deviation in various sections (X-Y plane) of the combustion chamber during intake stroke at $CA = 105°$.

The intensity of cycle-to-cycle fluctuations in the cross section of the combustion chamber is shown in figure 5.9 in terms of rms of velocity (b) and the standard deviation of velocity normalized with the local mean value (c). Maximal values are achieved near the cylinder walls in the head and piston bowl areas where the turning of the flow is observed. The pronounced side-cut peaks of the normalized standard velocity deviation are well visible at $z = 0.03\,\mathrm{m}$ and $z = 0.08\,\mathrm{m}$ (figure 5.9.c) and reach values up to $u_{rms} / u_{mean} \approx 0.5$. When the

flow passes in parallel to the cylinder walls, the maximal intensity is found in the center of the tumble motion with a peak of $u_{rms} / u_{mean} \approx 0.4$.

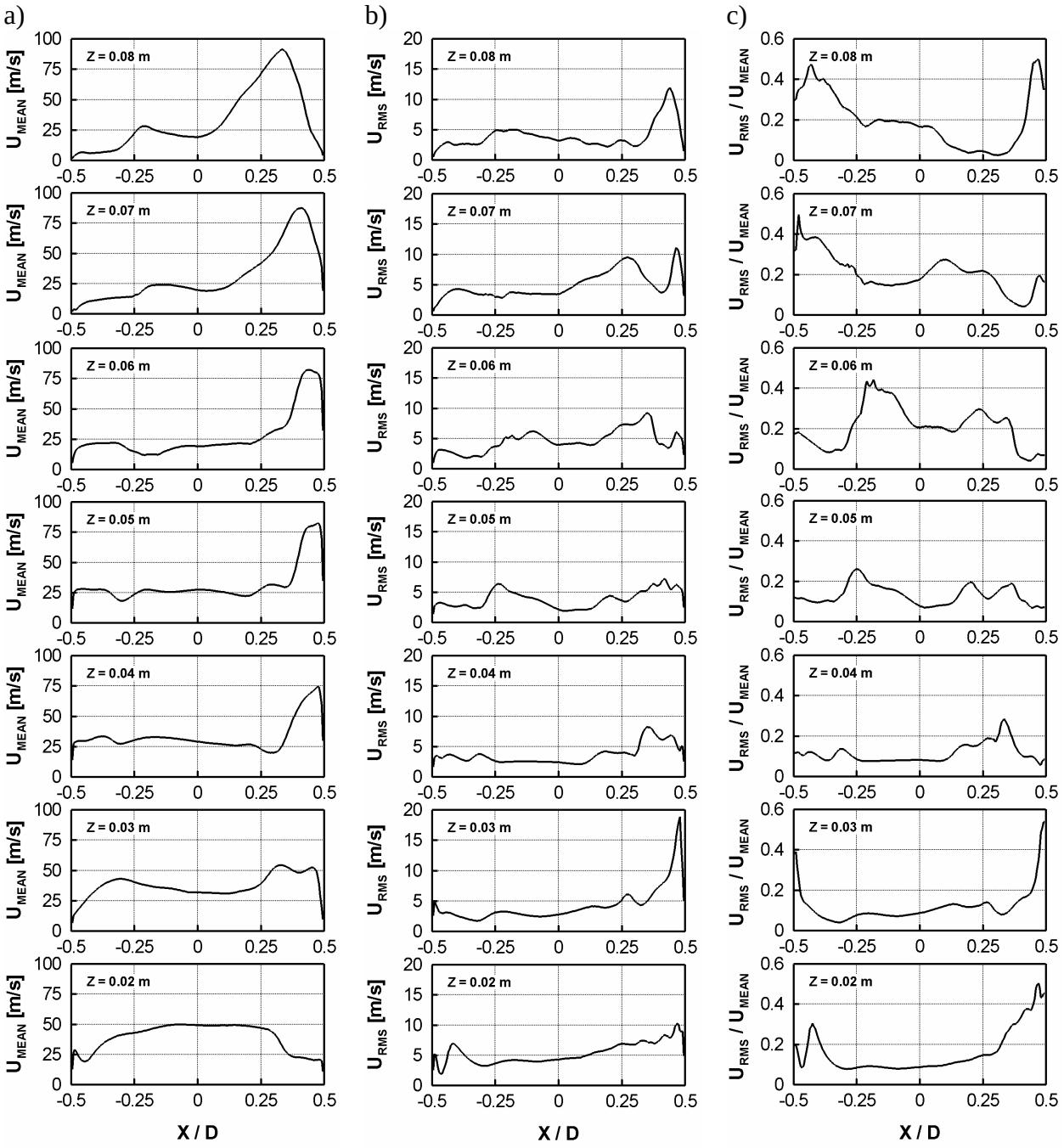

Figure 5.9: Mean velocity profiles (a), standard velocity deviation (b) and rms of velocity normalized with the local mean velocity (c) at selected z positions during intake stroke, $CA = 105°$.

b. Compression stroke

The flow field during the compression stroke ($CA = 255°$, see figure 5.10) shows a pronounced tumble flow with the vortex center located at the center of the combustion chamber. $CA = 15°$ after intake valve closure, the peak velocity, i.e. the tip of the intake jet, has moved to

the intake side as it is illustrated in figures 5.10.a and 5.13.a. Velocity magnitudes during the compression stroke are considerably smaller, e.g. the peak value is 3 times less compared to the intake stroke. The same holds true for the velocity fluctuations as it is confirmed by figures 5.10.d and 5.13.b. Minimum values of velocity are realized in the center of charge motion which coincides with the center of the combustion chamber. A rather uniform velocity flow field (figures 5.10.c and 5.13.a) has established revealing homogenous cycle-to-cycle variations (see figures 5.10.d and 5.13.b) with up to $5\ \mathrm{m/s}$ deviation from the mean velocity.

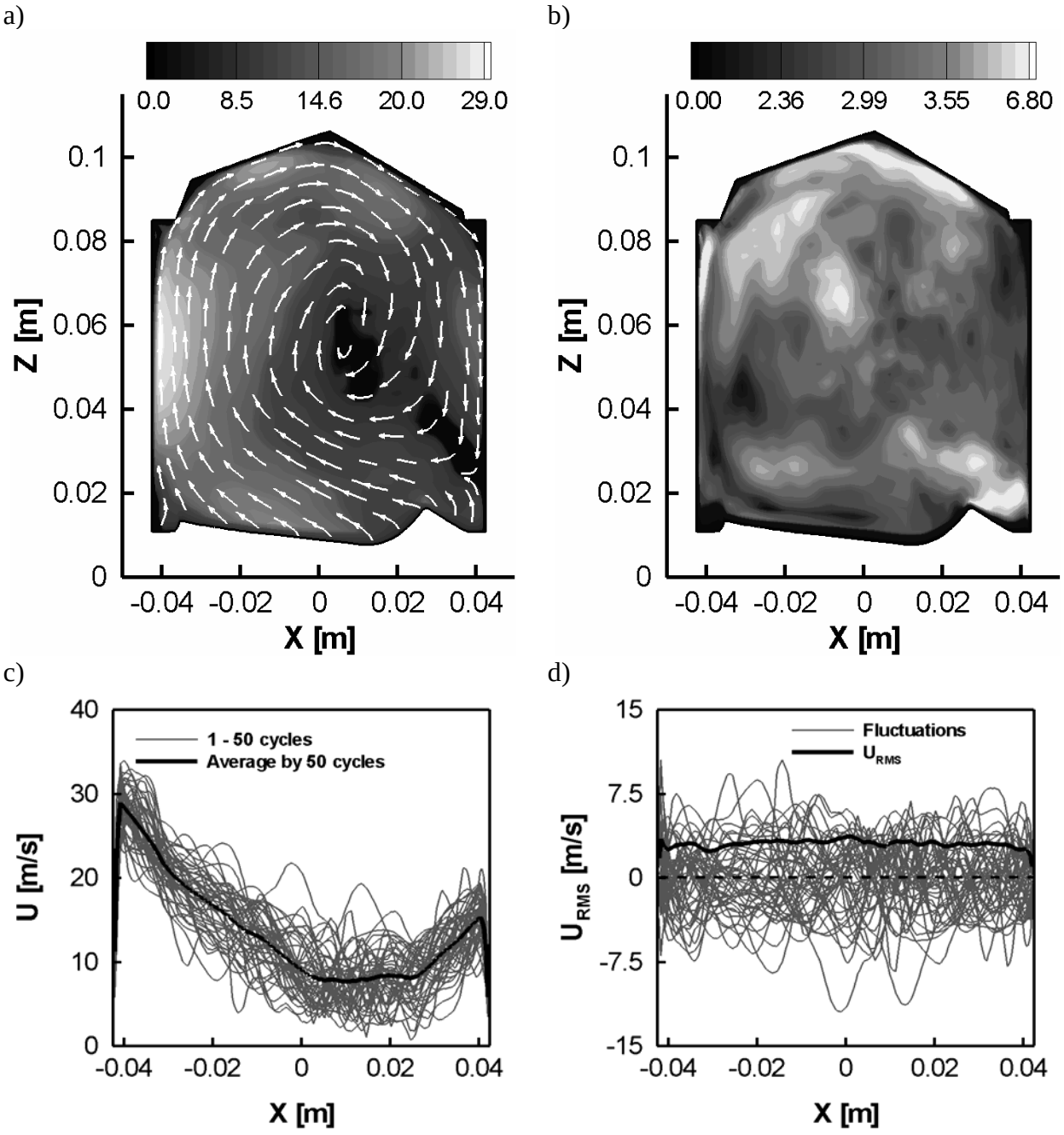

Figure 5.10: Velocity vector plot and mean velocity flow field in the cross section of the combustion chamber at $\mathrm{CA} = 255°$, averaged over 50 engine cycles (a), standard deviation of velocity (b), instantaneous velocity profiles at $z = 0.05\,\mathrm{m}$ for each individual cycle and mean velocity profile (c), u_{rms} profile at $z = 0.05\,\mathrm{m}$ together with the instantaneous fluctuations for each individual cycle (d).

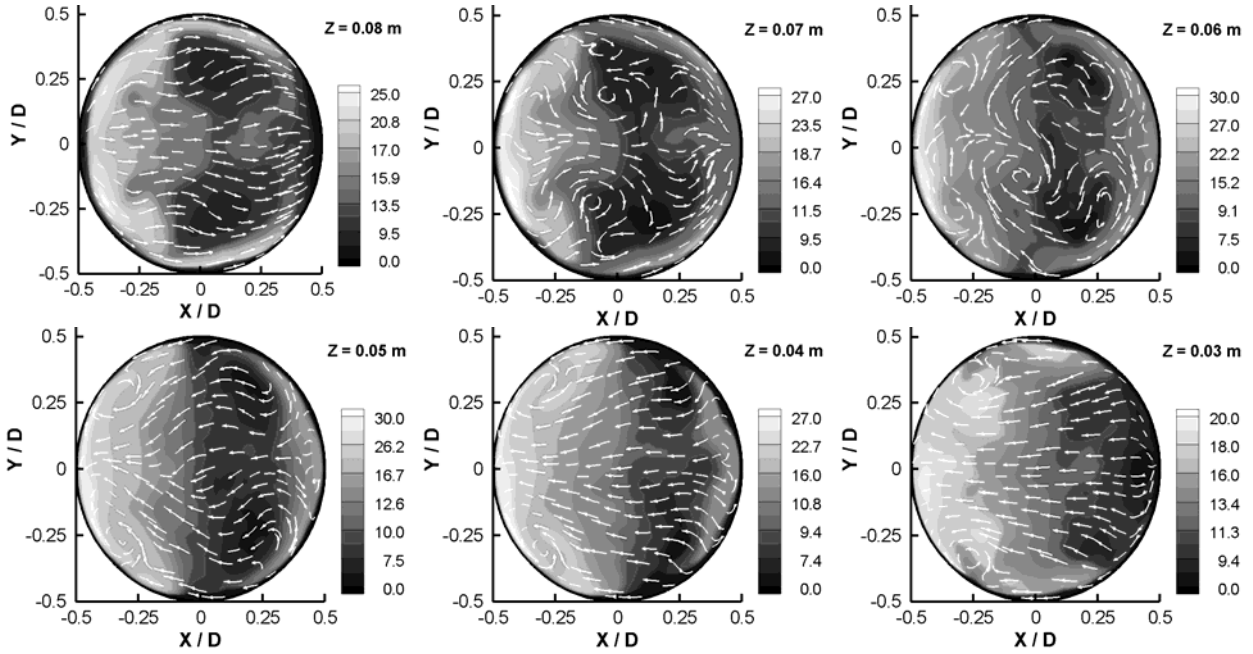

Figure 5.11: Streamlines and average velocity flow field for different sections (X-Y plane) of the combustion chamber during compression stroke at $CA = 255°$.

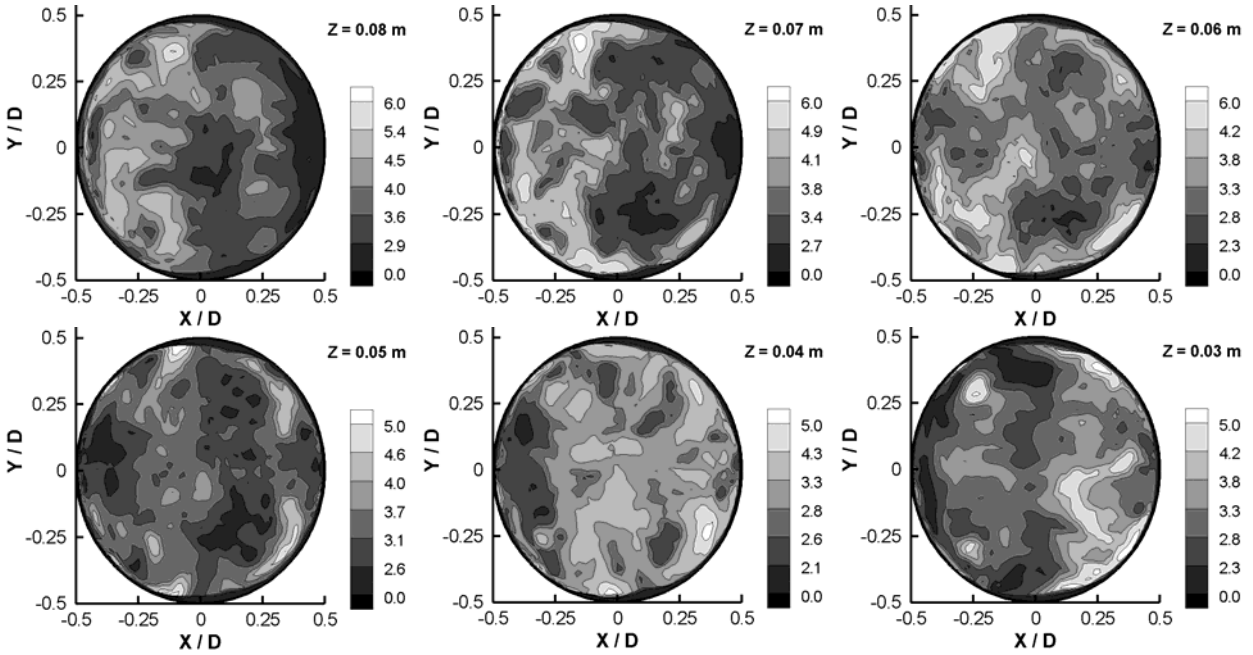

Figure 5.12: Isolines of the standard velocity deviation in various sections (X-Y plane) of the combustion chamber during compression stroke at $CA = 255°$.

However, the normalized standard velocity deviation (figure 5.13.c) reaches the values comparable with the intake stroke with a peak intensity of $u_{rms} / u_{mean} > 0.4$. These peak values are found at the center of the tumble motion ($z = 0.04 – 0.06\,m$) and in the regions of flow turn ($z = 0.02\,m$ and $z = 0.08\,m$) as depicted in figure 5.13 (c).

The structure of tumble motion in the X-Y plane is given in figure 5.11. The velocity flow field represents ordered structures close to the head and piston bowl where gas streams longitudinally the wall in the opposite directions, e.g. from intake to exhaust side at the top

(z = 0.08 m) and vise versa at the bottom (z = 0.02 m). The interval between these sections can be characterized by irregular flow structures. Both the in-cylinder tumble motion and the characteristic property of the combustion chamber geometry result in an irregularity of the standard velocity deviation in various sections of cylinder as it is illustrated in figure 5.12. The zone with higher intensity of cyclic variations can be found on the intake side near the cylinder head. At the same time this zone shifts to the exhaust side as approaching to the piston-bowl. It should be also mentioned that the tumble charge motion is dominating in the considered configuration of IC-engine while swirl and sideways-tumble do not form under the considered operation conditions.

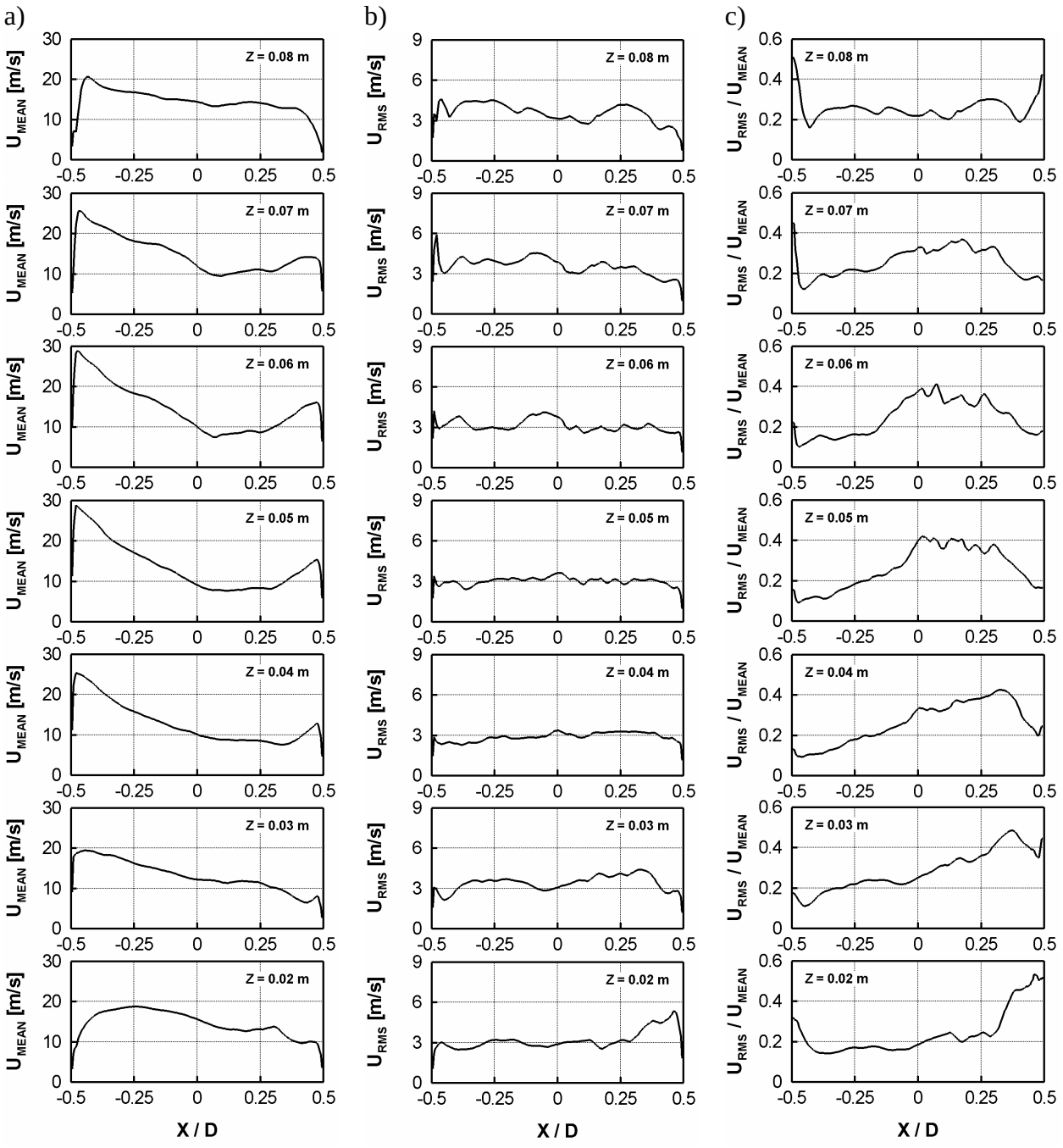

Figure 5.13: Mean velocity profiles (a), standard velocity deviation (b) and rms of velocity normalized with the local mean velocity (c) at selected z positions during compression stroke, $CA = 255°$.

c. Expansion stroke

The mean flow during the expansion stroke as illustrated at crank angle 450° (figure 5.14) is determined by the descending piston. The fluid inside the combustion chamber follows the piston with a maximum velocity of approximately $12\,\mathrm{m/s}$ at the piston wall, while there is a low-velocity area at the top of the cylinder. Absolute velocity (figure 5.14 (a, c)) and fluctuations (figure 5.14 (b, d)) are rather small compared to the intake and compression stroke. Inside the cylinder filamentary structures reveal slight fluctuations from cycle to cycle. It should be noted that the flow field under realistic conditions, including injection and combustion, would look quite differently in this phase.

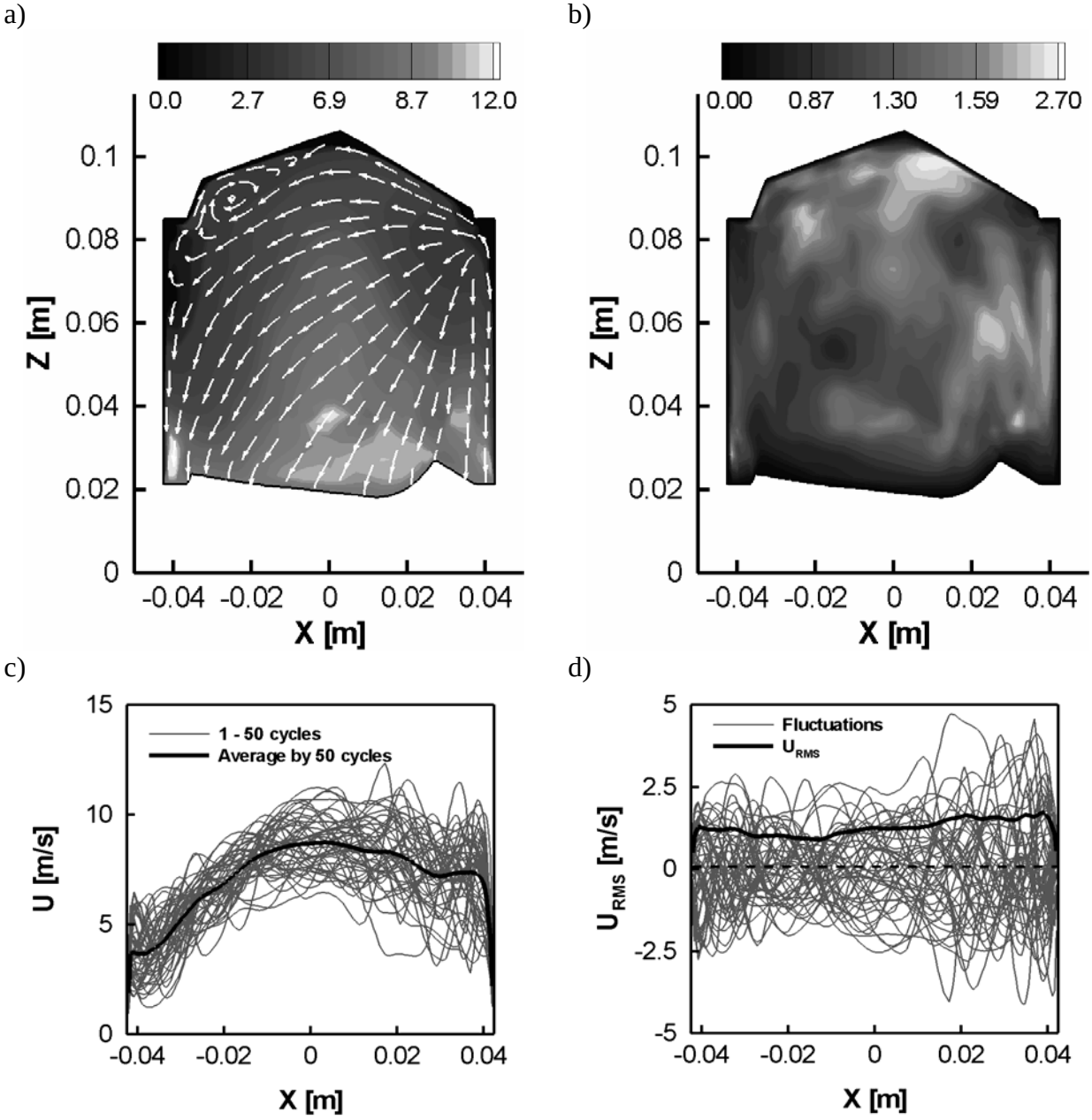

Figure 5.14: Velocity vector plot and mean velocity flow field in the cross section of the combustion chamber at $\mathrm{CA} = 450°$, averaged over 50 engine cycles (a), standard deviation of velocity (b), instantaneous velocity profiles at $z = 0.05\,\mathrm{m}$ for each individual cycle and mean velocity profile (c), u_{rms} profile at $z = 0.05\,\mathrm{m}$ together with the instantaneous fluctuations for each individual cycle (d).

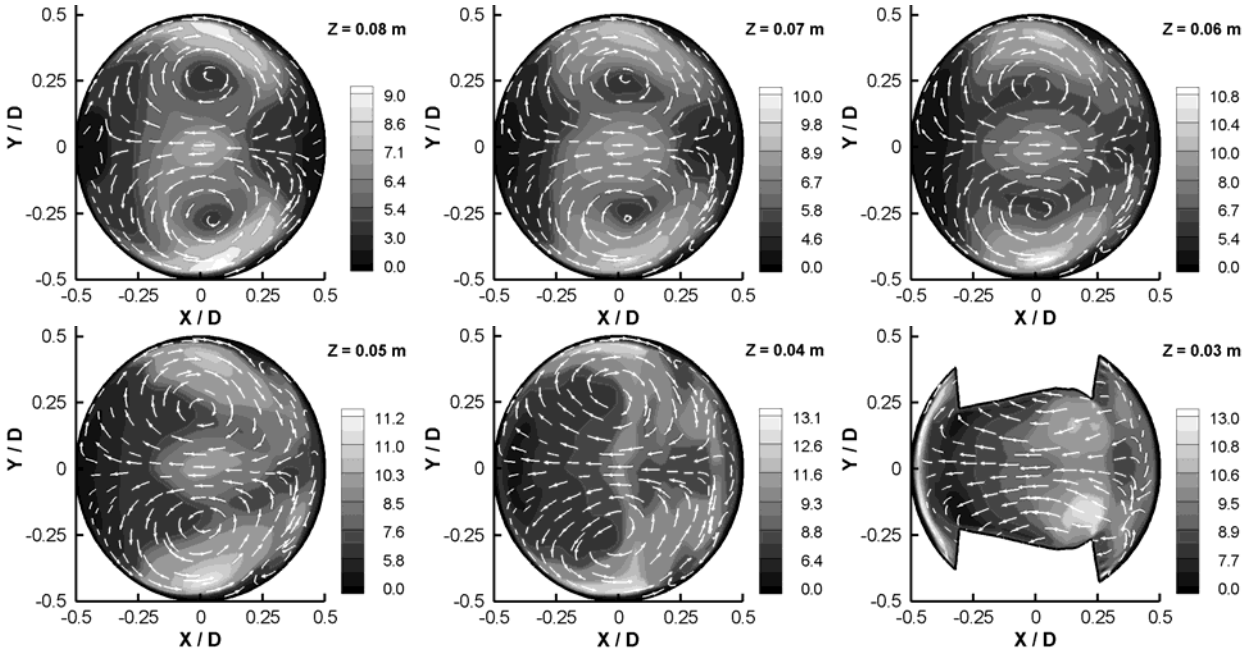

Figure 5.15: Streamlines and average velocity flow field for different sections (X-Y plane) of the combustion chamber during expansion stroke at $CA = 450°$.

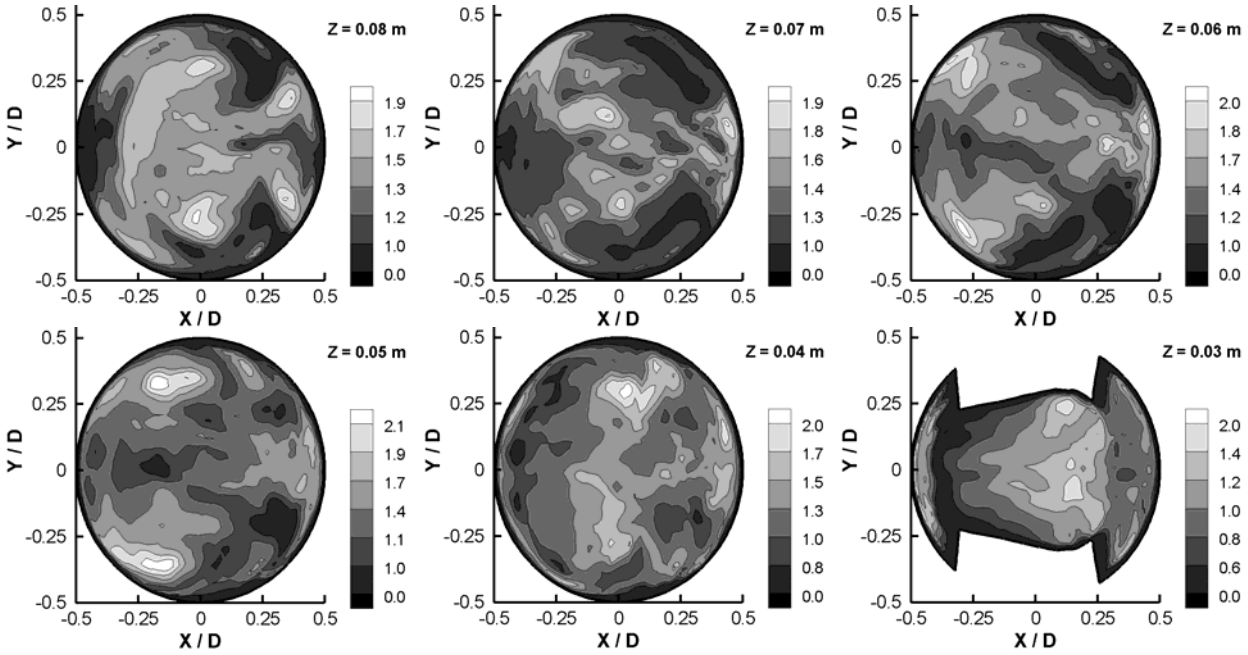

Figure 5.16: Isolines of the standard velocity deviation in various sections (X-Y plane) of the combustion chamber during expansion stroke at $CA = 450°$.

The velocity flow field in the X-Y plane shown in figure 5.15 is determined by a well-defined symmetrical two vortex structures having the characteristic size of the order of the cylinder radius. Generally, the local maximums of fluctuations (see figure 5.16) are roughly located at the centers of vortex motion (figure 5.15) as well as in the area of their interaction. Velocity magnitude monotonously increases from $9\,\mathrm{m/s}$ till $13\,\mathrm{m/s}$ moving from the cylinder head to the piston. The expansion stroke is determined by the minimal intensity of velocity

fluctuations as it can be seen in figure 5.17.b for the whole engine cycle. Due to the small velocity magnitude at the top of cylinder figure 5.17.c shows high values of the normalized standard velocity deviation which are comparable with the values obtained during the intake or compression strokes, nevertheless, as approaching to the piston the normalized standard velocity deviation reaches the minimal value of $u_{rms} / u_{mean} < 0.15$.

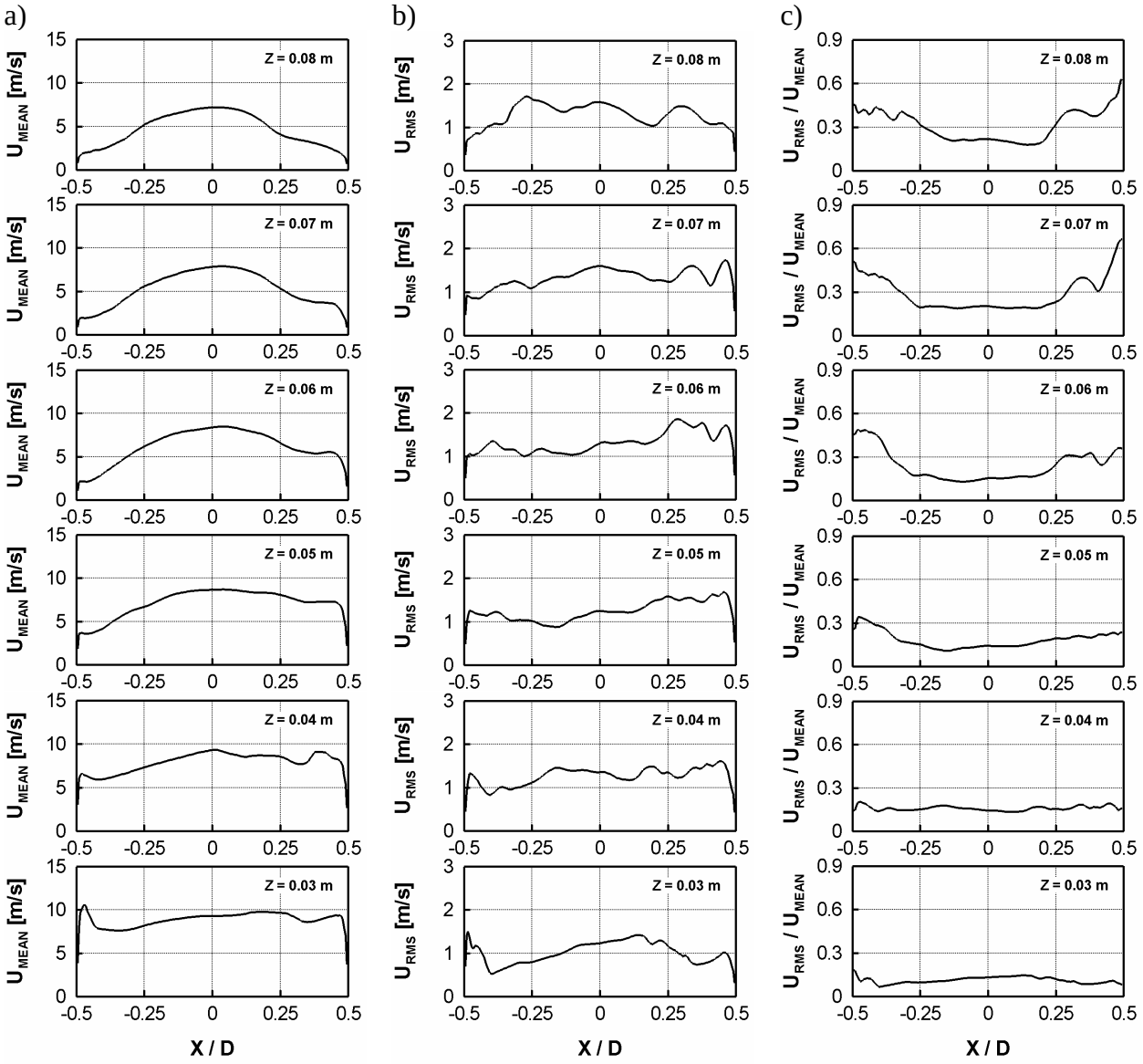

Figure 5.17: Mean velocity profiles (a), standard velocity deviation (b) and rms of velocity normalized with the local mean velocity (c) at selected z positions during expansion stroke, $CA = 450°$.

d. Exhaust stroke

The ascending piston presses the fluid inside the combustion chamber through the valves slit into the exhaust port. Figure 5.18.a shows a typical flow field structure during the exhaust stroke at crank angle 630°. In the initial stage of exhaust stroke the flow field in the combustion chamber maintains the structure which was formed during the expansion stroke. Figure 5.18 also shows the instantaneous and mean velocity profiles (c) and the standard deviation of velocity (d)

similar to the corresponding parameters obtained for the expansion stroke. The flow structure in the X-Y plane also is kept in the initial stage of the exhaust stroke as shown in figure 5.19. The standard velocity deviation is rather homogeneous through the whole combustion chamber (figures 5.18.b and 5.20). Mean velocity (a), rms of velocity (b) and normalized standard deviation (c) are shown in figure 5.21. The peak values of plotted quantities are similar to the corresponding parameters of the expansion stroke.

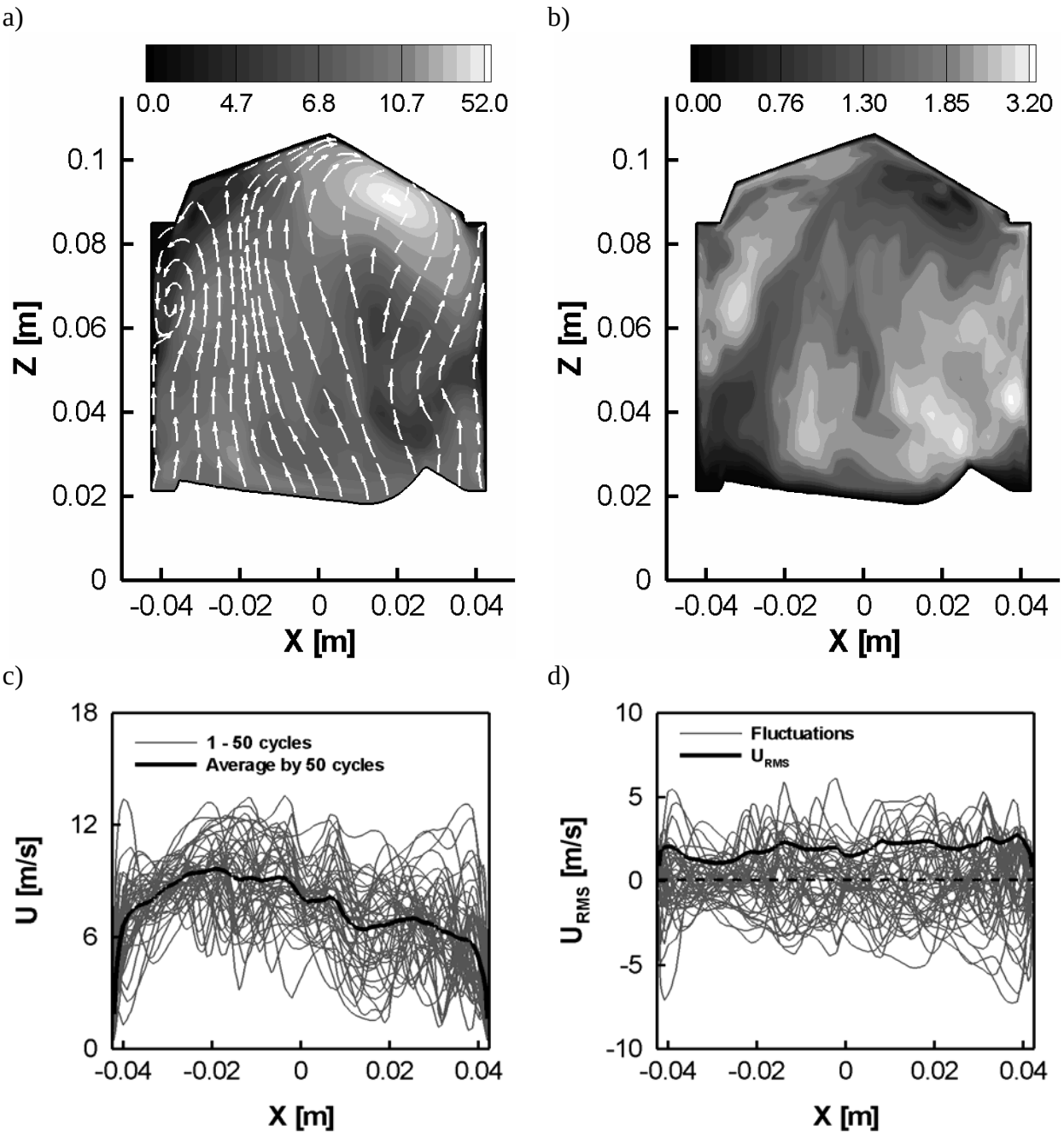

Figure 5.18: Velocity vector plot and mean velocity flow field in a cross section of the combustion chamber at $CA = 630°$, averaged over 50 engine cycles (a), standard deviation of velocity (b), instantaneous velocity profiles at $z = 0.05\,m$ for each individual cycle and mean velocity profile (c), u_{rms} profile at $z = 0.05\,m$ together with the instantaneous fluctuations for each individual cycle (d).

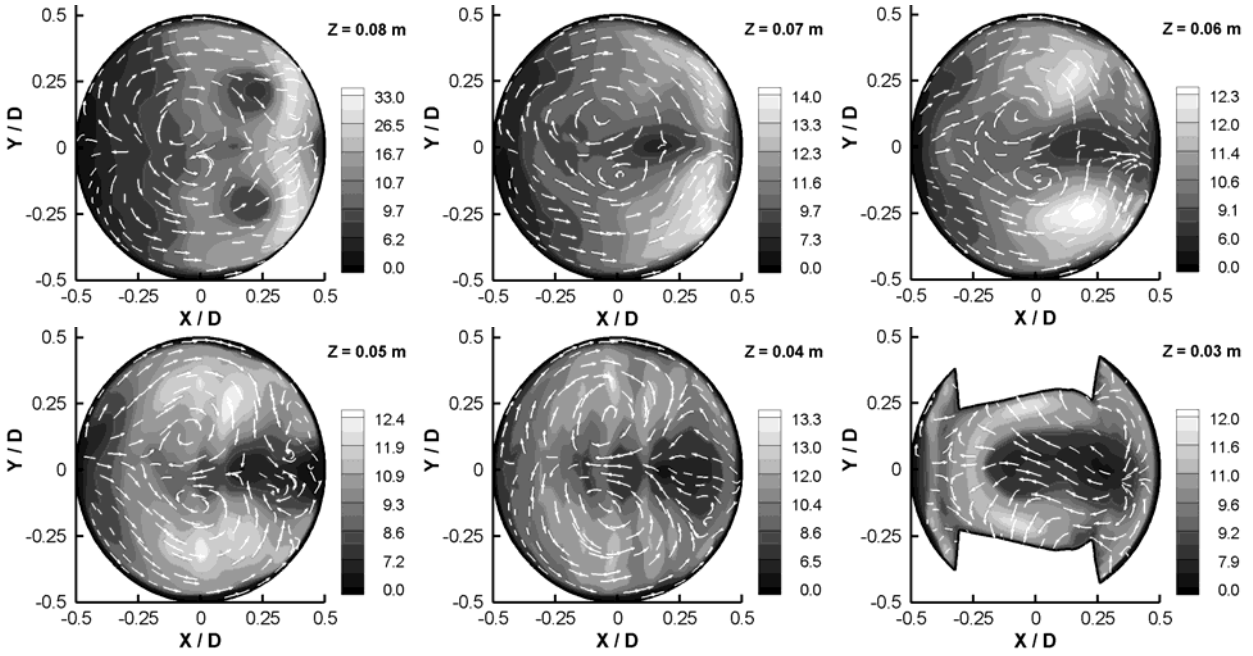

Figure 5.19: Streamlines and average velocity flow field for different section of the combustion chamber during exhaust stroke at $CA = 630°$.

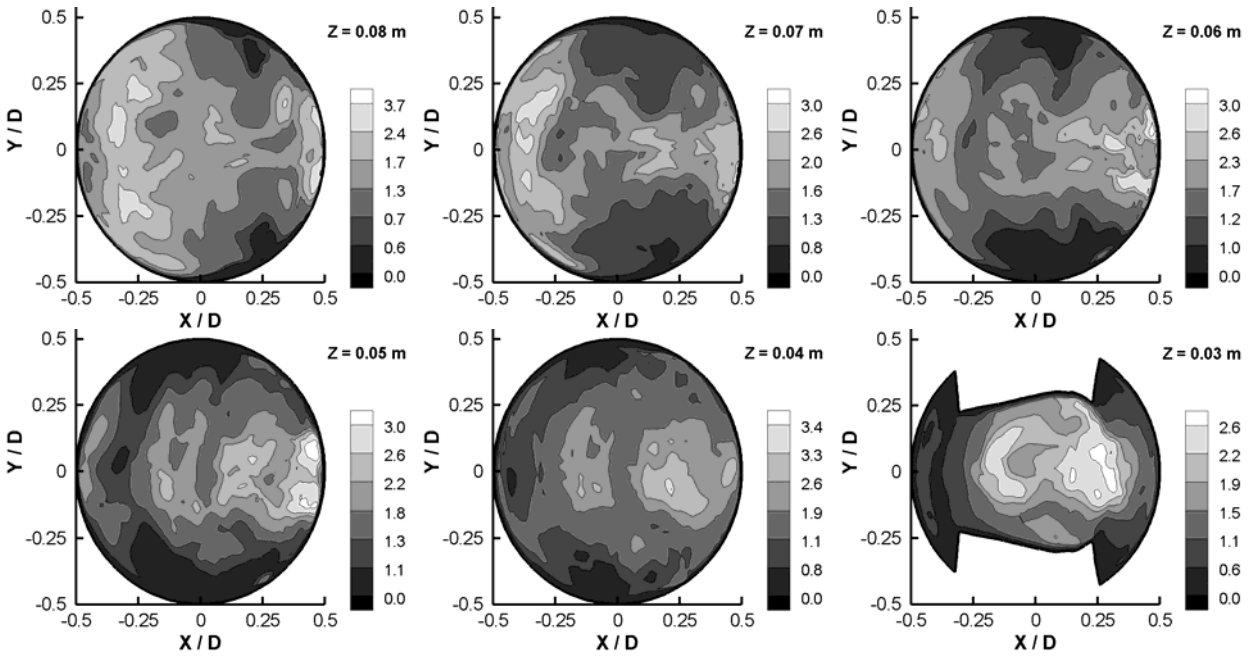

Figure 5.20: Isolines of the standard velocity deviation in various sections of the combustion chamber during exhaust stroke at $CA = 630°$.

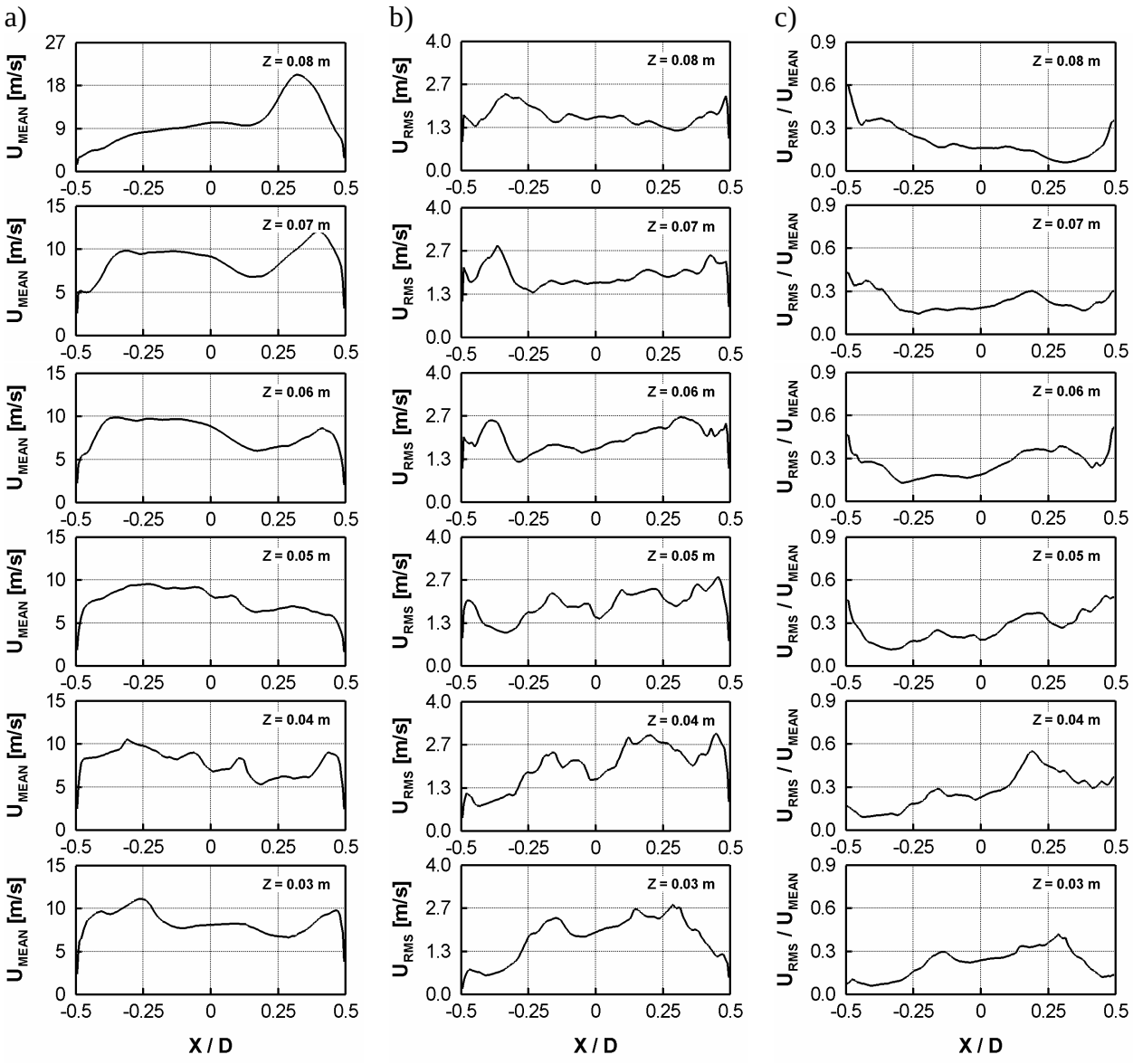

Figure 5.21: Mean velocity profiles (a), standard velocity deviation (b) and rms of velocity normalized with the local mean velocity (c) at selected z positions during exhaust stroke, $CA = 630°$.

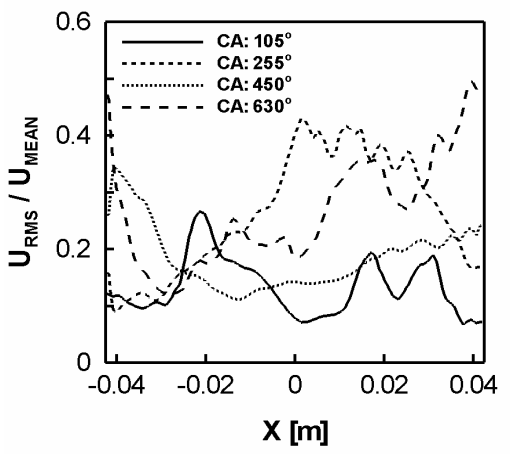

Figure 5.22: Standard velocity deviation normalized with the local mean velocity at $z = 0.05\,\mathrm{m}$ for different engine strokes, 50 engine cycles.

One of the most important in-cylinder flow field areas at the end of compression stroke is the region below the spark plug especially close to the ignition point. The inspection of the results obtained for the full engine cycle reveals that the normalized standard velocity deviation reaches highest values over the whole engine cycle with a peak intensity of $u_{rms} / u_{mean} > 0.4$ at the center of tumble motion (except the peak values close to the cylinder wall in the corner areas of turn of in-cylinder flow) as depicted in figure 5.22. Taking into consideration that the center of tumble motion roughly corresponds to the location of spark plug at the ignition point, it can be concluded that the cycle-to-cycle fluctuations in this area strongly influence the fuel vapor cloud close to the ignition time (see chapter 7 for more details) and can be one of the reasons for engine misfires.

5.2.2. Variability of global charge motion

The controlling of the in-cylinder charge motion plays a key role in an air-guided combustion system to guarantee high performance and low emissions of IC-engines. Especially the behavior of in-cylinder flow at the end of the compression stroke is very critical for the combustion processes in air-guided DISI IC-engines. As it was mentioned above, the in-cylinder charge motion is mostly generated during the intake stroke and also during the compression stroke as a result of interaction of the in-cylinder flow with the specific configuration of cylinder head and piston bowl geometry. The characteristics of swirl and tumble in-cylinder flows are usually expressed by dimensionless parameters which are known as swirl (SR_z) and tumble (TR_x and TR_y) ratios, respectively, where the tumble motion in the X-Z plane is denoted as the sideways tumble and in the Y-Z plane as the normal tumble. They are defined as organized rotations of the charge motion around the specific cylinder axes, such as X, Y and Z as illustrated in figure 1.3 (see chapter 1). The mass center of the charged in-cylinder air is considered as an origin for the calculation. Mathematically TR_x, TR_y and SR_z are given by

$$TR_x = \frac{\sum_{i=1}^{n} (L_x)_i}{\sum_{i=1}^{n} (I_{xx})_i\,\omega}, \qquad TR_y = \frac{\sum_{i=1}^{n} (L_y)_i}{\sum_{i=1}^{n} (I_{yy})_i\,\omega}, \qquad SR_z = \frac{\sum_{i=1}^{n} (L_z)_i}{\sum_{i=1}^{n} (I_{zz})_i\,\omega}, \tag{5.1}$$

where L is the angular momentum per unit mass, I is the inertia momentum per unit mass and ω is the engine speed in radian per second, given by

$$\omega = \frac{2\pi n}{60}, \tag{5.2}$$

where n is the equivalent engine speed in rpm.

Figure 5.23 shows globally averaged flow quantities for the whole cycle (left column) as well as for a smaller range $CA = 300° - 360°$ where ignition takes place (right). The thin lines correspond to individual cycles, the thick line depicts the average value. From top to bottom cylinder mass (a), tumble (b), swirl (c) and kinetic energy (d) are shown. The cylinder mass directly affects the effective output of the engine whereas the charge motion influences mixture preparation, flame center movement and turbulent flame speed.

The cyclic variability in cylinder mass is with 0.3% rather small. Due to the variable charge motion system employed in this engine a pronounced tumble motion is clearly visible in figure 5.23.b. Tumble flows generally last up to the time of compression and decay into turbulence close to the ignition top dead center. The cycle-to-cycle variations are of the order of 5%. Mean swirl value is zero as depicted in figure 5.23.c with moderate cyclic variations. Swirl and tumble together contribute to the total charge motion which can be measured in terms of kinetic energy (figure 5.23.d). Kinetic energy cycle-to-cycle variations amount to approximately 15%.

5.2.3. Comparison of LES and PIV measurement data

A comparison of the LES results for single-phase flow has been performed with available experimental PIV data [39, 63, 132]. Measurement data were obtained using the same engine configuration under identical operating conditions. As mentioned in [132], the PIV filter width was limited by the interrogation area of the PIV algorithm to approximately 2.4 mm. In the LES calculations the filter width based on the computational cell size is approximately $\Delta_{\text{fine}} \approx 1.0\,\text{mm}$, corresponding to the fine grid resolution. LES results averaged over 40 engine cycles have been compared with PIV measured data averaged over 20 samples for certain crank angles. Figure 5.24 depicts the mean velocity flow field measured with PIV (a) and predicted with LES (b) in the cross section of the combustion chamber during the intake stroke at $CA = 108°$. The comparison of LES with experiment at the initial stage of compression ($CA = 208°$) and at the end of the compression stroke ($CA = 300°$) is shown in figures 5.25 and 5.26, respectively. Inspection of the results reveals that LES predictions of the velocity flow field, i.e. velocity magnitudes, and the flow structure can be found in a good agreement with experimental data. The difference in peak velocity magnitude obtained with LES and PIV does not exceed 7%. LES provides a flow structure similar to PIV with the vortex at the intake side of cylinder during the intake stroke (figure 5.24). The in-cylinder charge motion and the center of tumble flow (figures 5.25 and 5.26) are also well predicted by LES for the other crank angles.

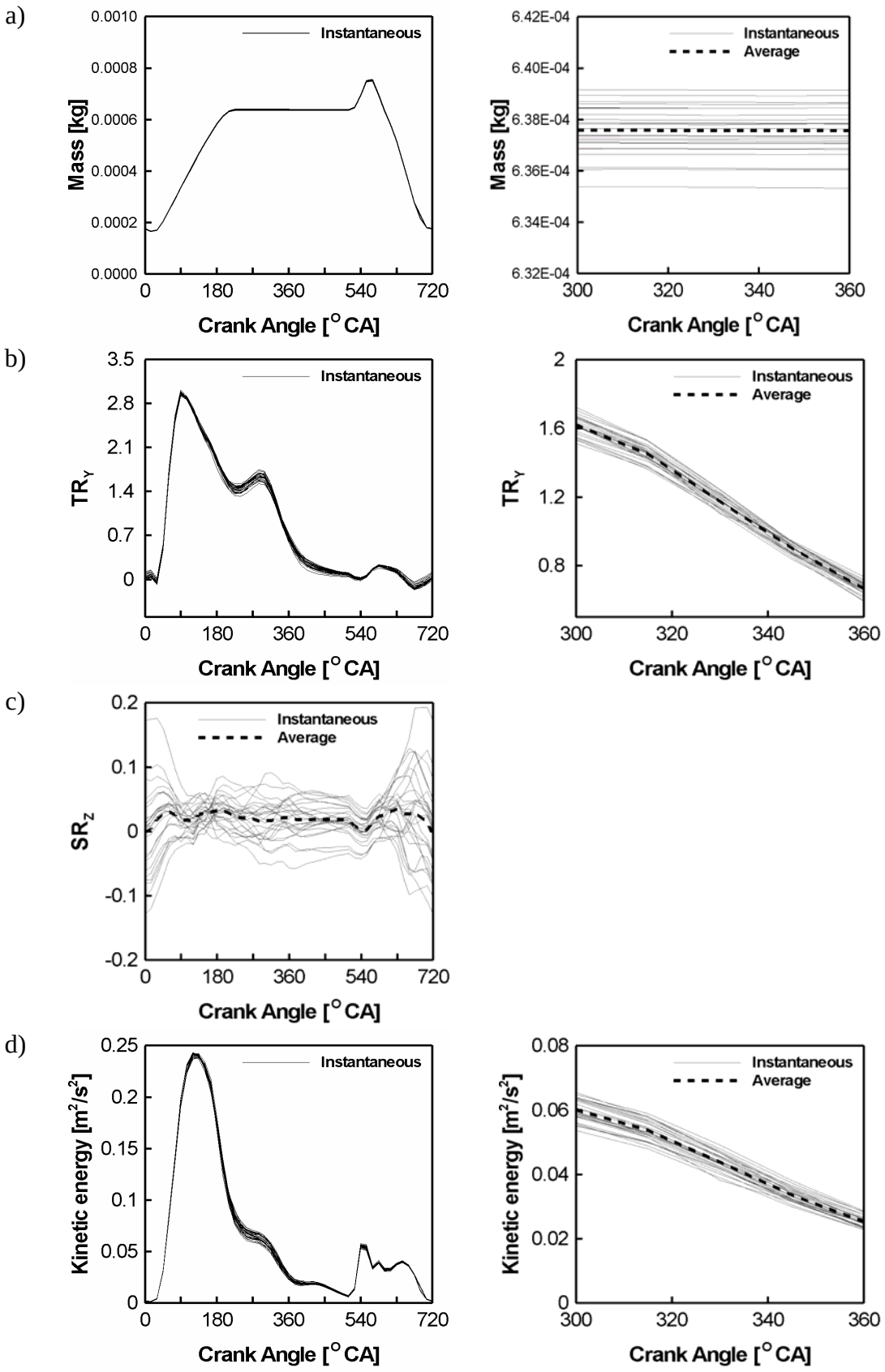

Figure 5.23: Globally averaged flow quantities for the whole cycle (left) and for $CA = 300° - 360°$ (right). The thin lines correspond to individual cycles, the thick line depicts the average value; a) Cylinder mass; b) Tumble ratio TR_y; c) Swirl ratio SR_z; d) Kinetic energy.

a) b)

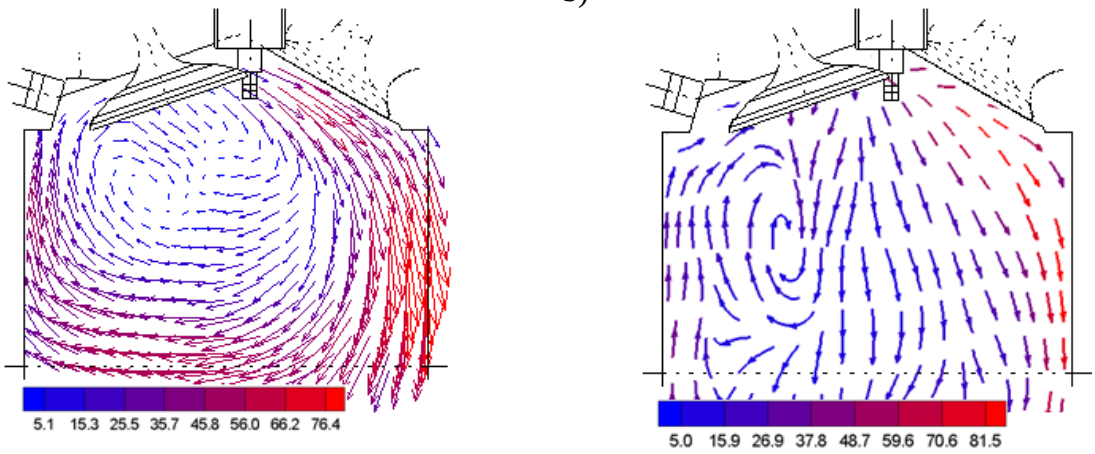

Figure 5.24: Velocity structure in the cross section of the combustion chamber during intake stroke at $CA = 108°$; a) PIV data averaged over 20 samples; b) LES averaged over 40 engine cycles.

a) b)

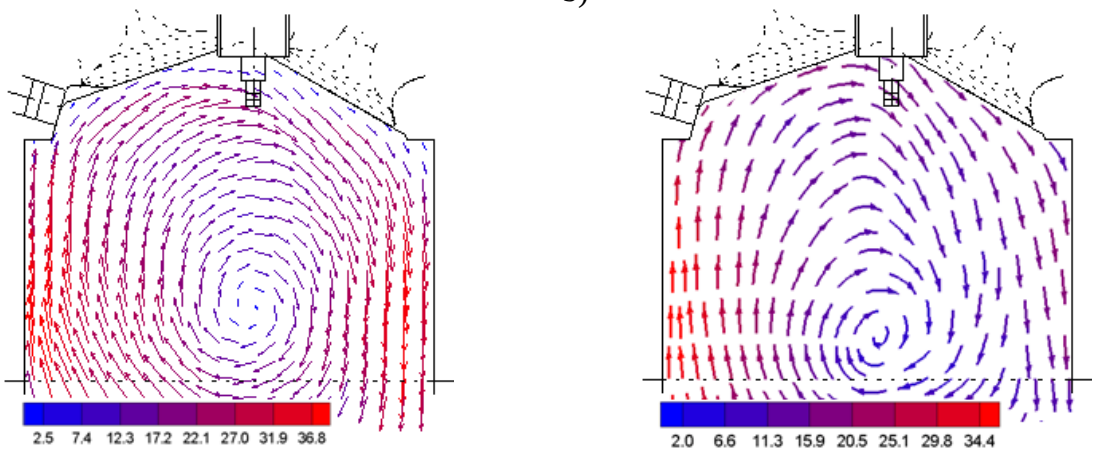

Figure 5.25: Velocity structure in the cross section of the combustion chamber during the initial stage of compression stroke at $CA = 208°$; a) PIV data averaged over 20 samples; b) LES, averaged over 40 engine cycles.

a) b)

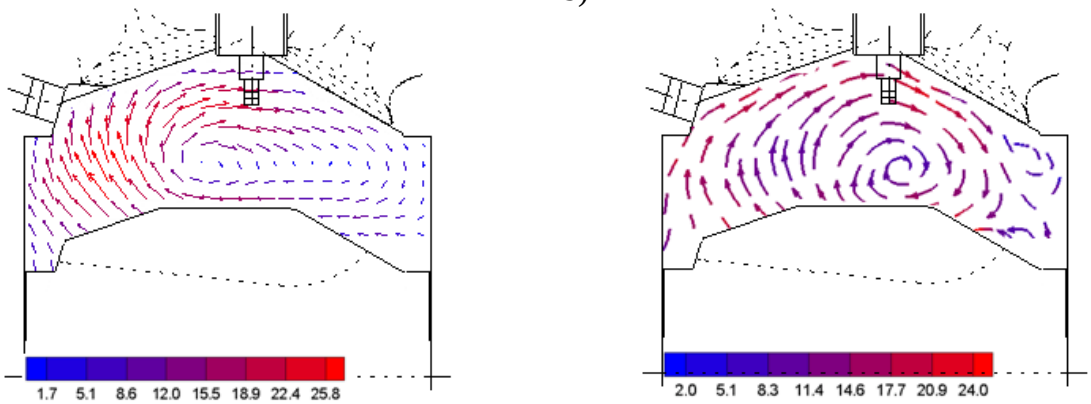

Figure 5.26: Velocity structure in the cross section of the combustion chamber at the end of compression stroke, $CA = 300°$; a) PIV data averaged over 20 samples; b) LES, averaged over 40 engine cycles.

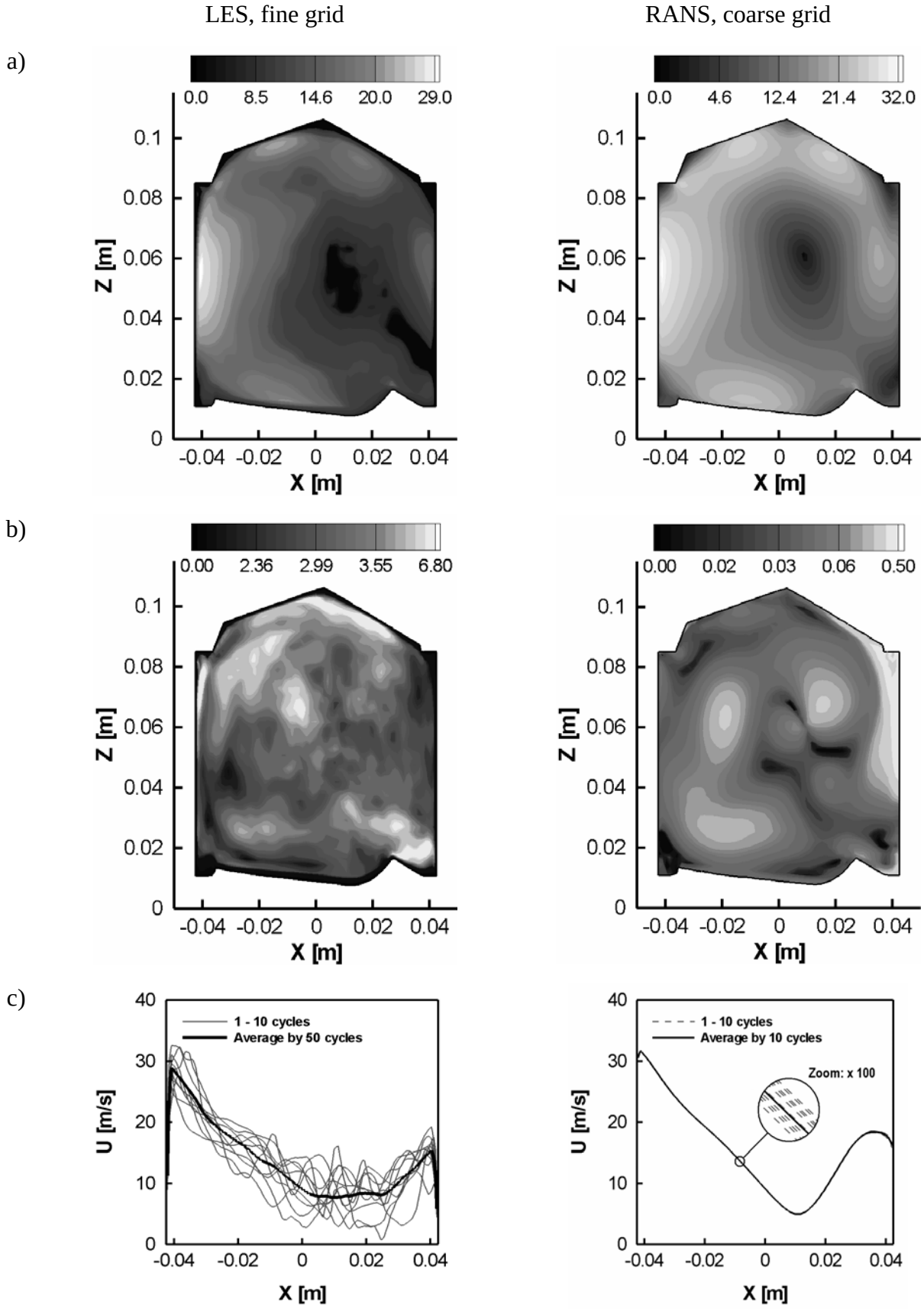

Figure 5.27: Comparison of LES (fine grid, 50 engine cycles) and RANS results obtained on the coarse grid for 10 engine cycles at $CA = 255°$; Velocity flow field (a) and standard deviation of velocity (b) in a cross section of the combustion chamber, instantaneous velocity profiles at $z = 0.05\,m$ (c).

5.2.4. Comparison of LES and RANS results

Results of the simulation of in-cylinder flows obtained with LES and RANS are discussed in this section. The RANS calculation of the "BMBF" IC-engine has been carried out by KIVA-3V using the standard $k-\varepsilon$ model. The coarse grid using 150.000 control volumes including the intake / exhaust ducts has been used to perform 10 consecutive engine cycles with RANS. LES results obtained on the fine grid for 50 engine cycles were described above. Figure 5.27 presents the comparison of the LES (left column) and RANS (right column) results for velocity flow field (a), standard velocity deviation (b) and instantaneous velocity profiles (c) in the cross section of the combustion chamber at $CA = 255°$. Examination of the results demonstrates that RANS is able to predict the mean flow structure well whereas all information regarding the cyclic variability of in-cylinder flow is lost, as shown in figure 5.27.c and 5.28.b. Figure 5.28.b shows the standard velocity deviation profiles normalized with the local mean velocity. Figure 5.28.a provides the comparison of the mean velocity profiles for the LES, averaged over 10 and 50 cycles and for the RANS, averaged over 10 cycles, respectively. Both the flow structure and the magnitudes of velocity obtained in LES can be found in a good agreement with the RANS prediction for the mean flow field.

a) b)

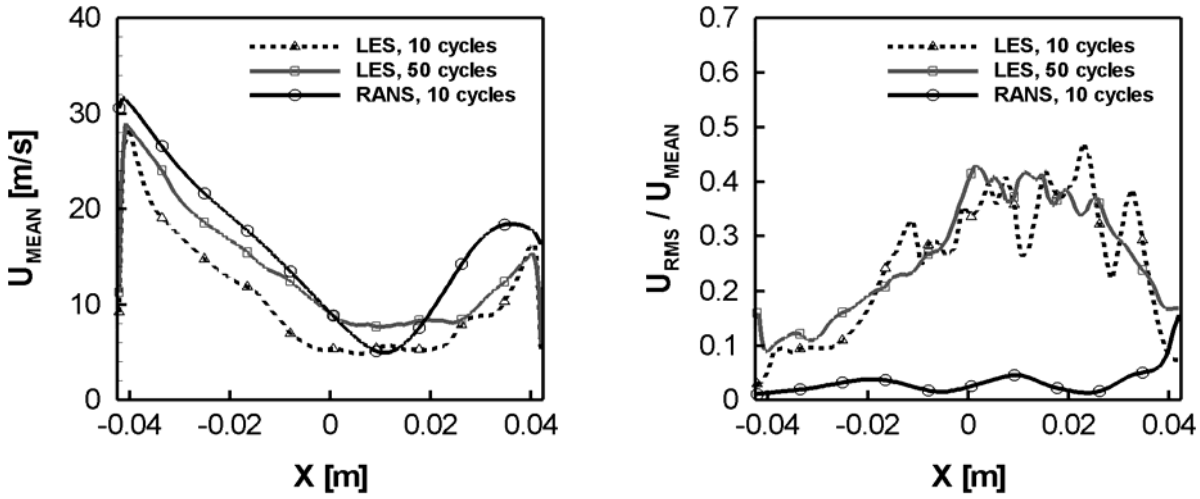

Figure 5.28: Comparison of LES and RANS results at $CA = 255°$. Mean velocity (a) and standard velocity deviation profiles normalized with the local mean velocity (b) at $z = 0.05\,m$.

5.3. Conclusions

In order to characterize the cycle-to-cycle variations of in-cylinder charge motion for single-phase flow in an air-guided internal combustion engine, LES calculations have been performed using a realistic four stoke IC-engine geometry. A suitable parallelization strategy has been used to simulate up to 50 full engine cycles. Phase-averaged statistics have been presented for characteristic crank angles.

During the intake stroke most of the turbulence is generated by both strong intake jet and specific configuration of the piston bowl. The incoming flow initiates the in-cylinder charge motion with predominant normal-tumble component. During the intake stroke the results show strong cycle-to-cycle fluctuations, mainly at the tip of the intake jet and at the center of the incipient tumble motion. Taking into account the results presented in this chapter together with the results discussed in previous work of author [59] it can be concluded, that the random nature

of turbulence coupled with the effects of the flow within the intake port are the most likely origins of the in-cylinder velocity cycle-to-cycle variations.

The turbulence induced during the intake stroke plays a key role in the evolution of the turbulence during the compression and also expansion strokes, where the turbulence is generated primarily by the piston bowl geometry. The highest intensity of cycle-to-cycle fluctuations is found at the center of in-cylinder tumble motion. At the end of compression stroke, i.e. close to the ignition point, the center of tumble motion is located close to the region of the spark plug. Therefore, the cyclic variations strongly affect the flow parameters in this crucial area and they have to be considered as the potential cause of a misfired engine cycle.

Both the expansion and exhaust strokes are characterized by a rather small intensity of velocity fluctuations compared to the intake and compression strokes. It should be also noted that the flow field structure, taking into account injection and combustion processes, would look quite differently during the expansion and exhaust strokes.

The analysis of the globally averaged flow quantities for various individual engine cycles shows the cycle-to-cycle fluctuations in cylinder mass, charge motion and kinetic energy. The maximal intensity of cyclic variations is observed during the compression stroke close to ignition time. These factors directly affect the effective work output for each engine cycle and cause other problems such as engine roughness.

The LES results were compared with available experimental data as well as with RANS prediction obtained on the same engine configuration. Generally, the LES results can be found in a good agreement with experimental PIV data. Comparison of LES and RANS solutions demonstrates the ability of RANS to predict the mean velocity properties while the information regarding the instantaneous quantities is lost in the process.

Chapter 6

Verification of the results

An attempt to verify the results obtained in the complex reciprocating engine configuration using LES is provided in the present chapter. Firstly, the effect of grid resolution on the LES predictions of a simplified in-cylinder configuration is investigated. Estimation of statistical errors is presented next. Finally, the quality of the LES results for the present in-cylinder flow is estimated by applying various indices for error assessment published in the literature.

6.1. Theoretical background

It is anticipated that LES will increasingly become the future engineering tool for development and design of IC-engines. However, a careful assessment of simulation errors for the application of LES to such complex configurations as an IC-engine can at present only rarely be found in the literature. A brief review of methods used to quantify uncertainty or accuracy of time-dependent calculations in the context of RANS, LES and detached eddy simulation can be found in [31]. The verification of LES calculations is difficult because of the fact that both the subgrid scale model contribution and numerical discretization errors are functions of the grid resolution. Celik et al. [32] discuss among several other LES quality measures the so-called LES Index of Quality E_{LESIQ}. Klein [86] and Freitag and Klein [47] present an extension of this approach by considering an additional error contribution for the modeling error with a scaling exponent different to the numerical discretization.

A discussion about the evaluation of commutation errors in LES on moving structured and unstructured grids, e.g. piston-engine flows, is given in the work of Moureau et al. [109]. These errors occur when the LES filter is a function of time, i.e. the instantaneous deformation rate of the mesh. It is found that commutation errors may be neglected to first order if the flow field and mesh deformation are generated by the same boundary movement. Discretization errors of various types of difference schemes for LES were evaluated through static and dynamic analyses in reference [124]. The static error analysis indicated that both the finite-differencing and aliasing errors increase as the amount of numerical dissipation increases. The dynamic analysis, however, shows that the aliasing error decreases as the numerical dissipation increases and the finite-differencing error overweights the aliasing error. It has been concluded that the discretization errors are properly characterized only by the dynamic analysis.

The verification of LES based on the so-called systematic grid and model variation has been proposed by Klein [86]. In contrast to RANS, where the quality of results can be estimated by performing grid refinement studies, based on variants of Richardson extrapolation, in the context of LES there is an interaction between modeling and numerical errors [47]. The method allows estimating the sensitivity of the simulation results on the modeling and numerical error contributions separately. The method is based on the idea to change the model contribution and the grid resolution and it consists of the following steps: 1) Choose fine and coarse grids with coarsening factor β; 2) Choose a SGS model variation factor α; 3) Three simulations are needed for this method, namely the standard LES solution on the fine and coarse grids as well as an LES solution with a modified SGS model on the coarse grid. This is in contrast to references

[47, 86] where the simulation with the modified model contribution is performed on the fine grid.

Details on the error estimation based on the LES index of quality E_{LESIQ} are given in [32] and for the systematic grid and model variation E_{SGMV} in [47, 86]. The definitions for E_{LESIQ} and E_{SGMV} are given below, where the expression for E_{SGMV} had to be modified in order to reflect that the model variation is performed on the coarse grid. It has to be mentioned that the E_{LESIQ} in its original formulation requires the evaluation of the turbulent kinetic energy rather than velocity. Furthermore, the E_{LESIQ} as presented by Celik et al. [32] calculates the amount of resolved turbulent kinetic energy rather than the unresolved part representing the error. Since the underlying physics and modeling does not change expression (6.1) is denoted E_{LESIQ} even if it is used in slightly different manner as originally proposed.

$$E_{LESIQ} = \frac{|u_3 - u_1|}{1-\beta^n}, \tag{6.1}$$

$$E_{SGMV} = \left|\frac{u_2 - u_3}{\beta^m(1-\alpha)}\right| + \left|\frac{(u_2-u_1)-(u_2-u_3)(1-\alpha\beta^m)/[(1-\alpha)\beta^m]}{(1-\beta^n)}\right|. \tag{6.2}$$

Here u_1 is the velocity obtained from the standard LES solution on the fine grid, u_3 is the velocity on the coarse grid and u_2 is the LES solution on the coarse grid with a modified model parameter α, given by $C_{S,2}^2 = \alpha \cdot C_{S,1}^2$, $\beta = 1.6$ is a grid refinement factor. The theoretical value of the numerical scheme n has been set equal $n = 2$. The scaling exponent of the modeling errors has been set to $m = 2/3$. Formula (6.1) is basically the classical Richardson extrapolation with known convergence order and assuming equal scaling exponents for modeling and numerical error. For E_{SGMV} the first term on the right hand side of equation (6.2) represents the modeling error (E_{MOD}) and the second term represents the numerical error (E_{NUM}) which are assumed to scale with the mesh spacing h:

$$E_{MOD} = \frac{u_2 - u_3}{\beta^m(1-\alpha)} = c_m h^m \tag{6.3}$$

and

$$E_{NUM} = \frac{(u_2-u_1)-(u_2-u_3)(1-\alpha\beta^m)/[(1-\alpha)\beta^m]}{(1-\beta^n)} = c_n h^n, \tag{6.4}$$

where h is the grid spacing and c is the unknown constant. Detailed information about the theoretical fundamentals of systematic grid and model variation and its application to various flow configurations can be found in references [47, 48, 86].

6.2. The effect of mesh resolution on the flow field in a simplified engine geometry

A short review and some results of grid dependency studies for the compression and expansion stroke of a motored engine with a flat piston can be found in [29]. The simulations of a generic four-stroke, two-valve engine geometry were carried out using a Smagorinsky SGS

model. Coarse and relatively fine computational grids with 220.000 and 440.000 control volumes, respectively, were used. The smallest cell size of the finer grid was $\Delta = 2\,\text{mm}$. It has been shown that smaller scales are resolved with the finer grid, leading to higher levels of resolved turbulence intensity.

The present paragraph focuses on evaluation of the effect of the grid resolution on LES results in a complex configuration. For this propose a numerical simulation, using a motored engine-like geometry shown in figure 6.1, was carried out for three different grid resolutions. The geometry and computational grids were created using ICEM CFD Hexa. The selected configuration is based on the vertical valve IC-engine geometry considered in paragraph 3.4. The main parameters of the engine under consideration are collected in table 6.1. The choice of this simplified configuration was first of all motivated by the limitations imposed through the meshing software and KIVA-3V. The generation of a high resolution computational grid for a complex reciprocating configuration is an intricate task as discussed in chapter 4. Therefore, the relatively simple geometry with a flat piston and a flat cylinder head with a single intake / exhaust duct without valve has been selected. Including the valve into the considered geometry leads to a significant complication in view of mesh generation.

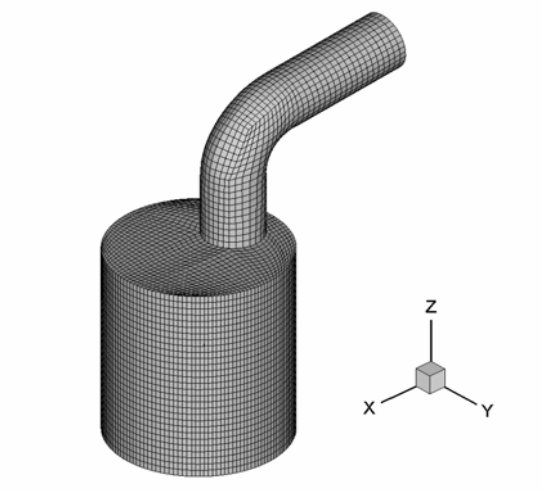

Figure 6.1: Single-port, non valve, engine-like geometry.

Table 6.1: Parameters of the simplified IC-engine with a single port.

Bore [mm]	Stroke [mm]	Clearance height [mm]	Engine speed [rpm]
82.55	92.075	5.70	1600

Table 6.2: Specification of computed variants.

Variant	**Grid resolution (cylinder), cells**	**Grid size Δ, [mm]**	**Time for 1 cycle (0° - 360°), P4-3.0GHz**
Case A	33×33×33	2.50	1.5 h.
Case B	66×66×66	1.25	28 h.
Case C	99×99×99	0.83	240 h.

The wall-flow interaction was treated with a no-slip velocity boundary condition and atmospheric pressure was set at the open boundary of the port. A description of the different meshes is given in table 6.2. The grid size for the finest mesh is $\Delta = 0.83\,\text{mm}$ (case C) with the amount of cells of about 1.2 millions. The maximal cell size on the coarsest grid is equal to $\Delta = 2.5\,\text{mm}$ (case A). Hence, the grid refinement factors relative to case A are 2 and 3, respectively. The total amount of engine cycles has been limited to 5, taking into account the considerable computational time required for the finest grid.

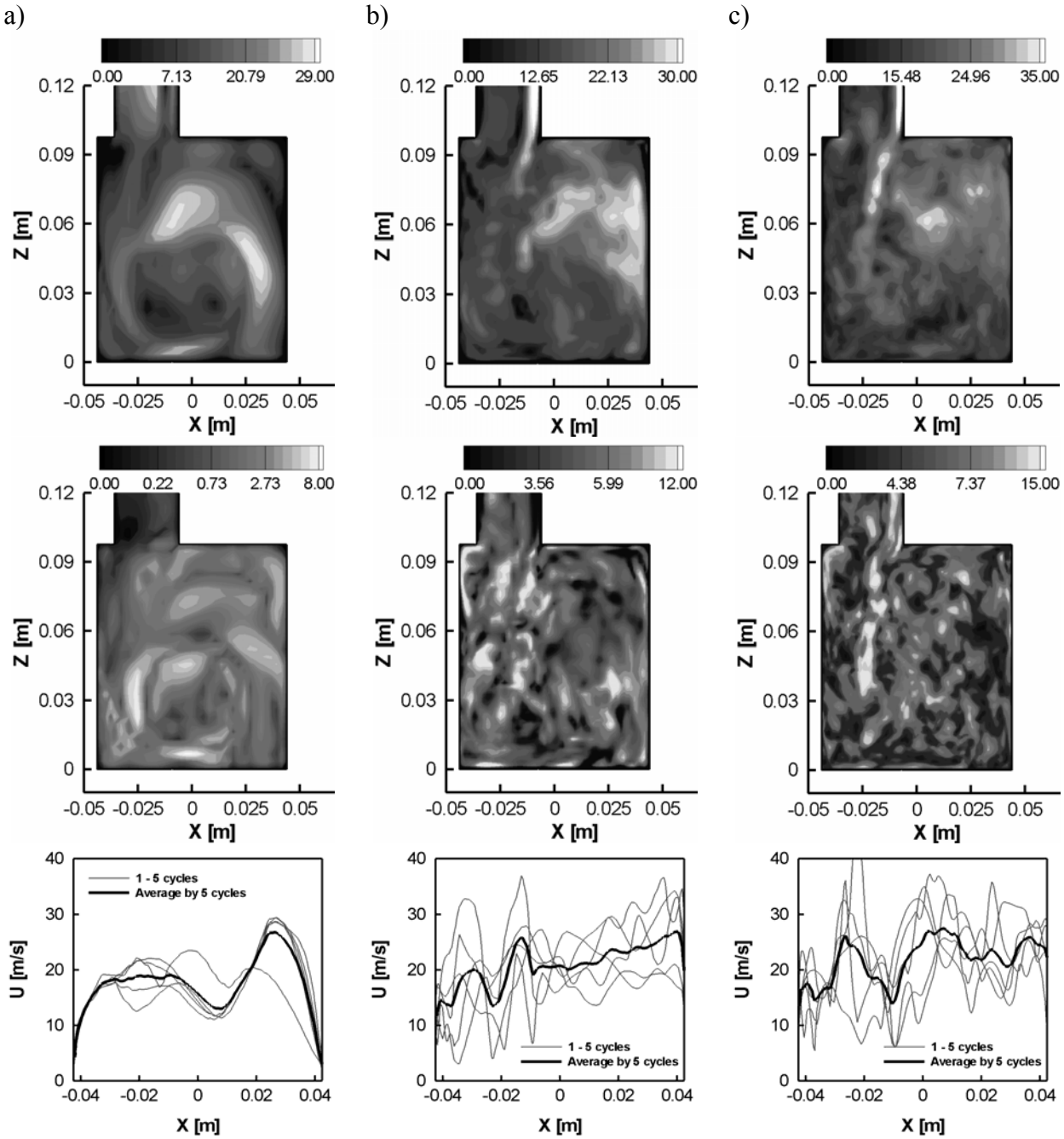

Figure 6.2: The effect of grid resolution on LES predictions in the engine-like geometry at BDC, $\text{CA} = 180°$; **top:** isocontours of velocity averaged over 5 cycles; **middle:** rms of velocity; **bottom:** velocity cycle-to-cycle variations at $z = 0.05\,\text{m}$; a) case A; b) case B; c) case C.

Figure 6.2 collects the averaged velocity flow fields (top) in the cross section of the cylinder, the standard deviation of velocity (middle) and the cycle-to-cycle velocity fluctuations (bottom) at $z = 0.05\,\text{m}$ obtained on the coarse (a), medium (b) and fine (c) grids, i.e. cases A, B and C, respectively. Inspection of the obtained results reveals that both flow structure and velocity magnitude are different especially comparing cases A and B. The maximal velocity in the cylinder predicted by LES in case C is 32% respectively 23% higher compared to cases A and B. Consideration of the standard deviation of velocity (figure 6.2, middle) shows that refining the computational mesh by a factor of 3 leads to an increase of intensity of fluctuations by a factor of 2.3. It can be seen from figure 6.2 (middle and bottom) that the information about instantaneous quantities including information about the cycle-to-cycle variations is nearly completely lost using the coarse grid (case A). Examination of the turbulent kinetic energy, shown in figure 6.3, let to conclude, that the amount of resolved turbulent kinetic energy in case C is 6 times more compared to case A. However, the peak values of turbulent kinetic energy in cases B and C are considerably closer to each other: Refinement of the grid by a factor of 1.5 results in a variation of turbulent kinetic energy in the order of 15%.

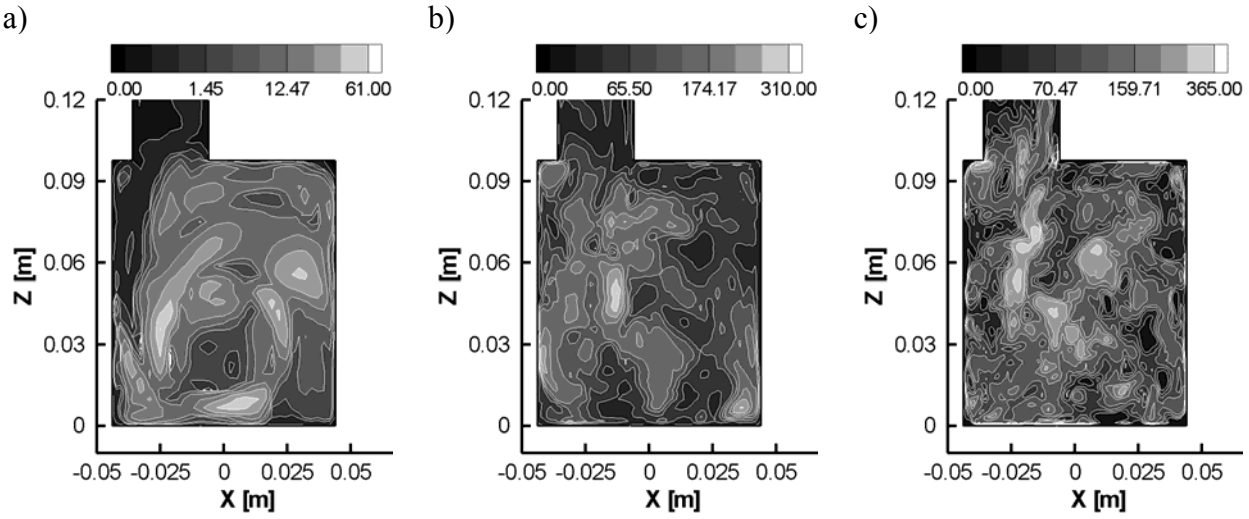

Figure 6.3: Isocontours of the turbulent kinetic energy in the cross section of the cylinder at BDC, $CA = 180°$ for coarse (a), medium (b) and fine (c) grids, averaged over 5 samples.

Since the geometry does not include a valve, either intake or exhaust strokes can be realized in the considered configuration. LES results for the so-called "exhaust stroke" at $CA = 270°$ for the mean velocity flow fields in the cross section of the cylinder (top), rms of velocity (middle) and velocity profiles (bottom) are depicted in figure 6.4. The velocity fields are predicted with similar velocity magnitudes for all examined cases as it can be seen from figure 6.4 (top). Nevertheless, figure 6.4 (middle and bottom) indicates big differences in the captured velocity fluctuations as well as in the turbulent kinetic energy shown in figure 6.5. Large eddy simulation does not predict cycle-to-cycle variations in case A, however they can be resolved in cases B and C. Comparison of figures 6.2 - 6.4 reveals that the intensity of cyclic fluctuations at $CA = 180°$ (BDC) is approximately 2 times more compared to their values during exhaust stroke at $CA = 270°$. Figure 6.6 shows that all cases give similar results for the mean velocity profiles during exhaust stroke (b) while differences between profiles are visible at BDC (a).

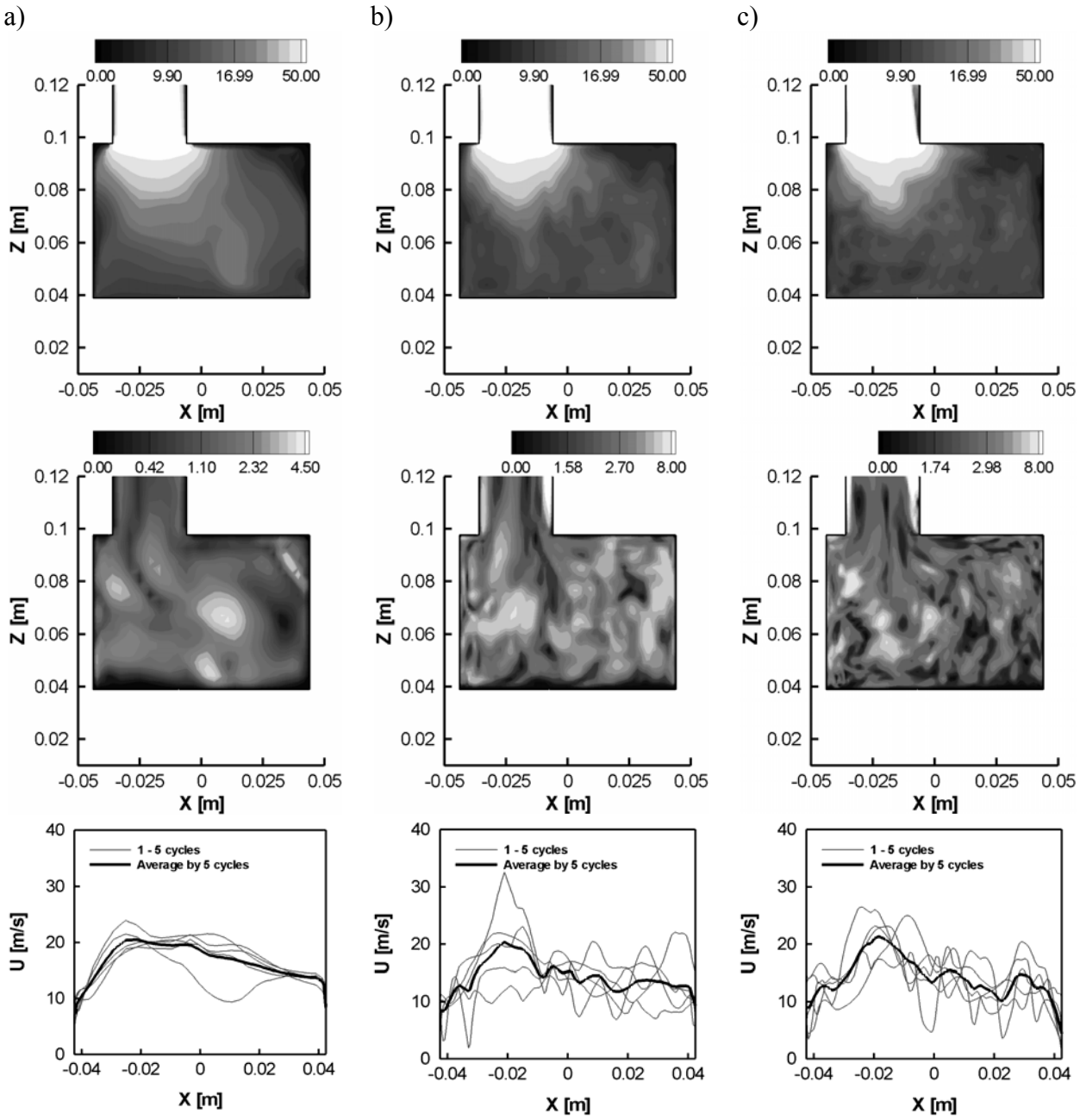

Figure 6.4: The effect of grid resolution on LES prediction in the simplified engine geometry during exhaust stroke at $CA = 270°$; **top:** isocontours of velocity averaged over 5 cycles; **middle:** rms of velocity; **bottom:** velocity cycle-to-cycle variations at $z = 0.05\,m$; a) case A; b) case B; c) case C.

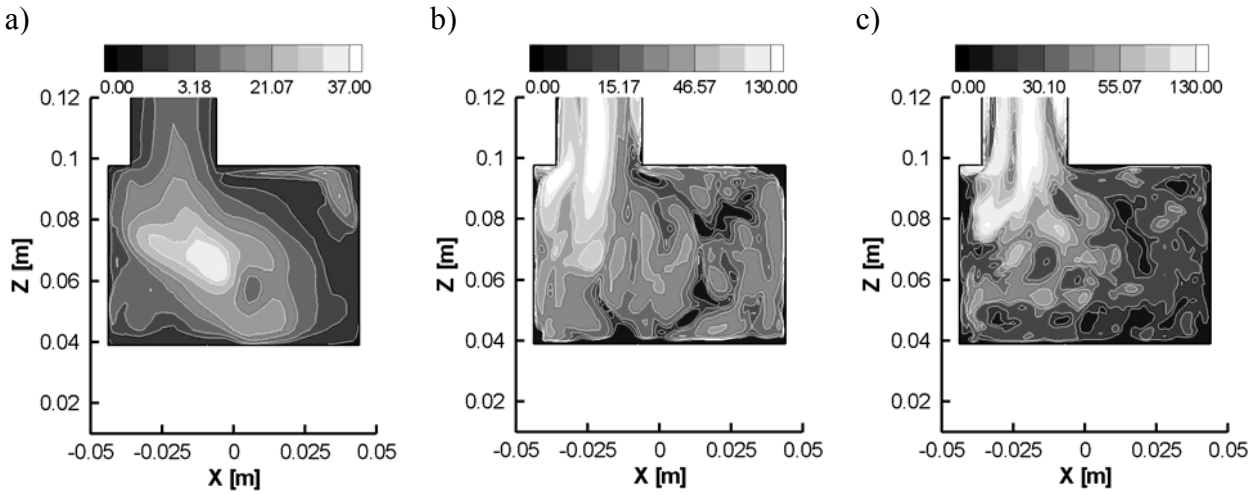

Figure 6.5: Turbulent kinetic energy in the cross section during exhaust stroke at $CA = 270°$ for coarse (a), medium (b) and fine (c) grids, averaged over 5 samples.

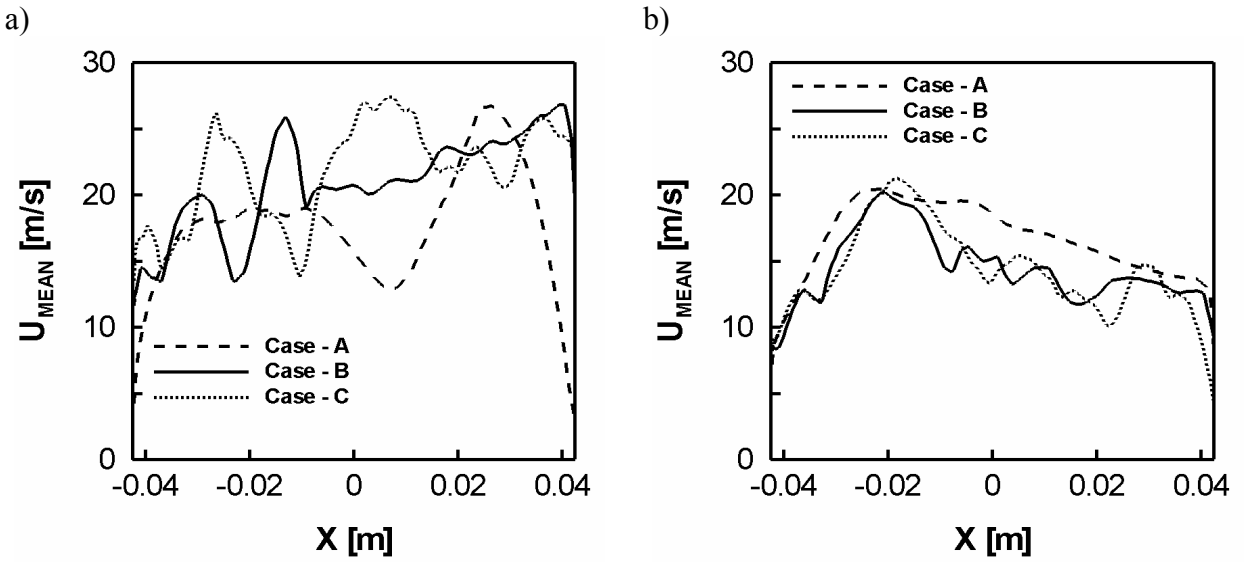

Figure 6.6: The mean velocity profiles at $z = 0.05\,\text{m}$ averaged over 5 samples; a) BDC, $CA = 180°$; b) Exhaust stroke, $CA = 270°$.

From the above results it can be concluded that the distinctions between cases A and B are considerable. At the same time LES predicts rather similar flow fields for cases B and C even in spite of a clear lack of sufficient statistical samples. Also the intensity of fluctuations is comparable for both cases B and C. Increasing the number of cells by a factor of 2 (cases A and B) leads to an increase of computation time by a factor of 18 using the QSOU advection scheme in the KIVA-3V program. Further increase of the number of cells up to 99 in each direction, i.e. 3 times more compared to case A, results in an increase of computation time by a factor of 160 (case A) and 8.5 (case B), respectively. For the realistic configurations, such as the "BMBF" IC-engine, the calculations will be even considerably more time expensive. One of the most critical parts in real configurations is the valve zone. In order to include all geometrical features and to provide the valve motion, the mesh in this area has often the highest resolution compared to the rest of the geometry. The flow passing through the valve slit region has the highest magnitude of

velocity over the whole computational domain. This results in a limitation of the computational time step based on the CFL condition. Hence, the computational costs for LES calculation in that case may be too high on a very fine grid and a compromise in grid resolution is required. The mesh resolution in case B is taken as a guideline for the realistic engine configuration presented in chapter 5.

6.3. Estimation of statistical errors

LES is a statistical method providing detailed information about instantaneous quantities and, after ensemble- or time-averaging, about mean values. Standard procedures can be used in order to quantify statistical errors. An extended discussion on statistical errors in LES application can be found in [31].

The IC-engine configuration features a three-dimensional unsteady flow. Consequently, ensemble averages have to be calculated resulting in huge computational time. Figures 6.7 - 6.9 show the mean velocity (a) and the normalized velocity fluctuations (b) averaged over 5, 10, 20, 40 and 50 engine cycles for crank angles $CA = 105°$, 255° and 285°, respectively. The results correspond to LES of the "BMBF" IC-engine obtained on the fine grid. Examination of the results reveals that the LES solution is converged for the first and second order moments. By visual inspection one could conclude that approximately 20 samples are needed to get the mean velocity right and 40 samples to determine the fluctuations properly. On the one hand, it is widely assumed that a minimum of 50 engine cycles have to be acquired experimentally to yield statistically relevant results [68, 180].

a) b)

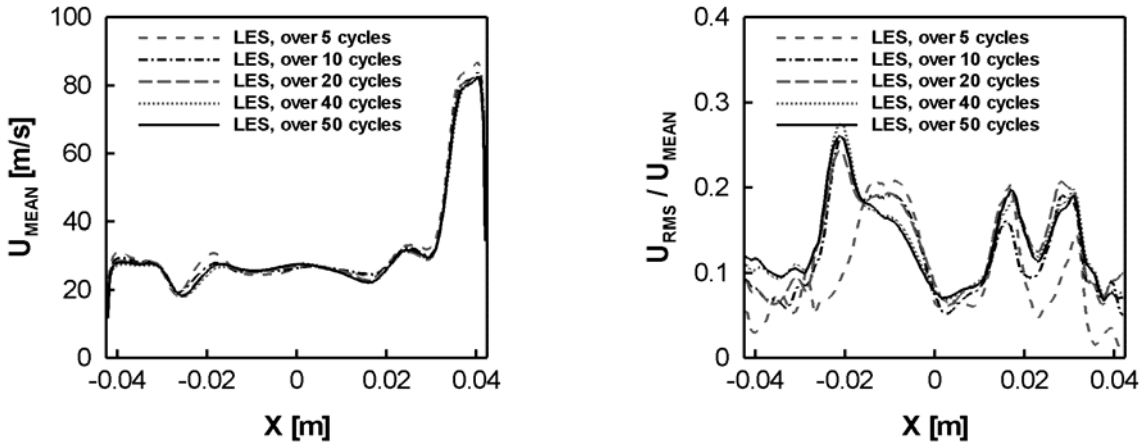

Figure 6.7: Mean velocity (a) and normalized velocity fluctuations (b) averaged over 5, 10, 20, 40 and 50 engine cycles. Intake stroke, $CA = 105°$, $z = 0.05\,\mathrm{m}$.

A more careful analysis (for details see [31]) shows that the uncertainty in mean velocity and mean velocity rms can be expressed as $100 \cdot 0.25/\sqrt{n}$ respectively $100/\sqrt{2n}$ where $u_{rms}/u_{mean} = 0.25$ has been assumed for simplicity (compare results discussed in chapter 5 and shown in figures 5.9.c, 5.13.c, 5.17.c and 5.21.c). Accepting a 5% statistical error for the mean velocity and a 10% error for the velocity standard deviation the above formulas roughly yield $n = 25$ respectively $n = 50$, where a confidence level of 68.3% has been used. This shows on the one hand that the sample number for the analysis is big enough but also that, due to limited computer power, a compromise has to be sought between numerical and statistical accuracy.

a) b)

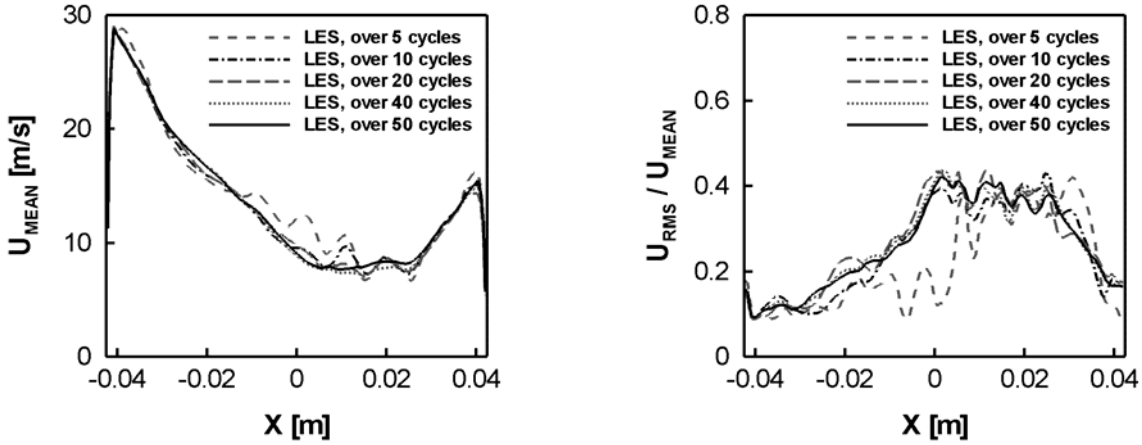

Figure 6.8: Mean velocity (a) and normalized velocity fluctuations (b) averaged over 5, 10, 20, 40 and 50 engine cycles. Compression stroke, $CA = 255°$, $z = 0.05\,\text{m}$.

a) b)

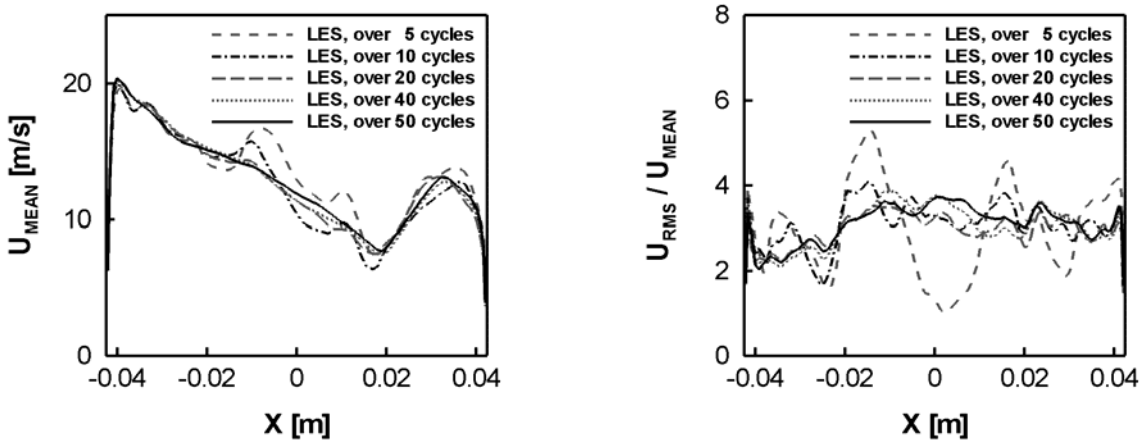

Figure 6.9: Mean velocity (a) and normalized velocity fluctuations (b) averaged over 5, 10, 20, 40 and 50 engine cycles. Compression stroke, $CA = 285°$, $z = 0.069\,\text{m}$.

6.4. Estimation of modeling and numerical errors

The methods described in paragraph 6.1 have been applied for estimation of LES errors in the "BMBF" IC-engine configuration. For this propose, LES calculations using a coarse grid have been carried out for two auxiliary cases: one with a standard SGS model constant of $C_S = 0.1$ and one with a modified model constant $C_S = 0.2$. Thus, the following LES simulations of 40 full engine cycles have been considered: a) fine grid with standard SGS model; b) coarse grid with modified SGS model; c) coarse grid with standard SGS model. A grid refinement factor of $\beta = 1.6$ and a model variation factor of $\alpha = 4$ have been used together with $n = 2$ and $m = 2/3$, compare equations (6.1) - (6.4).

The effects of grid variation and model variation are depicted in figure 6.10. The examination of the results reveals that the flow structure is qualitatively well captured on both grids (see a, b). Also the normalized velocity fluctuations are in a reasonable agreement as depicted in figure 6.11.b. However, quantitative differences in the mean velocity are not

negligible (figure 6.11.a) and indicate that a finer grid would be desirable. Figure 6.10.c shows the damping effect of the Smagorinsky parameter on the cycle-to-cycle fluctuations.

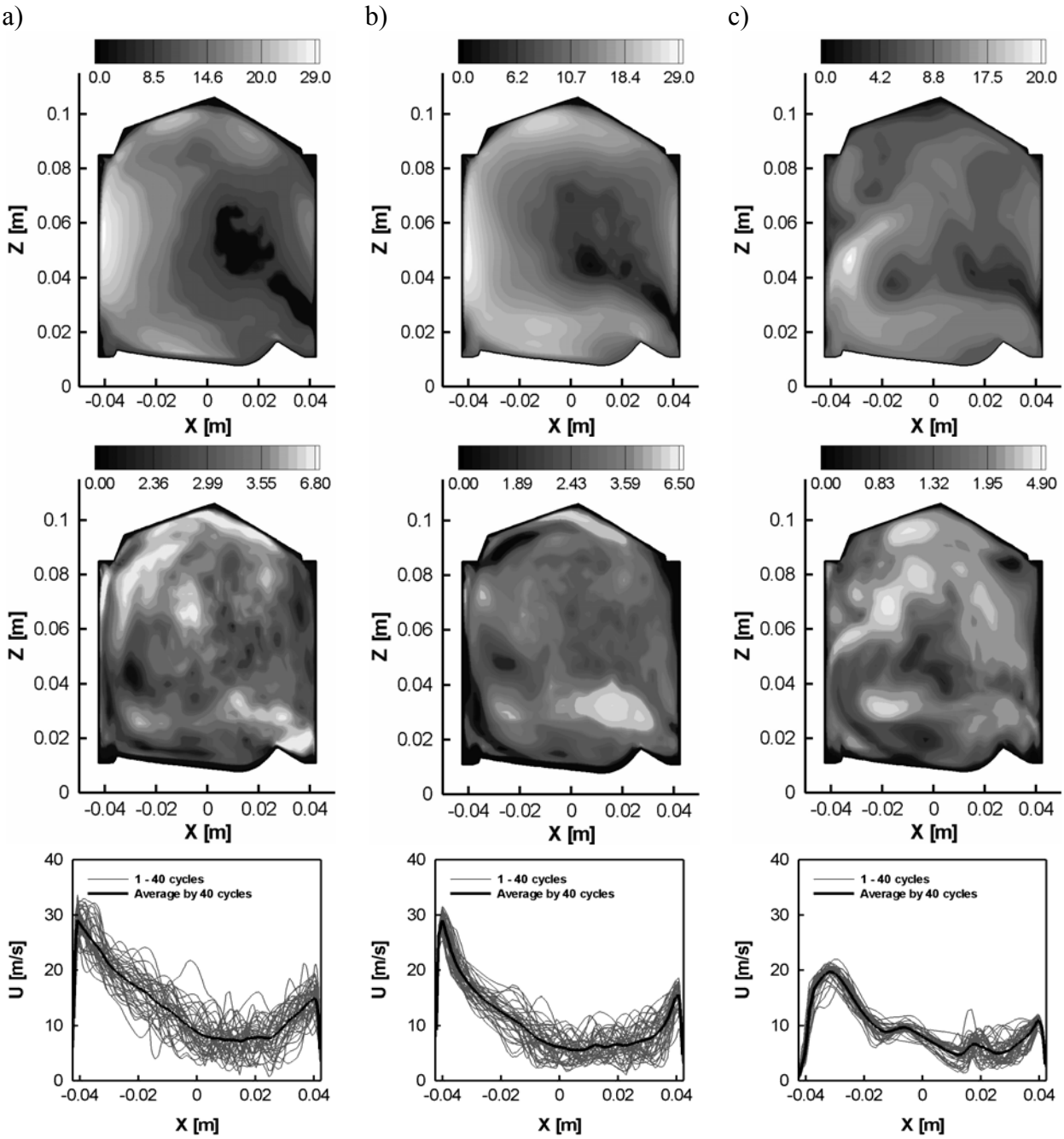

Figure 6.10: Isocontours of velocity averaged over 40 engine cycles (top), standard deviation of velocity (middle) and velocity cycle-to-cycle variations at $z = 0.05\,\mathrm{m}$ (bottom) during compression stroke at $CA = 255°$; a) Fine grid LES with $C_S = 0.1$; b) Coarse grid LES with $C_S = 0.1$; c) Coarse grid LES with modified model constant $C_S = 0.2$.

To assess the error more thoroughly the systematic grid and model variation (E_{SGMV}) and the LES Index of quality (E_{LESIQ}) have been used to provide an error estimation for mean velocity, see figure 6.12. All results have been normalized with the local mean velocity. As a

general trend the results from E_{SGMV} are more conservative compared to E_{LESIQ}. The highest estimated error occurs during intake stroke when the flow leaves the ports to enter the combustion chamber. This is not surprising because of the high flow velocity in this region resulting in high mesh resolution requirements at the valve and valve seat. During the rest of the engine cycle the estimated error is smaller, with values between 10% and 40% of the mean flow. Of course it has to be mentioned that figure 6.12 is only an order of magnitude analysis. Furthermore both estimators are based on the assumption of asymptotic behavior of the error which can not be ensured for a given grid resolution a priori.

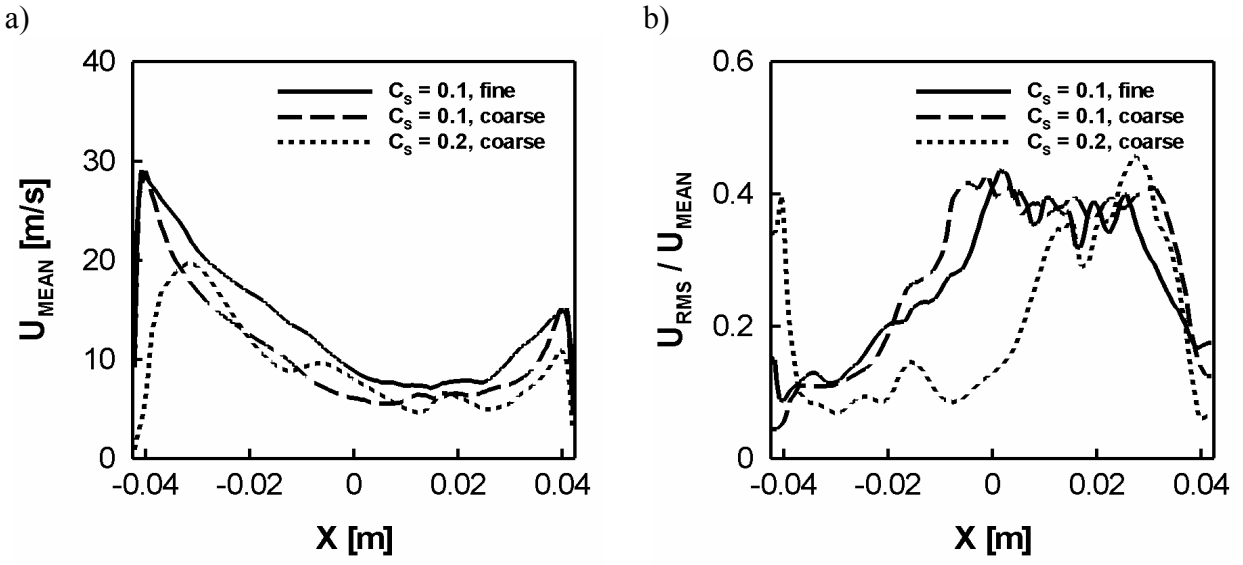

Figure 6.11: Effects of grid resolution and model parameter on LES predictions during compression stroke at $CA = 255°$, profiles taken at $z = 0.05\,m$; a) Mean velocity profiles averaged over 40 engine cycles; b) Normalized standard velocity deviation u_{rms}/u_{mean}.

Figure 6.13 shows the calculated ratio of resolved to total turbulent kinetic energy based on the error estimators given in equation 6.1 and 6.2, where the turbulent kinetic energy instead of velocity has been used. It is generally believed that a good LES should resolve 80% of the turbulent kinetic energy. During the whole engine cycle 70% - 90% of the turbulent kinetic energy have been captured by the computational mesh which is a very satisfactory value considering the complexity of the configuration. Nevertheless, based in figure 6.12 and equation 6.1 it is speculated that a well resolved LES withstanding a proper validation would probably require grid refinement at least by a factor of 2, perhaps even more close to the walls.

6.5. Conclusions

The quality of the LES simulations applied to complex engine configurations has been assessed. The effect of the mesh resolution on LES prediction, using a simplified engine geometry, has been analyzed first. As expected, the finer mesh allows resolving smaller scales hence it causes higher levels of resolved turbulence intensity. It can be also concluded that in respect to computational speed, the limitation on the value of time step, based on the CFL criterion, is more significant compared to the mesh resolution requirements, especially in such complex configurations as IC-engines. It results in long computational time needed for calculations of multiple engine cycles and, consequently a compromise in mesh resolution is

required. The analysis of numerical and statistical errors in a realistic engine geometry has shown that a computational mesh with grid size $\Delta \approx 1\,\text{mm}$ seems to be the minimum requirement to represent the flow field with reasonable accuracy. As a general guideline it is recommended to perform roughly 25 engine cycles in order to get the proper values of mean velocities and 50 cycles to ensure a good prediction of cyclic fluctuations.

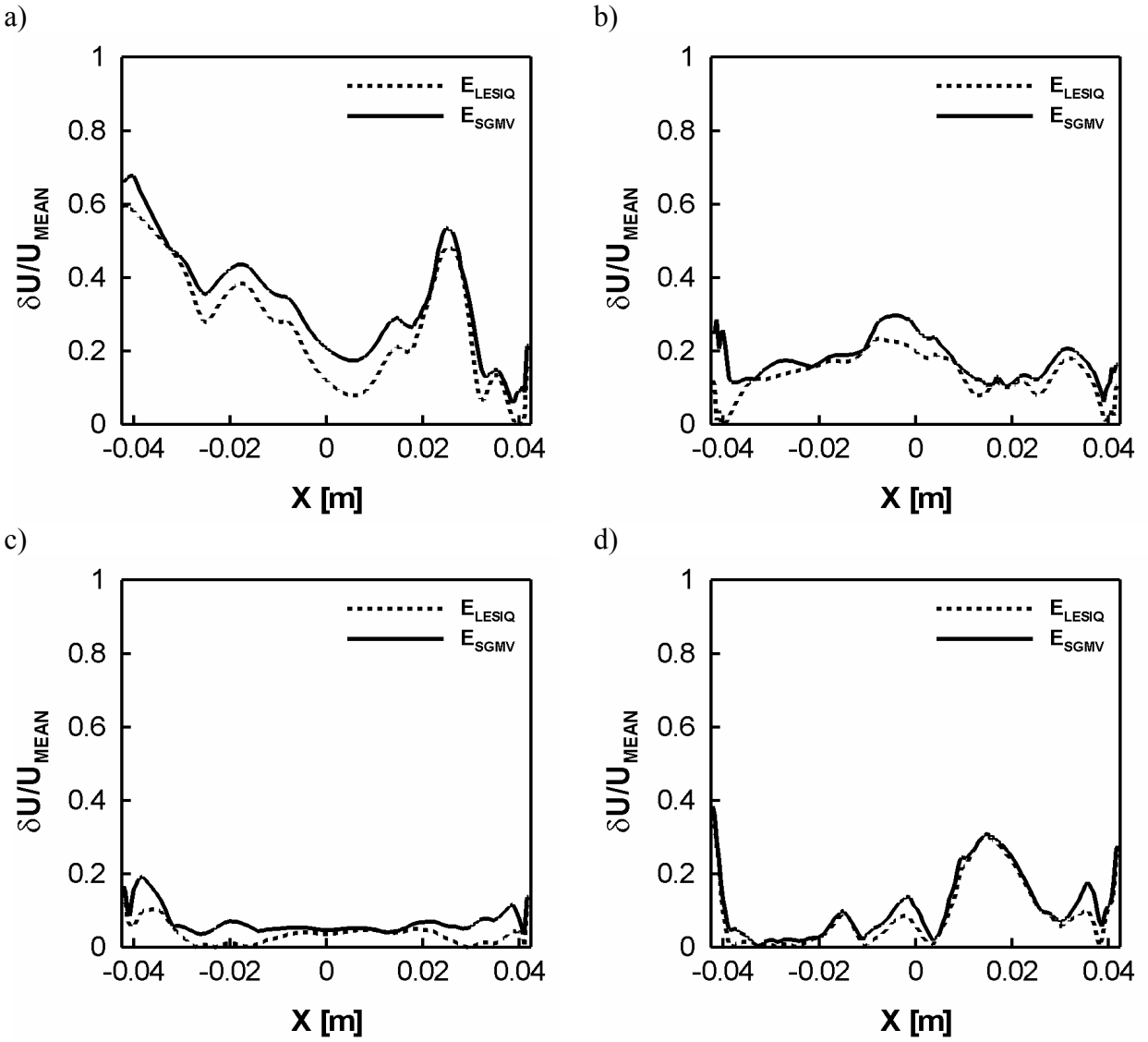

Figure 6.12: Estimated relative velocity errors using the systematic grid and model variation (E_{SGMV}) and the LES Index of quality (E_{LESIQ}) for mean velocity profile at $z = 0.05\,\text{m}$, averaged over 40 engine cycles; a) Intake stroke, $CA = 105°$; b) Compression stroke, $CA = 255°$; c) Expansion stroke, $CA = 450°$; d) Exhaust stroke, $CA = 630°$.

It was pointed out, that an assessment of simulation errors of LES is difficult since both the subgrid scale model contribution and numerical discretization errors are functions of the grid resolution, therefore, special techniques have to be utilized. A systematic grid and model variation procedure (E_{SGMV}) proposed by Klein [86] has been applied to access the quality of LES for in-cylinder flow. An error estimation using E_{SGMV} and the so-called LES index of quality E_{LESIQ} [32] has been provided for both the mean velocity and the turbulent kinetic

energy. The results reveal that the highest estimated error occurs during intake stroke as well as near the cylinder walls. For the rest of the engine cycle the estimated error for mean velocity ranges between 10% and 40%. Also the results show that the computational grid allows resolving about 70% - 90% of the turbulent kinetic energy. Despite the large errors in mean velocities the amount of resolved turbulent kinetic energy is in the range of a well resolved LES. A note of caution is however that this value does not represent the turbulent fluctuations only. It contains in addition the effect of cycle-to-cycle fluctuations.

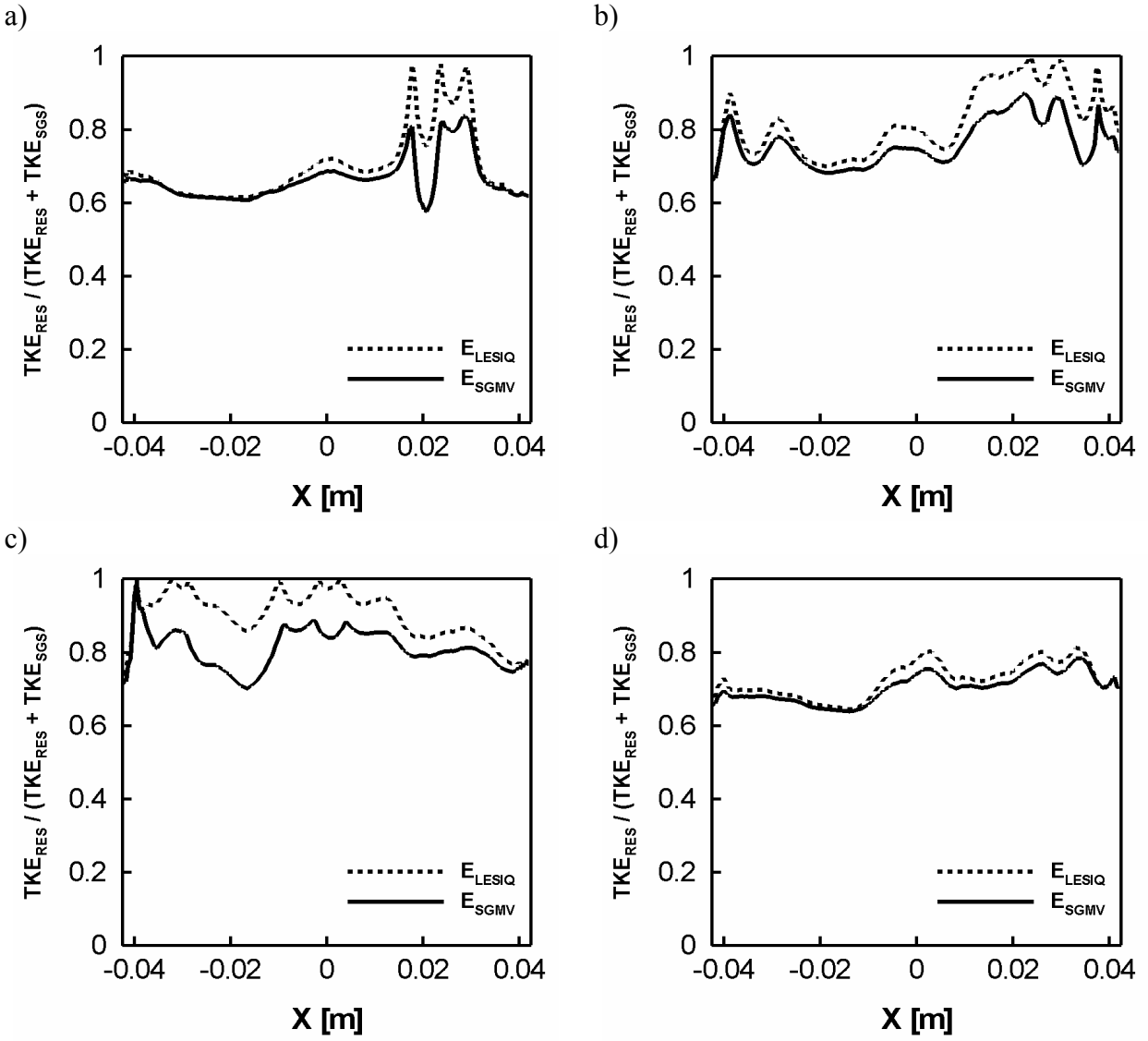

Figure 6.13: Estimated ratio of resolved to total turbulent kinetic energy using the systematic model variation (E_{SGMV}) and the LES Index of quality (E_{LESIQ}) for mean turbulent kinetic energy profiles at $z = 0.05\,\mathrm{m}$, averaged over 40 engine cycles; a) Intake stroke, $CA = 105°$; b) Compression stroke, $CA = 255°$; c) Expansion stroke, $CA = 450°$; d) Exhaust stroke, $CA = 630°$.

Chapter 7

Results and discussion: two-phase flow

The main results of IC-engine simulation for a two-phase flow are collected in this chapter. The impact of velocity cycle-to-cycle fluctuations on the fuel spray penetration, mixture preparation and cyclic variability of the fuel vapor clouds near the spark plug is discussed taking into consideration the results obtained for a single-phase flow. The investigation has been started with calibration of the standard KIVA-3V spray model. Then the effect of cycle-to-cycle velocity fluctuations on the fuel-air-mixing processes close to the ignition point is discussed. Further, the impact of the fuel spray on variability of global charge motion is considered. RANS simulations of two-phase flow are finally compared with existing LES data.

7.1. Calibration of the spray model

Simulation of fuel spray injection processes is based on the utilization of different sub-models. As it can be seen from [111], successful modeling of injection and mixture formation is very often sensitive to the setting of initial parameters of injection, boundary conditions and it also depends on the grid resolution. Therefore, a number of spray bomb simulations has been carried out in order to calibrate the spray model, determine the effects of various initial and boundary conditions as well as the sensitivity to the model coefficients, initial droplet size and the influence of the nozzle-resolution on the spray prediction. Available experimental data corresponding to the injector used in this work has been utilized to adjust the governing parameters and to calibrate the spray model.

For the test cases a simple cylindrical geometry shown in figure 7.1.a and computational grids with 3 various resolutions (33×33×33, 66×66×66 and 99×99×99) were used. The injector was located at the top of cylinder. The configuration of the injector and the coordinate system are shown in figure 7.1.b. The main parameters of injection are summarized in table 7.1. For the spray simulation a hollow spray profile shown in figure 7.1.c has been used.

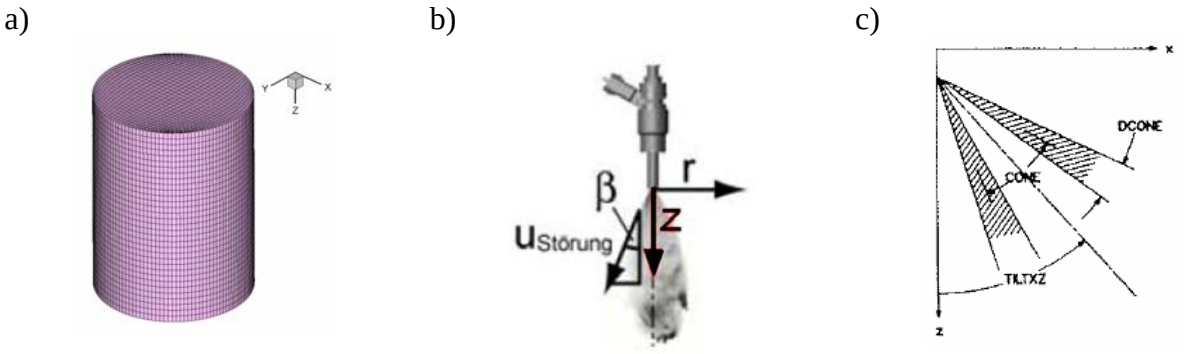

Figure 7.1: a) Geometry of a spray bomb; b) Injector and coordinate system; c) Definition of a hollow spray profile.

Spray simulations were carried out using the standard Smagorinsky subgrid-scale model for the SGS stress tensor implemented in the KIVA-3V code. The so-called DDM (discrete droplet model of Dukowicz (1980)) [42] with Lagrangian computational particles that represent

parcels of spray droplets with uniform properties was applied for the spray description. The spray and fluid interactions are thereby accounted for by a number of sub-models including the droplet aerodynamic drag, turbulence effects, evaporation, droplet oscillation and distortion, droplet breakup, collision and coalescence [7]. The properties of each computational particle at the time of injection are assigned by a Monte Carlo sampling technique with appropriate probability distribution. Different validation tests of these sub-models are reported by Sone et al. [159].

Table 7.1: Parameters of injection.

p_{gas}	T_{gas}	p_{inj}	T_{inj}	Fuel	Duration	Cone	DCone	Area of nozzle
5 bar	573.15 K	60 bar	363.15 K	C_8H_{18}	2.01 ms	40°	12°	$1.452 \cdot 10^{-3}$ cm^2

A qualitative comparison of spray penetration at $t = 1.0$ ms between numerical (instantaneous velocity flow fields, obtained using LES on the coarse (a) and the fine (c) grid) and experimental data (b) is shown in figure 7.2. Laser correlation velocimetry and phase Doppler anemometry measurements [175] were used to validate the KIVA-3V-LES code regarding the spray prediction.

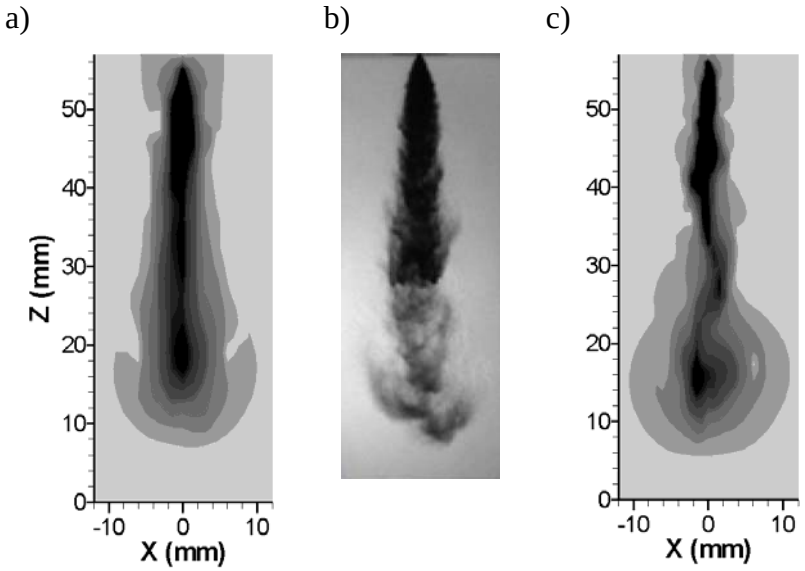

Figure 7.2: Comparison of fuel spray jet propagation at time 1.0 ms; a) Instantaneous velocity obtained on the coarse grid; b) Experimental data; c) Instantaneous velocity obtained on the fine grid.

Figure 7.3 shows a direct comparison of the spray jet shape between experimental data and mean LES data at $t = 1.0$ ms averaged over 20 samples (a) and the jet penetration (b), accordingly. A small delay of the spray jet penetration is visible in the LES in the time-range 0.2-0.8 ms, however the agreement is reasonable. Averaged velocity and mixture fraction fields at different times were obtained on the coarse and fine grid for the comparison of LES results with experimental data. Averaging was carried out over 30 samples for the results obtained on the coarse grid (figure 7.4 (a - c)) and over 20 samples for the results obtained on the fine grid (figure 7.4 (d - f)). The axial velocity of the spray can be found in a good agreement with experimental data for both cases.

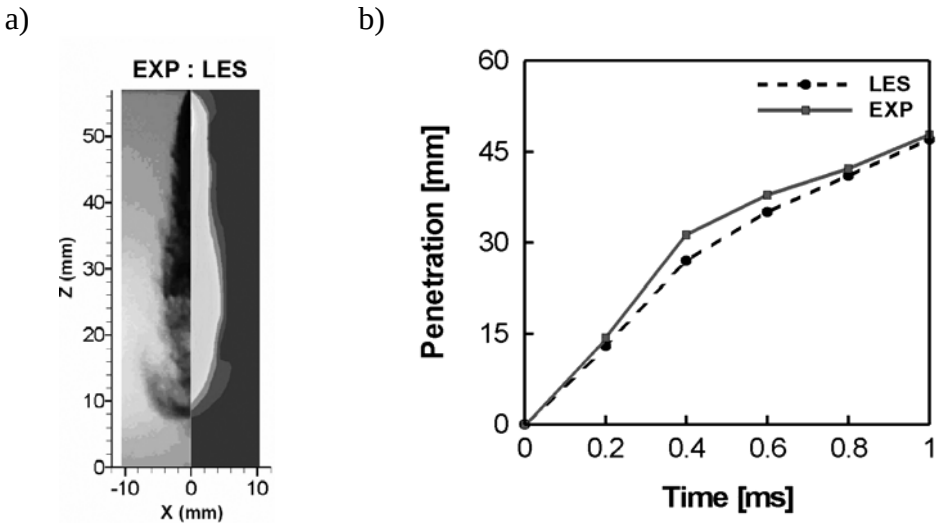

Figure 7.3: Comparison of the spray jet shape at $t = 1.0\,ms$ (a) and spray jet penetration (b) between experimental and LES data.

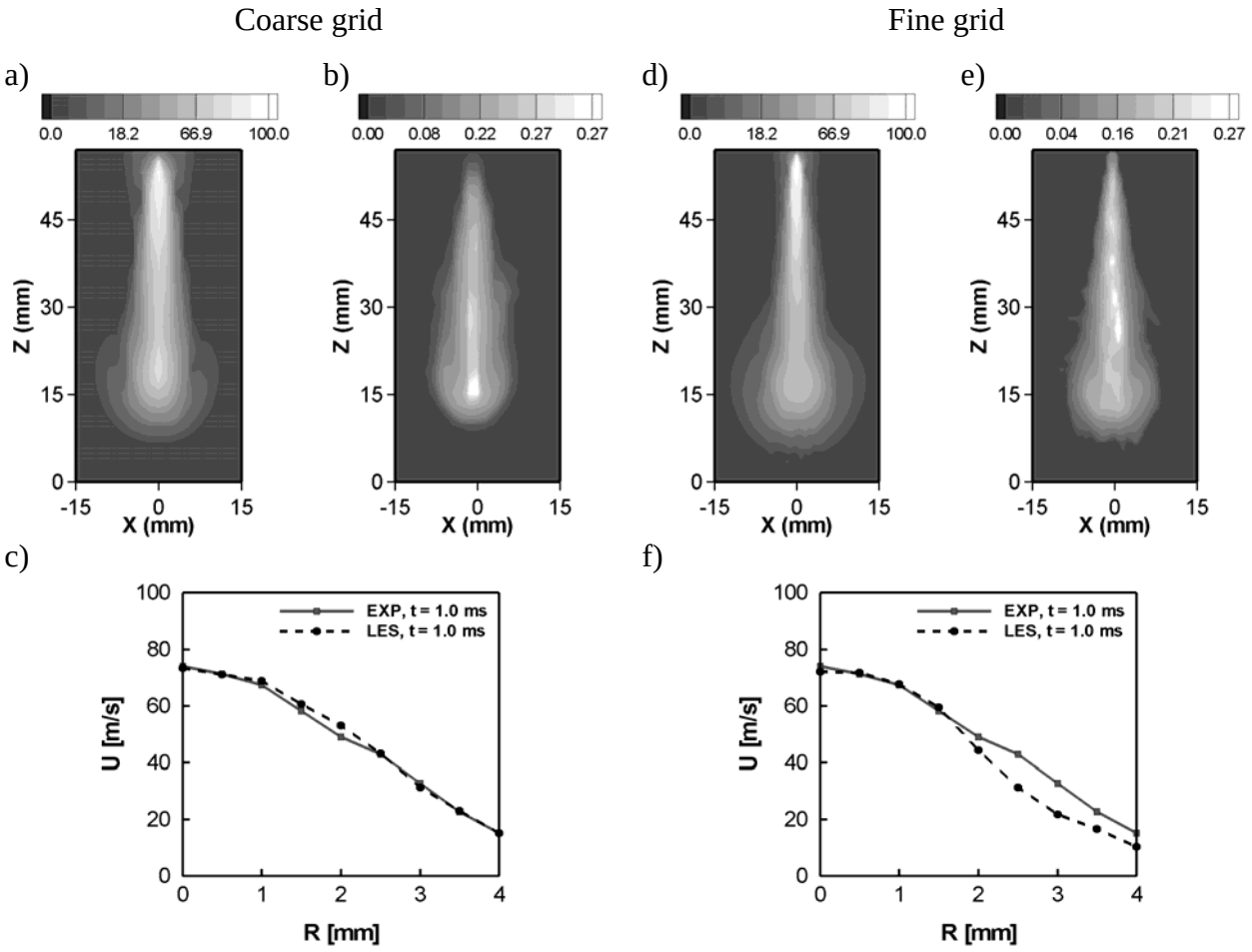

Figure 7.4: Averaged velocity flow field and mixture fraction at time 1.0 ms; **Coarse grid:** Velocity flow field (a) and mixture fraction (b), averaged over 30 samples. Axial velocities (c) of the spray at a distance of 20 mm away from the nozzle. **Fine grid:** Velocity flow field (e) and mixture fraction (f), averaged over 20 samples. Axial velocities (g) of the spray at a distance of 20 mm away from the nozzle.

It is important to define the initial and boundary conditions of the spray injection properly, since the simulation is especially sensitive to these parameters [111]. Nevertheless, the using of the parameters obtained from experiments does not always yield the best result in the simulation as it also depends on the model used. The spray bomb calculations offer the possibility to investigate the influence of each parameter of interest and calibrate the spray model using available experimental data.

7.2. Large eddy simulation of an IC-engine considering two-phase flow

The comparison of the velocity structure of in-cylinder flow and cycle-to-cycle variations for single- and two-phases flows is presented in this section. LES simulations of two-phase flow in the "BMBF" IC-engine (see chapter 5 for more details concerning geometry and operating parameters) have been carried out for 20 consecutive engine cycles in order to characterize the impact of velocity cycle-to-cycle fluctuations and the in-cylinder charge motion on the fuel spray injection and mixing processes. The injector has been located below the intake port symmetrical relative to the cross section with an installation angle of 107° relative to the vertical axis. The parameters of fuel injection for the spray simulation of IC-engine are listed in table 7.2. In order to highlight the impact of velocity cycle-to-cycle fluctuation on the processes of mixture preparation and interaction between spray jet and in-cylinder charge motion, the initial and boundary conditions for the spray injection have been kept identical for all considered engine cycles. Thereby, the identical fuel spray has been injected during every engine cycle into the combustion chamber and it interacts with the cycle-to-cycle velocity variations and the in-cylinder charge motion. As the properties of the injection are strictly reproducible, the interaction of the cyclic fluctuating flow with the fuel injection can be studied in detail. The opportunity to define initial and boundary conditions precisely and repeatably (applied here to the injector) is an indubitable advantage of CFD. Simulations allow to examine the processes of interest separated from other influencing factors. It should be also noted that the fuel history effects as well as the ignition processes are not considered here. The simulation of each new cycle starts from a fresh in-cylinder charge which does not contain residuals from the previous engine cycles. Ignition and combustion are kept beyond the scope of this work. Special emphasis has been put on a detailed consideration of characteristic criteria of fuel vapor cloud preparation and ignition conditions near the spark plug location. The discussion of the considered effects is conducted in terms of both mean and instantaneous quantities including mean and rms of velocity, turbulent kinetic energy $k = \frac{1}{2}(u'^2 + v'^2 + w'^2)$ and relative air-fuel ratio λ given by

$$\lambda = \frac{(air/fuel)_{actual}}{(air/fuel)_{stoichiometric}}. \tag{7.1}$$

Fuel-lean mixtures are characterized by $\lambda > 1$, for stoichiometric mixtures $\lambda = 1$ and for fuel-rich mixtures $\lambda < 1$. Isooctane (C_8H_{18}) in liquid phase has been used as a fuel. Material properties of isooctane are listed in table 7.3.

Table 7.2: Parameters of fuel injection.

Start of injection	293.4° (66.6° before TDC)
Injection duration	21.6°
Injection installation angle	107°
Injection mass flow rate	0.0076 kg/s
Possible ignition points	312°, 330° and 342°

Table 7.3: Material properties of isooctane [68].

Fuel	Formula	Phase	Molecular weight	$(A/F)_s$	$(F/A)_s$	Octane number
Isooctane	C_8H_{18}	Liquid	114.23	15.13	0.0661	100

7.2.1. Evolution of the mixture formation process in an air-guided DISI IC-engine

The structure of the in-cylinder flow together with the mean velocity flow field (left) and the sequence of the of mixture preparation (right) in different sections of the combustion chamber are presented in figures 7.5 and 7.6, respectively. The considered mean quantities were averaged over 20 engine cycles. The fuel spray jet interacts with the in-cylinder charge motion, especially with the dominant normal-tumble TR_y component. The evolution of the spray jet intrusion into the tumble flow is illustrated in figure 7.5 (left). At the initial stage (at $CA = 305° - 310°$) the spray jet shifts the large vertex to the right side of the combustion chamber. At the same time the process of fuel-air mixing, shown in figure 7.5 (right) by means of the relative air-fuel ratio λ, takes place. Near one of the possible ignition point at $CA = 312°$ the fuel vapour cloud reaches the spark plug zone (figure 7.5 (right), $CA = 310°$, 315°). At the end of injection, at $CA = 315°$, the injected fuel spray continues to spread into the combustion chamber, affecting the structure of normal-tumble motion. In consequence of the specific piston-bowl geometry which assists to maintain the tumble motion, the fuel jet passing through the combustion chamber disturbs but does not destroy the global charge motion. In fact the tumble motion gradually recuperates its own structure. A pronounced central vertex can for example be seen again at $CA = 345°$, see figure 7.7 (top).

The evolution of the fuel-air mixing process in a section perpendicular to the vertical axis is shown in figure 7.6. The streamlines together with the mean velocity flow fields are depicted on the left, the distribution of λ is shown on the right. The flow field during injection is characterized by the high velocity magnitude on the axis of the spray fuel jet. Directly after the end of injection the velocity decreases to the level observed for the single-phase flow. It should be also mentioned that the typical structure in the X-Y plane (observed for the single-phase flow) is destroyed by injection and does not rehabilitate itself as opposed to the normal-tumble structure. The flow structure in the X-Y plane at the end of the compression stroke is presented in figure 7.7 (bottom). It can be seen that the injected spray jet initiates two symmetric rotating flows at the intake side of the combustion chamber.

It is rather important to note that the fuel spray injection does not influence much the global averaged flow quantities such as TR_x, SR_z and kinetic energy. At the same time the injection process slightly decreases the intensity of normal-tumble motion (TR_y) compared to the single-phase flow, especially close to the TDC of the compression stroke. Taking into consideration the results obtained for the single-phase flow (see chapter 5, figure 5.23) it can be

concluded that the cycle-to-cycle variability as well as the character of evolution of the charge motion are determined by the structure of the single-phase flow. Figure 7.8 (left) shows average components TR_x, TR_y, SR_z of in-cylinder charge motion and kinetic energy for the two-phase flow starting from $CA = 290°$ till TDC. The standard deviation of these quantities is plotted in figure 7.8 (right). The pattern of change and the intensity of fluctuations are the same as the results obtained for the single-phase flow (see chapter 5, section 5.2.2 for more details). The normal-tumble motion is the predominant component of in-cylinder charge motion which appears during the intake stroke (it is typical for the considered type of direct injection combustion systems). During injection the normal-tumble motion is maintained by the specific piston-bowl configuration which plays a key role for supporting tumble at the end of compression stroke. Nevertheless, the intensity of normal-tumble monotone decreases as verging towards TDC of compression. The analysis of in-cylinder charge motion has shown that the intensity of sideways-tumble as well as swirl motion is very low (see figure 7.8). Therefore they are not considered any further.

7.2.2. Influence of cycle-to-cycle fluctuations on the mixing field

Figure 7.9 presents contour plots (top), cyclic variations (middle) and standard deviation (bottom) of velocity for single phase flow (a) and two-phase (b) flow at $CA = 315°$, respectively. The mixing field is shown in figure 7.9.c. The profiles were obtained along the white line marked “A” (see figure 7.9.c, top). The differences between the single-phase flow and the fuel spray injection case are well visible. As it was already mentioned above, at the end of compression stroke the velocity flow field in the combustion chamber for the undisturbed case is determined by a pronounced tumble motion. The flow structure for two-phase flow in this stage is much different and represents a superposition of the tumble flow and the fuel spray jet. Cyclic velocity fluctuations result in the cycle-to-cycle variations of mass fraction as depicted in figure 7.9.c. It has to be mentioned that the outlier curves for the single-phase flow (figure 7.9.a, middle) correspond to the outlier curves for the two-phase flow (figure 7.9 (b, c), middle).

It has been noted in chapter 5 that the normalized standard velocity deviation reaches the highest values at the center of the tumble motion (see figure 7.9.a, bottom). In the case of two-phase flow the highest value of standard deviation of velocity is observed on the tip of the fuel spray jet as shown in figure 7.9.b (bottom). At the time when the fuel jet reaches the center of tumble motion, there is a significant increase of cycle-to-cycle variations. Taking into account the fact that the center of in-cylinder charge motion is located near the spark plug at the ignition time, the cyclic fluctuations of velocity and mass fraction achieve their maximum values exactly in this most critical region.

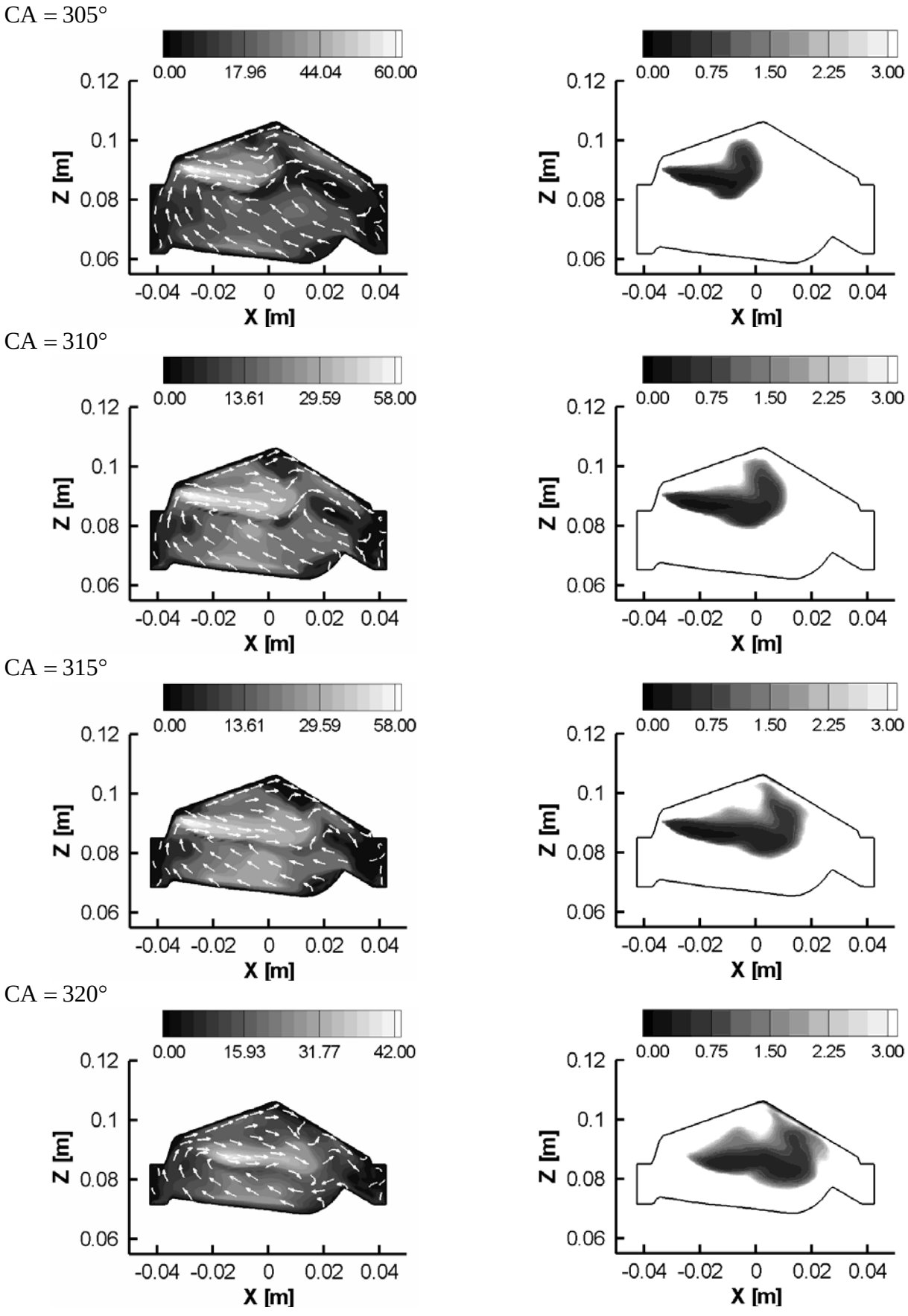

Figure 7.5: Evolution of the fuel spray penetration and mixing process in an air-guided DISI IC-engine. Streamlines and mean velocity flow field (left) in the cross section (X-Z plane) of the combustion chamber averaged over 20 engine cycles and relative air-fuel ratio λ (right).

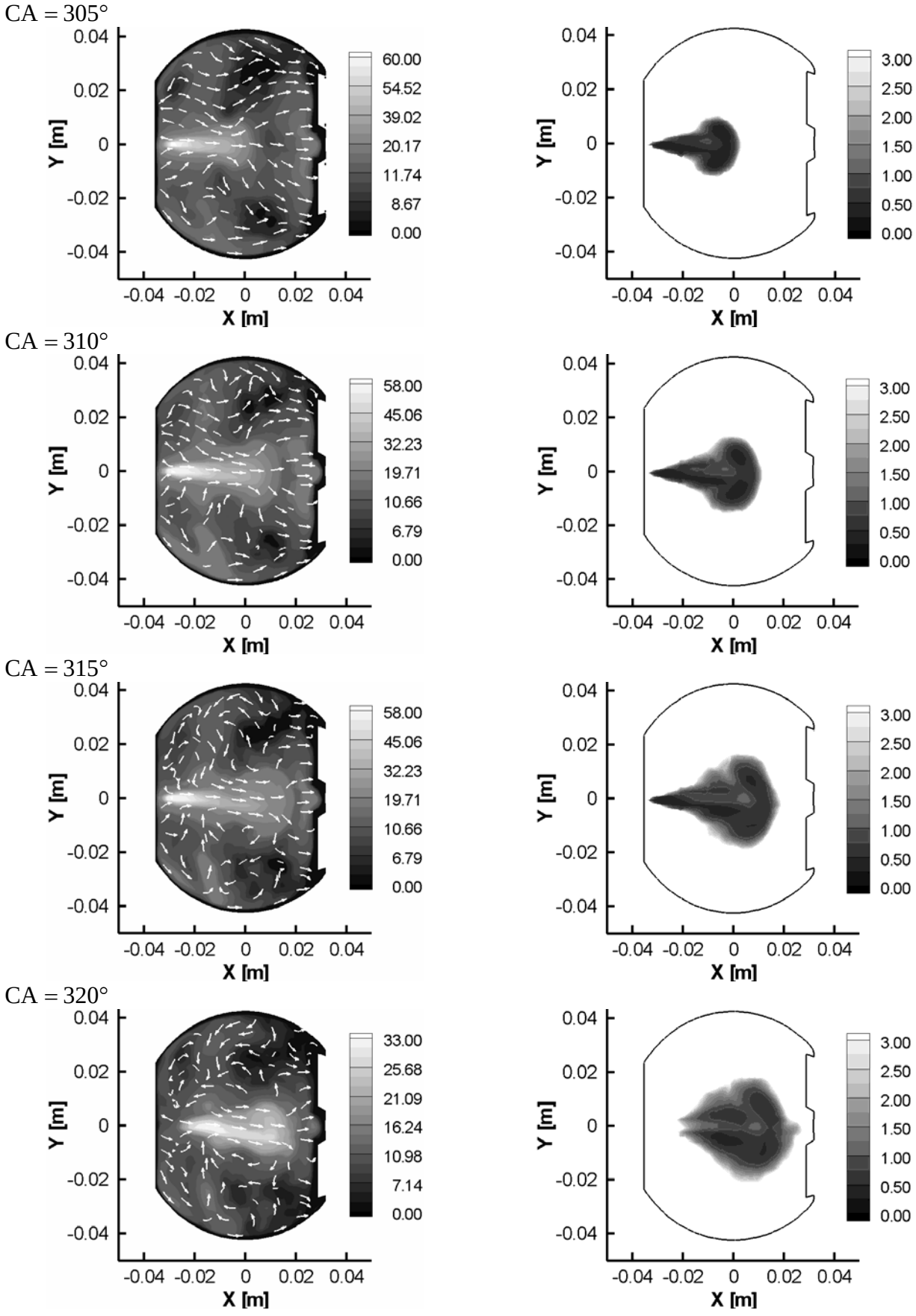

Figure 7.6: Evolution of the fuel spray penetration and mixing process in an air-guided DISI IC-engine. Streamlines and mean velocity flow field (left) in the X-Y plane, $z = 0.09\,\mathrm{m}$, averaged over 20 engine cycles and relative air-fuel ratio λ (right).

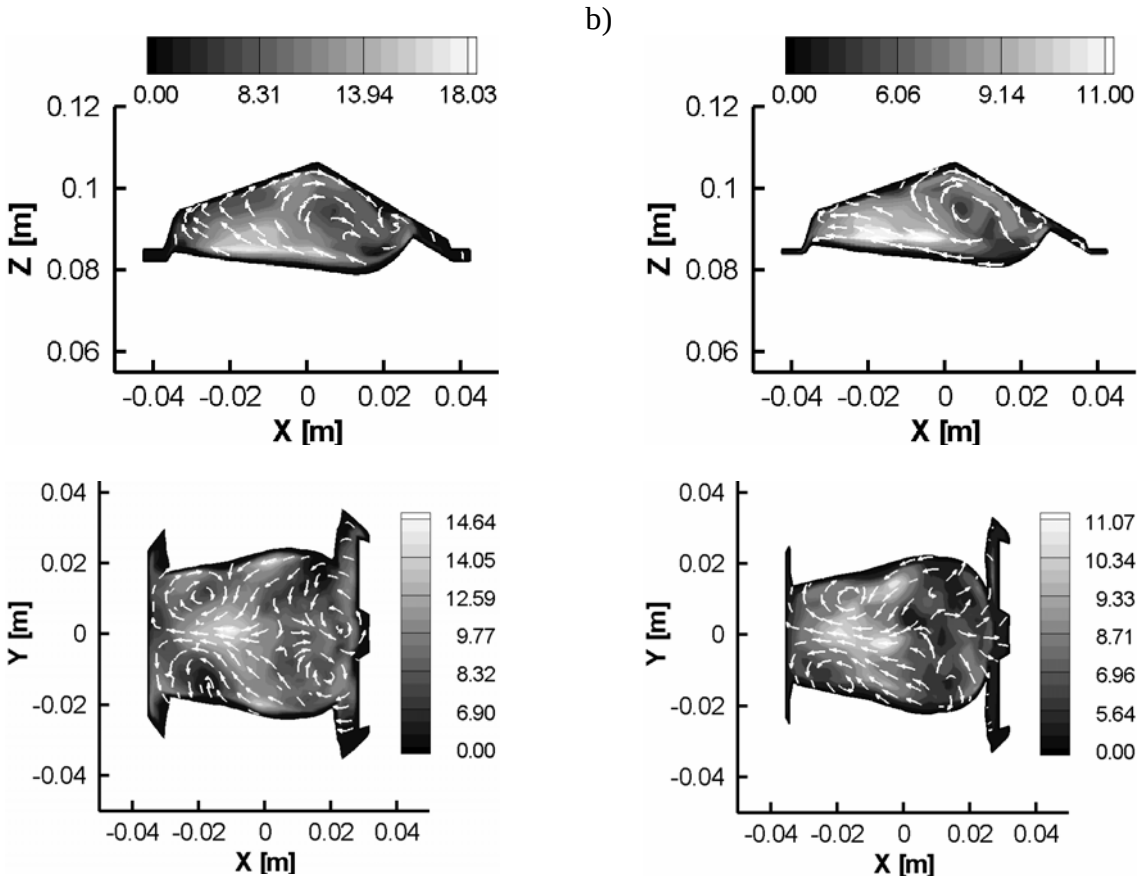

Figure 7.7: The structure of the flow and velocity flow field in the cross section (top) and in the X-Y plane (bottom) at the end of compression stroke at $CA = 345°$ (a) and at TDC, $CA = 360°$ (b) for two-phase flow.

The cycle-to-cycle changes of the shape of the fuel vapor clouds near the ignition point in the cross section of the combustion chamber are shown in figure 7.10. The relative air-fuel ratio λ is shown for 9 consecutive engine cycles. Figure 7.11 provides the cycle-to-cycle fluctuations of λ in the X-Y plane for the same engine cycles, accordingly. The range of λ in figures 7.10 - 7.11 corresponds to $\lambda = 0.85 - 1.15$ close to its stoichiometric value. Instantaneous fuel vapor clouds have pronounced asymmetrical shapes in the cross section of the combustion chamber as well as in the X-Y plane for consecutive cycles. The upper part of the fuel vapor cloud is at the spark plug level as shown in figure 7.10 while the cycle-to-cycle fluctuations appear mainly in the region directly below the spark plug.

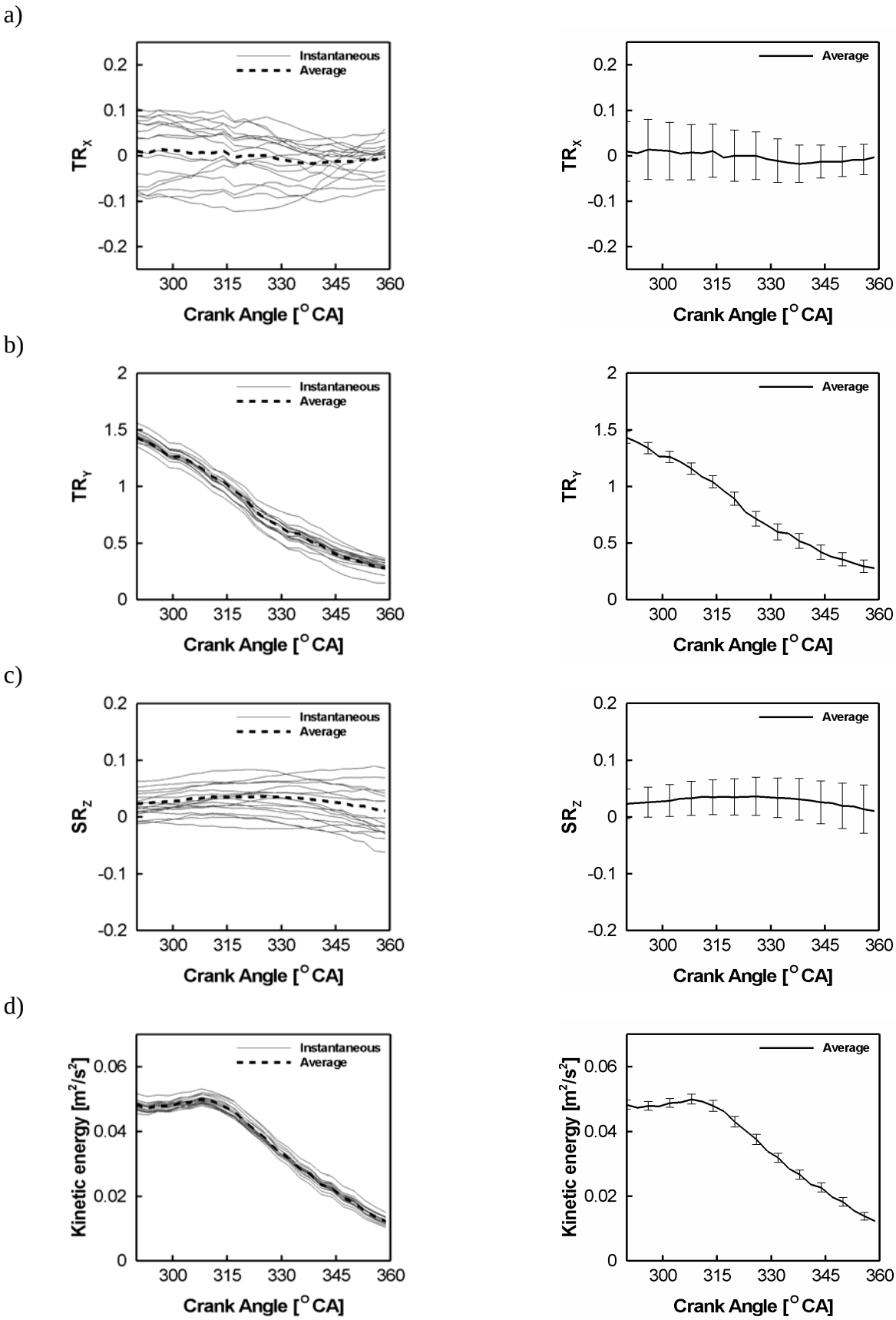

Figure 7.8: Instantaneous (right) and standard deviation (left) of globally averaged in-cylinder flow quantities for $CA = 290° - 360°$; a) Sideways-tumble TR_x; b) Normal-tumble TR_y; c) Swirl SR_z; d) Kinetic energy.

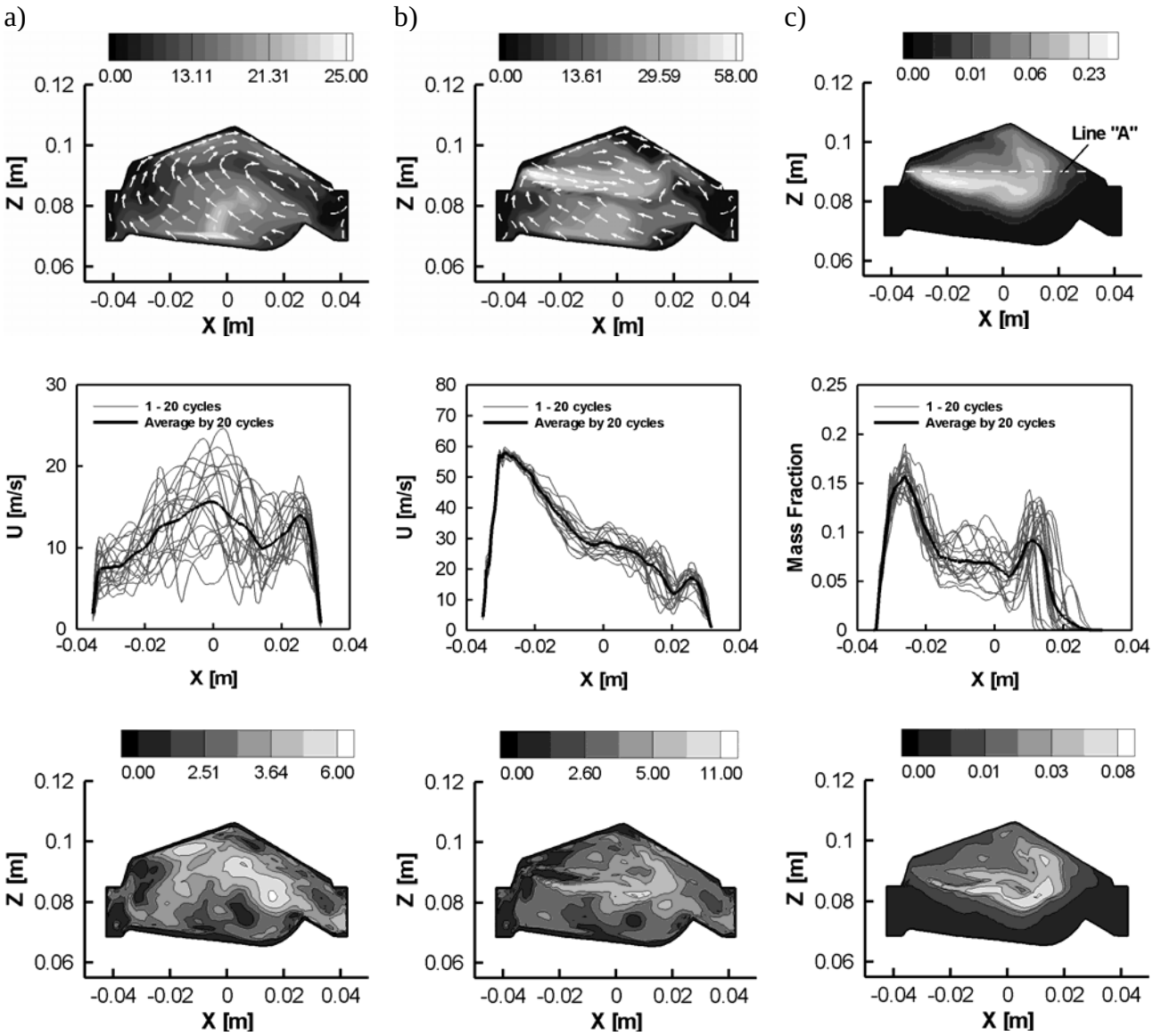

Figure 7.9: Contour plot (top), instantaneous profiles at $z = 0.09\,\mathrm{m}$ for 20 consecutive engine cycles (middle) and standard deviation of velocity and mass fraction (bottom) at $CA = 315°$; a) Velocity from single-phase flow; b) Velocity from two-phase flow; c) Mass fraction from two-phase flow.

The qualitative analysis of the intensity of cyclic fluctuations 7 mm below the spark plug is shown in figure 7.12.a for 20 engine cycles in terms of mean profile and standard deviation of λ. Three possible ignition points at $CA = 312°$, 330° and 345° are marked with dashed vertical rectangles, the flammable range of λ is shown with grey background. The mean profile and rms of velocity is plotted in figure 7.12.b. The inspection of the results reveals that at the first ignition point ($CA = 312°$) various states of fuel composition including fuel-lean, stoichiometric and fuel-rich mixtures are realized. However, at the other two ignition points ($CA = 330°$ and 345°) the fuel mixture is predominantly lean. As it has been mentioned above, the spray calculations are sensitive to the grid size. In contrast to spray bomb in the case of an engine simulation the grid size is more difficult to control and experimental data are required for validation. The obtained LES results of flow and mixture preparation can be found in a good agreement with available measured data [132] for the identical engine configuration at the same operation condition.

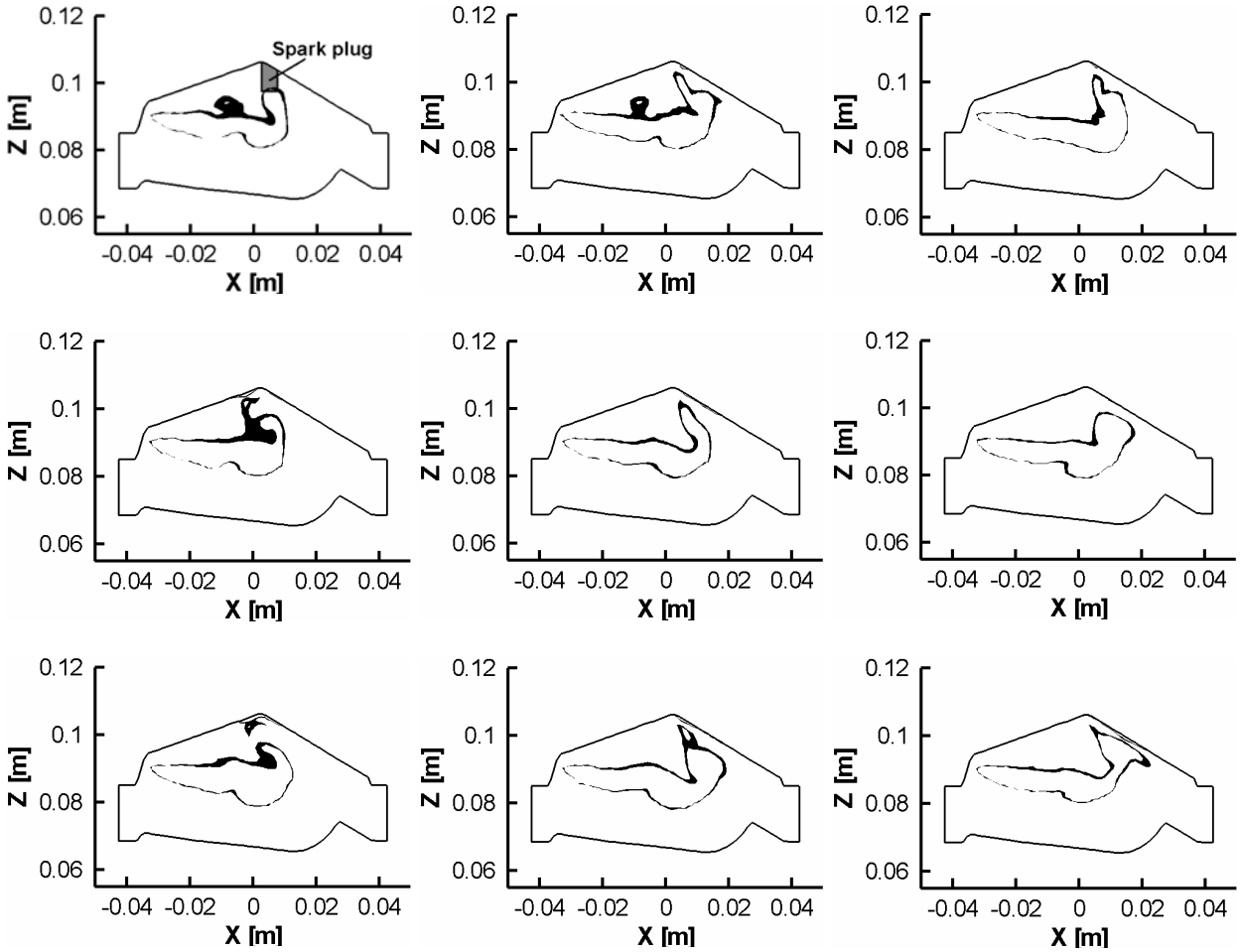

Figure 7.10: Cycle-to-cycle fluctuations of relative air-fuel ratio $\lambda = 0.85 - 1.15$ in the cross section (X-Z plane) of the combustion chamber for 9 consecutive engine cycles at $CA = 315°$.

7.2.3. Comparison of LES and RANS results

Figure 7.13 presents the comparison of the in-cylinder flow structure obtained by LES (a) and RANS (b) in the cross section of the combustion chamber at the end of the injection process at $CA = 315°$. Generally, both methods provide a good prediction of the mean flow structure with the same values of velocity magnitude and with eddies at the tip of the fuel spray jet. The inspection of the mean velocity profiles shown in figure 7.13.c reveals that a good coincidence of LES and RANS results is observed in prediction of the spray jet velocity for $x < 0.0\,\text{m}$ whereas significant differences can be observed for $x > 0.0\,\text{m}$. The effects of the application of LES and RANS to the prediction of the shape of the fuel vapor cloud are demonstrated in figure 7.14 (a, b) in the cross section of cylinder. The mean mass fraction profiles are depicted in figure 7.14 (c). The differences include the shape of the fuel vapor cloud, the location of the upper stoichiometric contour of the cloud and also the different spray jet penetration. The comparison of turbulent kinetic energy obtained by LES and RANS reveals that the maximal turbulent kinetic energy appears at the tip of the fuel spray jet in the LES case while RANS predicts its maximum near the area of the injector and on the bottom boundary of the jet (not shown here).

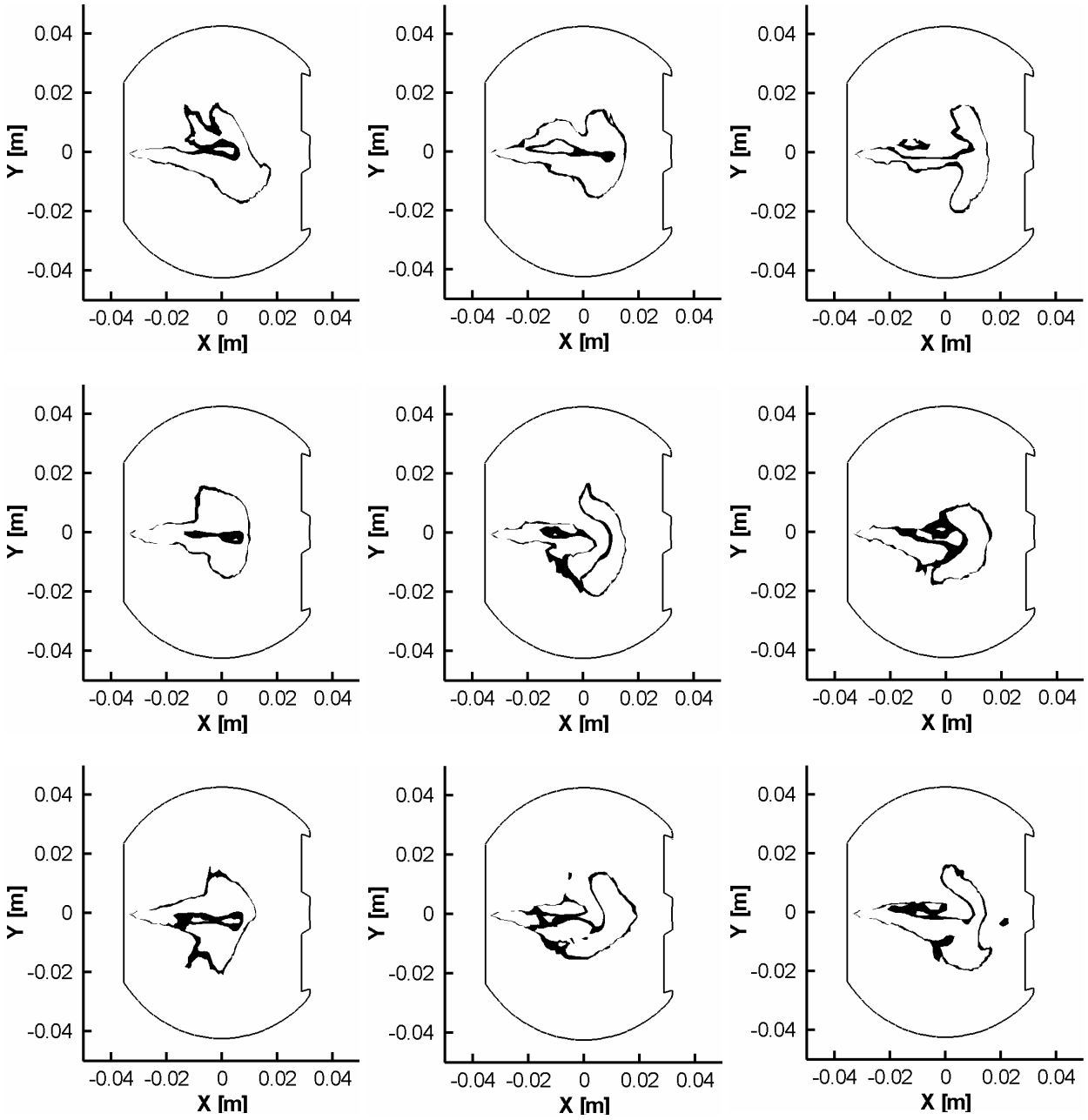

Figure 7.11: Cycle-to-cycle fluctuations of relative air-fuel ratio $\lambda = 0.85 - 1.15$ in the X-Y plane for 9 consecutive engine cycles at $CA = 315°$.

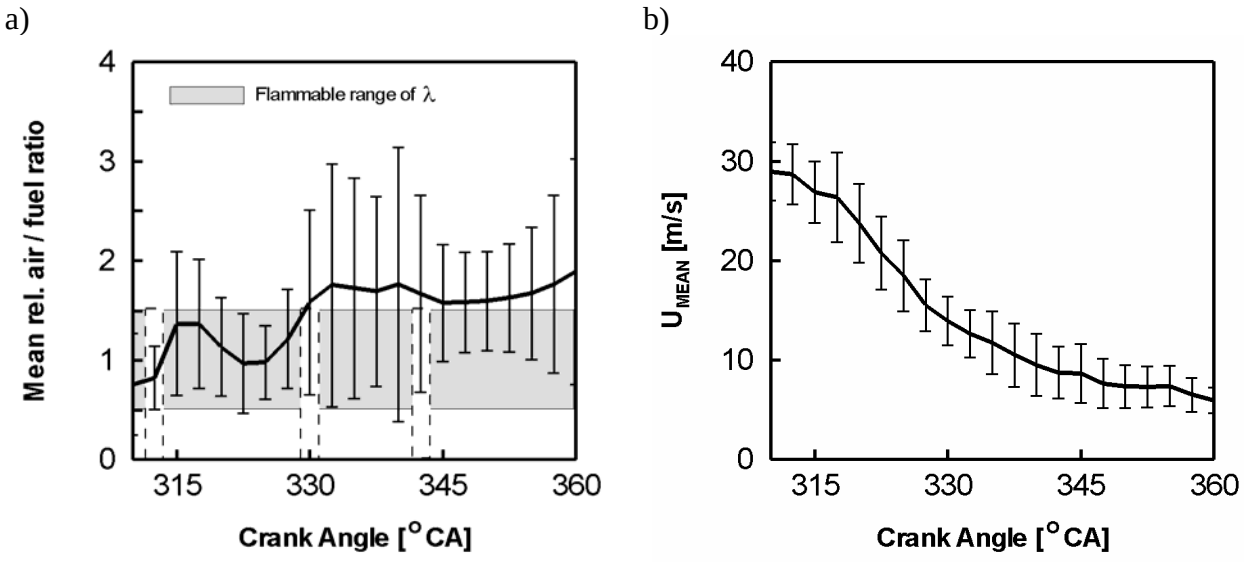

Figure 7.12: Mean profiles and standard deviation of relative air-fuel ratio λ (a) and velocity (b) near spark plug for 20 engine cycles, data correspond to a point 7 mm below the spark plug, the possible ignition points are at $CA = 312°$, 330° and 342°.

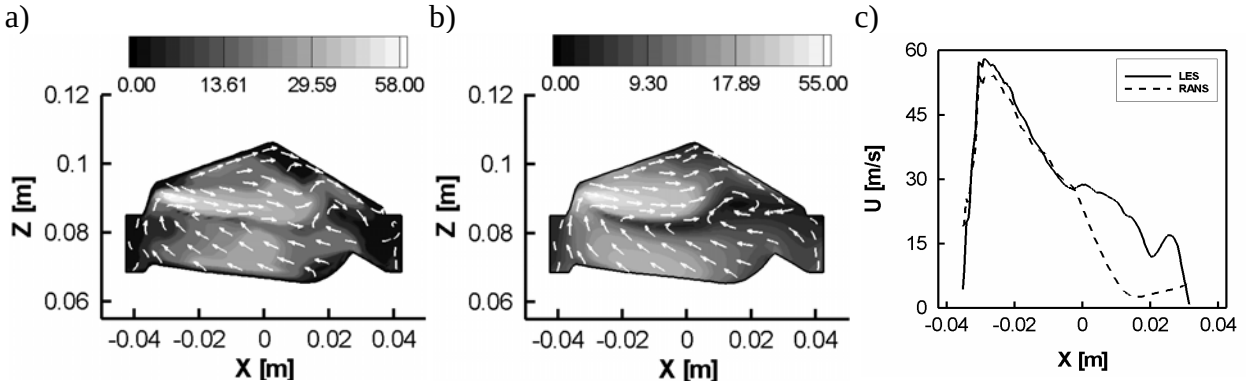

Figure 7.13: Streamlines and mean velocity flow field at $CA = 315°$ for LES (a) and RANS (b), mean velocity profiles (c).

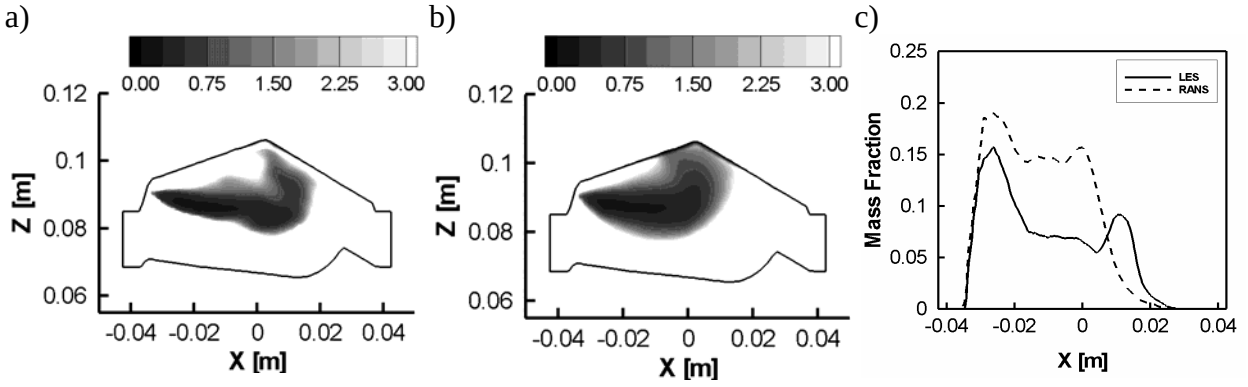

Figure 7.14: Relative air-fuel ratio λ and mean mass fraction profiles at $z = 0.09\,\text{m}$, $CA = 315°$; a) LES; b) RANS; c) Mean profiles of mass fraction.

7.3. Conclusions

The present chapter extends the investigation of the in-cylinder velocity cycle-to-cycle variations discussed in chapter 5 to the consideration of fuel spray injection and the air-fuel mixing processes. LES of two-phase flow in the "BMBF" engine has been carried out to calculate 20 consecutive engine cycles by using the KIVA-3V code. In order to assign the impact of cyclic variability on injection and mixture formation the fuel spray injection has been realized with identical initial conditions. The calibration of the standard KIVA-3V spray model was validated by a number of spray bomb benchmark cases which allowed adjusting the initial parameters of injection. The verification of the LES spray bomb results has been carried out by comparing with available measured data. Results have been found in a reasonable agreement with experimental data.

The effects of the velocity cycle-to-cycle fluctuations on the spray jet penetration, the fuel-air mixture preparation and the shape of the fuel vapor cloud close to the ignition point have been investigated in detail. In the case of two-phase flow the flow field in the combustion chamber is determined by a superposition of in-cylinder charge motion and fuel spray jet. As it was shown in chapter 5, the region with maximal intensity of velocity cyclic variations, i.e. the center of tumble motion, is directly located below the spark plug close to the ignition time. The interaction of the high speed fuel jet with the in-cylinder charge motion results in a significant increase in the intensity of the cyclic fluctuations in this crucial area. The same holds true for the turbulent kinetic energy, which reaches a maximum at the end of injection, e.g. close to the ignition point, with a value several times higher compared to the single-phase flow. Nevertheless, the effect of injection processes on the globally averaged in-cylinder flow quantities is negligible.

The consideration of a number of consecutive engine cycles demonstrates a clearly visible asymmetrical shape of the fuel vapor cloud. A lean fuel mixture is mostly found at the spark plug location for the considered ignition points under the given operating condition. Inflammable air-fuel mixtures lead to engine misfires which directly affect the work output and the vehicle driveability. These effects have to be considered in the development of modern DISI IC-engines.

Chapter 8

Conclusions

A parametric investigation of the cycle-to-cycle phenomena of in-cylinder flow in an air-guided DISI internal combustion engine has been done in the present work. The main goals are formulated in the following way:

1. The evaluation of the LES potential for modeling highly unsteady complex phenomena using the KIVA-3V code;

2. The detailed crank angle resolved investigation of the cycle-to-cycle fluctuations with regard to their magnitude and occurrence but also to their nature and possible origin in a realistic IC-engine configuration;

3. The characterization of the impact of cycle-to-cycle velocity fluctuations on the fuel spray injection processes and air-fuel mixture preparation.

The following strategy has been used in order to solve the formulated tasks:

1. RANS approach is not able to capture all features of interest hence, LES has to be applied. Since the access to the source code was an important part of this work, the well-known KIVA-3V code has been selected. The LES approach based on the classical Smagorinsky model has been implemented into KIVA-3V and the code has been validated by simulating the turbulent flow in a square duct configuration. Obtained LES results were found to be in a good agreement with available DNS and LES data.

2. LES is a statistical method therefore it needs a big number of samples to obtain good statistics. Simulation of one single engine cycle requires up to 1 week using a standard P4-3MHz CPU. Since a straightforward parallelization of KIVA-3V is impossible, a parallelization strategy based on variation of initial conditions has been developed, tested and applied to simulate up to 50 engine cycles for each configuration.

3. The examined air-guided DISI IC-engine represents a realistic four stroke direct spray injection engine with four canted valves, with asymmetric head and asymmetric piston crown. The in-cylinder flow is controlled by a variable charge motion system. The generation of a computational grid with a reasonable resolution was one of the most complicated, important and time consuming tasks of the present work. The only grid generation tool with an interface to KIVA-3V able to deal with complex geometries has been found to be ICEM CFD. Since the methodology of mesh generation using ICEM CFD for KIVA-3V was inaccessible, the common strategy of grid generation has been developed. A relatively fine computational mesh reflecting all geometrical features of the ”BMBF” IC-engine has been created and tested. Several auxiliary grids with different grid resolutions and geometry were also generated.

4. In connection with the complicated design features of the “BMBF” IC-engine several principal limitations of the KIVA-3V program were revealed. They were caused by the peculiarities of the block-structured grid and the ruling logic of the moving mesh. The

main problem was that KIVA-3V did not support the possibility to simulate a configuration where the piston crown moves into the head zone. A relatively simple strategy has been therefore developed to overcome this restriction.

5. In order to characterize the cycle-to-cycle fluctuations within the combustion chamber, LES calculations have been performed for up to 50 consecutive engine cycles. The analysis of the in-cylinder charge motion as well as the cycle-to-cycle phenomena included: 1) Consideration of the cyclic variations through the whole engine cycle (during intake, compression, expansion and exhaust strokes) in terms of mean and standard deviation of gas dynamics parameters; 2) Consideration of the variability of global in-cylinder charge motion. Reliability of obtained data has been justified by the comparison of LES obtained results with available experimental data; 3) The comparison of RANS and LES results has confirmed that in contrast to LES, the RANS approach is not able to capture the highly unsteady flow field in an IC-engine configuration.

6. It is meanwhile well recognized that LES is a well suited tool for the investigation and the design of internal combustion engines. However, a careful assessment of the simulation errors for LES application to such complex configurations is very important. In order to estimate the quality of the predicted results, several criteria published in the literature have been used. The statistical, modeling and numerical errors have been estimated. As a general guideline a mesh with grid size $\Delta \approx 1\,\mathrm{mm}$ seems to be the minimum requirement to represent the flow field with reasonable accuracy. In order to control the statistical errors it can be recommended to perform roughly 25 engine cycles in order to get mean velocities right and 50 cycles to ensure a good prediction of cyclic fluctuations. It was shown that the computational grid allows to resolve about 70%-90% of the turbulent kinetic energy. The amount of resolved turbulent kinetic energy is in the range of a well resolved LES.

7. Finally, LES of two-phase flow has been calculated for 20 consecutive engine cycles. Special attention was paid on the consideration of the influence of cycle-to-cycle velocity fluctuations on fuel spray jet penetration and processes of mixture preparation. The cyclic variability of air-fuel ratio relative to the stochiometric composition near the spark plug has been also taken into consideration.

The main conclusions can be summarized as following:

1. The obtained results justify the following definition of the cycle-to-cycle phenomena, given in the first chapter: *Cyclic fluctuations are non-repeatable statistically independent variations of gas-dynamics parameters which are induced by the turbulence nature of the flow*. It is shown that the cycle-to-cycle phenomena are directly linked to the turbulence and can not be considered separately from each other.

2. In the case of single-phase flow, the maximal intensity of cycle-to-cycle velocity variations in the combustion chamber is reached during the intake and compression strokes. At the end of compression stroke the highest intensity of cyclic fluctuations is found at the center of the in-cylinder tumble motion which is roughly located near the spark plug close to the ignition point. At the same time the examination of the expansion and exhaust strokes shows relatively low intensity of the cycle-to-cycle velocity fluctuations.

3. In the case of two-phase flow, the flow field in the combustion chamber is defined by a superposition of in-cylinder charge motion and injected fuel spray jet. This interaction results in a considerable increase of the intensity of cyclic velocity fluctuations. The analysis has shown a great impact of velocity cyclic variations on the air-fuel mixing processes as well as fuel jet penetration and forming of fuel vapor cloud in the area near the spark plug. A lean fuel mixture is mostly found at the spark plug location for the considered possible ignition points under the given operating condition. Inflammable air-fuel mixtures lead to engine misfires which directly affect the work output and the vehicle driveability. These effects have to be considered in the development of modern DISI IC-engines.

The results obtained in the framework of the present study allow a detailed characterization of the flow field pattern within the combustion chamber of a realistic air-guided IC-engine. The results can represent a basis for further systematical analysis of the complex and manifold phenomenon as cycle-to-cycle fluctuations and can be exploited for the investigation of ignition and combustion processes, detailed characterization of combustion variability, influence of cyclic variations on soot formation and emissions. For this purpose, a consideration of appropriate combustion model is necessary.

References

[1] Adomeit P., Gieger J., Herrmann H.O., Ballauf J., Becker M., Vogt B., Greis A.: Laseroptical diagnostics and numerical analysis of modern DI-combustion systems. 5th Int. Symposium for Combustion Diagnostics (ed. Ziegler, P.), Baden-Baden, 2002.

[2] Adomeit P., Lang O., Vogt B.: Computational analysis of flow and mixture formation in DISI engines. 12th International Multidimensional Engine Modeling User's Group Meeting, March 3, 2002.

[3] Akula R.K.: Study of the performance of different subgrid-scale models and large eddy simulation of premixed combustion. PhD thesis, Fachbereich Maschinenbau, Technische Universität Darmstadt, 2006.

[4] Aleiferis P.G., Hardalupas Y., Taylor A.M.K.P., Ishii K., Urata Y.: Cyclic variations of fuel-droplet distribution during the early intake stroke of a lean-burn stratified-charge spark-ignition engine. Experiments in Fluids, Vol. 39, No. 5, pp. 789-798, 2005.

[5] Amr A., Cazzoli G., Kong S.C., Reitz R., Mongomery C.: Improvement in computational efficiency for HCCI engine modelling by using reduced mechanisms and parallel computing. Central State Section Meeting, 2003.

[6] Amsden A.A., Butler T.D., O'Rourke P.J., Ramshaw J.D.: Kiva: A comprehensive model for 2-D and 3-D engine simulations. SAE Technical Papers, 850554, 1985.

[7] Amsden A.A., O'Rourke P.J., Butler T.D.: KIVA-II: A computer program for chemically reactive flows with sprays. Tech. Rep. LA-11560-MS, Los Alamos National Laboratory, 1989.

[8] Amsden A.A.: KIVA-3: A KIVA Program with block-structured mesh for complex geometries. Tech. Rep. LA-12503-MS, Los Alamos National Laboratory, 1993.

[9] Amsden A.A.: KIVA-3V: A block-structured kiva program for engines with vertical or canted valves. Tech. Rep. LA-13313-MS, Los Alamos National Laboratory, 1997.

[10] Amsden A.A.: KIVA-3V, Release 2, Improvements to KIVA-3V. Tech. Rep. LA-13608-MS, Los Alamos National Laboratory, 1999.

[11] Ansys ICEM CFD, 2006. http://www.ansys.com/products/icemcfd.asp

[12] Assanis D.N., Hong S.J., Nishimura A., Papageorgakis G., Vanzieleghem B.: Studies of spray breakup and mixture stratification in a gasoline direct injection engine using KIVA-3V. Journal of Engineering for Gas Turbines and Power-Transactions of the Asme, Vol. 122, No. 3, pp. 485-492, 2000.

[13] Atzler F.: On the future of the piston engine with internal combustion. Mari Curie Fellowship Conference, 16th – 19th of May, at Profactor GmbH, Steyr, Austria, 2001.

[14] Ball J.K.: Cycle-by-cycle variation in spark ignition internal combustion engines. PhD thesis, Department of Engineering Science, Merton College, Oxford, 1998.

[15] Bates St.C.: Flame imaging studies of cycle-by-cycle combustion variation in a SI four-stroke engine. SAE Technical Papers: 892086, 1989.

[16] Baumgarten C.: Mixture formation in internal combustion engine. Springer-Verlag Berlin-Heidelberg, 2006.

[17] Belardini P., Bertoli C., DeMarino P., Avolio G.: A new parallel numerically improved KIVA3V program for diesel combustion computations. The Engine Research Center, University of Wisconsin-Madison, 2004.

[18] Berselli L.C., Iliescu T., Layton W.J.: Mathematics of large eddy simulation of turbulent flows. Springer, 2005.

[19] Bird G.A.: Molecular gas dynamics (Russian translation). Mir, Moscow, 1981.

[20] Bird G.A.: Molecular gas dynamics and the direct simulation of gas flows. Oxford University Press, 1994.

[21] Bird R.B., Stewart W.E., Lightfoot E.N.: Transport phenomena, John Wiley and Sons, 1960.

[22] Bogdanov A.V., Grishin I.A., Khanlarov G.O., Lukianov G.A., Zakharov V.V.: Algorithm of two-level parallelization for direct simulation Monte Carlo of unsteady flows in molecular gasdynamics. Lecture Notes in Computer Science, Vol.1593, Springer-Verlag, Berlin-Heidelberg-New-York, 1999.

[23] Bonnet J.P., Moser R.D., Rodi W.: AGARD advisory report 345. A selection of test cases for the validation of large-eddy simulations of turbulent flows. Advisory Group for Aerospace Research & Development, 7 Rue Ancelle, 92200 Neuilly-sur-Seine, France, 1998.

[24] Bracco F.N.: Modeling of engine sprays. SAE Paper 850394, 1985.

[25] Bradshaw P.: An Introduction to turbulence and its measurement. Pergamon Press, London, 1976.

[26] Bykov N.Y., Lukianov G.A.: Parallel direct simulation Monte Carlo of non-stationary rarefied gas flows at the supercomputers with parallel architecture. Institute for High Performance Computing and Data Bases, Vol.5-97., 1997.

[27] Castagne M., Dumas J. P., Henriot S., Pierre P.: Use of advanced tools for the analysis of gasoline direct injection engines. Oil & Gas Science and Technology-Revue De L Institut Francais Du Petrole, Vol. 58, No. 1, pp. 79-100, 2003.

[28] CD-adapco: http://www.cd-adapco.com/

[29] Celik I., Yavuz I., Smirnov A., Smith J., Amin E., Gel A.: Prediction of in-cylinder turbulence for IC engines. Combustion Science and Technology, Vol. 150, pp. 1-30, 2000.

[30] Celik I., Yavuz I., Smirnov A.: Large eddy simulations of in-cylinder turbulence for IC-engines: a review. Int. Journal of Engine Research, Vol. 2, No. 2, 2001.

[31] Celik I., Klein M., Freitag M., Janicka J.: Assessment measures for URANS/DES/LES: an overview with applications. Journal of Turbulence, Vol. 7, No. 48, pp. 1-27, 2006.

[32] Celik I. B., Cehreli Z.N., Yavuz I.: Index of resolution quality for large eddy simulations. Journal of Fluids Engineering-Transactions of the Asme, Vol. 127, No. 5, pp. 949-958, 2005.

[33] Center Combustion Engine Research: Annual Report. Chalmers University of Technology, Sweden, 2005.

[34] Chryssakis C.A.: Modeling gasoline sprays emerging from high-pressure swirl injectors for DISI engines. Dissertation, Mechanical Engineering, University of Michigan, 2002.

[35] Correa Ch.: Combustion simulation in diesel engines using reduced reaction mechanisms. PhD thesis, Combined Faculties for the Natural Sciences and for Mathematics of the Rupertus Carola University of Heidelberg, Germany, 2000.

[36] de Risi A., Donateo T., Laforgia D.: Theoretical investigation on variable-density sprays. Atomization and Sprays, Vol. 12, No. 1-3, pp. 329-358, 2002.

[37] Devesa A., Moreau J., Poinsot T., Helie J.: Large eddy simulations of jet / tumble interaction in a GDI model engine flow. SAE International, 2004-01-1997, 2004.

[38] Devesa A., Moreau J., Helie J., Faivre V., Poinsot T.: Initial conditions for large eddy simulations of piston engine flows. Computers & Fluids, Vol. 36, No. 4, pp. 701-713, 2007.

[39] Dilthey J., Pischinger S.: Zyklische Schwankungen beim direkteinspritzenden Ottomotor. Workshop, Turbulenz in der Energietechnik, RWTH Aachen, 2004.

[40] Druault P., Guibert P., Alizon F.: Use of proper orthogonal decomposition for time interpolation from PIV data. Application to the cycle-to-cycle variation analysis of in-cylinder engine flows. Experiments in Fluids, Vol. 39, pp. 1009-1023, 2005.

[41] Dugué V., Veynante D., Gauchet N.: Applicability of large eddy simulation to the fluid mechanics in a real engine configuration by means of an industrial code. SAE Technical Papers, 2006-01-1194, 2006.

[42] Dukowicz J.K.: A particle-fluid numerical-model for liquid sprays. Journal of Computational Physics, Vol. 35, No. 2, pp. 229-253, 1980.

[43] Ewald J., Freikamp F., Peters N.: Modellierung und Simulation der zyklischen Scgwankungen der motorischen Verbrennung mittels VLES Turbulenzmodellen und dem

Flamelet Ansatz zur Verbrennungsmodellierung. BMBF Workshop, Turbulenz in der Energietechnik, Darmstadt, 2005.

[44] Fischer J., Kettner M., Nauwerck A., Pfeil J., Spicher U.: Influence of an adjustable tumble-system on in-cylinder air motion and stratification in a gasoline injection engine. SAE Technical Paper Series, 2002-01-1645, 2002.

[45] Fischer J., Spicher U.: Experimentelle Untersuchung zyklischer Schwankungen der Verbrennung im Hinblick auf Reduzierung der Motor-Rohemissionen bei Ottomotoren mit Benzin-Direkteinspritzung. Programm Lebensgrundlage Umwelt und ihre Sicherung (BWD 21012), 2004.

[46] Freitag M., Klein M.: Direct numerical simulation of a recirculating, swirling flow. Flow Turbulence and Combustion, Vol. 75, No. 1-4, pp. 51-66, 2005.

[47] Freitag M., Klein M.: An improved method to assess the quality of large eddy simulations in the context of implicit filtering. Journal of Turbulence, Vol. 7, No. 40, pp. 1-11, 2006.

[48] Freitag M.: On the simulation of premixed combustion taking into account variable mixtures. PhD thesis, Fachbereich Maschinenbau, Technische Universität Darmstadt, 2007.

[49] Frohn A., Roth N.: Dynamics of droplets. Springer, 2000.

[50] Fuchs T.R., Rutland C.J.: Intake flow effects on combustion and emissions in a diesel engine. SAE Technical Papers, 980508, 1998.

[51] Fujikawa T., Nomura Y., Hattori Y., Kobayashi T., Kanda M.: Analysis of cycle-by-cycle variation in a direct injection gasoline engine using a laser-induced fluorescence technique. International Journal of Engine Research, Volume 4, No. 2, pp. 143-153(11), 2003.

[52] Funk C., Sick V., Reuss D.L., Dahm W.J.A.: Turbulence properties of high and low swirl in-cylinder flows. Society of Automotive Engineers, 2002-01-2841, 2002.

[53] Funk C.O.: An in-depth comparison of experimental and computational turbulence parameters for in-cylinder engine flows. PhD thesis, The University of Michigan, 2005.

[54] Germano M., Piomelli U., Moin P., Cabot W. H.: A dynamic subgrid-scale eddy viscosity model. Physics of Fluids a-Fluid Dynamics, Vol. 3, No. 7, pp. 1760-1765, 1991.

[55] Golovitchev V., Nordin N., Jarnicki R., Chomiak J.: 3-D diesel spray simulations using a new detailed chemistry turbulent combustion model. SAE Paper, 2000-01-1891, 2000.

[56] Golovitchev, V.I., Nordin, N., Detailed chemistry sub-grid scale model of turbulent spray combustion for the KIVA code, Paper 99-ICE-237, ICE-Vol. 33-3, pp.17-25, 1999.

[57] Goryntsev D., Klein M., Janicka J.: LES der Strömung und Mischung in einem direkteinspritzenden Ottomotor. BMBF Workshop, Turbulenz in der Energietechnik, RWTH Aachen, 16. Juli 2004.

[58] Goryntsev D., Klein M., Janicka J.: Charakterisierung der zyklischen Schwankungen in einem direkteinspritzenden Ottomotor mittels der Grobstruktursimulation. BMBF Workshop, Turbulenz in der Energietechnik, Darmstadt, 2005.

[59] Goryntsev D., Stein O., Klein M., Janicka J.: characterization of cyclic fluctuations of the in-cylinder flow field of a direct injection SI engine using large eddy simulation. 7th International Congress: Engine Combustion Process, Munich, Germany, 2005.

[60] Goryntsev D., Klein M., Janicka J.: Large eddy simulation of cycle-to-cycle variations in a realistic direct injection SI Engine. 8th International Congress: Engine Combustion Process, Munich, Germany, 2007.

[61] Goryntsev D., Klein M., Sadiki A., Janicka J.: Large eddy simulation of fuel-air-mixing in a direct injection SI engine. Fifth International Symposium on Turbulence and Shear Flow Phenomena, Vol. 2, pp. 879-884, 2007.

[62] Goryntsev D., Klein M., Sadiki A., Janicka J.: LES of influence of cyclic variations on fuel-air-mixing and combustion in a DISI engine. 23. Deutscher Flammentag, Verbrennung und Feuerung, Berlin, 12. und 13. September, pp. 265-270, 2007.

[63] Graf M., Aymanns R., Vogt B., Fricke F., Pischinger S.: Zyklische Schwankungen beim direkteinspritzenden Ottomotor. BMBF Workshop, Turbulenz in der Energietechnik, RWTH Aachen, 2005.

[64] Guzzella L., Onder C.: Introduction to modeling and control of internal combustion engine systems. Springer Verlag, Berlin, 2004.

[65] Haworth D. C.: Large-eddy simulation of in-cylinder flows. Oil & Gas Science and Technology-Revue De L Institut Francais Du Petrole, Vol. 54, No. 2, pp. 175-185, 1999.

[66] Haworth D. C., Jansen K.: Large-eddy simulation on unstructured deforming meshes: towards reciprocating IC engines. Computers & Fluids, Vol. 29, No. 5, pp. 493-524, 2000.

[67] Heywood J. B.: Fluid motion within the cylinder of internal-combustion engines - the 1986 Freeman Scholar Lecture. Journal of Fluids Engineering-Transactions of the Asme, Vol. 109, No. 1, pp. 3-35, 1987.

[68] Heywood J.B.: Internal combustion engine fundamental. McGraw-Hill International Editions, New York, 1988.

[69] Hill S.St., Asadamongkon P., Lee K.C.: A study of turbulence and cyclic variation levels in internal combustion engine cylinders. 10th International Symposium on Applications of Laser Techniques to Fluid Mechanics, Lisboa, 10-13 July, 2000.

[70] Hinze J. O.: critical speeds and sizes of liquid globules. Applied Scientific Research Section Mechanics Heat Chemical Engineering Mathematical Methods, Vol. 1, No. 4, pp. 273-288, 1949.

[71] Hinze J.O.: Appl. Sci. Research, Vol. 1, 541, 1948.

[72] Hinze J.O.: Turbulence. McGraw-Hill, New-York, 1956.

[73] Hirt C. W., Amsden A. A., Cook J. L.: Arbitrary Lagrangian-Eulerian computing method for all flow speeds. Journal of Computational Physics, Vol. 14, No. 3, pp. 227-253, 1974.

[74] Hoffmann G.: Engineering application of large eddy simulation to turbulent free and wall-bounded shear layers. Von Karman Institute for Fluid Dynamics, 1995.

[75] Hong C. W., Tarng S. D.: In-cylinder tumble flow field measurements and predictions. Journal of Engineering for Gas Turbines and Power-Transactions of the Asme, Vol. 123, No. 1, pp. 139-145, 2001.

[76] Hong S., Wooldridge M.S., Im H.G., Assanis D.N., Kurtz E.: modeling of diesel combustion, soot and NO emissions based on a modified eddy dissipation concept. Combustion Science and Technology, 2006, submitted, 2006.

[77] Hu B., Rutland C. J.: Flamelet modeling with LES for diesel engine simulations. SAE Technical Paper Series, 2006-01-0058, 2006.

[78] Huijnen V., Somers L. M. T., Baert R. S. G., de Goey L. P. H., Olbricht C., Sadiki A., Janicka J.: Study of turbulent flow structures of a practical-steady engine head flow using large-eddy simulations. Journal of Fluids Engineering-Transactions of the Asme, Vol. 128, No. 6, pp. 1181-1191, 2006.

[79] Inagaki M.: Large eddy simulation as a powerful engineering tool for predicting complex turbulent flows and related phenomena. R&D Review of Toyota CRDL, Vol.39, No. 1, 2004.

[80] INVENT Computing GmbH: FASTEST-3D-CFD-Code, Handbuch. Schottkystr. 10, D-91058 Erlangen, in Kooperation mit dem Lehrstuhl für Strömungsmechanik (LSTM), Erlangen, zweite Auflage, 1997.

[81] Kempf A., Klein M., Janicka J.: Efficient generation of initial- and inflow-conditions for transient turbulent flows in arbitrary geometries. Flow Turbulence and Combustion, Vol. 74, No. 1, pp. 67-84, 2005.

[82] Kim Y., Lee S.H., Cho N.: Effect of air motion on fuel spray characteristics in a gasoline direct injection engine. SAE Technical Paper Series, 1999-01-0177, 1999.

[83] Klein A., Sadiki A., Janicka J.: A digital filter based generation of inflow data for spatially developing direct numerical or large eddy simulations. Journal of Computational Physics, Vol. 186, No. 2, pp. 652-665, 2003.

[84] Klein M.: Direkte Numerische Simulation des primären Strahlzerfalls in Einstoffzerstäuberdüsen. PhD thesis, Fachbereich Maschinenbau, Technische Universität Darmstadt, 2003.

[85] Klein M., Kempf A., di Mare L., Janicka J.: On the artificial generation of inlet and initial data for unsteady turbulent flow simulation. 2004.

[86] Klein M.: An attempt to assess the quality of large eddy simulations in the context of implicit filtering. Flow Turbulence and Combustion, Vol. 75, No. 1-4, pp. 131-147, 2005.

[87] Kolmogorov A.N.: The local structure of turbulence in incompressible viscous fluids for very large Reynolds numbers. C. r. Acad. Sci USSR, 30, 301-305, in Russian, 1941.

[88] Kolmogorov A.N.: Dissipation of energy in locally isotropic turbulence. C. r. Acad. Sci USSR, 32, 19-21, in Russian, 1941.

[89] Korolev M., Marov Y., Shorov Y., Aspnas M.: An implementation of Monte-Carlo weighting method on multiprocessor systems. Reports of Computer Schience & Mathematics, Abo Akademy, Ser. A, No. 125, 1991.

[90] Kutlar O.A., Arslan H., Calik A.T.: Methods to improve efficiency of four stroke, spark ignition engines at part load. Energy Conversion and Management, Vol. 46, No. 20, pp. 3202-3220, 2005.

[91] Launder B.E., Spalding D.B.: Mathematical models of turbulence. Academic Press, New York, 1972.

[92] Lee E., Park J., Huh K.Y. , Choi J., Bae C.: Simulation of fuel/air mixture formation for heavy-duty liquid phase LPG injection (LPLI) engines. SAE Technical Papers, 2003-01-0636, 2003.

[93] Lee K., Bae C., Kang K.: The effects of tumble and swirl flows on flame propagation in a four-valve SI engine. Applied Thermal Engineering, Vol. 27, No. 11-12, pp. 2122-2130, 2007.

[94] Lesieur M., Metais O., Comte P.: Large-eddy simulations of turbulence. Cambridge University Press, Cambridge, 2005.

[95] Li Y., Liu S., Shi S. X., Feng M., Sui S.: An investigation of in-cylinder tumbling motion in a four-valve spark ignition engine. Proceedings of the Institution of Mechanical Engineers Part D-Journal of Automobile Engineering, Vol. 215, No. D2, pp. 273-284, 2001.

[96] Libby P.A.: Introduction to turbulence. Taylor and Francis, London, 1996.

[97] Lilly D. K.: A proposed modification of the Germano-subgrid-Scale closure method. Physics of Fluids a-Fluid Dynamics, Vol. 4, No. 3, pp. 633-635, 1992.

[98] Liu A.B., Mather D., Reitz R.D.: Modeling the effects of drop drag and breakup on fuel sprays. SAE Technical Paper Series, 930072, 1993.

[99] Lyon D.: Knock and cyclic dispersion in a spark ignition engine, petroleum based fuels and automotive applications. I. Mech. E. Conf. Proc. MEP, London, 1986.

[100] Maltsev A.: Towards the development and assessment of complete CFD models for the simulation of stationary gas turbine combustion processes. PhD thesis, Fachbereich Maschinenbau, Technische Universität Darmstadt, 2004.

[101] Masahiro O., Tetsuya T.: On the parallel processing of direct simulation Monte Carlo method. Proceedings of the 8th NAL Symposium on Aircraft Computational Aerodynamics, pp. 39-44, 1990.

[102] Matthey Johnson: Emission control technologies, 2007. http://ect.jmcatalysts.com

[103] Meneveau C., Lund T. S., Cabot W. H.: A Lagrangian dynamic subgrid-scale model of turbulence. Journal of Fluid Mechanics, Vol. 319, pp. 353-385, 1996.

[104] Meneveau C., Katz J.: Scale-invariance and turbulence models for large-eddy simulation. Annual Review of Fluid Mechanics, Vol. 32, pp. 1-32, 2000.

[105] Mengler C.: Grobstruktursimulation der Strömungs- und Mischungsfelder komplexer, anwendungsnaher Konfigurationen. PhD thesis, Fachbereich Maschinenbau, TU-Darmstadt, 2001.

[106] Merker G.P., Schwarz Ch., Steisch G., Otto F.: Simulating combustion. Simulation of combustion and pollutant formation for engine-development. Springer-Verlag Berlin-Heidelberg, 2006.

[107] Moin P., Mahesh K.: Direct numerical simulation: A tool in turbulence research. Annual Review of Fluid Mechanics, Vol. 30, pp. 539-578, 1998.

[108] Moureau V., Lartigue G., Sommerer Y., Angelberger C., Colin O., Poinsot T.: Numerical methods for unsteady compressible multi-component reacting flows on fixed and moving grids. Journal of Computational Physics, Vol. 202, No. 2, pp. 710-736, 2005.

[109] Moureau V.R., Vasilyev O.V., Angelberger A., Poinsot T.: Commutation errors in Large eddy simulation on moving grids: application to piston engine flows. Proceedings of the Summer Program, pp. 157-168, 2004.

[110] Naitoh K., Itoh T., Takagi Y.: Large eddy simulation of premixed-flame in engine based on the multilevel formation and the renormalization group theory. SAE Technical Paper, 920590, 1992.

[111] Nordin N.: Complex chemistry modeling of diesel spray combustion. PhD thesis, Chalmers University of Technology, Sweden, 2000.

[112] O'Rourke P. J., Amsden A. A.: A Spray / Wall Interaction submodel for the Kiva-3 Wall film model. SAE Technical Papers, 2000-01-0271, 2000.

[113] O'Rourke P.J., Amsden A.A.: Implementation of a conjugate residual iteration in the KIVA computer program. LA-10849-MS, Los Alamos National Laboratory, 1986.

[114] O'Rourke P.J.: Collective drop effects in vaporizing liquid sprays. PhD thesis, Princeton University, 1981.

[115] O'Rourke P.J.: Statistical properties and numerical implementational of a model for droplet dispersion in a turbulent gas. LA-UR 87 2376, Los Alamos National Laboratory, accepted by J. Comput. Phys., 1987.

[116] O'Rourke P.J., Amsden A.A.: The TAB method for numerical calculation of spray droplet breakup. SAE Technical Paper Series, 872089, 1987.

[117] O'Rourke P.J., Amsden A.A.: Three dimensional numerical simulations of the UPS-292 stratified charge engine. SAE Paper 870597, 1987.

[118] O'Rourke P.J., Amsden A.A.: A particle numerical model for wall film dynamics in port-injected engines. SAE Technical Paper, 961961, 1996.

[119] Ortega J.M.: Introduction to parallel and vector solution of linear systems. Plenum Press, New York, 1988.

[120] Ozdor N., Dulger M., Sher E.: Cyclic variability in spark ignition engines, A Literature Survey. SAE paper, 940987, 1994.

[121] Pai G.M., Subramaniam S.: Accurate numerical solution of spray vaporization models using particle methods. ILASS Americas, 16th Annual Conference on Liquid Atomization and Spray Systems, Monterey, CA, May, 2003.

[122] Pannala Sr.: On large eddy simulations of reacting two-phase flows. PhD thesis, Georgia Institute of Technology, 2000.

[123] Papageorgakis G., Assanis D.N.: Optimizing gaseous fuel-air mixing in direct injection engines using an RNG based k-eps model. SAE Technical Paper Series, 980135, 1998.

[124] Park N., Yoo J. Y., Choi H. C.: Discretization errors in large eddy simulation: on the suitability of centered and upwind-biased compact difference schemes. Journal of Computational Physics, Vol. 198, No. 2, pp. 580-616, 2004.

[125] Patankar S.V.: Numerical heat transfer and fluid flow. Hemisphere Pub. Corp., Waschington D.C., 1980.

[126] Payri F., Benajes J., Margot X., Gil A.: CFD modeling of the in-cylinder flow in direct-injection diesel engines. Computers & Fluids, Vol. 33, No. 8, pp. 995-1021, 2004.

[127] Pfeil J., Fischer J., Kettner M., Spicher U.: Influence of spray propagation on the gas phase in a direct injection gasoline engine. The 10th International Symposium on Flow Visualization, Kyoto, Japan, 2002.

[128] Piomelli U., Moin P., Ferziger J. H.: Model consistency in large eddy simulation of turbulent channel flows. Physics of Fluids, Vol. 31, No. 7, pp. 1884-1891, 1988.

[129] Piomelli U., Ferziger J., Moin P., Kim J.: New approximate boundary-conditions for large eddy simulations of wall-bounded flows. Physics of Fluids a-Fluid Dynamics, Vol. 1, No. 6, pp. 1061-1068, 1989.

[130] Piomelli U., Balaras E.: Wall-layer models for large-eddy simulations. Annual Review of Fluid Mechanics, Vol. 34, pp. 349-374, 2002.

[131] Piomelli U.: Large-Eddy and direct simulation of turbulent flows. Dep. of Mechanical Engineering, University of Maryland, USA, 2005.

[132] Pischinger S., Aymanns R., Graf M., Stapf G., Adomeit P.: Analysemethoden zyklischer Schwankungen in direkteinspritzenden Ottomotoren. Motorische Verbrennung. Aktuelle Probleme und moderne Lösungsansätze (VIII. Tagung), München, 2007.

[133] Poinsot T., Veynante D.: Theoretical and numerical combustion. Edwards, 2001.

[134] Poinsot T.J., Lele S.K.: Boundary-conditions for direct simulations of compressible viscous flows. Journal of Computational Physics, Vol. 101, No. 1, pp. 104-129, 1992.

[135] Pope S.B.: Turbulent flows. Cambridge University Press, Cambridge, 2000.

[136] Pracht W.E.: Calculating three-dimensional fluid flows at all speeds with an Eulerian-Lagrangian computing mesh. Journal of Computational Physics, Vol. 17, No. 2, pp. 132-159, 1975.

[137] Reeves M., Garner C.P., Dent J.C., Halliwell N.A.: Particle image velocimetry analysis of IC engine in-cylinder flows. Optics and Lasers in Engineering, Vol. 25, No. 6, pp. 415-432, 1996.

[138] Reitz R.D., Rutland C.J.: Development and testing of diesel-engine CFD models. Progress in Energy and Combustion Science, Vol. 21, No. 2, pp. 173-196, 1995.

[139] Reitz R.D.: Modeling atomization processes in high-pressure vaporizing sprays. Atomisation and Spray Technology, Vol. 3, No. 4, p. 309-337., 1987.

[140] Reuss D.L.: Cyclic variability of large-scale turbulent structures in directed and undirected IC engine flows. SAE of Automotive Engineers, 2000-01-0246, 2000.

[141] Reynolds O.: On the dynamical theory of incompressible viscous flows and the determination of the criterion. Phil. Trans. Roy. Soc. QA 186, 123-164, 1894.

[142] Reynolds W.C.: Modeling of fluid motions in engines: an introductory overview. Combustion Modeling in Reciprocating Engines, Editors: Mattavi J.N. and Amann C.A., Plenum Press, New York, 1980.

[143] Richard S., Colin O., Vermorel O., Benkenida A., Angelberger C., Veynante D.: Towards large eddy simulation of combustion in spark ignition engines. Proceedings of the Combustion Institute, 31, 3059-3066, 2007.

[144] Rodi W.: DNS and LES of some engineering flows. Fluid Dynamics Research, Vol. 38, No. 2-3, pp. 145-173, 2006.

[145] Rotondi R.: Modeling mixture formation in a gasoline direct injection engine. Journal of Applied Mechanics-Transactions of the Asme, Vol. 73, No. 6, pp. 931-939, 2006.

[146] Rotondi R., Bella G.: Gasoline direct injection spray simulation. International Journal of Thermal Sciences, Vol. 45, No. 2, pp. 168-179, 2006.

[147] Sadiki A., Hahn F., Chrigui M., Janicka J.: LES-based methods for the prediction of turbulent reacting two-phase flows: a review. Progress in Energy and Combustion Science, submitted, 2006.

[148] Schäfer M.: Computational engineering - introduction to numerical methods. Springer-Verlag Berlin Heidelberg, 2006.

[149] Schänzlin K.: Experimenteller Beitrag Zur Charakterisierung Der Gemischbildung Und Verbrennung In Einem Direkteigespritzten, Strahlgeführten Ottomotor. PhD thesis, Zurich, 2002.

[150] Schmidt D.P., Rutland C.J.: A new droplet collision algorithm. Journal of Computational Physics, Vol. 164, No. 1, pp. 62-80, 2000.

[151] Schmidt D.P., Nouar I., Senecal P.K., Rutland C.J., Martin J.K., Reitz R.D., Hoffman J.A.: Pressure-swirl atomization in the near field. SAE Technical Paper, 1999-01-0496, 1999.

[152] Selle L., Lartigue G., Poinsot T., Koch R., Schildmacher K.U., Krebs W., Prade B., Kaufmann P., Veynante D.: Compressible large eddy simulation of turbulent combustion in complex geometry on unstructured meshes. Combustion and Flame, Vol. 137, No. 4, pp. 489-505, 2004.

[153] Senecal P.K., Schmidt D.P., Nouar I., Rutland C.J., Reitz R.D., Corradini M.L.: Modeling high-speed viscous liquid sheet atomization. International Journal of Multiphase Flow, Vol. 25, No. 6-7, pp. 1073-1097, 1999.

[154] Shah P., Markatos N.C.: Computer-simulation of turbulence in internal-combustion engines. International Journal for Numerical Methods in Fluids, Vol. 7, No. 9, pp. 927-952, 1987.

[155] Smagorinsky J.S.: General circulation experiments with the primitive equations, 1. The Basic Experiment. Monthly Weather Review, Vol. 91, No. 3, pp. 99-164, 1963.

[156] Smirnov A., Yavuz I., Celik I.: Diesel combustion and LES of in-cylinder turbulence for IC-engines. In-Cylinder Flows and Combustion Processes, No. 33-3 in 99-ICE-247, pp.119-127. ASME Fall Technical Conference, Michigan, 1999, 1999.

[157] Smirnov A., Celik I., Shi S.: LES of bubble dynamics in wake flows. Computers & Fluids, Vol. 34, No. 3, pp. 351-373, 2005.

[158] Soltau P.J.: Cylinder pressure variations in petrol engines. ImechE Conference Proceedings, July, pp.96-116., 1960.

[159] Sone K., Patel N., Menon S.: Large-eddy simulation of fuel-air mixing in an internal combustion engine. AIAA Paper, 2001-0635, 39th AIAA Aerospace Sciences Meeting, Reno, NV, 2001.

[160] Sone K., Menon S.: The effect of subgrid modeling on the in-cylinder unsteady mixing process in a direct injection engine. Journal of Engineering for Gas Turbines and Power-Transactions of the Asme, Vol. 125, No. 2, pp. 435-443, 2003.

[161] Staffelbach G., Gicquel L.Y.M., Poinsot T.: Highly parallel large eddy simulations of multiburner configurations in industrial gas turbines. Complex Effects in Large Eddy Simulations, Springer Berlin Heidelberg, Vol. 56, pp. 325-336, 2007.

[162] Stein O.: Grobstruktursimulation und Analyse der Strömung in direkteinspritzenden Ottomotoren. Diplomarbeit, Technische Universität Darmstadt, 2004.

[163] Stone R.: Introduction to internal combustion engines. Society of Automotive Engineers, 1992.

[164] Suck G.: Untersuchung der HC-Quellen an einem Ottomotor mit Direkteinspritzung. PhD thesis, Maschinenbau, Otto-von-Geuricke-Universität Magdeburg, 2001.

[165] Suh E.S., Rutland C.J.: Numerical study of fuel/air mixture preparation in a GDI Engine. Society of Automotive Engineers, 1999-01-3657, 1999.

[166] Tatschl R., Künsberg Sarre C., Berg E.: IC-engine spray modeling - status and outlook. International Multidimensional Engine Modeling User's Group Meeting at the SAE Congress, 2002.

[167] Tennekes H., Lumley J.L.: A first course in turbulence. MIT Press, Cambridge and London, 1972.

[168] Thinking Convergent. http://www.c-think.com/grid.htm

[169] Thobois L., Rymer G., Souleres T., Poinsot T.: Large-eddy simulation in IC engine geometries. SAE International, 2004-01-1854, 2004.

[170] Thobois L., Rymer G., Souleres T., Poinsot T., Van den Heuvel B.: Large-eddy simulation for the prediction of aerodynamics in IC engines. International Journal of Vehicle Design, Vol. 39, No. 4, pp. 368-382, 2005.

[171] Thompson K. W.: Time-dependent boundary-conditions for hyperbolic systems. Journal of Computational Physics, Vol. 68, No. 1, pp. 1-24, 1987.

[172] Torres D. J., Trujillo M. F.: KIVA-4: An unstructured ALE code for compressible gas flow with sprays. Journal of Computational Physics, Vol. 219, No. 2, pp. 943-975, 2006.

[173] Torres D.J., O'Rourke P.J., Amsden A.A.: A Discrete multicomponent fuel model. Atomization and Sprays, Vol. 13, No. 2-3, pp. 131-172, 2003.

[174] Towers D.P., Towers C.E.: Cyclic variability measurements of in-cylinder engine flows using high-speed particle image velocimetry. Measurement Science and Technology, Vol. 15, pp. 1917-1925, 2004.

[175] Unterlechner P., Kneer R.: Experimentelle und numerische Untersuchung zum Einfluss Zyklischer Schwankungen auf die Struktur Motorischer Einspritzstrahlen. BMBF Workshop, Turbulenz in der Energietechnik, Darmstadt, 2005.

[176] van Leer B.: Towards the ultimate conservative difference scheme v. A second-order sequel to Godunov's method. J. Comput. Phys., Vol. 32, No. 101–136, 1979.

[177] Vanzieleghem B.P., Chryssakis C.A., Grover R.O., Assanis D.N., Im H.G., Sick V.: gasoline direct injection modeling and validation with engine planar laser induced fluorescence experiments. 14th International Multidimensional Engine Modeling User's Group Meeting, Detroit, MI, March, 2004.

[178] Vanzieleghem B.P., Chryssakis C.A., Grover R.O., Sick V., Im H.G., Assanis D.N.: Modeling of gasoline direct injection mixture formation using KIVA-3V: development of spray breakup & wall impingement models and validation with optical engine planar laser induced fluorescence measurements. COMODIA 2004, Yokohama, Japan, August 2004, 2004.

[179] Vanzieleghem B.P., Sick V., Im H.G., Assanis D.N.: Modeling of gasoline direct injection mixture formation with KIVA-3V and validation with optical engine planar laser induced fluorescence measurements. W.E. Lay Automotive Laboratory, Department of Mechanical Engineering, University of Michigan, 2004.

[180] Vermorel O., Richard S., Colin O., Angelberger A., Benkenida A., Veynante D.: Multi-cycle LES simulations of flow and combustion in a PFI SI 4-valve production engine. SAE Technical Paper Series, 2007-01-0151, 2007.

[181] Wilcox D.: Turbulence modeling for CFD. California, DCW Industr. Inc., 1993.

[182] Williams F.A.: Phys. Fluids, Vol. 1, 541, 1958.

[183] Wu H.W., Perng S.W.: LES analysis of turbulent flow and heat transfer in motored engines with various SGS models. International Journal of Heat and Mass Transfer, Vol. 45, No. 11, pp. 2315-2328, 2002.

[184] Yavuz I., Celik I.: Assessment of various turbulence models for IC-engine applications. In ASME ICE Devision Fall Technical Conference, Ann Arbor, Michigan, 1999.

[185] Yavuz I.: Refined turbulence models for simulation of IC engine cylinder flows. Dissertation, Mechanical and Aerospace Engineering Department, West Virginia University, 2000.

[186] Yi J.: Rapid mesh generation and dynamic mesh management for KIVA-3V. Tenth International Multidimensional Engine Modeling User's Group Meeting, Detroit, Michigan, U.S.A., March 5, 2000, 2000.

[187] Zervas E.: Correlations between cycle-to-cycle variations and combustion parameters of a spark ignition engine. Applied Thermal Engineering, Vol. 24, No. 14-15, pp. 2073-2081, 2004.

[188] Zhao F., Lai M.-C., Harrington D.L.: A review of mixture preparation and combustion control strategies for spark-ignited direct-injection gasoline engines. SAE Paper 970627, 1997.

[189] Zimmermann F.P.: Neue Ansätze zur optischen und mikrooptischen Diagnostik in Verbrennungsmotoren. PhD thesis, Ruprecht-Karls-Universität, Heidelberg, 2006.

Curriculum Vitae

M.Sc. Dmitry Goryntsev

27.11.1977	Born in Saint-Petersburg single
1985 – 1995	State Grammar School No. 156, St.-Petersburg
1995 – 1999	Baltic State Technical University “VOENMECH” (BSTU), St.-Petersburg, Russia. Bachelor of engineering and technologies in the direction of "Applied mechanics"
1999 – 2001	Baltic State Technical University “VOENMECH” (BSTU), St.-Petersburg, Russia. Master of engineering and technologies in the direction of "Aircraft and rocket construction".
1999 – 2001	Institute for High Performance Computing and Data Bases, St.-Petersburg, Russia. Senior programmer C/C++
2001 – 2002	Center for Advanced Studies of the St.-Petersburg State Technical University, St.-Petersburg, Russia. Research officer / Developer C/C++
2001 – 2002	The State Scientific Center of Russia - Central R&D Institute for Robotics and Technical Cybernetics, St.-Petersburg, Russia. Research officer / Developer C/C++
2002 – 2007	Technical University of Darmstadt, The Institute for Energy and Powerplant Technology, Germany. Doctoral candidate